Structure and Dynamics of Plasma Layers Associated with Magnetic Reconnection in the Solar Wind - Cluster Spacecraft Observations

Alice Chloe Foster

Mullard Space Science Laboratory

Department of Space and Climate Physics

University College London

A thesis submitted to UCL for the degree of Doctor of Philosophy

May 18, 2017

I, Alice Chloe Foster confirm that the work presented in this thesis is my own. Where information has been derived from other sources, I confirm that this has been indicated in the thesis.

Abstract

We study magnetic reconnection events in the solar wind, using observations by the 4 Cluster spacecraft during periods where they are located in this region. Use of data from the 4 Cluster spacecraft allows us to look at the three dimensional structure of events at high time resolution, up to 0.04s for magnetic field data.

We present a case study of a magnetic reconnection event that was observed within the solar wind flow on the 2nd March 2006. This event enables us to test the consistency of the temporal and spatial structure of magnetic reconnection from large- to small-scales. We use data from the four Cluster spacecraft to study the three-dimensional structure of the event at sub-second resolution. This showed significant differences in the magnetic field data between spacecraft, despite the fact that they are separated by distances of only order $10^4 km$. Thus the structure appears to have variations over relatively small scales. We conclude that magnetic reconnection in the solar wind is not necessarily large-scale but, contrary to previous results, may be somewhat patchy in nature.

We also present a sketch for magnetic reconnection which has a more complicated structure than previous sketches of magnetic reconnection events in the solar wind. In addition we have introduced the observed magnetic field and ion velocities over the event depending on the inflow parameters and the strength of the diamagnetic effect of the outflow ions and electrons. We also compare a similarly structured mathematical model (*Owen and Cowley*, 1987b) with 3 case studies in the solar wind and compare the outflows predicted by the model with the observed outflows.

Finally we present the workings of an algorithm to find magnetic reconnection events in the solar wind and the subsequent statistical analysis of the events found.

The statistical analysis revealed that magnetic reconnection events occur for a wide range of solar wind conditions. We found that the exhaust speed was between $0.1 - 2\times$ Alfvén speed leading to the conclusion that, for ratios of less than 1, not all the magnetic field energy is converted to kinetic energy and, for those ratios greater than 1, that the reconnection site had a higher local Alfvén speed than where the exhaust was observed by the spacecraft. We also compared the data between Cluster spacecraft and determined that the spacecraft usually witness magnetic field structures that are strongly correlated with each other.

Acknowledgements

I would like to thank my parents and my little brother for the support, encouragement and enthusiasm they have given for my work (and everything else!).

I would like to thank my supervisors past and present Professor Christopher Owen, Dr Jonathan Rae and Professor Andrew Fazakerley for all their help and advice for the last 4 years, as well as the Plasma group as a whole. A lot of thanks to Dr Colin Forsyth in particular for the invaluable IDL help and support.

I would like to thank Dr Daisuke Kawata for all his help and support without which I would not have been able to finish.

I will always be very grateful to my office mates and house mates and students for making my time at MSSL enjoyable and for some great times.

To my university friends I want to say thanks for letting me offload my thesis woes, and for generally being very supportive.

I would like to thank STFC for funding this research.

Contents

List of Figures

List of Tables

Chapter 1

Introduction

1.1 Basic Plasma Physics

1.1.1 What is a Plasma?

A plasma is a quasi-neutral gas comprised of charged (and possibly some neutral) particles which exhibit collective behaviour and obeys the following plasma criteria.

1.1.2 Plasma Criteria

For an ionised gas to be considered a plasma it must obey the 3 criteria known as the plasma criteria. These are the quasi-neutrality condition, the plasma parameter and the collision condition.

The quasi-neutrality condition requires the plasma over its entire scale length to be quasi-neutral i.e. that the fluid volume is sufficiently large compared to its volume elements that any concentrations of charge will be shielded. This implies:

$$L \gg \lambda_D = (\frac{\epsilon_0 k_B T_e}{nq^2})^{1/2} \tag{1.1}$$

where L is the scale length of the system, λ_D is the Debye length, ϵ_0 is the per-

mittivity of free space, k_B is Boltzmann's constant, T_e is the electron temperature, n is the electron density and q is the electron charge. The Debye length is the distance at which there is a balance between the thermal particle energy which acts to perturb quasi-neutrality and the electrostatic potential energy which acts to restore neutrality.

There must be a sufficient number of particles in the Debye sphere in order for the shielding effect to occur. The Debye sphere is a sphere of radius, λ_D. Therefore:

$$N_D \gg 1 \tag{1.2}$$

$$N_D = (\frac{4\pi}{3})(n\lambda_D^3) \propto \frac{T^{3/2}}{n^{1/2}} \tag{1.3}$$

where N_D is the number of particles in the Debye sphere, also known as the plasma parameter, and n is the number density of the plasma. Finally the collision criterion states that the frequency of collisions with neutral particles must be much less than the period of plasma oscillations, so:

$$\omega_p \tau_n \gg 1 \tag{1.4}$$

$$\omega_p^2 = \frac{n_e q^2}{m_e \epsilon_0} \tag{1.5}$$

Where ω_p is the plasma frequency, n_e is the electron number density, τ_n is the mean period between collisions, q is the charge on an electron, and m_e is the mass of an electron.

1.2 Maxwell's Equations and the Lorentz Force

To describe an electric and/or magnetic field environment we use Maxwell's equations. In the following equations, **E** and **H** are electric and magnetic field respectively, **D** is the electric displacement, **B** is the magnetic induction vector, ϵ_0 and

μ_0 are the permittivity and the permeability of free space respectively, ρ is the total electric charge density and $\mathbf{j}$ is the current density.

$$\nabla \times \mathbf{E} = \frac{-\delta \mathbf{B}}{\delta t} \tag{1.6}$$

Equation 1.6 is known as Faraday's law of induction; a time varying magnetic field will produce a spatially varying electric field.

$$\nabla \cdot \mathbf{B} = 0 \tag{1.7}$$

Gauss' law for magnetism, given by the Equation 1.7, indicates that a magnetic field is divergenceless, which leads to the conclusion that magnetic monopoles do not exist.

$$\nabla \cdot \mathbf{E} = \frac{\rho}{\varepsilon_0} \tag{1.8}$$

Gauss' Law, Equation 1.8, states that the electric flux through any closed surface is proportional to the enclosed electric charge.

$$\nabla \times \mathbf{B} = \mu_0 \mathbf{j} + \mu_0 \varepsilon_0 \frac{\delta \mathbf{E}}{\delta t} \tag{1.9}$$

The final equation (1.9) is the Ampere - Maxwell law for magnetic field loops where the latter term indicates the depolarization term added by Maxwell and the first term is the original Ampere law where a time-varying electric current produces a spatially-varying magnetic field.

When considering Maxwell's equations it is also useful to note the following relations (in a vacuum):

$$\mathbf{D} = \epsilon_0 \mathbf{E} \tag{1.10}$$

$$\mathbf{H} = \mu_0 \mathbf{B} \tag{1.11}$$

1.3 Single Particle Motion

The most important force acting on a charged particle in a plasma, in the context of the solar wind, is usually the Lorentz force, which is given by:

$$\mathbf{F} = q(\mathbf{E} + \mathbf{v} \times \mathbf{B}) \tag{1.12}$$

q is the charge on the particle, **E** is the electric field, **v** is the particle velocity and **B** is the magnetic field. Thus if a non-stationary charged particle is in an electric or magnetic field (or both) then forces will act on the particle as described in Sections 1.3.1 - 1.3.3.

1.3.1 Uniform Magnetic Field

In a uniform magnetic field, the particle acceleration, given that no other force is acting (no E field), will be described by:

$$m\frac{d\mathbf{v}}{dt} = q(\mathbf{v} \times \mathbf{B}) \tag{1.13}$$

so the acceleration will be in a direction perpendicular to both **v** and **B**. This means that a particle with no velocity (**v** =0) will remain at rest, and a particle travelling in the direction parallel to the **B** field (**v** $\parallel$ **B**) will not be accelerated (as there are no forces acting upon it). If **v** is non-zero and not parallel to **B**, the particle will feel a force and be accelerated. Given that this force acts perpendicularly to both **v** and **B** the motion must be curved. If the initial velocity is entirely perpendicular to **B** then the motion will describe a circle, otherwise, as is the general case, there will be a component of the velocity parallel to **B** and thus the motion will describe

a helix: circular motion of a particle around a moving guiding centre. The motion is described by the angular frequency (gyrofrequency):

$$\omega_c = \frac{qB}{m} \tag{1.14}$$

and radius (gyroradius)

$$r_L = \frac{V_\perp}{\omega_c} \tag{1.15}$$

The acceleration is dependent on particle charge q and so positive and negatively charged particles will gyrate around the guiding centre in opposite directions.

1.3.2 Uniform Electric and Magnetic Fields

In an environment with a uniform electric field as well as a uniform magnetic field a particle will experience both an electric field force of $m\frac{d\mathbf{v}}{dt} = q\mathbf{E}$ and the force of $q(\mathbf{v}\times\mathbf{B})$ and thus the motion will be curved. In the case of a stationary particle it will initially only accelerate along $\mathbf{E}$ until there is a velocity component $\mathbf{v}$ and the particle experiences the force due to $q(\mathbf{v}\times\mathbf{B})$. The resulting motion is the gyration of a particle around a guiding centre moving at a drift velocity perpendicular to $\mathbf{E}$ and $\mathbf{B}$:

$$\mathbf{v_E} = \frac{\mathbf{E}\times\mathbf{B}}{B^2} \tag{1.16}$$

substituting $\mathbf{E} = \mathbf{F}/\mathrm{q}$ in Equation 1.16 we convert the equation for guiding centre drift into a form valid for any force acting on a charged particle in a magnetic field:

$$\mathbf{v_E} = \frac{\mathbf{F}\times\mathbf{B}}{qB^2} = \frac{1}{\omega_c}\left(\frac{\mathbf{F}}{m}\times\frac{\mathbf{B}}{B}\right) \tag{1.17}$$

1.3.3 Non- Uniform Fields

A more realistic situation will include non-uniform fields. In many cases there will be a magnetic field gradient ($\nabla \mathbf{B} \neq 0$) or the magnetic field will have curvature ($\nabla \times \mathbf{B} \neq 0$). For both of these cases there will be a resultant magnetic drift of charged particles. We first consider a non-homogeneous magnetic field in order to find the drift due to a magnetic field gradient:

$$\mathbf{B} = \mathbf{B_0} + (\mathbf{r}.\nabla)\mathbf{B_0} \tag{1.18}$$

where $\mathbf{B_0}$ is the magnetic field strength at the guiding centre and $\mathbf{r}$ is the distance from the guiding centre. The second term on the right hand side describes the changes in the magnetic field with distance from the guiding centre. In this case it is assumed that $\mathbf{B}$ is changing in a particular direction. Then the equation of motion (Equation 1.13) becomes:

$$m\frac{dv}{dt} = q(\mathbf{v} \times \mathbf{B}) = q(\mathbf{v} \times \mathbf{B}_0) + q[\mathbf{v} \times (\mathbf{r}.\nabla)\mathbf{B_0}] \tag{1.19}$$

The velocity of the particles is made up of a gyration and drift component $\mathbf{v} = \mathbf{v_g} + \mathbf{v}_\nabla$. In this case we make the assumption that $v_\nabla \ll v_g$ this means that we can omit $v_\nabla \times (r.\nabla)B_0$ as a negligible small term. There is no net drift due to gyration in a homogeneous field and so we can also omit the $\mathbf{v_g} \times \mathbf{B_0}$ term here to obtain:

$$m\frac{d\mathbf{v}_\nabla}{dt} = q(\mathbf{v}_\nabla \times \mathbf{B_0}) + q[\mathbf{v_g} \times (\mathbf{r}.\nabla)\mathbf{B_0}] \tag{1.20}$$

Rearranging and generalising the above equation we find the gradient dirft to be:

$$V_\nabla = \frac{mv_\perp^2}{2qB^3}(\mathbf{B} \times \nabla B) \tag{1.21}$$

This drift is perpendicular to the direction of the magnetic field $\mathbf{B}$, and the direction of the gradient ∇B.

Next we consider field which is curved in order to find the drift of charged particles due to the curvature of magnetic field, curvature drift. In this situation a particle will experience a centrifugal force:

$$\mathbf{F_c} = mv_{\parallel}^2 \frac{\mathbf{R_c}}{R_c^2} \tag{1.22}$$

where R_c is the radius of curvature. The curvature drift will therefore be:

$$\mathbf{V_c} = \frac{1}{\omega_c}\left(\frac{\mathbf{F_c}}{m} \times \frac{\mathbf{B}}{B}\right) = \frac{mv_{\parallel}^2}{q}\frac{\mathbf{R_c} \times \mathbf{B}}{R_c^2 B^2} \tag{1.23}$$

By adding Equations 1.21 and 1.23 we can say that the overall drift velocity is:

$$\mathbf{V}_m = \mathbf{V}_\nabla + \mathbf{V}_c = (v_{\parallel}^2 + \frac{1}{2}v_{\perp}^2)(\frac{\mathbf{B} \times \nabla B}{\omega_c B^2}) \tag{1.24}$$

It can be written in this form as $-\nabla B = (\frac{B}{R_c^2})\mathbf{R_c}$ in a cylindrically symmetric field. For more detail on single particle motion please refer to *Baumjohann and Treumann* (1997).

1.4 Magnetohydrodynamics (MHD)

Magnetohydrodynamics (MHD) is a way of modelling the dynamics of a plasma in which the single particle effects are ignored and the plasma is treated as a single magnetised fluid, thus combining the principles of fluid dynamics and Maxwell's equations. MHD is valid for low frequency and large time and length scales; thus plasma particle speeds $\ll$ speed of light, time between collisions $\ll$ time scales, the mean free path of particles $\ll$ overall length scale of the plasma and the Lamour radius $\ll$ overall length scale of the plasma.

1.4.1 MHD Equations

Mass Conservation: The mass conservation equation is as follows:

$$\frac{\partial \rho}{\partial t} + \nabla(\rho \mathbf{v}) = 0 \tag{1.25}$$

where ρ is mass density and v is velocity. Here the change in ρ for a fixed region of space is given by $\frac{\partial \rho}{\partial t}$ and the $\nabla(\rho \mathbf{v})$ term denotes the rate at which mass enters or leaves the region (no mass is spontaneously created or destroyed in this region). Thus mass is conserved.

Equation of motion: The equation of motion of a particle under MHD conditions is given by:

$$\rho(\frac{\partial}{\partial t} + \mathbf{v}.\nabla)\mathbf{v} = -\nabla.\mathbf{P} + \rho_q \mathbf{E} + \mathbf{j} \times \mathbf{B} + \rho \mathbf{g} \tag{1.26}$$

where $\mathbf{P}$ is the pressure tensor, $\mathbf{j} \times \mathbf{B}$ is the Lorentz Force where $\mathbf{j}$ is the electric current ρ_q is the charge density and so $\rho_q \mathbf{E}$ is the electric field force and ρg is the gravitational force. The pressure tensor is the plasma pressure. It is represented thus as in a magnetised plasma the pressure is not necessarily isotropic and often has different pressures parallel and perpendicular to the field. If $p_\perp = nk_B T_\perp = nk_B T_\parallel = p_\parallel$ then the pressure is isotropic and therefore $\nabla.\mathbf{P} = \nabla p$. As the plasma can be considered quasi-neutral we can effectively ignore the $\tau|\mathbf{E}|$ term as negligible, the same applies to the gravitational term in most cases to get:

$$\rho(\frac{\partial}{\partial t} + \mathbf{v}.\nabla)\mathbf{v} = -\nabla.\mathbf{P} + \mathbf{j} \times \mathbf{B} \tag{1.27}$$

Ohm's Law: The generalised Ohm's law is given by:

$$\mathbf{E} + \mathbf{v} \times \mathbf{B} = \eta \mathbf{j} + (\frac{1}{n_e})\mathbf{j} \times \mathbf{B} - (\frac{1}{n_e})\nabla \mathbf{P}_e + (\frac{m_e}{n_e^2})\frac{\partial \mathbf{j}}{\partial t} \tag{1.28}$$

where $\eta\mathbf{j}$ is the resistive term, $(\frac{1}{n_e})(\mathbf{j}\times\mathbf{B})$ is the term due to the Hall effect, $(\frac{1}{n_e})\nabla\mathbf{P}_e$ is the electron pressure term, and $(\frac{m_e}{n_e^2})\frac{\partial\mathbf{j}}{\partial t}$ is the term due to the electron inertia to the current.

Ideal MHD (IMHD): In the ideal MHD situation the following assumptions can be made with regard to Ohm's Law:

1. Resistivity vanishes, $\eta = 0$ (therefore the fluid is infinitely conducting) and so the resistive term is lost.

2. The 3rd and 4th terms on the RHS are often small enough to be considered negligible due to the length and time-scales relevant to MHD.

3. Assume that the currents perpendicular to the field are weak, thus the Hall term is negligible.

and thus the ideal Ohm's law becomes:

$$\mathbf{E} + \mathbf{v} \times \mathbf{B} = 0 \tag{1.29}$$

which corresponds to the 'frozen-in-flow' situation, which will be explained further in Section 1.4.2.

Resistive MHD (RMHD): If the plasma has a finite resistivity due to Ohmic losses (joule heating) the result is resistive MHD or RMHD and Ohm's Law becomes:

$$\mathbf{E} + \mathbf{v} \times \mathbf{B} = \eta\mathbf{j} = \mathbf{j}/\sigma \tag{1.30}$$

where σ is the conductivity. RMHD is useful for the discussion of magnetic reconnection and hence essential in this thesis.

1.4.2 Frozen - in Field Condition

When the frozen-in-field condition holds, cold plasma particles in a collisionless plasma will be bound to a specific flux tube, as will more energetic particles in the absence of strong magnetic field gradients or curvature. Therefore whenever a flux tube starts to move, the plasma will move with it. The opposite is also true: as a moving plasma can not leave the flux tube it is bound to, it will transport the flux tube along with it. The magnetic Reynolds number is used to define to what degree the frozen in field condition is satisfied. This depends on the characteristic scale length over which the magnetic field varies and the conductivity of the plasma. To define this mathematically we will start with 3 basic equations: Faraday's law (Equation 1.6), Ampere's law (Equation 1.9), and resistive Ohm's law (Equation 1.30).

Rearranging Ohm's law to make $\mathbf{E}$ the subject gives:

$$\mathbf{E} = \frac{\mathbf{j}}{\sigma} - \mathbf{v} \times \mathbf{B} \tag{1.31}$$

And taking the curl:

$$\nabla \times \mathbf{E} = -\nabla \times (\mathbf{v} \times \mathbf{B} - \frac{\mathbf{j}}{\sigma}) \tag{1.32}$$

Then equating Ohm's Law and Faraday's law:

$$-\frac{d\mathbf{B}}{dt} = -\nabla \times (\mathbf{v} \times \mathbf{B} - \frac{\mathbf{j}}{\sigma}) \tag{1.33}$$

$$\frac{d\mathbf{B}}{dt} = \nabla \times (\mathbf{v} \times \mathbf{B} - \frac{\mathbf{j}}{\sigma}) \tag{1.34}$$

Substituting Ampere's law (Equation 1.9) into this equation where $\frac{d\mathbf{E}}{dt} = 0$ rearranging to make $\mathbf{j}$ the subject $\mathbf{j} = \frac{1}{\mu_0}\nabla \times \mathbf{B}$

$$\frac{d\mathbf{B}}{dt} = \nabla \times (\mathbf{v} \times \mathbf{B} - \frac{1}{\mu_0 \sigma}\nabla \times \mathbf{B}) = \nabla \times (\mathbf{v} \times \mathbf{B}) + \frac{1}{\mu_0 \sigma}\nabla^2 \mathbf{B} \tag{1.35}$$

A dimensional analysis using $\nabla \rightarrow \frac{1}{L_B}$ where L_B is the characteristic length over which the field varies produces the following:

$$\frac{B}{\tau} = \frac{VB}{L_B} + \frac{B}{\tau_d} \tag{1.36}$$

where we define the magnetic diffusion time-scale as $\tau_d = \mu_o \sigma_0 L_B^2$ and τ is the characteristic time over which the magnetic field varies. The ratio of the first and second terms on the RHS define the magnetic Reynolds number. This can be used to determine if a medium is diffusion (second term) or flow (first term) dominated.

$$R_M = \frac{VB/L_B}{B/\tau_d} = \frac{V/L_B}{1/\mu_0 \sigma_0 L_B^2} = \mu_o \sigma_0 L_B V \tag{1.37}$$

When $R_M \gg 1$ the diffusion term can be neglected as it is much smaller than the flow term. The plasma is deemed frozen-in as the magnetic field moves together with the plasma flow. Note that in a diffusion-dominated region the plasma is able to move across the magnetic field lines.

The Lundquist number is an alternative ratio which can help determine what the dominant forces in a plasma are. The Lundquist number is given by:

$$S = \frac{v_A L}{\eta^*} \tag{1.38}$$

where v_A is the Alfvén speed $= \frac{B}{\sqrt{\mu_0 \rho}}$, $\eta^* = \frac{1}{\mu_0 \sigma}$ and L is the global scale length. High Lundquist numbers indicate a plasma that is highly conducting and, as with a high magnetic Reynolds number, indicate frozen-in-flow (*Schindler and Hornig*, 2001). In this thesis, we investigate the plasma in the solar wind environment which is a region with high Lundquist and magnetic Reynolds numbers. This indicates that this is a region in which the plasma is frozen-in to the magnetic field.

1.4.3 Magnetic Pressure and Tension

The magnetic total force term in MHD equations is given by:

$$\mathbf{F}_m = \mathbf{j} \times \mathbf{B} \tag{1.39}$$

Using Ampere's law (Equation 1.9) this can be re-written as:

$$\mathbf{F}_m = \frac{1}{\mu_0}[(\nabla \times \mathbf{B}) \times \mathbf{B}] \tag{1.40}$$

Which can be expressed as:

$$\mathbf{F}_m = -\nabla_\perp(\frac{B^2}{2\mu_0}) + \frac{B^2}{\mu_0}\frac{\mathbf{R}_c}{R_c} \tag{1.41}$$

Where $\mathbf{R_c}$ is the radius of curvature of the magnetic field lines and R_c is the magnitude of this radius. The first term is the magnetic pressure acting in the direction perpendicular to B caused by a gradient in magnetic field strength and the second term is the magnetic tension force which acts to 'straighten' curved magnetic field lines. These forces are relevant for any non-uniform field. In the solar wind, the subject of investigation in this thesis, we would not expect the magnetic field to be completely uniform at any time and thus these forces are relevant to any study.

1.4.4 Plasma Beta, β

Plasma β is the ratio of the plasma to magnetic pressure. Plasma pressure, assuming an isotropic plasma, is given by:

$$p_p = nk_BT \tag{1.42}$$

and magnetic pressure is given by:

$$p_m = \frac{B^2}{2\mu_0} \tag{1.43}$$

Thus the plasma β is given by:

$$\beta = \frac{2\mu_0 n k_B T}{B^2} \tag{1.44}$$

where n is the number density of the medium, k_B is the Boltzman constant, T is the temperature, B is the magnetic field strength and μ_0 is the permeability of free space. For more detail on MHD in its various forms please refer to *Baumjohann and Treumann* (1997).

1.5 Other Relevant Plasma Structures

This section contains a brief description of some terms which will be used later in this thesis.

Flux Tubes and Flux Ropes

A flux tube is a region of enclosed magnetic field with constant flux (for examples in the solar wind context see: *Moldwin et al.*, 2000; *Bruno et al.*, 2001, 2007). The magnetic field orientation at the boundary of the flux tube is parallel to the boundary (the boundary is often modelled as a current sheet). These regions are often cylindrical and tube-like in nature (hence the name flux tube). Flux ropes are groups of twisted magnetic flux tubes (*Solanki*, 1996).

Shocks

Shocks are transitional layers between regions of different plasma parameters (*De Hoffmann and Teller*, 1950). There are three different types of shock to consider in a plasma that obeys the laws of magnetohydrodynamics: slow mode, intermediate and fast-mode shocks (*Kantrowitz and Petschek*, 1966). Slow and fast-mode

shocks are both compressive: the difference between them being that the tangential component of the magnetic field decreases as plasma flows across a slow mode shock and increases across a fast mode shock. An intermediate-mode shock is non-compressive (*Kennel et al.*, 1985). For a more detailed look at shocks in plasmas see *Balogh and Treumann* (2013).

Current Sheets

Current sheets (e.g. *Speiser*, 1973; *Scheper and Hassam*, 1998) appear between regions of oppositely-directed magnetic field lines. Charged particles move around magnetic field lines in a helix shape, the direction of which depends on the sign of the charge of the particle in question (as previously discussed in Section 1.3.3). Figure 1.1 shows the basic concept of how a current sheet is formed. The red and green arrows indicate the magnetic field at opposite sides of the current sheet. Because the two magnetic field regions are oppositely-directed, like charges around each of the regions will be moving in the same direction in the boundary between the two. This will cause a current in the region between the magnetic field regions which is shown here by the black circles, to be directed out of the page. In the solar wind, many such current sheets will form as there are many regions of magnetic field directed towards and away from the Sun (*Priest*, 1985; *Li*, 2008).

Turbulence

Turbulence (*Kolmogorov*, 1941), which is defined as chaotic changes in a substance, can occur in any situation that has a flow. In turbulent flows we often see that the pressure or flow velocity of the substance changes over time scales much shorter than that of the lifespan of the system. Turbulence is increased in a plasma environment the further the plasma is from thermodynamic equilibrium

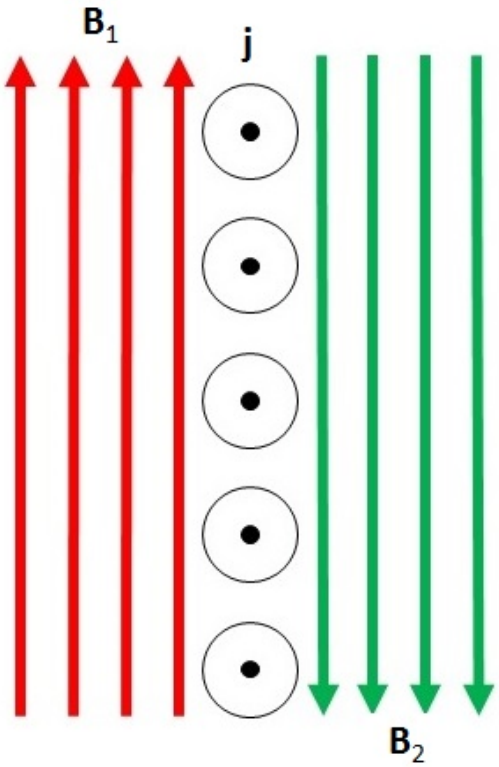

Figure 1.1: This sketch shows the basic shape of a current sheet between two sets of oppositely directed magnetic field lines, indicated by the red and green arrows. The black circles indicate the direction of the current out of the page as denoted by the curl of the field.

(*Tu and Marsch*, 1995; *Bruno and Carbone*, 2013). There are two main ways that turbulence is caused by the movement away from equilibrium: plasma currents and spatial gradients (*Pupodopoulos*, 2009).

1.6 The Sun and the Solar Wind

1.6.1 Basic Solar Parameters

The Sun is the source of the space plasma that is analysed in this thesis. It is a 4.5 billion year old star that is approximately halfway through its lifespan (*Meyer*, 2007). The Sun has a mass of 2×10^{30} kg, a radius of 6.9×10^{8} m and is made up predominately of hydrogen (90%) and helium (10%) (*Güdel*, 2007). The Sun consists of many layers; the central part of the Sun, the 'Core', is the source of energy via proton- proton chain, the next section is the 'Radiative zone', energy is transported outwards via predominately radiative methods, the outer section of the Sun is called the 'Convection zone' where convection is now the dominant form of energy transport (*Marsch*, 2006; *Howe*, 2009).

The Solar atmosphere is made up of a further three layers. The photosphere is the innermost region, then the chromosphere and finally the corona which is the outer atmosphere of the Sun and extends out into the heliosphere. The Sun rotates differentially; the equator rotates much more rapidly than the poles (*Meyer*, 2007).

1.6.2 The Solar Cycle

The solar cycle is the cyclic fluctuation of solar activity over the course of approximately 11 years (*Hathaway*, 2010). The periodic activity is most clearly reflected in the sunspot number which fluctuates greatly, from zero at the solar minimum

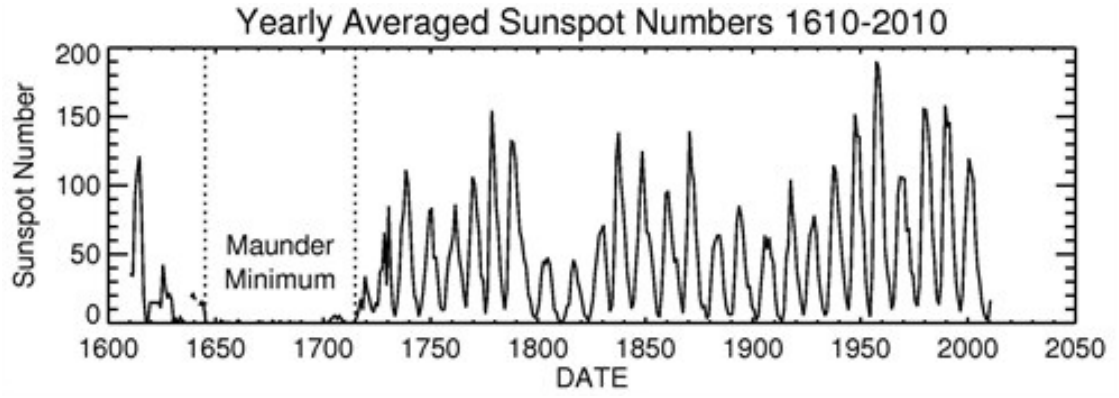

Figure 1.2: The yearly-averaged sunspot numbers from 1610-2010, image credit NASA.

to sometimes over 200 at solar maximum during a given cycle. The daily sunspot number has been recorded since 1849 which gives us a long term (in terms of human life at least) idea of the fluctuation of sunspot numbers (see Figure 1.2). It is shown that there is a great variation in the sunspot number for various solar maxima, from less than 10 sunspots to almost 200. The Maunder Minimum (*Eddy*, 1976), shown in Figure 1.2, in which there was a consistent period of very low sunspot number, corresponds to a period of significantly below average temperatures in Europe (*Mullan*, 2009). Figure 1.3 shows the direct connection between the total solar irradiance (shown on the top panel) and the sunspot number (shown on the bottom panel). At the point of maximum solar irradiance we see the highest number of sunspots (*Borrero and Ichimoto*, 2011).

The sunspot location changes over the solar cycle as shown by Figure 1.4. At the start of the cycle the sunspots appear at approximately $\pm 30^{\circ}$ but towards the end of the cycle sunspots are found nearer the equator (*Solanki*, 2008).

The Babcock model is used to help explain the changes in solar activity over the solar cycle (*Babcock*, 1961). A sketch of the Babcock model is shown in Figure 1.5. The first two images, stage 1, on the left of Figure 1.5 shows the Sun in its initial bipolar field at the start of a solar cycle. The plasma of the Sun is frozen into the

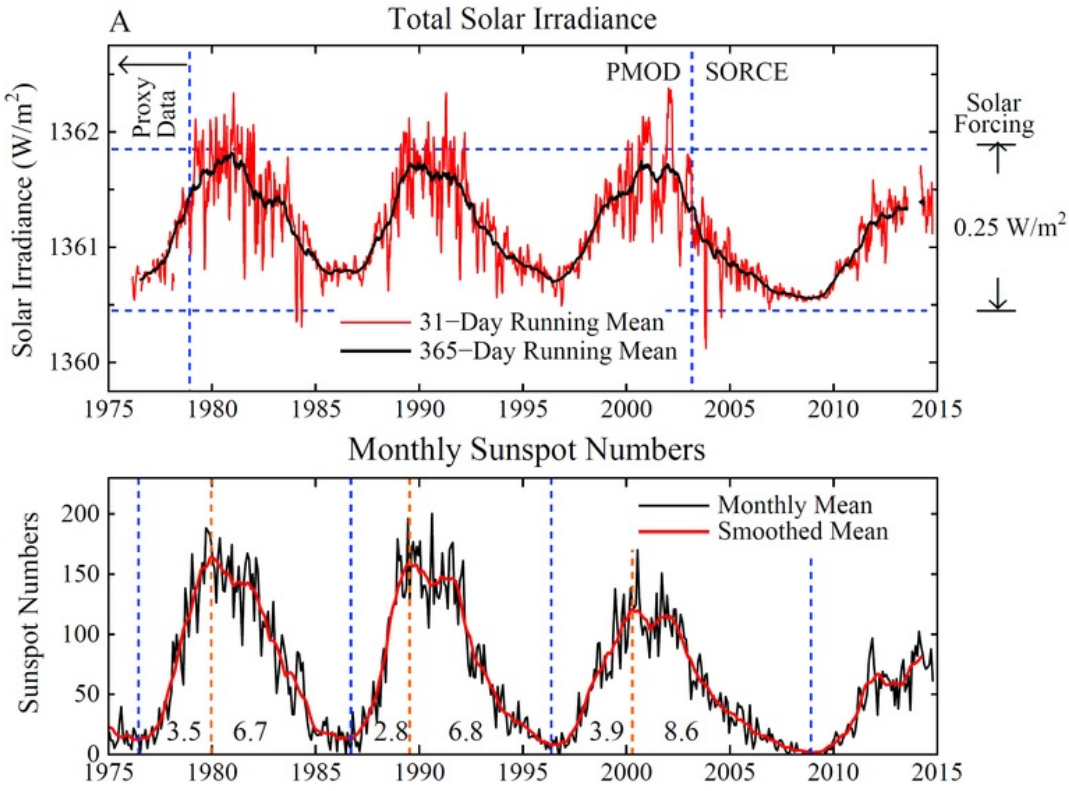

Figure 1.3: The total solar irradiance and the monthly sunspot numbers for the years from 1975 to 2015 (*Hansen*, 2013).

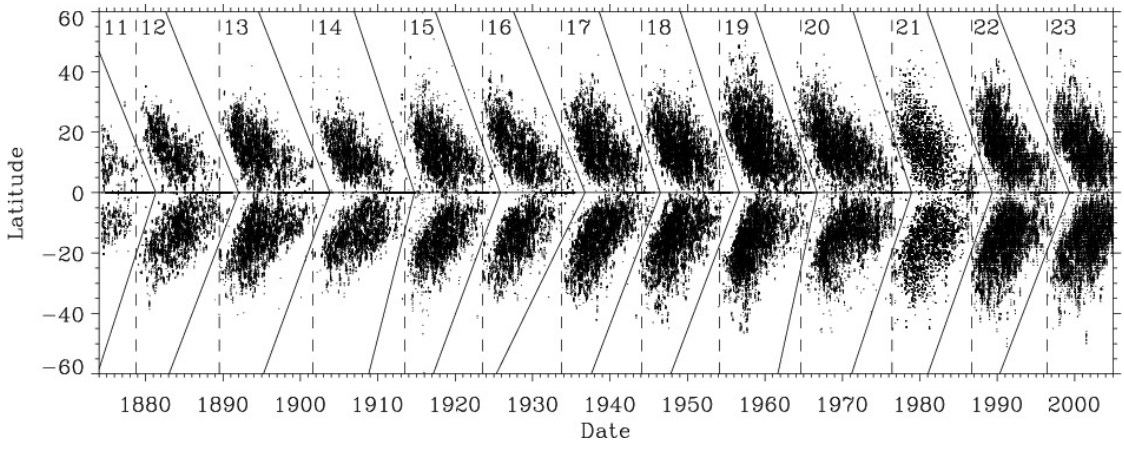

Figure 1.4: The diagram shows the positions of sunspots in latitude on the sun from 1873 to 2010. The vertical dashed lines indicate the sunspot minimum (*Solanki*, 2008).

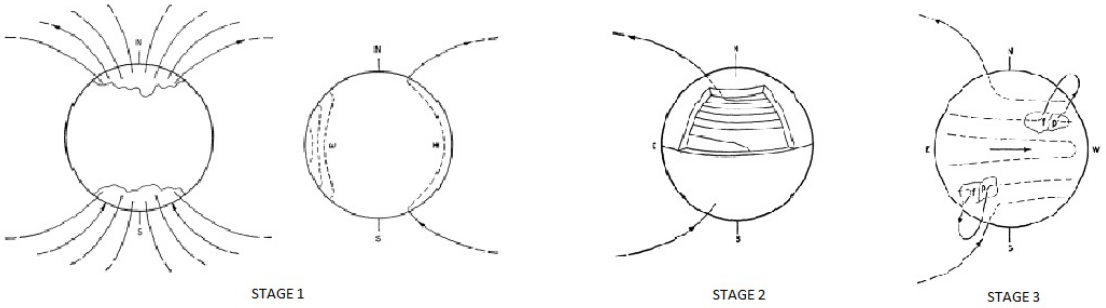

Figure 1.5: The 3 main stages of the Babcock model. At stage 1 the Sun has a dipole field, at stage 2 the magnetic field lines have been twisted under the surface of the Sun by differential rotation, in the 3rd stage bipolar magnetic field regions form and loops of magnetic field break the surface. These bipolar loops neutralise and merge at the equator and the polarity of the solar dipole switches around. Adapted from *Babcock* (1961)

solar magnetic field and so the plasma will move with the magnetic field and vice versa. As the Sun rotates differentially with the plasma at the equator rotating much quicker than that at the poles the magnetic field will get stretched out at the equator. This is seen at stage 2 where the submerged magnetic field lines have been dragged around. Stage 3 shows where the magnetic field has formed loops due to instabilities formed by twisting. In a fourth stage these loops naturally move towards the surface due to their magnetic buoyancy and produce bipolar magnetic regions (BMRs) associated with the formation of sunspot regions. These BMRs move towards the solar equator and the magnetic field is neutralised and reversed (*Babcock*, 1961; *Charbonneau*, 2010).

Coronal Mass Ejections (CMEs) and flares are associated mostly with stage 3 of the Babcock model in the active regions (although they can occur at any time during the solar cycle). CMEs and flares are caused by the reconnection of magnetic field on the surface of the Sun and they expel matter out into the solar wind. For more details see *Mullan* (2009).

1.6.3 The Solar Wind

The solar wind is an ionised, highly-conducting plasma that flows continuously and near radially outward from the Sun at speeds which are both supersonic and super-Alfvénic (*Parker*, 1958, 1965). It arises as the inward force of solar gravity is less than the outward corona pressure, and thus the plasma is driven outwards (*Marsch*, 2006; *Meyer*, 2007).

The atmosphere of the Sun is not in static equilibrium. In the Parker model of the solar wind the atmosphere is considered to be steady, spherically symmetric and isothermal. The following equations are those for a steady atmosphere with a radial velocity, v.

$$\frac{d}{dr}(r^2 \rho v) = 0 \tag{1.45}$$

$$\rho v \frac{dv}{dr} = -\frac{dp}{dr} - \frac{G m_p \rho}{r^2} \tag{1.46}$$

Here r = radial distance from the sun, ρ = mass density, v = flow speed, p = the gas pressure, G = the gravitational constant and m_p = is the proton mass. Substitute in $c_s = (p/\rho)^{1/2}$ the speed of sound:

$$\rho v \frac{dv}{dr} = -c_s^2 \frac{d\rho}{dr} - \frac{G m_p \rho}{r^2} \tag{1.47}$$

Dividing through by ρ:

$$v \frac{dv}{dr} = -\frac{c_s^2}{\rho} \frac{d\rho}{dr} - \frac{G m_p}{r^2} \tag{1.48}$$

Substituting $\rho = \frac{1}{r^2 v}$:

$$v \frac{dv}{dr} = -c_s^2 r^2 v \frac{d}{dr}(\frac{1}{r^2 v}) - \frac{G m_p}{r^2} \tag{1.49}$$

rearrange:

$$v \frac{dv}{dr} = -c_s^2 r^2 v (\frac{2}{r^3 v} - \frac{1}{r^2 v^2} \frac{dv}{dr}) - \frac{G m_p}{r^2} \tag{1.50}$$

$$v \frac{dv}{dr} - \frac{c_s^2}{v} \frac{dv}{dr} = \frac{2 c_s^2}{r} - \frac{G m_p}{r^2} \tag{1.51}$$

$$(v - \frac{c_s^2}{v})\frac{dv}{dr} = \frac{2c_s}{r^2}(r - r_c) \tag{1.52}$$

where $r_c = \frac{m_p GM}{4kT}$. There are several sets of solutions to this equation. Of the two physical solutions one gives a 'solar breeze' where the outflow is very slow. The other is the now accepted solution where the solar wind is subsonic near the Sun and increases in speed with radial distance.

The real solar wind (*Ogilvie and Coplan*, 1995) is comprised of both a fast and slow component. Each have sightly different properties. The most obvious difference is the speed of the two components; the slow solar wind (*Schwadron and McComas*, 2003) has a speed of approximately 400 $km\ s^{-1} \pm 100\ km\ s^{-1}$ whereas the fast solar wind (*Hassler et al.*, 1999) has a speed in the region of 800 $km\ s^{-1} \pm 100\ km\ s^{-1}$. The slow solar wind is on average much more dense than the fast solar wind with the slow solar wind having an average density of approximately 10 cm^{-3} and the fast wind 3 cm^{-3}. In the slow solar wind the electron temperature is higher than that of the protons (but the reverse is true in the fast solar wind). In the slow solar wind the proton temperature is near isotropic but in the fast solar wind the parallel temperature is higher than the perpendicular temperature. The slow solar wind tends to have a much larger proportion of helium particles. The fast solar wind streams have been linked to coronal holes as their open magnetic field structure is thought to accelerate solar wind plasma to higher speeds. The slow solar wind's origin is not well-defined but is thought to be emitted from regions of closed magnetic field lines (*Marsch*, 2006).

The solar wind, being highly conductive, and with a magnetic Reynolds number $R_M \simeq 7 \times 10^{16}$, is considered frozen into the magnetic field of the Sun at least for the distances which we will be considering in this thesis, and thus the outward solar wind flow drags the magnetic field lines along with a footpoint anchored in

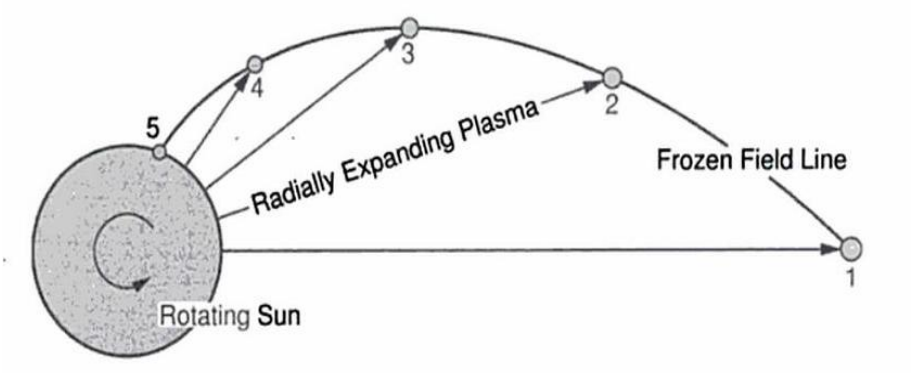

Figure 1.6: The magnetic field lines of the Sun are frozen into the outflowing solar wind plasma and so are dragged out with it, with a footpoint anchored in the solar atmosphere. Due to solar rotation the footpoint is rotated round the Sun bending the field lines into an archimedian spiral shape (*Baumjohann and Treumann*, 1997; *Parker*, 1968).

the solar atmosphere. Due to the additional effect of solar rotation, the magnetic field lines are bent into an Archimedean spiral shape (*Parker*, 1968), as shown in Figure 1.6. Here the frozen in plasma is indicated by the circles labelled 1-5. The arrows indicate the movement of this plasma away from the Sun and the bold black line shows the shape of the frozen-in field line.

The radial and azimuthal field components are the basis of a simple mathematical model of the interplanetary magnetic field. The radial field strength B(r) is given by:

$$B_r = \frac{B_0 dA_0}{dA} \tag{1.53}$$

where B_0 is the strength of the magnetic field at the solar surface, dA_0 is a unit area at the solar surface, dA is an area with equal B flux passing through it as dA_0 at a distance r from the Sun.

Here the magnetic field strength B_r is a ratio of the areas that the initial magnetic flux B_0 passes through as we move away from the Sun. We need to put this into a form we can define with variables that can easily be measured. We can

consider that dA is the same fraction of a sphere of radius r as dA_0 is to a sphere of the solar radius, R_0. $dA = dA_0(\frac{4\pi r^2}{4\pi R_0^2}) = dA_0(\frac{r^2}{R_0^2})$. Substituting this into Equation 1.53:

$$B_r = \frac{B_0 dA_0}{(\frac{r}{R_0})^2 dA_0} = B_0(\frac{R_0}{r})^2 \tag{1.54}$$

The azimuthal field strength is:

$$B_\phi = \frac{-\Omega}{U_r} B_0(\frac{R_0^2}{r}) \tag{1.55}$$

where Ω is the angular frequency of solar rotation and U_r is the radial velocity component of the solar wind. The azimuthal magnetic field is dependent on the ratio between the angular frequency of the solar rotation and the radial velocity component of the solar wind (*Parker*, 1968).

As $B_r \propto \frac{1}{r^2}$ and $B_\phi \propto \frac{1}{r}$ the spiral winds tighter with increasing distance away from the Sun. Additionally the interplanetary magnetic field lines can be divided into sectors depending on whether they are directed sunward or antisunward. The boundaries between two sectors of oppositely-directed field lines must have current sheets. The overall structure of the solar magnetic field gives rise to the heliospheric current sheet whose shape has been likened to that of a ballerina's skirt, as shown in Figure 1.7. The black lines indicate the magnetic field, and the surface shown is that of the HCS. However this is a simplified version.

Solar Cycle effect on the Solar Wind

The solar cycle effect is also seen in the solar wind (*Marsch*, 2006; *McComas et al.*, 2008), which is illustrated in Figure 1.8: the top 3 images show the solar wind speed over each orbit over the poles of the Sun as measured by the Ulysses spacecraft. The first orbit, shown on the left hand panel, was made during the solar minimum, the time of lowest solar activity during a cycle. It showed that there are

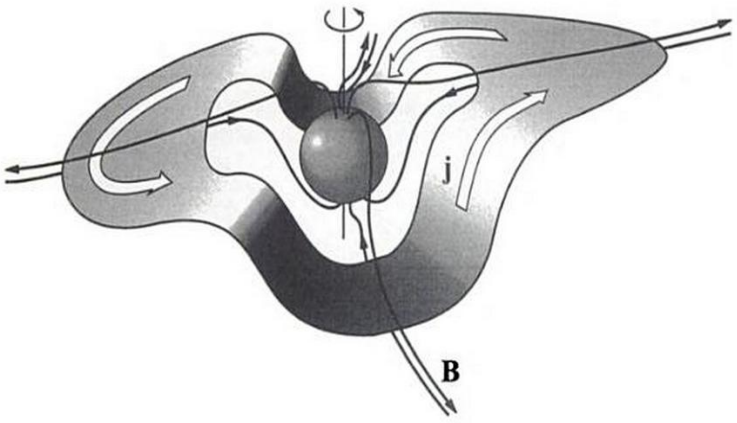

Figure 1.7: A simplified view of the heliospheric current sheet (*Baumjohann and Treumann*, 1997; *Parker*, 1968).

two distinct regions; around the equator the solar wind is predominately slow, at speeds of approximately 300 $km\ s^{-1}$ whereas, at higher latitudes the solar wind is much faster at speeds of up to 1000 $km\ s^{-1}$. The second orbit, shown in the middle panel, occurred during the solar maximum. In this image there is no longer the distinction in solar wind speed between the equator and higher latitudes, instead the fast and slow solar wind speeds occur at all latitudes. The panel on the right shows the final orbit of the Ulysses spacecraft during the next solar minimum. The bottom panel shows the solar activity with the sunspot number in black and the average current sheet tilt in red. The current sheet tilt is the angle between the heliospheric current sheet and the equator. Thus any observations of the solar wind will be affected by the solar cycle (*McComas et al.*, 2008).

1.6.4 Solar Events

Solar Flares

Solar flares (*Carrington*, 1859) occur predominantly in the corona at or between regions of flux cancellation (*Haisch*, 1989). They release energy at a rate of ap-

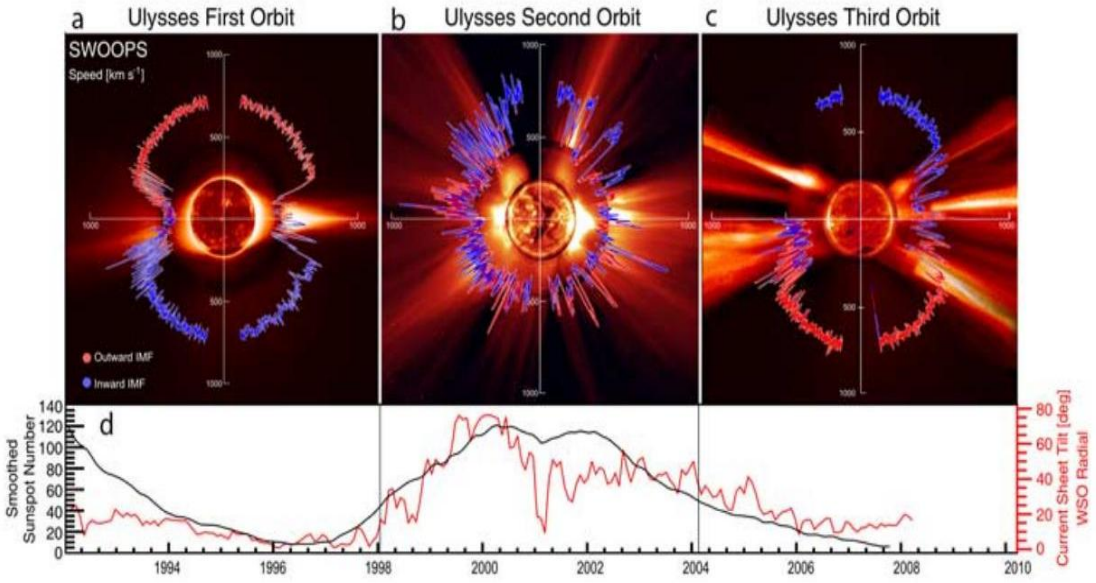

Figure 1.8: The top 3 panels show the three orbits that the Ulysses spacecraft made around the Sun. The leftmost panel, Ulysses first orbit, is during the solar minimum, the second orbit is during solar maximum and and the final panel showing the final orbit is during the next solar minimum. The graphs show the solar wind speeds over each latitude that the spacecraft encountered, where the red line shows instances where the solar IMF was facing outward and the blue line shows instances where the solar IMF was facing inward. The bottom panels show the solar activity levels over the time period that Ulysses was active with the black line indicating the number of sunspots and the red line indicating the tilt of the heliospheric current sheet. (*McComas et al.*, 2008)

proximately 10^{23} J in a total time frame of between $10 - 100$ ms (*Machado et al.*, 1988). Flares release radiation from across the electromagnetic spectrum. They are often associated with Coronal Mass Ejections (*Haisch*, 1989).

Coronal Mass Ejections

Coronal Mas Ejections (CMEs) are large 'bubbles' of coronal plasma and magnetic field being ejected at speed from the Sun which are thought to be propelled outwards via magnetic reconnection in the solar atmosphere (*Hansen et al.*, 1971). The properties of CMEs vary greatly: speeds are often in the range of $300-3000$ $km\ s^{-1}$, masses range from $5 \times 10^{12} - 5 \times 10^{13}$ kg and the energy contained ranges between $10^{23} - 10^{24}$ J (*Gosling et al.*, 1974, 1976). The daily occurrence frequency of CMEs ranges from approximately once per day during the solar minimum to approximately 4 times per day at solar maximum (*Howard et al.*, 1985; *Bothmer*, 2006).

Co-rotating Interaction Regions (CIRs)

Co-rotating interaction regions (*Hundhausen*, 1973; *Bryant et al.*, 1963; *Hundahausen and Burlaga*, 1975), so called as they co-rotate with the Sun (as the plasma is frozen-in to the Sun's magnetic field which is rotating), are formed due to the compression between regions of fast and slow solar wind. CIRs are particularly observed in the region of the heliosphere between 2-6 AU (*Smith and Wolfe*, 1976). The compression occurs as the high speed solar wind streams 'catch up' with slow solar wind streams. The leading edge of the CIR is a pressure wave that moves into the slow region and the trailing edge is a pressure wave moving into the fast region (*Hundhausen and Gosling*, 1976). Figure 1.9 shows an illustration of a CIR (*Hundhausen*, 1973). The solid lines indicate the magnetic field and the arrows

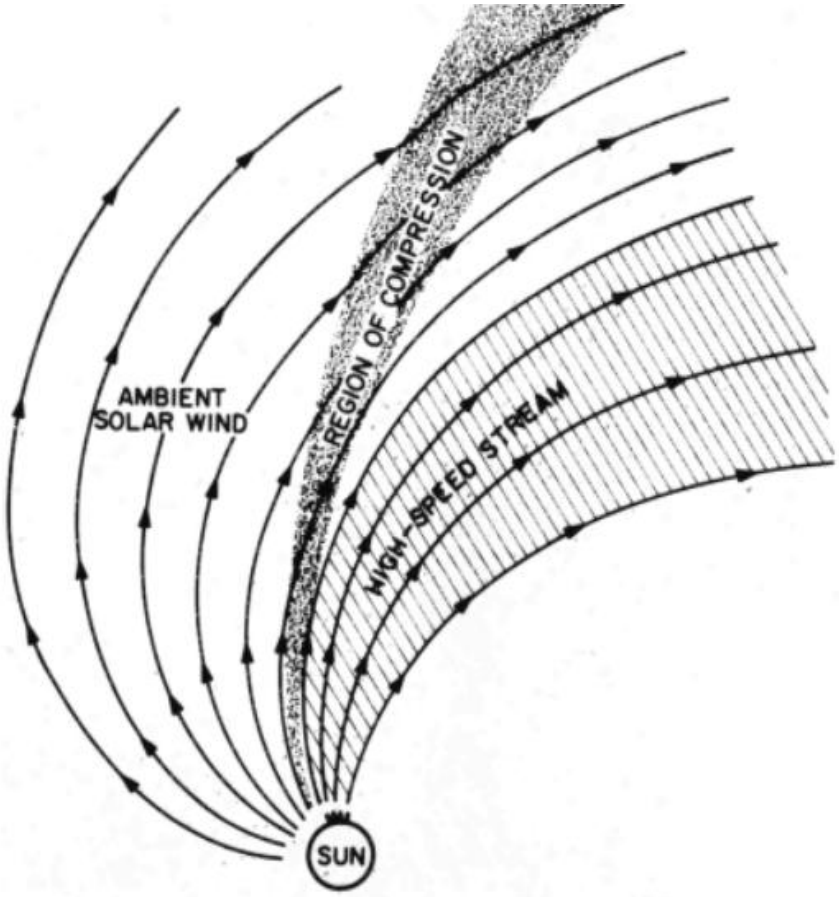

Figure 1.9: An illustration of a co-rotating interaction region The solid lines indicate the magnetic field and the arrows show the direction of the IMF. The darkest shaded region shows the compressed slow solar wind and the other shaded region shows the fast solar wind. (*Hundhausen*, 1973)

show the direction of the solar wind flow. The darkest shaded region shows the compressed slow solar wind and the other shaded region shows the fast solar wind (*Hundhausen*, 1973).

1.7 Earth's Bowshock and Foreshock

In this thesis we will be considering the ambient solar wind, but as we are using the Cluster spacecraft to obtain data we must be able to determine whether Cluster is in the ambient solar wind and/or if its observations can be affected by the Earth's magnetosphere. Figure 1.10 shows a representation of the magnetic field

environment around Earth. The blue circle indicates the location of Earth, the green lines show the Earth's magnetic field, the orange shaded area shows the plasma sheet, the red line indicates the position of the Earth's bow shock and the yellow arrows show the incoming solar wind.

In this thesis we are not concerned with any of the data within the Earth's bow shock, instead we ensure that the data that we use is outside and not connected to it.

1.7.1 Bow shock

The Earth's bow shock is formed as the supersonic solar wind encounters the Earth's magnetic field (*Ness et al.*, 1964; *Gosling et al.*, 1967). The solar wind downstream of the bowshock, in the magnetosheath must be slowed to subsonic speeds as it consists of shocked plasma (*Argo et al.*, 1967).

The angle of incidence of the solar wind IMF to the bow shock causes different types of shocks to appear along the boundary. The two extreme of these are perpendicular and parallel shocks. Perpendicular shocks (*Kennel et al.*, 1985), which are often located on the evening side of the bow shock have a small 'foot' and overshoot on either side of the discontinuity as is shown in Figure 1.10.

1.7.2 Foreshock

The parallel shock (*Parker*, 1961) found on the morning side of the bow shock is known as the foreshock (*Asbridge et al.*, 1968; *Fairfield*, 1969; *Greenstadt*, 1976). There are oscillations of the magnetic field travelling up and downstream, these oscillations can be found at large distances upstream of the shock (*Kennel et al.*, 1985).

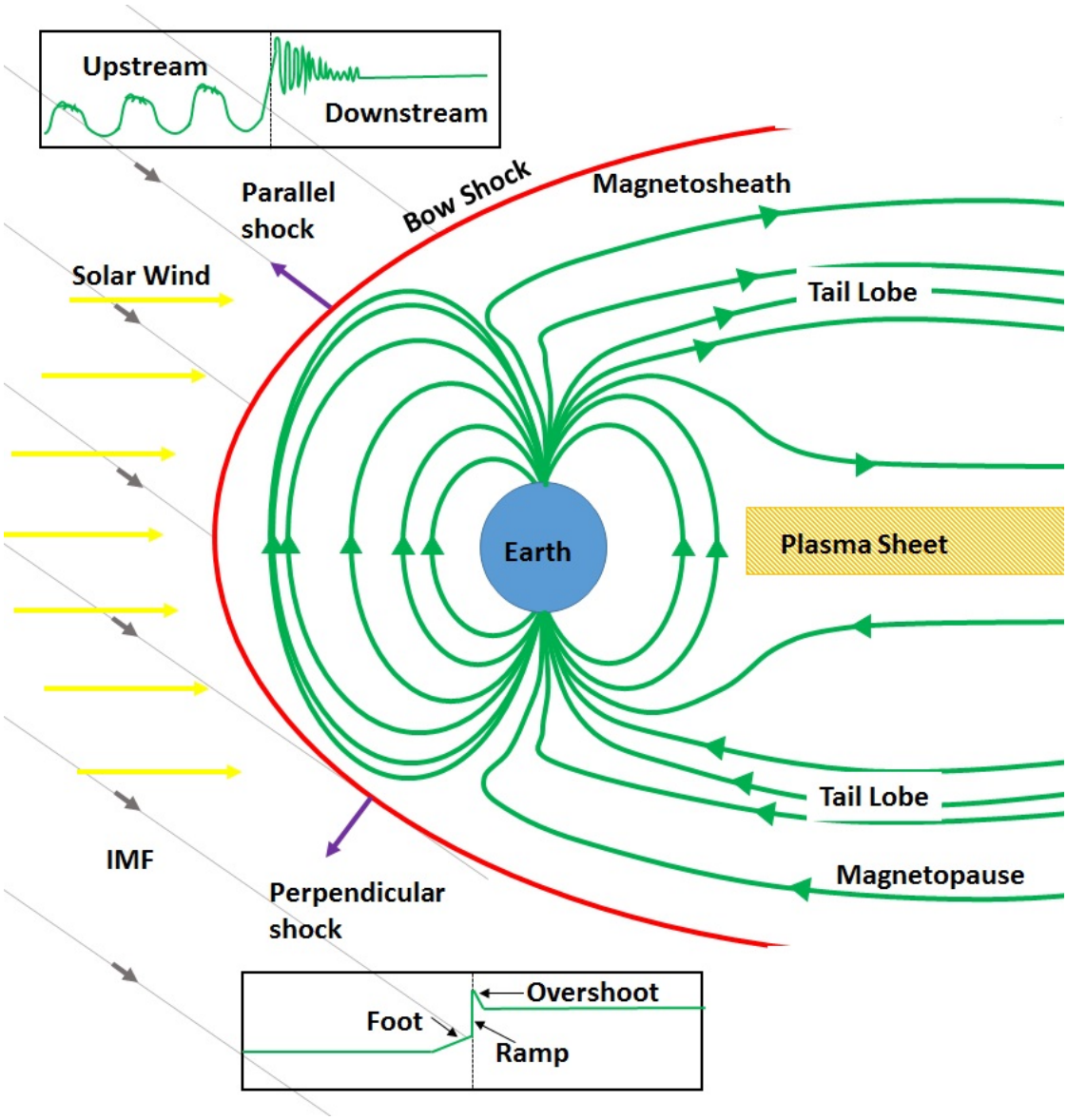

Figure 1.10: A schematic representation of a typical solar wind - magnetic field interaction. The yellow arrows indicate a typical solar wind flow, the red line the Earth's bow shock, the green lines the Earth's magnetic field and the orange shaded region in the plasma sheet. The grey arrows indicate a typical IMF and the purple arrows indicate the direction of the shock on the morning side (in the parallel shock case) and on the evening side (in the perpendicular shock case). The boxes next to each of the shock arrows indicates what the magnetic shock profile looks like in each case.

This means that if the Cluster spacecraft were upstream of the foreshock and magnetically connected to the bowshock it is likely that the Cluster spacecraft will see a highly oscillatory magnetic field (*Russell et al.*, 1983) and suprathermal ions propagating upstream (*Gosling et al.*, 1984).

The spacecraft could also encounter foreshock events such as foreshock cavities in which the plasma density and magnetic field is depressed and there is an increased flux of energetic ions (*Parks et al.*, 2006).

1.8 Magnetic Reconnection

Magnetic reconnection is a fundamental plasma process that occurs in thin current sheets, in which the frozen-in field condition of MHD is violated in such a manner that pairs of magnetic field lines merge to produce topological changes in the global field (*Giovanelli*, 1947; *Parker*, 1957, 1963; *Sweet*, 1958; *Vasyliunas*, 1975; *Gosling et al.*, 2005). The process of magnetic reconnection converts magnetic field energy to bulk flow energy and plasma heating (*Parker*, 1963; *Gosling et al.*, 2006). The amount of energy converted depends on the reconnection rate, duration of reconnection and the extent of the reconnection X-line (*Petschek*, 1964; *Phan et al.*, 2009). Reconnection allows magnetic field regions and plasma that were previously independent to interact. For example the reconnection of the interplanetary magnetic field with the Earth's magnetic field at the magnetopause allows the solar wind plasma to stream down reconnected field lines into the magnetosphere (*Dungey*, 1961). Magnetic reconnection, as shown in Figure 1.11, involves magnetic field lines, which have an anti-parallel component, merging. Figure 1.11 is a 2-dimensional cut through a reconnection region. A point appears where the two magnetic field lines merge (X-point) and reconnect to form new magnetic field

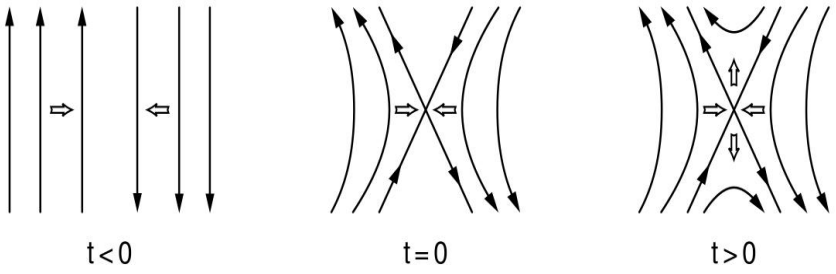

Figure 1.11: Oppositely directed field lines merge together to change the topology of the magnetic field. A point appears where the two magnetic field lines merge (X-point) and reconnect to form new magnetic field lines which move away from the X-point due to magnetic tension forces (*Baumjohann and Treumann*, 1997).

lines which move away from the X-point due to magnetic tension forces (*Dungey*, 1953).

A simple 2D model of steady state magnetic reconnection is shown in Figure 1.12. Here there are 2 main regions: the 'external region' and the 'diffusion region' (*Petschek*, 1964). In this configuration there is a non-vanishing electric field in the direction out of the page and the magnetic field vanishes at the neutral point (in the centre of the diffusion region). In the 'external region' the 2 inflow regions have oppositely-directed magnetic field lines which move towards each other in the x direction as denoted by the grey arrows. The magnetic field lines are moving towards each other due to the force acting on them directed towards the centre supplied by the non-vanishing electric field directed out of the page. In the external region IMHD applies as the plasma is highly ideal ($S \gg 1$) (*Schindler and Hornig*, 2001).

The 'diffusion region' is separated on Figure 1.12 into the ion diffusion region (shaded in red), and the electron diffusion region (shaded in blue). In the diffusion region the Reynolds number is near 1, and the locally defined Lundquist number (where L is replaced by δ) is much smaller than the global Lundquist number and

so the plasma is not frozen in, resistive diffusion can occur and plasma can move across magnetic field lines (*Biskamp*, 1986). As is shown on Figure 1.12 the size of the diffusion region for electrons and ions is different. The ion diffusion region is the larger of the two regions and encompasses the electron diffusion region. This is because the electrons and ions have different inertias and so the electrons remain frozen in closer to the reconnection site. The differing sizes of the ion and electron diffusion regions means that there is a dielectric effect between the two regions where there is a gradient in charge density. This effect produces the Hall current which is indicated by the dotted arrowed lines. These currents also produce the Hall magnetic field indicated inside the Hall current loops.

The outflow region contains reconnected magnetic field lines along with plasma from both inflow regions that has been accelerated by reconnection (*Sato*, 1979). This outflow is often referred to as a reconnection exhaust (and is how we will refer to it for the remainder of this thesis) and is characterised by an increase in ion velocity in the direction away from the reconnection site. Models of reconnection have been updated and revised since the theory was first introduced, we discuss some of the relevant theories below.

1.8.1 Sweet-Parker Model

The Sweet-Parker model (*Sweet*, 1958; *Parker*, 1957) is one of the first attempts to describe reconnection. Sweet's mechanism for magnetic reconnection is described in Figure 1.13. Here there are two regions of magnetic field lines embedded in a conducting fluid (a plasma) which are directed anti-parallel to each other. If these two regions are pressed together (as indicated by the short arrows) then this plasma will get 'squeezed out' between the two regions as shown by the long

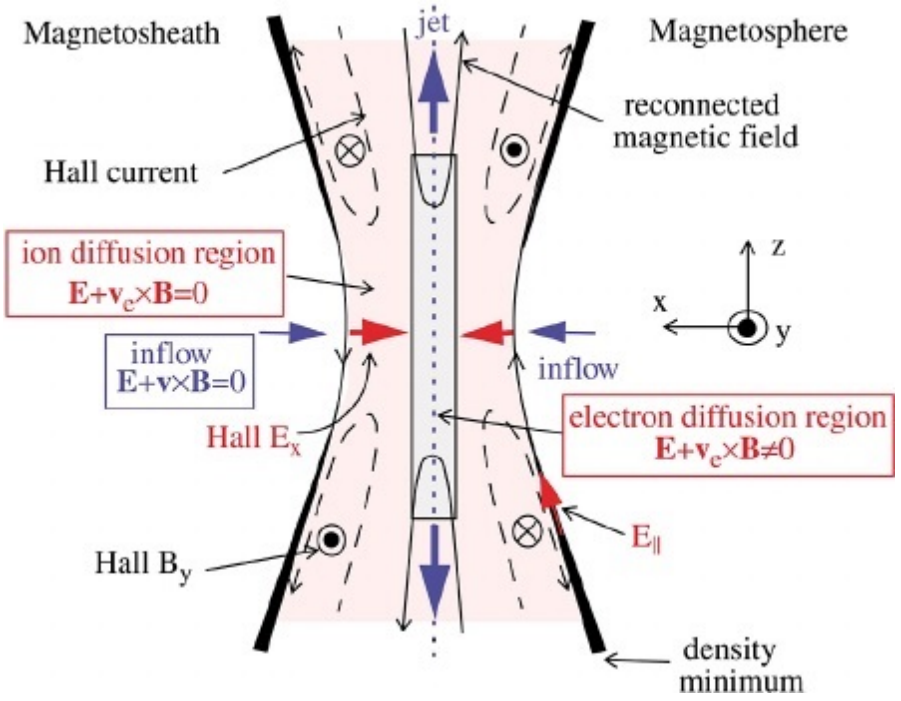

Figure 1.12: A simple 2D model of magnetic reconnection (*Torbert et al.*, 2016). The thick black vertical lines represent the magnetic field lines that are moving towards each other, the reconnected field lines are indicated by the thin black lines and the outflow jets are indicated by the thick blue arrows. The plasma inflow is shown by the thin blue arrows and the red arrows show the electron inflow in the ion diffusion region. The ion diffusion region in indicated by the red shaded region and the electron diffusion region is indicated by the blue shaded area. The Hall currents are indicated by the dashed arrows and the Hall magnetic fields are indicated by the dotted and crossed circles.

arrows, which allows the field lines to move closer together and merge. In this diagram there is a neutral point in the centre where the magnetic field lines merge. The transition layer where the plasma is being squeezed is indicated by the width 2l and the overall size of the two regions is given by the width 2L (*Parker*, 1963). In this model it is assumed that the diffusion region is thin and that it's length is of the same order of magnitude as the scale length, l, and the external region is homogeneous. From these assumptions the reconnection rate is given by the ratio between the inflow speed and the Alfvén speed:

$$M = \frac{V_{in}}{V_A} = \sqrt{\frac{\eta}{\mu_0 L V_A}} = \frac{1}{\sqrt{S}} \tag{1.56}$$

where V_{in} is the inflow speed, η is the resistivity and S is the Lunquist number. The main limitation with the Sweet - Parker model is that it gives reconnection rates which are much too low to explain the rapid energy release in, for example, solar flares (*Parker*, 1963). An example of a laboratory test of the Sweet-Parker theory is given in *Ji et al.* (1999)

1.8.2 Petschek Model

The Sweet-Parker model only takes into account diffusion for the conversion of magnetic field energy into other forms. The Petschek model (*Petschek*, 1964) also includes the effects of propagation of Alfvén waves and thus we get a slightly different topology for the reconnection as shown in Figure 1.14. In this model the original current sheet is bifurcated into two slow mode shock waves which propagate away from the Sweet-Parker current sheet, indicated on the figure as the length 2y*, which is much smaller than the overall length of the system. In the Petschek model both diffusion and wave propagation are important mechanisms for the annihilation of magnetic field energy in different regions of the reconnection.

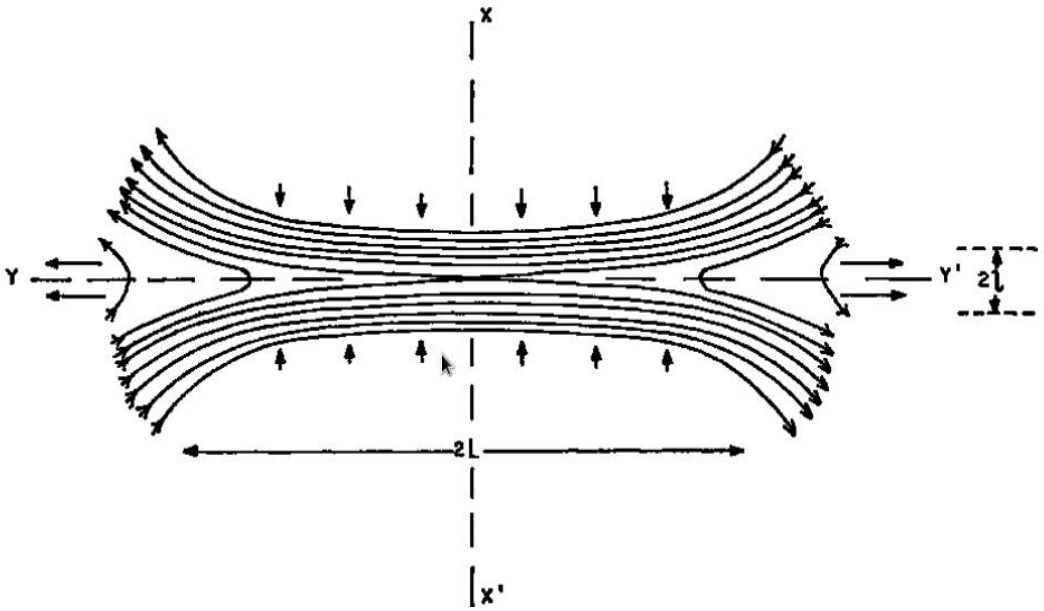

Figure 1.13: The Sweet mechanism for magnetic reconnection. Regions of oppositely directed field lines embedded in a plasma are pushed together, the plasma is squeezed out between the two regions allowing the magnetic field lines to move closer together and merge. The distance 2l indicates the transition layer where the plasma is being squeezed out and 2L indicated the width of the two regions. (*Parker*, 1963)

Diffusion is faster and therefore more dominant near the X-point and central Sweet-Parker current sheet. The rate of diffusion decreases with distance from the X-point and thus further from the X-point wave-propagation will be the dominant mechanism. This means that local to the X-point the Sweet-Parker model holds (*Parker*, 1957; *Kulsrud*, 2001). Where wave propagation dominates, the field lines will be bent sharply at the wave rather than bending gradually over the whole boundary (*Petschek*, 1964). In this case the maximum reconnection rate is where the magnetic field at the diffusion region is half that of the magnetic field outside the reconnection region, $B_{diff} = \frac{1}{2}B$ where $B_{diff} = B(1 - \frac{4M}{\pi} ln(\frac{L}{L_e}))$ and L_e is the global external length scale. Thus the reconnection rate is given by:

$$M < \frac{\pi}{8} \frac{1}{lnR} \tag{1.57}$$

where R is the magnetic Reynolds number. In this model the reconnection rates can be much larger than those found in the Sweet-Parker model which helps to better explain solar flare phenomenon (*Petschek*, 1964). However the numerical simulation conducted by *Biskamp* (1986) concluded that the Sweet-Parker mechanism is the more realistic solution.

1.8.3 Fast Reconnection Model

We define fast reconnection (*Priest and Forbes*, 1992) as being where the reconnection rate is faster than the maximum rate predicted by the Sweet-Parker Model. There are two different models of fast reconnection (*Sonnerup*, 1988); almost-uniform reconnection, where the magnetic fields are approximately uniform and anti-parallel, and non-uniform reconnection, where the magnetic field lines are strongly curved. In the almost-uniform model Petschek's model is a special case, as the magnetic field lines are only slightly curved. Fast reconnection is achieved

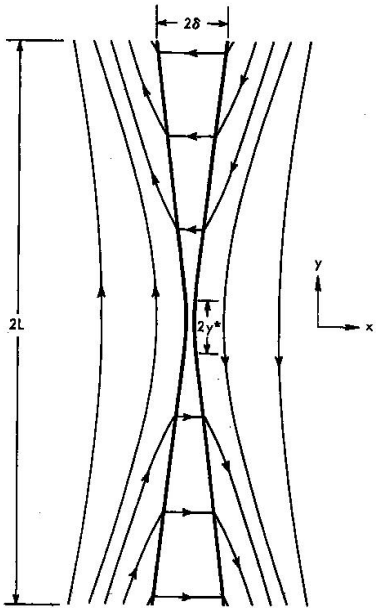

Figure 1.14: The Petschek model which includes wave propagation. The thick solid lines indicate the boundary layer where the magnetic field lines bend sharply (*Petschek*, 1964).

in this case as the x-line diffusion region shortens as the driving rate of reconnection is increased. The other, non-uniform case has strongly curved magnetic field lines and so the magnetic field strength at the diffusion region is increased (*Priest and Forbes*, 1986). This is often known as flux pile-up as the magnetic flux near the diffusion region has been increased. It also differs from the uniform case as the diffusion region lengthens with increased driving rate of reconnection. The non-uniform model has some similar features to the almost-uniform case but also includes some features that were found in numerical simulations (e.g. *Biskamp*, 1986; *Lee and Fu*, 1986); spikes of reversed current at the end of the diffusion region and strong jets of plasma along the separatrix lines. The separatrix lines are those lines that divide different regions of magnetic flux.

In the next chapter we will discuss magnetic reconnection in more detail in the solar wind environment.

Chapter 2

Literature Review

2.1 Introduction

It was discovered by *Gosling et al.* (2005) that magnetic reconnection occurs in the solar wind environment. Solar wind reconnection events give us a unique opportunity to study various aspects of magnetic reconnection that had not previously been possible to observe, as the solar wind current sheets do not have the limiting and fluctuating boundary conditions, in both time and space, that are seen in environments such as the laboratory or in the Earth's magnetosphere (*Davis et al.*, 2006). The solar wind rapidly convects structures associated with a magnetic reconnection event over a spacecraft, allowing us to see a snapshot of the event. Additionally, we may view individual events using multiple spacecraft due to their number in the solar wind. For example, the Advanced Composition Explorer (ACE) and Wind spacecraft are permanently situated in the solar wind and Cluster and Geotail spend large portions of their orbit in the solar wind at certain times of the year. This allows us to do multi-spacecraft analysis on e.g. a reconnection exhaust over large distances, spanning 100s of R_E, and time scales of a few

hours or greater.

The current idealised 2D magnetic reconnection model for the solar wind as devised by Gosling is as show in Figure 2.1. Reconnection acts to bifurcate the original undisturbed current sheet into the two current sheets labelled A1 and A2, due to the continual inflow into the reconnection site and propagation of pairs of Alfvénic disturbances along the field (*Gosling*, 2011). These two current sheets bound the reconnection exhaust, which is shown pointing away from the reconnection site. The magnetic field is represented by the solid arrows and can be seen to rotate significantly over each of the current sheets. The figure also shows an example of a spacecraft trajectory through such an exhaust as represented by the dotted arrowed line. From the point of view of the spacecraft, a magnetic field rotation should occur as it crosses each of the two current sheets and it should observe an acceleration of the plasma (the reconnection exhaust) between the two current sheets.

From this information it is clear that the main signature of magnetic reconnection should be the finding of accelerated or decelerated flows within a bifurcated magnetic field reversal region. The reconnection exhuast accelerates ions to speeds of the order 30 $km\ s^{-1}$. Depending on the orientation of the magnetic reconnection event this acceleration will appear as an accelerated or decelerated flow. If the reconnection site is positioned sunward of the traversing spacecraft the ions will appear to have been accelerated, as the increase in ion velocity is in the same direction as the bulk flow. If, however, the reconnection site is anti-sunward of the traversing spacecraft then the ions will appear to have been decelerated, as the increase in ion velocity is in the opposite direction to the bulk solar wind flow. It is therefore often necessary to calculate the sum of the changes to the components

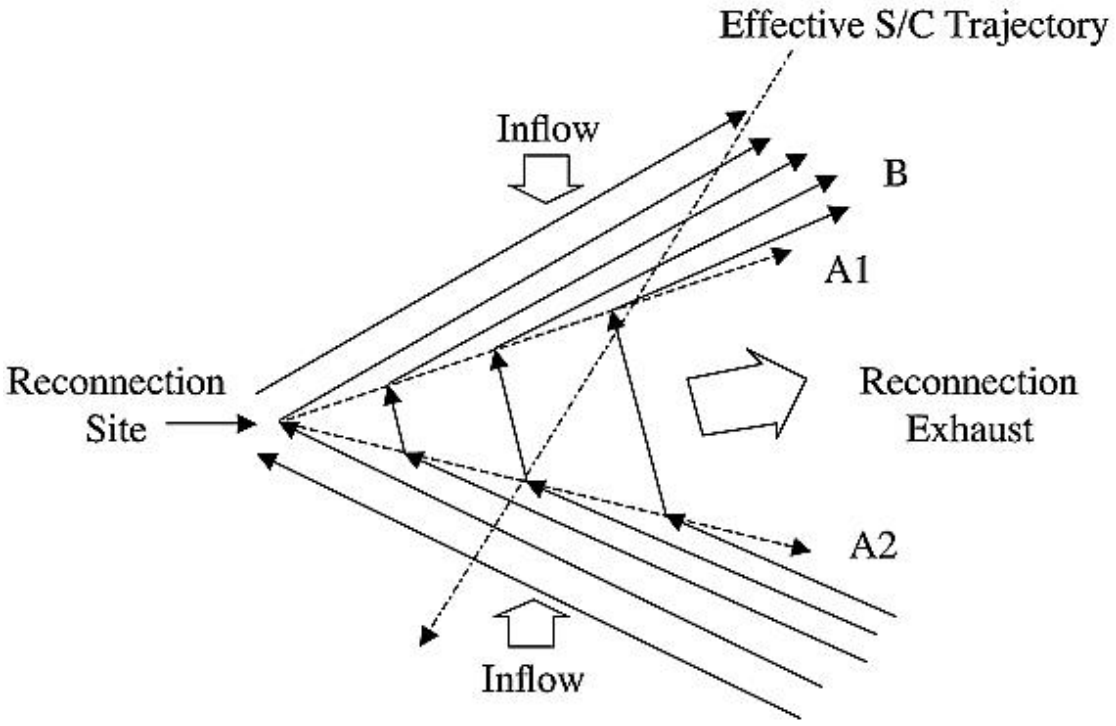

Figure 2.1: An idealised view of 2D reconnection in the solar wind. The original current sheet has been bifurcated to form two current sheets labelled A1 and A2 which bound the reconnection exhaust flowing away from the reconnection site. The magnetic field lines (shown by the solid black arrows) are seen to rotate over each of the two current sheets. A typical spacecraft trajectory is also shown by the dotted arrow (*Gosling et al.*, 2005).

of the ion velocity to get an accurate view of the ion velocity change.

The accelerated flows should theoretically be Alfvénic as the plasma in the reconnection exhaust is frozen into the magnetic field (*Parker*, 1963; *Petschek*, 1964). This magnetic field is moving away from the X-point due to the magnetic tension forces. Alfvén waves propagate due to the ion mass density and the magnetic tension force, driving the reconnected magnetic field lines away from the reconnection X-point (*Alfvén*, 1942). Therefore the magnetic field lines will move away from the X-point at a maximum of the Alfvén velocity:

$$V_A = \frac{B}{\sqrt{\mu_0 \rho}} \tag{2.1}$$

where B is the magnetic field strength, μ_0 is the permeability of free space, and ρ is the mass density of the plasma. It is possible to have a velocity lower than this if the transition from magnetic energy to kinetic energy is not 100% efficient.

An example of spacecraft encountering a magnetic reconnection event in the solar wind is shown in Figure 2.2. This data is taken from 3 spacecraft, ACE, Cluster-3 and Wind which all saw the same magnetic reconnection event on the 2nd February 2002 (*Phan et al.*, 2006). The panels (a) and (b) show data from the ACE spacecraft in GSE coordinates, with the magnetic field data shown in panel (a) and the ion velocity data shown in panel (b). Data from Cluster 3 and Wind are shown in panels (c) and (d) and (e) and (f) respectively. The data shows a bifurcated magnetic field structure: there are two distinct rotations, between which there is an increase in ion velocity. For example Cluster spacecraft observations show two rotations of the magnetic field at 02:32UT and 02:34UT predominately in the GSE_z direction (red trace). ACE initially sees the event at approximately 01:30 UT with Cluster 3 and Wind and observing at approximately 02:30 UT and 04:00 UT respectively. This means that reconnection was occurring for at least

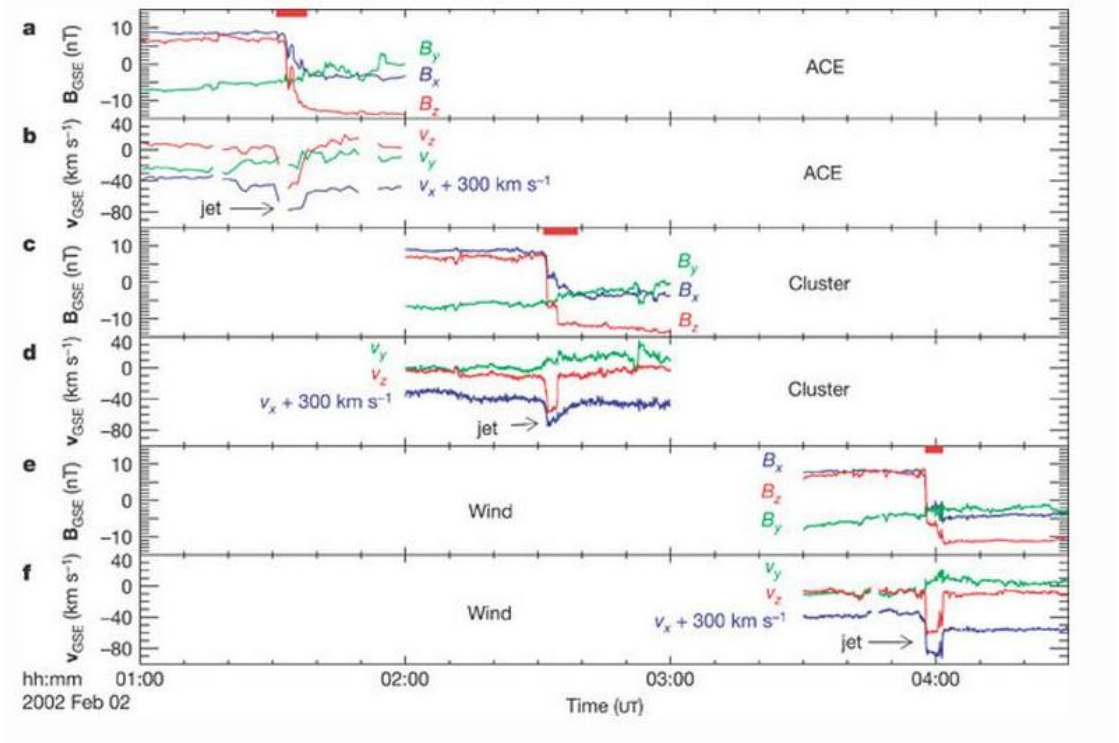

Figure 2.2: Magnetic field data and ion velocity data in GSE co-ordinates for the spacecraft ACE, Cluster and Wind of the same magnetic reconnection event that passed over the 3 spacecraft over a time frame of a few hours. The magnetic field data shows a magnetic field rotation predominately in the z-direction and the ion velocity data shows a velocity enhancement over the rotation also predominately in the z direction. (*Phan et al.*, 2006)

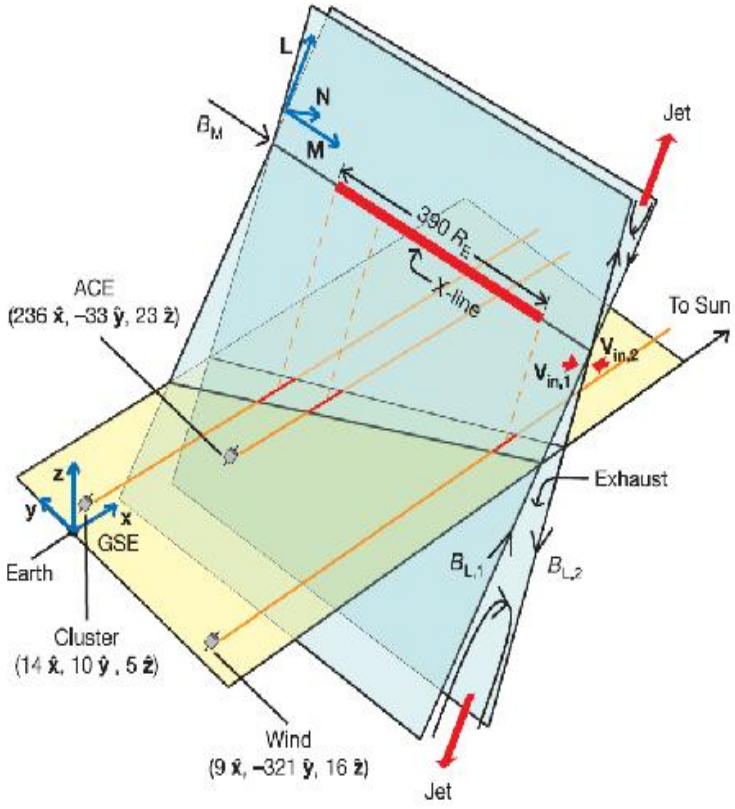

Figure 2.3: 3D representation of the event on the 2nd February 2002 with the positions of the two current sheets, indicated in blue, relative to the ecliptic plane, indicated in yellow, and the position of the 3 spacecraft relative to the Sun-Earth frame are shown. The two red arrows indicate the direction out the outflow exhaust and the red line indicates the position and direction of the X-line as measured by the 3 spacecraft. The orange lines indicate the motion of the spacecraft relative to the exhaust. (*Phan et al.*, 2006)

2.5 hours. Additionally, the positions of the spacecraft can be used to determine the lower limit to the length of the X-line. In this instance the X-line was found to be at least 390 R_E in length as illustrated by Figure 2.3. This figure shows the extrapolated structure of a magnetic reconnection event in the solar wind based on the magnetic field and ion velocity data shown in Figure 2.2. The blue planes are the current sheets, the red line indicates the X-line and the red arrow indicates the direction of the exhaust jet. The yellow plane indicates the ecliptic plane and the Earth, Cluster, ACE and Wind spacecraft are marked.

However there are several models for magnetic reconnection that have been used to describe this phenomenon in other situations or environments.

2.2 Reconnection in the Magnetospheric Context

2.2.1 Reconnection at the Magnetopause

Paschmann et al. (1979) found evidence for magnetic reconnection associated particle acceleration at the magnetopause. The reconnection model they devised is as shown in Figure 2.4. Here the dashed line marks the magnetopause separating the magnetosheath on the left, and the magnetosphere on the right. The magnetic field in the magnetosheath is directed southward (indicated by the solid lines) whereas in the magnetosphere it is directed northwards. Thus, where the two magnetic field lines meet at the magnetopause, reconnection may occur. The reconnected field lines and the plasma frozen into it are ejected poleward and equatorward at high speed. Data from the ISEE mission which flew through this region (as indicated by the dotted arrow) revealed the first evidence of these high speed jets.

A paper by *Heyn et al.* (1985) looked at the possible layers which may result from reconnection at the dayside magnetopause. They used essentially a 2D MHD compressible Petschek-type model but generalised for the conditions at the magnetopause. There are 4 possible discontinuities that can be present in the reconnection in this model (as shown in Figure 2.5): A contact discontinuity, C, inside the boundary layers separates plasma flow from the magnetosheath and magnetosphere, a large amplitude Alfvén rotational wave appearing on either side, A and $\tilde{\text{A}}$, which deflects and accelerates plasma, a slow shock or rarefaction on

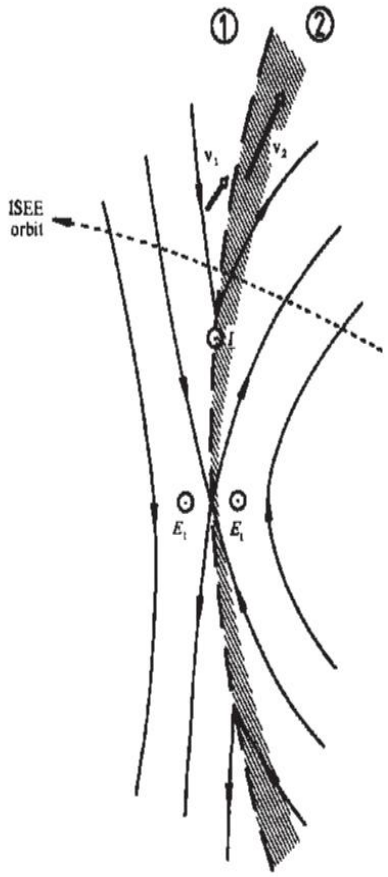

Figure 2.4: Magnetic reconnection at the magnetopause. The dashed line marks the magnetopause thus region 1 is the magnetosheath and region 2 is the magnetosphere. The solid lines indicate the magnetic field lines and the hatched region is the boundary layer. The reconnected field lines are convected poleward. The dotted arrow shows the trajectory that the ISEE spacecraft took when it flew through this region (*Paschmann et al.*, 1979).

either side (depending on the inflow conditions), S^- and $\tilde{\mathrm{S}}^-$ or R^- and $\tilde{\mathrm{R}}^-$. At each of the discontinuities the magnetic field is slightly rotated, except at A where there is a large rotation.

A slow mode shock is a a shock in which the magnetic pressure is lower in the disturbed side of the shock than on the undisturbed side (the opposite is true of a fast mode shock). A rarefaction is the reduction of density, thus a rarefaction wave is a moving wave of low density. These rarefaction waves often occur with shock waves. A switch off type shock is where the tangential magnetic field component is switched off over the shock (a switch on type would have the tangential component being switched on) *Boyd and Sanderson* (2003).

The general configuration in the Heyn model is $\mathrm{A}S^-(R^-)\mathrm{C}\tilde{\mathrm{S}}^-(\tilde{\mathrm{R}}^-)\tilde{\mathrm{A}}$. The Petschek model (*Petschek*, 1964) has symmetrical inflow conditions, which means that for this case the Alfvén wave and the slow shock on each side of the reconnection event will merge into a single, switch off type, slow shock. With non-symmetrical inflow conditions the two waves will be separate and must be considered as such. If we consider the problem in 2D, with no transverse magnetic fields or plasma flows, one of the Alfvén discontinuities disappears and therefore the configuration would be as shown in Figure 2.5; the heavy black lines represent the magnetic field lines, the plasma flow is represented by the dashed lines, the magnetosphere is labelled region $\tilde{\mathrm{I}}$ and the magnetosheath region I. At the Alfvén wave, A and the slow shock wave $\tilde{\mathrm{S}}^-$ the plasma is accelerated and escapes along the magnetopause. This diagram also shows the slow rarefaction R^-, red shaded region, and a contact discontinuity C, the green arrow. The structure of reconnection here is $\mathrm{A}S^-(R^-)\mathrm{C}\tilde{\mathrm{S}}^-(\tilde{\mathrm{R}}^-)$. Whether the wave is a slow shock wave or a slow rarefaction wave depends on the inflow conditions. A slow shock will form if

$v > v_{ACS}$ and a slow rarefaction wave will form if $v < v_{ACS}$ where:

$$v_{ACS} = \frac{(\mu-1)^2}{4}\frac{\gamma(\beta+1)+(2-\gamma)\mu}{\gamma(\beta+1)-(\mu+1)+(2-\gamma)\mu} \tag{2.2}$$

where $v = \tilde{\rho_0}/\rho_0$, $\mu = \tilde{B_0}$, $\beta = \frac{8\pi p_0}{B_0^2}$ and $\gamma = \frac{c_p}{c_v}$ the ratio of specific heats. This is shown in Figure 2.5. Thus a spacecraft travelling through an exhaust of a reconnection event should be able to distinguish these regions, given high enough resolution data.

A spacecraft travelling through the event (for example from the magnetosphere, $\bar{\text{I}}$, to the magnetosheath, I) would observe a reconnection exhaust of the deflected and accelerated magnetosphere plasma in the yellow region between the slow shock $\tilde{\text{S}}$ and the contact discontinuity, a reconnection exhaust of deflected and accelerated magnetosheath plasma which could be encountered in a number of regions depending on where the spacecraft crosses, a region of low density plasma at the rarefaction wave R^- (red shaded region) and a large rotation of the magnetic field at the Alfvén wave, A, where a component of the magnetic field at either side of the Alfvén wave will be anti-parallel.

Recently the Magnetospheric Multiscale spacecraft (MMS) has been studying magnetic reconnection at the dayside magnetopause. The MMS spacecraft is a set of 4 identical spacecraft that was launched in 2015. *Burch et al.* (2016) describes an encounter with a reconnection dissipation region on 8 December 2015 during the first scan of the magnetopause. This event involved the radial traversal of guide field reconnection. Other studies have reported electron energisation and mixing in the diffusion region (*Chen et al.*, 2016), observations of parallel electric fields associated with reconnection (*Ergun et al.*, 2016) and observations of an electron outflow jet for asymmetric reconnection (Khotyaintsev et al., 2016).

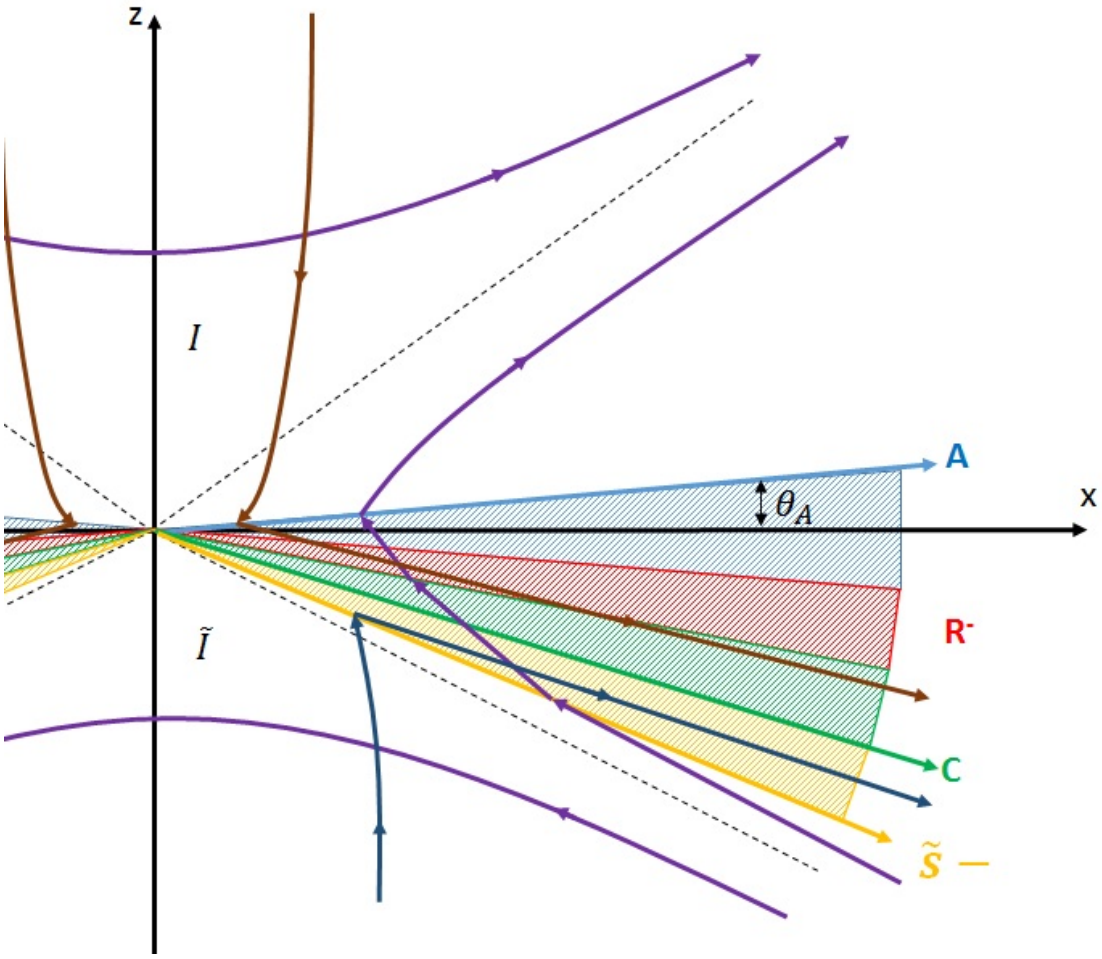

Figure 2.5: The heavy purple arrowed lines indicate the magnetic field lines, the separatrix by the dashed lines, the magnetosphere is labelled region $\tilde{\text{I}}$ and the magnetosheath region I. the ion flow from the magnetosphere is indicated by the brown lines and the ion flow from the magnetopause region by the navy blue lines. At the Alfvn wave, A (the blue arrowed line) and the slow shock wave $\tilde{\text{S}}^-$ (the yellow arrowed line) the plasma is accelerated and escapes along the magnetopause. This diagram also shows the slow rarefaction R^- (the red hatched wedge) and a contact discontinuity C (green arrowed line) (*Heyn et al.*, 1985).

2.2.2 Reconnection Models Including Hall Magnetic Fields

In *Phan et al.* (2007), a model for magnetic reconnection initiated in the magnetosheath was devised based on observations made by the Cluster 1 spacecraft as it travelled though the magnetosheath. This region contains accelerated plasma outflows, inter-penetrating ion beams, reconnection inflows, associated tangential reconnection electric fields and Hall magnetic fields. This magnetic reconnection configuration is summarised in Figure 2.6. This figure is drawn in the LMN coordinate system where L is along the plasma outflow direction, M is in the X-line direction and N is in the direction normal to the current sheet. Here the X-line is indicated in the centre of the diagram with the inflow of plasma pointing towards and the outflow jets pointing away from it. The Hall magnetic fields are located either side of the outflow jet with the Hall current flowing round them, as indicated by the dashed lines (*Phan et al.*, 2007). The Hall currents exist because the ion diffusion region and the electron diffusion region are not the same size. In fact the ion diffusion region extends further from the reconnection X-line than the electron diffusion region. This means that there will be a dielectric effect at the boundary between the two regions as there is a charge gradient as well as between the ion diffusion region and the background. These currents, labelled on Figure 2.6 as Hall currents, form a loop. This current loop produces a magnetic field due to Ampere's Law and is labelled on Figure 2.6 as the Hall magnetic field (*Craig et al.*, 2003).

2.2.3 Multiple Magnetic Reconnection Sites

It has also been suggested, initially by *Lee and Fu* (1986), that there could be multiple reconnection sites in the same region, i.e. reconnection occurs in a ad-

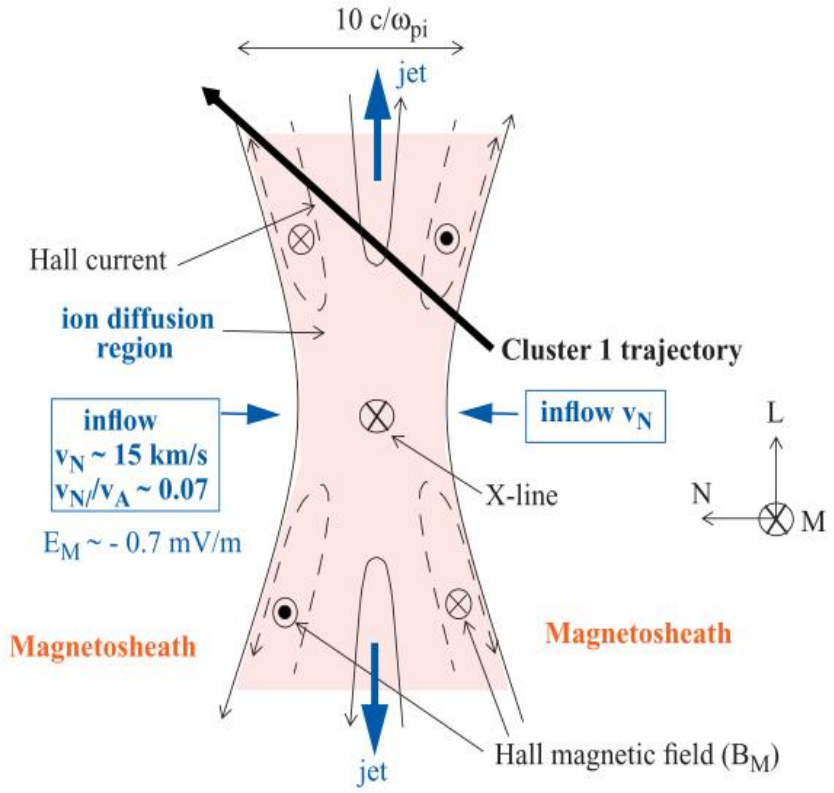

Figure 2.6: Hall magnetic fields are included in this model, located at either side of the outflow jets. The Hall currents are indicated by the dashed arrows (*Phan et al.*, 2007).

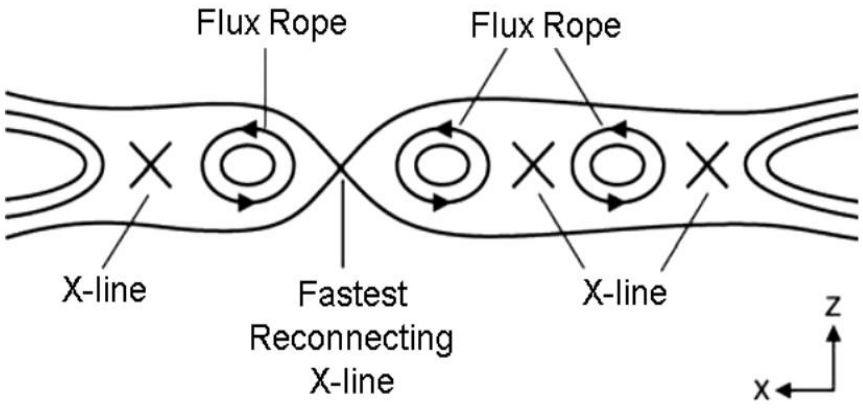

Figure 2.7: Multiple reconnection X-lines (adapted from *Slavin et al.* (2003)). Flux rope structures have been formed due to a cross-tail current. The X-line with the fastest reconnection rate is located in the centre and the reconnecting magnetic field has enveloped the X-lines and flux ropes at either side of this line and thus they will be ejected away from the dominant X-line. (*Slavin et al.*, 2003)

jacent sites, which creates a magnetic loop between them. Multiple reconnection sites will, in general, create flux rope structures (helical magnetic field). Where there are several X-lines it is inevitable that one of them will reconnect at a faster rate than the others and so will reconnect the field lines further out first. Thus, the X-line with the highest reconnection rate will be the first to reconnect the outer magnetic field lines which will serve to envelope all the flux ropes forming on either side of the dominant X-line. This will force the plasma and magnetic field structures away from the dominant X-line, along the current sheet. Figure 2.7 shows the configuration of the multiple X-line idea. The fastest reconnecting field line in the centre has forced the magnetic field to envelope the other X-lines and flux ropes at either side which will be expelled outwards (*Lee and Fu*, 1986).

2.3 *Owen and Cowley* (1987a)

There are also single particle models of reconnection (e.g. *Owen and Cowley*, 1987a), which are taken in the context of the geomagnetic tail. In the model described in *Owen and Cowley* (1987a), which we will discuss in this section, it is assumed that there is symmetrical inflow of plasma on either side of the current sheet.

The time-independent model must be considered first. In the plane normal to the neutral line, the configuration is as shown in Figure 2.8. In this case the X-line, labelled X_N is stationary. The central current sheet is indicated by the black solid line, the magnetic field by the solid arrowed lines, the plasma sheet (occupied by the plasma beams) by the blue hatched regions bounded by the blue dashed line and the outer boundary of the high speed ions by the black dashed line. This diagram illustrates reconnection for an inflow plasma velocity of $0.3V_A$, where V_A is the Alfvén speed, and a reconnection rate of $E_y = V_A B/4$. It is possible to illustrate other reconnection rates by scaling the vertical axis proportionally with the change in reconnection rate (*Owen and Cowley*, 1987a).

This model can then be used as the foundation for time-dependent reconnection models in which, for example, the reconnection rate varied, or there was motion of the neutral line. Considering first the model with time-dependant reconnection rate, we use the steady state model shown in Figure 2.8 as a reference. In this case we assume that the reconnection rate E_y is now time dependent; $E_{yN}(t)$. Information about any changes in the reconnection rate are propagated along the current sheet with the reconnecting X-lines and thus this information travels at approximately the Alfvén speed. Figure 2.9 shows the case where the reconnection rate has been increased from that of Figure 2.8, to a rate 3 times as large after

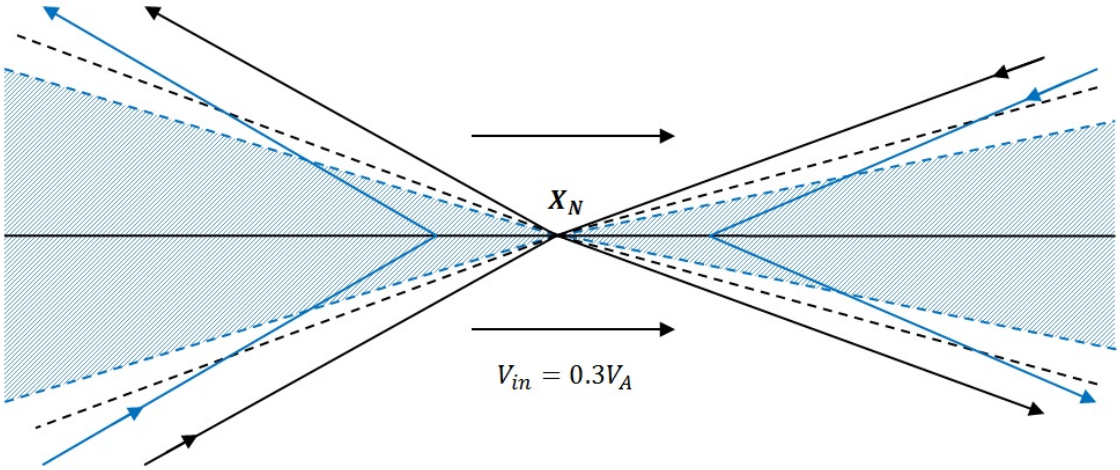

Figure 2.8: Steady state reconnection looking along the stationary X-line (labelled X_N). The horizontal solid black line indicates the current sheet, the solid arrowed lines indicate the magnetic field, the blue hatched region is the plasma sheet (occupied by the plasma beams) and the black dashed lines show the boundary for the high speed ions. This diagram shows reconnection for inflow plasma speeds of 0.3 V_A and a reconnection rate of $E_y = V_A B/4$ however it is possible to represent other reconnection rates by scaling the vertical axis proportionally with the change in reconnection rate (*Owen and Cowley*, 1987a).

an arbitrary time τ has elapsed. The B_z has been tripled, and thus the event boundaries are wider up to the point that the information regarding the change in reconnection rate has travelled to: $V_f\tau$. Lines $a-a$ and $b-b$ represent the last reconnected field lines before the change and pass through the current sheet at $V_f\tau$ at either side of the neutral line (*Owen and Cowley*, 1987a).

Secondly, time-dependent reconnection in the form of movement of the X-line is considered; steady movement and an increase or decrease of the X-line speed. In the situation where the X-line is in constant steady motion the resulting reconnection configuration should appear as shown in Figure 2.10 (i). The neutral line is moving at a speed of $0.7V_A$ going from left to right. Previously in Figure 2.8 it was shown that there was an asymmetry around the neutral line with a larger B_z to the left of the neutral sheet due to the lobe moving from left to right whereas in this case the neutral line speed exceeds the lobe speed and thus the asymmetry is switched around. In part (ii) the neutral line has suddenly begun to travel at the speed in (i) after initially being at rest. During the time τ that the neutral line has been moving it has translated from point $X_N(0)$ to $X_N(\tau)$. The last magnetic field lines to be reconnected ($a-a$ and $b-b$) have travelled a distance $v_f\tau$ away from the original neutral point location $X_N(0)$. Part (iii) shows a similar configuration to part (ii) only this time the X-line has stopped moving from an original speed of $0.7V_A$ going from left to right (*Owen and Cowley*, 1987a).

A variant on this time dependent model was produced by *Semenov et al* (1983) and *Biernat* (1987) which is structured as Figure 2.11. In this case the time dependence is due to a varying reconnection rate. The reconnected field lines are caused to move by their tension with the Alfvén velocity in the direction of the reconnection exhaust. This unstable surface creates slow mode standing

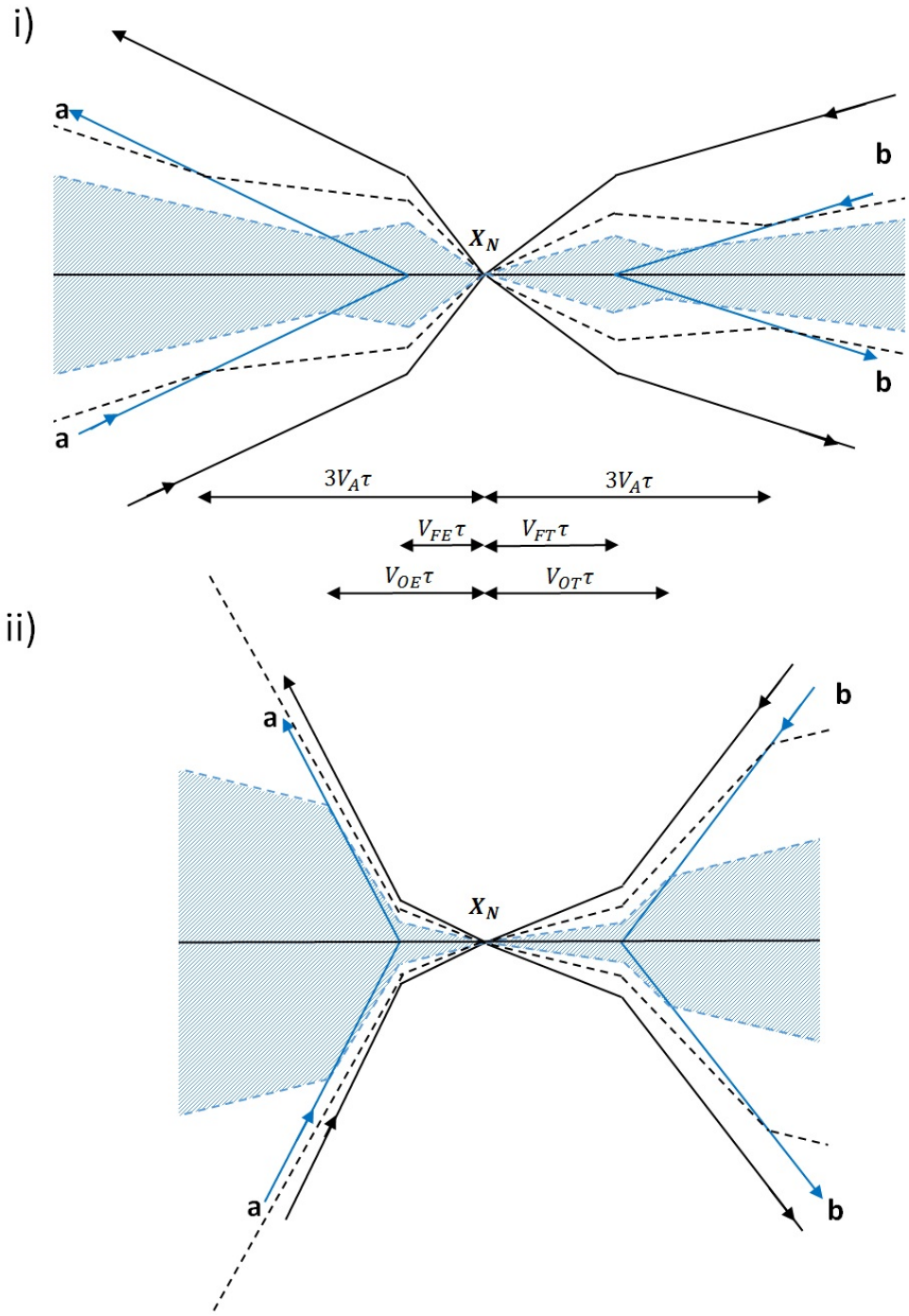

Figure 2.9: (i) shows the change in configuration with a $\times 3$ increase in the reconnection rate. As information about variations in E_y at the neutral line propagates at V_F then only within the distance $V_f\tau$ has the field reached the new equilibrium. Further than this the field is still in its original configuration. The change between the two regimes occurs at a discontinuity at the point $V_f\tau$ either side of the neutral line. Lines $a-a$ and $b-b$ represent the last reconnected field lines before the change and pass through the current sheet at $V_f\tau$ at either side of the neutral line. (ii) similar set up to (i) but in this case the reconnection rate is going from that in (i) back down to the original reconnection rate (*Owen and Cowley*, 1987a).

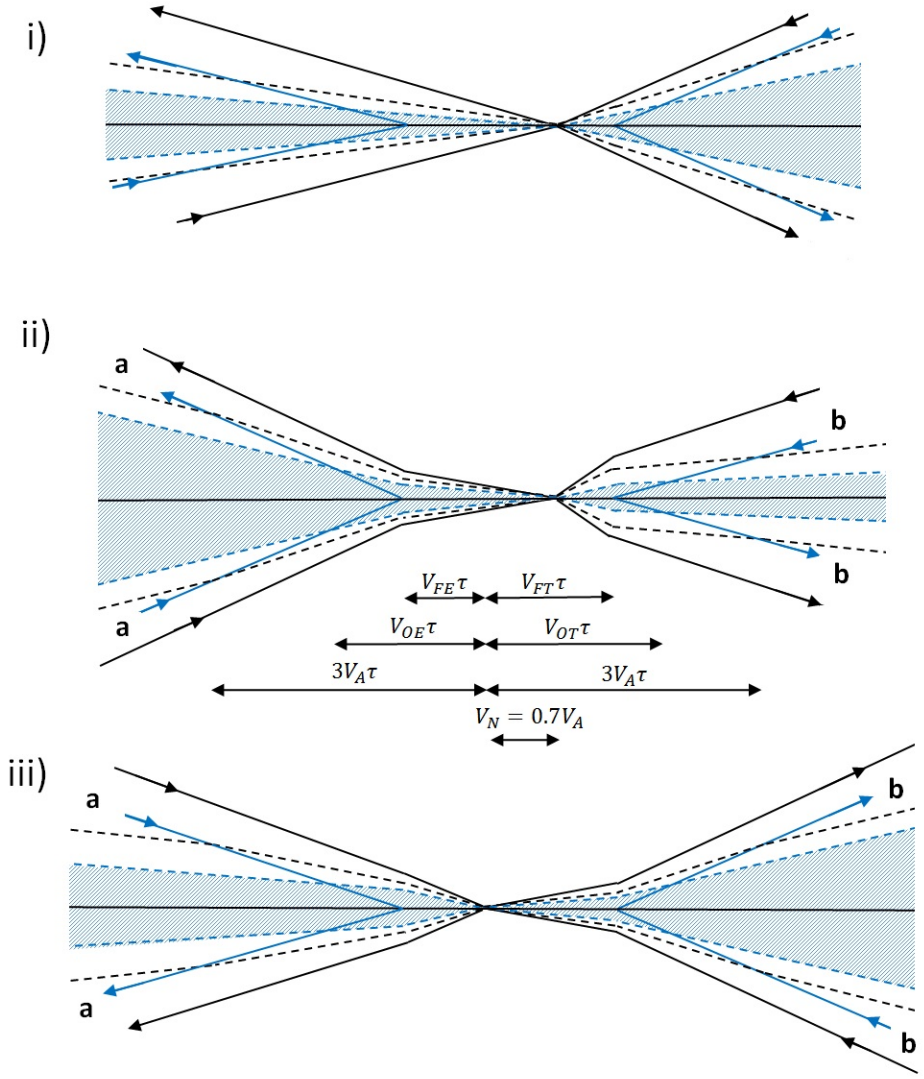

Figure 2.10: Part (i) shows the steady motion of the neutral line at a speed of 0.7 V_A going from left to right. There is asymmetry to the right of the neutral line as the neutral line velocity exceeds that of the inflow plasma velocity. Part (ii) shows the configuration after an arbitrary time τ when the neutral line has, after being initially at rest, started moving at the velocity stated in part (i). $X_N(0)$ is the position of the neutral line before it has started to move and the position $X_N(\tau)$ indicates the position that the neutral line has moved to after time τ. The magnetic field lines that were the last to be reconnected before the change are indicated by $a-a$ and $b-b$ which cross the current sheet at a distance of $v_f\tau$ from the original neutral line position $X_N(0)$. Part (iii) shows a similar configuration to part (ii) except it shows the cessation of the motion shown in part (i) (*Owen and Cowley*, 1987a).

shocks which form the boundary of the plasma outflow region which is the shaded area on Figure 2.11. Due to the reconnection rate being time-dependent, these outflow regions form a bulge shape rather than the open-ended triangles seen in Figure 2.9. This is because the change in reconnection rate changes the width of the outflow region and so the reconnection structure evolves over time. If to begin with there is no reconnection there will be a single un-bifurcated current sheet. Once reconnection has begun the current sheet is bifurcated but only from the point at which reconnection started; hence the bulge shape. The magnetic field lines on either side of the bulge are 'draped' around it forming the travelling compression region (TCR). They roughly follow the standing shocks boundary but those magnetic field lines that come close to the current sheet are partially threaded through the outflow region. Reconnection rate is dependent on the electric field strength thus if the electric field strength tends towards 0 then reconnection will stop, leading to the plasma outflow region and the reconnected magnetic field lines to be expelled away from the X-line along the current sheet (*Beyene et al.*, 2011).

The width of the outflow region is dependent on the rate of reconnection, which is in turn dependent on the electric field strength. Increases (decreases) in the reconnection rate will cause the width of the outflow to increase (decrease) and so in a time-dependent magnetic reconnection event the structure will evolve over time.

Moving into a more general model from the one devised in *Owen and Cowley* (1987a) is one devised by *Owen and Cowley* (1987b), in which asymmetric inflow conditions were introduced. In this case the reconnection would look as in Figure 2.12.

The inflow densities on either side of the current sheet (hatched region), n_1 and

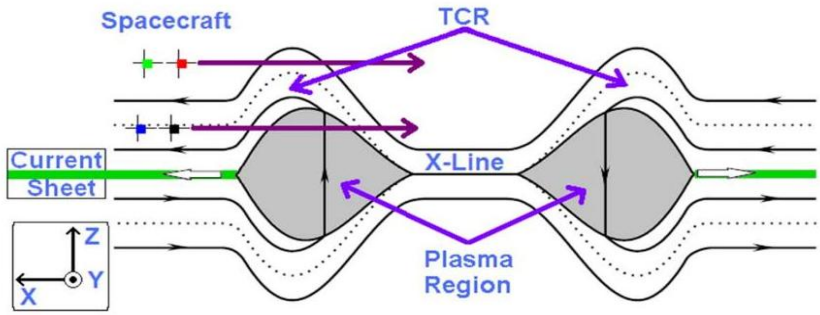

Figure 2.11: A 2D representation of the time dependent magnetic reconnection model (adapted from *Kiehas et al.*, 2009). The magnetic field lines are indicated by the black lines which point in opposite directions on either side of the current sheet (indicated in green). The X-line is the line where the two magnetic field regions merge. There is a plasma outflow region (shaded area) at either side of the X-line due to reconnection. A spacecraft travelling through this region (possible trajectories indicated by the purple arrows) may pass though the travelling compression region (TCR) typical of this model, though the travelling compression region may equally be a bulge due to the motion of a flux rope under a spacecraft (*Beyene et al.*, 2011).

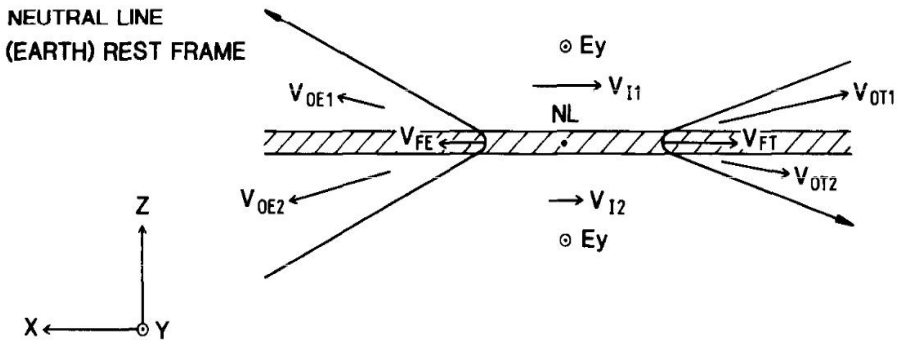

Figure 2.12: Asymmetric inflow and outflow conditions (inflow velocities and densities not symmetric) mean that the outflow beams at either side of the neutral line (indicated by NL) and at either side of the current sheet (hatched region) will not be the same (*Owen and Cowley*, 1987b).

n_2 are not equal and thus the outflow beam velocities V_{0E1}, V_{0E2}, V_{0T1} and V_{0T2} are different from each other. The velocities of the outflow regions are given by the following equations: (*Owen and Cowley*, 1987b)

$$V_{0E1} = 2R - v_{IM} - \frac{n_1}{n_1 + n_2}\Delta v_1 \tag{2.3}$$

$$V_{0E2} = 2R - v_{IM} + \frac{n_2}{n_1 + n_2}\Delta v_1 \tag{2.4}$$

$$V_{0T1} = 2R + v_{IM} + \frac{n_1}{n_1 + n_2}\Delta v_1 \tag{2.5}$$

$$V_{0T2} = 2R + v_{IM} - \frac{n_2}{n_1 + n_2}\Delta v_1 \tag{2.6}$$

where R is given by:

$$R = \sqrt{\frac{\mathbf{B}^2}{\mu_0 m_i (n_1 + n_2)} - \frac{n_1 n_2 (v_{I1} - v_{I2})^2}{(n_1 + n_2)^2}} \tag{2.7}$$

Δv_1 is given by:

$$\Delta v_1 = v_{I1} - v_{I2} \tag{2.8}$$

and v_{1M} is given by

$$v_{IM} = \frac{(n_1 V_{IM} + n_2 v_{I2})}{n_1 + n_2} \tag{2.9}$$

As the outflow jets do not have the same velocities it stands that the boundaries of the outflow particles are not the same angle away from the central current sheet. The equation below gives the angle between the current sheet and the boundary of the outflow jet:

$$\phi \approx (1 - \frac{v_f}{v_0})\theta \tag{2.10}$$

where θ is the angle between the reconnected magnetic field lines and the current sheet:

$$\theta = \frac{|B_z|}{B} = \frac{E_y}{v_f B} \tag{2.11}$$

An example of this is given by Figure 2.13 where $v_{I1} = 0.5V_{A1}$, $v_{I2} = 0$, $n_2 = 0.23n_1$ and $\frac{E_y}{B} = 0.2V_{A1}$.

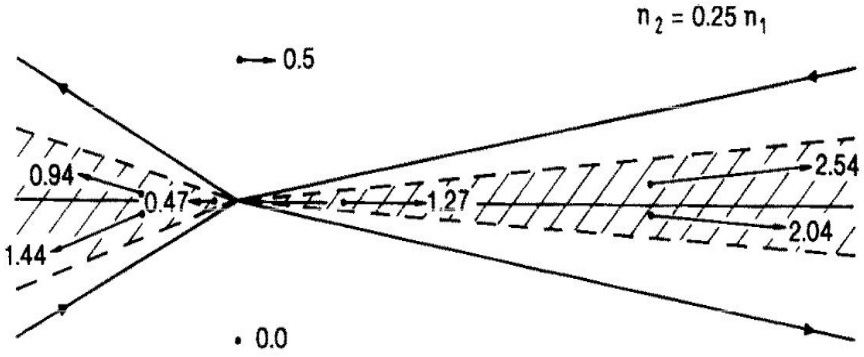

Figure 2.13: An example of reconnection with asymmetric inflow conditions given by $v_{I1} = 0.5V_{A1}$, $v_{I2} = 0$, $n_2 = 0.25n_1$ and $\frac{E_y}{B} = 0.2V_{A1}$. The angle between the current sheet and the outflow boundaries and current sheet and reconnected field lines are different for all 4 outflow jets as is the outflow jet velocity (*Owen and Cowley*, 1987b).

2.4 Characteristics of Events

Previous studies of magnetic reconnection events in the solar wind have given some insight into the characteristics of, and the common conditions for, magnetic reconnection. Using 2 or more spacecraft the scale of a reconnection event can be determined. For example, as previously mentioned, an X-line that extended to distances greater than 390 R_E was found by *Phan et al.* (2006). This is not an isolated find, in a paper by *Phan et al.* (2009) studying 51 events in which two spacecraft, ACE and Wind, observed the same current sheets and where one of the spacecraft saw a reconnection exhaust, it was found that 50 times out of 51 the exhaust was also observed by the other spacecraft. Thus it was concluded by these authors that magnetic reconnection is fundamentally extended and not patchy. The ACE spacecraft is situated at the Lagrangian point 1 whereas Wind orbits the Earth in various orbital configurations with apogee distances ranging from 100- 400 R_E. Thus 7 of the magnetic reconnection X-lines in this study were found to be at least 100 R_E in length. In addition to this, (*Phan et al.*, 2009)

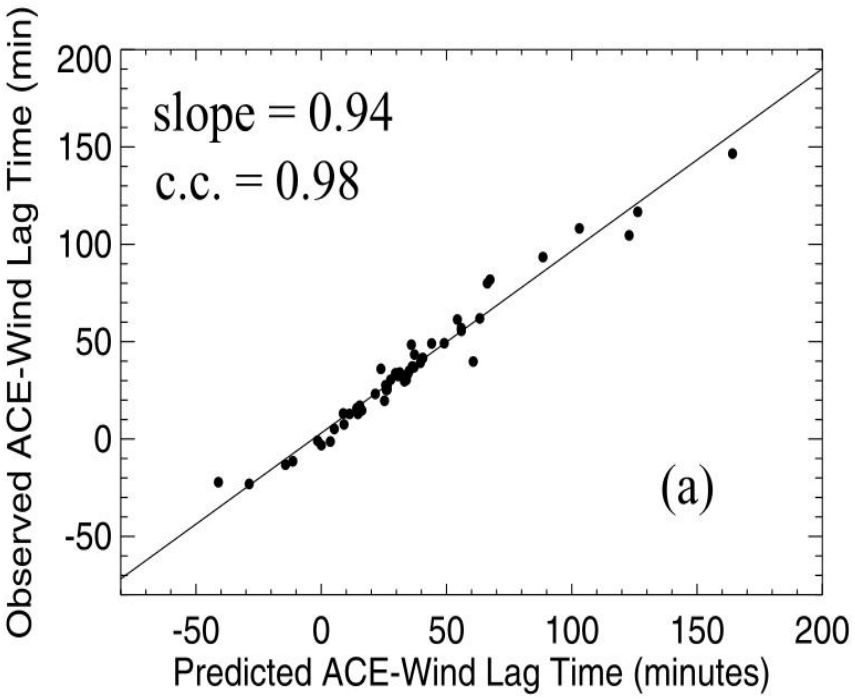

Figure 2.14: The observed time lag between the two spacecraft encountering the events vs the predicted time that this would take. (*Phan et al.*, 2009)

tested the previous assumption that extended current sheets in the solar wind are inherently planar in nature and not warped by the reconnection process. This was done by predicting the time lag between the event reaching each spacecraft and testing the correlation with the observed time lag. Figure 2.14 shows that the observed and predicted time lags are highly positively correlated. This suggests strongly that the current sheets are as predicted; highly planar, at least over these length scales.

These distances between observing spacecraft also allow us to observe reconnection over large time-scales, i.e. there may be several hours between the encounters of different spacecraft observing the same event.

2.4.1 Prevalence at Low Speed

It has also been found that the majority of magnetic reconnection events in the solar wind occur during periods of low solar wind speed. A study by *Gosling et al.* (2007d) showed that, out of the 46 exhausts found in March 2001, only 1 was observed in high solar wind speed conditions. This observation is significant as it has been suggested (*Matthaeus et al.*, 2003) that turbulence, which is much more abundant in the fast solar wind, drives reconnection. Evidence for turbulence-driven magnetic reconnection in the shocked solar wind downstream from the Earth's bow shock has been found (*Retino et al.*, 2007). However, it being the case that magnetic reconnection is much more prevalent in the low-speed solar wind than the high-speed solar wind, turbulence is unlikely to be the main driver (*Gosling et al.*, 2007d).

2.4.2 Plasma β and Magnetic Shear

Magnetic reconnection events also tend to occur in low β plasmas. Thus looking at plasma β in order to understand the conditions for reconnection is a natural step. A paper by *Phan et al.* (2010) looked at the dependence of magnetic reconnection on plasma β and also the magnetic shear over the events. The paper surveyed 197 reconnection exhausts in the solar wind found by the Wind spacecraft. They found that the occurrence of magnetic reconnection events did appear to be dependent on magnetic field shear angle and the difference in plasma β values on the two side of the current sheet, $\Delta\beta$. For low $\Delta\beta$, i.e. the change in plasma β is small, magnetic reconnection exhausts with both low and high magnetic field shears were found. For example they argue that for $\Delta\beta < 0.1$ the magnetic field shears can reach values as low as $\theta \approx 11°$. However for high $\Delta\beta$ only exhausts with high

magnetic field shear are found. In the case of $\Delta\beta > 1.5$ all of the magnetic field shears $\theta > 100°$. It was also found that magnetic reconnection was more prevalent where the plasma β was low. It is thought that this suppression of reconnection at low shears in high β plasma is due to super Alfvénic drift of the X-line by plasma pressure gradients across the current sheet. These results are in very good agreement with a prediction made by *Swisdak et al.* (2010) which stated that magnetic reconnection is allowed if:

$$\Delta\beta < 2(\frac{L}{\lambda_i})tan(\frac{\theta}{2}) \tag{2.12}$$

where $\frac{L}{\lambda_i}$ is the width of the density gradient layer. This prediction leads to only reconnection at high shears being possible for large $\Delta\beta$ (*Phan et al.*, 2010).

2.4.3 Heliospheric Current Sheet (HCS) Related Exhausts

The study by *Gosling et al.* (2007d) found that none of 46 identified reconnection events occurred at the HCS, even though there were at least 4 crossings of the HCS during the month. However, this does not mean that it never occurs. A study of ACE data over a period of 7 years of observations (*Gosling et al.*, 2005a) managed to reveal one event out of the 42 events found, that was associated with a crossing of the HCS. It was found that the heliospheric magnetic field lines that were disconnected from the Sun due to the reconnection process could be identified by a dropout in strahl electrons. Magnetic connection to the Sun can be determined by the presence of strahl electrons moving sunward or anti-sunward depending on which direction the magnetic field is pointing. If both the magnetic footpoints are connected to the Sun then there should be beams in both directions. However, when neither magnetic footpoint is connected to the Sun then there will be no strahl beam (*Gosling et al.*, 2005a).

There is also a case study of an observation by 5 spacecraft of an X-line within the HCS (*Gosling et al.*, 2007c). This particular exhaust was very broad, hence the observation by so many spacecraft, with a width of at least 1.85×10^6 km and a reconnection duration of at least 5 hours. Again this reconnection event produced magnetic field lines that were disconnected from the Sun (*Gosling et al.*, 2007c).

2.4.4 High Solar Wind Speed

Though magnetic reconnection is predominant in the low speed solar wind (*Gosling et al.*, 2007d) it does sometimes occur in the high speed solar wind. A study, (*Gosling*, 2007a), of 1358hr of high speed solar wind data from the spacecraft Wind yielded 34 magnetic reconnection exhausts. These exhausts had magnetic shears which ranged from $24^\circ - 160^\circ$ and mostly had very narrow widths; the majority of the exhausts were convected past the spacecraft in less than 66 s. This indicates that current sheets are generally much less extensive in the high speed solar wind than in other solar wind conditions. Due to the low occurrence frequency and narrow widths of the exhausts it is probable that reconnection is not the dominant mechanism in which turbulence is dissipated (*Gosling*, 2007a).

2.4.5 CME-Related Events

The first 6 reconnection events discovered in the solar wind were found to be within ICMEs *Gosling et al.* (2007b). The majority of magnetic reconnection events are found to be in either the low speed solar wind or in association with ICMEs, and (at least until 2007) half of the magnetic reconnection events in the solar wind were found to have an association with ICMEs (*Gosling et al.*, 2007b). It is thought that reconnection is likely to occur in ICMEs partially due to their structure; ICMEs

often contain very thin current sheets that separate magnetic field regions that have quite different orientations. In addition, reconnection seems to be closely associated with low beta plasma, which is generally the case for the plasma in ICMEs (*Gosling et al.*, 2007b). They most often occur inside or at the trailing edge of the ICME, but can occasionally occur at the leading edge.

2.4.6 Frequency of Events

The frequency of events is to some extent unknown as with each improvement of temporal resolution the number of reconnection events detected per unit time increases. This is because there are many exhaust widths which are very narrow leading to spacecraft crossing times of < 100 s and thus the temporal resolution required to detect these exhaust must be high. For example, a study of ACE data over a period of approximately 7 years yielded only 42 events (*Gosling et al.*, 2005a), whereas a later study on Wind data yielded 46 events in the month of March 2006 (*Gosling et al.*, 2007d).

2.4.7 Absence of Energetic Particle Events

A paper by *Gosling et al.* (2005b) found that there was a no evidence for any increase in the flux of energetic particles in the vicinity of a sample of 7 Petschek-like exhausts. Though this is quite a small sample size, there being no substantial increase in any of them would certainly suggest that magnetic reconnection is not a primary source of energetic particles (particles of energies > 38 keV for electrons or > 47 keV for protons).

2.4.8 Distances from the Sun

Due to the number of spacecraft in the solar wind it is possible to observe magnetic reconnection exhausts over a wide range of distances from the Sun. For example, the spacecraft Ulysses has an orbit which took it to distances well beyond 1AU (between 1.4-5.4AU) in addition to a wide range of heliocentric latitudes (S79° - N65°) (*Gosling et al.*, 2006) and the spacecraft Helios travelled as close to the Sun as 0.31AU (*Eriksson et al*, 2006). Analysis by *Eriksson et al* (2006) of the data from both spacecraft yielded the result that magnetic reconnection exhausts are seen almost universally in low speed solar wind plasma or in association with ICMEs and also in low β plasma. Both studies observed local magnetic field shears of $\sim 90° - 180°$. Analysis of the Ulysses data found that the exhausts were not significantly broader at greater heliocentric distances, which is surprising as the exhausts would have had a greater time to propagate away. There are a few explanations for this; 1. that the exhausts die out or disperse after a day or two due to interaction with the ambient solar wind, or 2. reconnection does not tend to go on for days at a time but stops after a finite amount of flux has been merged from each side due to changes in magnetic field orientation (*Gosling et al.*, 2006). At distances greater than about 4AU exhausts were often found at magnetic field strengths of $< 1\ nT$ and at Alfvén speeds of $< 30\ km\ s^{-1}$ (*Gosling et al.*, 2006).

2.4.9 Oppositely-Directed Exhaust Jets

Each magnetic field reconnection model predicts that there will be two oppositely directed exhaust jets, thus a detection of such jets would be strong evidence for reconnection. In the solar wind it is a rare occurrence for both jets to be observed, simply due to spacecraft positioning. In order for two spacecraft to observe

oppositely-directed jets the X-line of the event must both pass between the two spacecraft and be large enough so that both of the spacecraft could detect it. There are a few occasions where spacecraft have detected these jets. *Davis et al.* (2006), using ACE and Wind data, observed that the spacecraft saw the same magnetic field rotation but the exhaust enhancement during the rotation was in opposite directions Similarly *Gosling et al.* (2007) used 5 spacecraft ACE, Wind, Geotail and STEREO A and B to observe a large exhaust at a distance of 1AU from the Sun. In this case STEREO A was positioned in such a way that it observed an oppositely-directed exhaust jet with respect to the other spacecraft.

2.4.10 High Frequency Plasma Waves

An association between magnetic reconnection in the solar wind and plasma wave activity in both the ion acoustic range and local electron plasma frequency has been observed by surveying 28 encounters with magnetic reconnection exhausts in the ambient solar wind by the Wind spacecraft (*Huttunen et al.*, 2007). This survey found that in 79% of the exhausts there were intense emission bursts in the ion acoustic range ($\sim 4\ kHz$) and in 39% of these exhausts there were such bursts in the local electron plasma frequency range. Three kinds of electric waveforms were detected by the time domain sampler (TDS) instrument; Langmuir waves, electron solitary waves (ESW) and Doppler shifted ion acoustic waves, the average amplitude of which were all below 1 mVm^{-1}. Intense plasma activity was observed more frequently where the spacecraft was situated closer to the reconnection X-line (*Huttunen et al.*, 2007). A representation of the Wind spacecraft observations is shown in Figure 2.15. On the left a typical 3D representation of a reconnection exhaust (thick red arrows) bounded by current sheets (blue planes). Here the co-

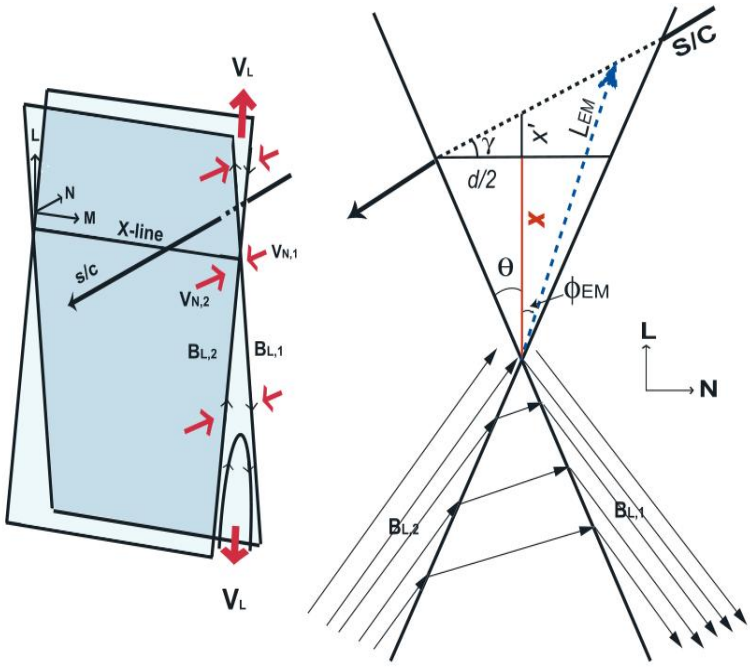

Figure 2.15: The image on the left shows a 3D representation of a magnetic reconnection exhaust (thick red arrows) bounded by two current sheets (blue planes). The small red arrows show the plasma inflow to the exhaust and the black arrow shows a typical spacecraft trajectory though the exhaust. The image on the right shows the exhaust in the LN co-ordinate system where the thick black lines are the current sheets, the thin black arrows are the magnetic field and the dotted arrow is the spacecraft trajectory through the exhaust. The blue dashed arrow is a position of emission along the spacecraft trajectory, θ is the wedge angle and L_{em} is the distance from the X-line to the spacecraft (*Huttunen et al.*, 2007).

ordinate system is LMN where L is the direction of the reconnection exhaust, M is along the X-line and N is along the exhaust normal (minimum variance direction). The image on the right shows the exhaust in the L−N coordinate system where the thick black lines are the current sheets, the thin black arrows are the magnetic field and the dotted arrow is the spacecraft trajectory through the exhaust. The blue dashed arrow is a position of emission along the spacecraft trajectory, θ is the wedge angle and L_{em} is the distance from the X-line to the spacecraft (*Huttunen et al.*, 2007).

2.4.11 Summary

There have been many observations and studies on magnetic reconnection in the space environment. However we have only just begun to study these events in the solar wind. The solar wind is a completely different environment in which to study magnetic reconnection and, with many available spacecraft, we can make multipoint studies over large and small time and length scales.

Chapter 3

Instrumentation and Analysis Techniques

In the following chapters we look at reconnection events in the solar wind. In order to study these events we use data from spacecraft that are situated in the undisturbed solar wind. Spacecraft providing data which have been used to study the solar wind include: STEREO A and B, Wind, Helios A and B, ACE, Geotail, Ulysses, and Cluster. In this thesis, the 4 Cluster spacecraft are primarily utilised, however ACE and Wind will be used to help determine the large scale topology and lifespan of reconnection events. For these studies we will be predominately using the magnetic field and ion velocity data from these spacecraft, with some additional input from Cluster's electrostatic energy analysers.

In this chapter we describe the spacecraft in the solar wind that we use in these studies. In Section 3.1 we describe the orbit of the 4 Cluster spacecraft, their formation and the instruments that we utilise, in Sections 3.2 and 3.3 we discuss the orbit and the instruments that we use from the ACE and Wind spacecraft respectively and in Section 3.5 we describe the methods of analysis that we use

in further chapters; the minimum variance technique, timing analysis, finding the exhaust flow enhancement, conducting a Walén test, and finding the natural co-ordinate system of a set of data.

3.1 Cluster

The 4 Cluster spacecraft were launched in 2000 into an elliptical orbit around Earth with an apogee of $\sim 18.3 R_E$, a perigee of $\sim 2.5\ R_E$, an inclination of $\sim 135°$ and a period of 54 hours. Each spacecraft follows a slightly different orbital path. There is an identical set of 11 instruments on-board each Cluster spacecraft which take a range of in-situ measurements of the plasma environment around Earth and in the solar wind.

In order to study solar wind reconnection events with the Cluster spacecraft data we will need to determine: when the spacecraft is situated in the solar wind (Cluster is situated in the solar wind for part of their orbit during the months January - April each year); when the magnetic field line orientation is such that the spacecraft is connected to the bowshock (these data points must be used with caution due to particles from the shock streaming back up the field lines) and finally what formation Cluster is in (as a tetrahedral formation makes for a more reliable study of 3D structures than a string-of-pearls formation).

3.1.1 Cluster Orbit, Formation and Separation

During January- April (between the years 2001-2015) the 4 Cluster spacecraft spent periods of their orbit outside the Earth's bow shock. During these periods, the spacecraft are periodically in the ambient solar wind and thus may encounter solar wind reconnection exhausts. Figure 3.1 shows the orbit of the Cluster space-

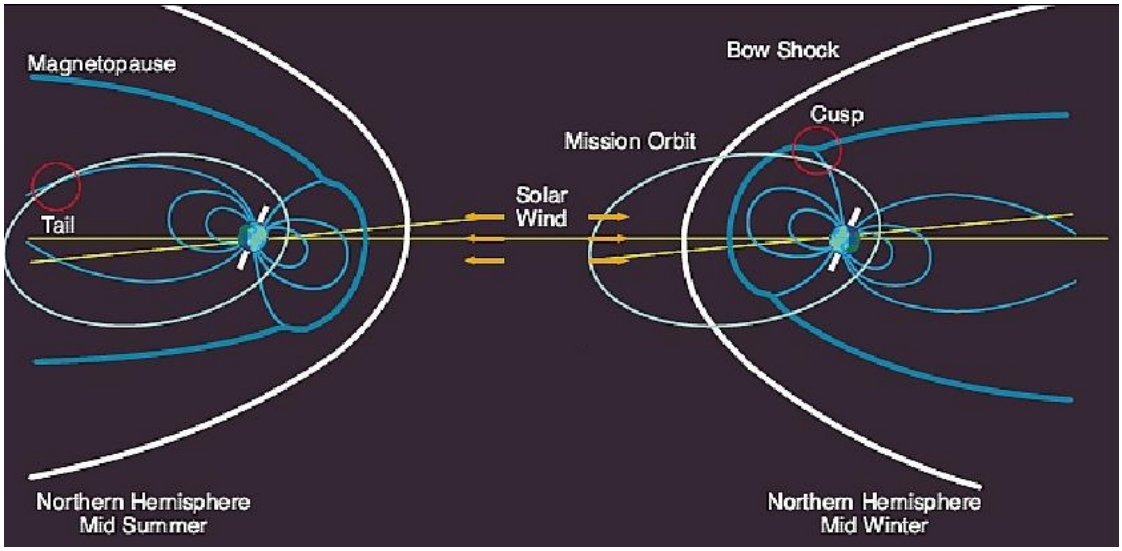

Figure 3.1: The orbits of the Cluster spacecraft at midsummer and midwinter. In each image the white curve is the Earth's bow shock, the blue lines represent the magnetic field of the Earth, the yellow line represents the Earth - Sun line, the yellow arrows the direction of the solar wind flow, and the white oval represents the orbit of the 4 Cluster spacecraft. Adapted from an image by *ESA*

craft at midsummer and midwinter. In this figure the white curve represents the Earth's bowshock, the blue lines the Earth's magnetic field, the yellow line the Earth - Sun line, the yellow arrows the direction of the solar wind, and the white oval the Cluster orbit. Figure 3.1 shows that during the period of time around midsummer the Cluster orbit is entirely within the Earth's bow shock and there is no opportunity to measure the solar wind. However in midwinter the Cluster spacecraft orbit spends a portion of its orbit in the ambient solar wind. During this time it is possible to take measurements of events that occur in the solar wind. The formation of Cluster has changed over its lifetime and the various orientations and configurations of the 4 spacecraft influence how the scientific data can be used, a tetrahedral formation is the most conducive to studying magnetic reconnection events in the solar wind.

3.1.2 The Fluxgate Magnetometer: FGM

FGM is a set of two, tri-axial fluxgate magnetometers and an on-board data processing unit (DPU) aboard each of the 4 Cluster spacecraft.

The fluxgate magnetometer is essentially a core of magnetic material surrounded by a pick-up coil. A magnetic field (in these case studies the field will be the IMF) along the core's axis produces a magnetic flux, if the permeability of the core changes, the flux changes and thus a voltage is induced in the pick-up coil from which it is possible to determine the strength of the ambient magnetic field (*Primdahl*, 1979). Figure 3.2 shows the a basic configuration of a fluxgate magnetometer. A tri-axial fluxgate magnetometer will have 3 of these sensors placed orthogonally to each other, so that 3D vector observations of the magnetic field can be taken.

The effect of the magnetic background of the spacecraft is removed by the dual sensor technique: one of the magnetometer sensors (known as the outboard sensor) is placed at the end of one of the two 5.2 m, radial booms and the other sensor (known as the inboard sensor) at 1.5 m in board from the end of the boom. The outboard sensor will be much less influenced by the spacecraft magnetic field and so, if both sensors are operating at the same resolution and rate it is possible to make an estimate of the magnetic field produced by the spacecraft and remove it from the observations (*Balogh et al.*, 1997). One of the two sensors is designated 'Primary Sensor' and the other the 'Secondary Sensor'; data collected from the Secondary Sensor is collected simultaneously with the Primary Sensor but generally at a much lower rate. The sensor that is designated the Primary Sensor can be changed, but as default is allocated to the outboard sensor on Cluster (*Balogh et al.*, 1997).

Range (nT)	Digital resolution (nT)
-64 to $+63.97$	7.8×10^{-3}
-256 to $+255.87$	3.1×10^{-2}
-1024 to $+1023.5$	0.125
-4096 to $+4094$	0.5
-16385 to $+16376$	2
-65536 to $+65536$	8

Table 3.1: The 5 possible operating ranges of the Cluster spacecraft FGM instruments (*Balogh et al.*, 1997).

Mode	Telemetry data rates (bits s^{-1})
Nominal	1211.13
Burst 1	3465.69
Burst 2	1347.77
Burst 3	5583.61

Table 3.2: The telemetry data rates during different Cluster spacecraft modes (*Balogh et al.*, 1997).

The magnetometers have 6 possible operating ranges, which are listed in Table 3.1. Different operating ranges are used depending on where the Cluster spacecraft are situated. In the solar wind, where the total magnetic field strength is expected to be quite low ($\lesssim 30\ nT$) then the smallest operating range -64 to $+64\ nT$ would be the most appropriate. However, in the magnetosphere where the magnetic field is expected to be much stronger (of the order 1000 nT) then a higher operating range would be more appropriate. This range selection can be triggered from the ground or controlled automatically (*Balogh et al.*, 1997).

The FGM telemetry operates in different modes corresponding to different data acquisition rates for the other instruments. The telemetry rates for each mode are shown and the vector rate for FGM for each of these modes is shown in Tables 3.2 and 3.3. Burst mode is scheduled collectively for all instruments with burst mode capabilities (*Balogh et al.*, 1997). In this thesis we do not utilise any of the non-standard FGM modes (such as the burst mode).

Spacecraft telemetry	FGM telemetry option	Primary sensor vector rate (vector s^{-1})	Secondary sensor vector rate (vector s^{-1})
Nominal 1,2,3	A	15.519	1.091
Burst 2	B	18.341	6.957
-	C	22.416	3.011
Burst 1	D	67.249	7.759

Table 3.3: The 5 possible operating ranges of the Cluster spacecraft FGM instruments (*Balogh et al.*, 1997).

3.1.3 Electrostatic Analysers For Charged Particles: Top Hat Geometry

For the studies in this thesis we use electrostatic analysers for charged particles to measure the 3D distribution of the electrons and ions. The electrostatic analysers on-board the Cluster spacecraft have top hat geometry. Figure 3.3 shows an example of an instrument with top hat geometry. There are 4 primary elements: an inner hemisphere, an outer hemisphere, a top cap which defines the entrance aperture and a detector. In order to detect particles of a specific input energy and direction a voltage is applied to both the inner and outer hemisphere such that there is a specific potential difference between the two plates. When a particle with the desired energy and input direction enters the instrument it will be deflected onto the detector. Particles with a higher energy will hit the outer hemisphere, while lower energy particles will hit the inner hemisphere (*Carlson et al.* , 1982).

3.1.4 CIS

The Cluster Ion Spectrometry instrument (CIS) aboard each of the four Cluster spacecraft consists of 2 instruments: a Hot Ion Analyser (HIA) and a time-of-flight ion COmposition and DIstribution Function analyser (CODIF), both of which have essentially a top hat geometry. The general structure of the instrument is shown

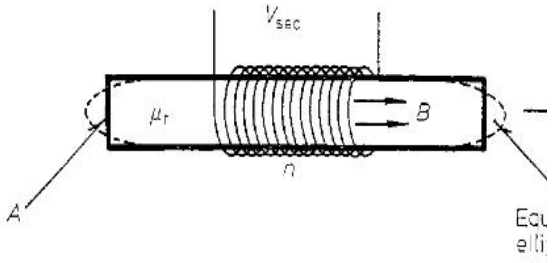

Figure 3.2: An example of a fluxgate magnetometer. Here a core of ferromagnetic material is surrounded by a pick up coil. A tri-axial fluxgate magnometer, like those aboard the Cluster spacecraft, will have 3 instruments placed orthogonally to each other so a full 3D view of the magnetic field environment can be observed. Each of the Cluster spacecraft have two, triaxial instruments located on one of the solid 5.2m booms (*Primdahl*, 1979).

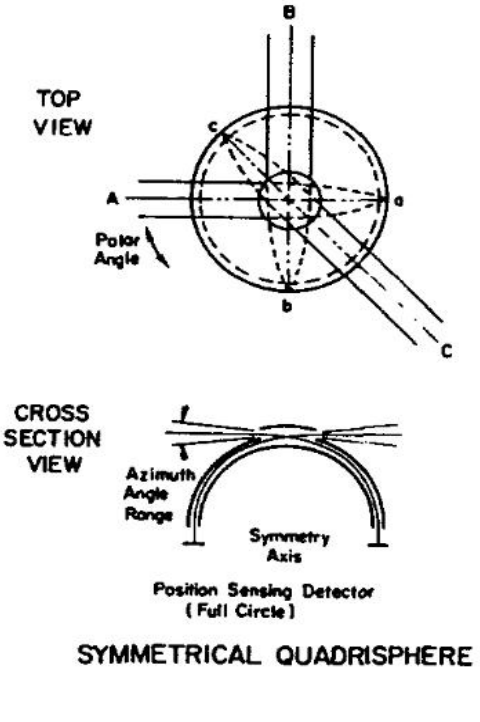

Figure 3.3: Top hat geometry: complete 360° field of view. A voltage is applied to the inner hemisphere and the outer hemisphere creating a potential difference between them such that, when a particle within the desired energy and input direction enters the instrument, it will be deflected onto the detector. Particles of higher energies will hit the outer hemisphere while particles with lower energies will hit the inner hemisphere (*Carlson et al.* , 1982).

in Figure 3.3 (*Reme et al.*, 1997), though the CODIF and HIA instruments differ slightly. In addition to the two instruments there is also a Data Processing System (DPS) which allows on-board data processing. CODIF investigates the distribution of major ions present in the solar wind and in the magnetosphere namely H^+, He^+, He^{++} and O^+ and has an energy range of 1-32amu meaning that the heaviest ion that can be analysed is O^+. The instantaneous field of view of CODIF is $8^\circ \times 360^0$ and the angular resolution is $11.2^\circ \times 22.5^\circ$. CODIF has a high sensitivity side (HS) and a low sensitivity side (LS) which is approximately 100 times less sensitive than the HS side (*Reme et al.*, 1997).

HIA has no mass resolution but it does have a very good angular resolution capability. It also has two levels of sensitivity. The low sensitivity side has 8 sectors of angular resolution 5.6° and 8 sectors with a resolution of 11.25°. The high sensitivity side has 16 sectors, all with an angular resolution of 11.25° and is approximately 25 times more sensitive than the low sensitivity side. HIA has an energy range of $5\ eV - 32\ keV$ and it's instantaneous field of view is identical to that of CODIF. It should be noted that the entire CIS instrument aboard Cluster 2 has been non-functional for the entirety of the mission - likewise the HIA instrument aboard Cluster 4. The CODIF instrument has had many technical difficulties aboard Clusters 1 and 3, with the instrument on Cluster 3 non-operational since 2012 and the instrument on Cluster 1 has not taken measurements in the solar wind since 2013. This thesis mostly uses HIA data, as it is more suitable for studying the solar wind (*Reme et al.*, 1997).

Sensor	LEEA	HEEA
Energy range	$0.59\ eV - 26.4\ keV$	$0.59\ eV - 26.4\ keV$
Energy Resolution (FWHM)	0.127 ± 0.006	0.165 ± 0.007
Energy Sweeps per spin	16,32 or 64	16,32 or 64
FOV polar	$179.4°$	$179.4°$
FOV azimuth	$2.79° \pm 0.14°$	$5.27° \pm 0.20^0$

Table 3.4: Operation of the two PEACE sensors (*Johnstone et al.*, 1997).

3.1.5 PEACE

The Plasma Electron And Current Experiment (PEACE) aboard each of the 4 Cluster spacecraft consists of 2 hemispherical electrostatic energy analysers which measure the 3D velocity distribution of electrons. As with CIS the PEACE instrument has a Top Hat Geometry. However the PEACE instrument has a larger top cap to include an input collimator to prevent high energy electrons and photons entering the instrument (*Johnstone et al.*, 1997), though again the Low Energy Electron Analyser (LEEA) and High Energy Electron Analyser (HEEA) instruments differ. Overall the instrument has an energy range so 0.59 eV - 26.4 eV but the two sensors, LEEA and HEEA, are each optimised for different energy ranges which overlap each other so as to achieve the most accurate and precise results. Table 3.4 shows the properties of the LEEA and HEEA sensors. In the solar wind it would be more appropriate to use the LEEA sensor as the majority of electrons typically do not have energies that go above approximately 200 eV (*Johnstone et al.*, 1997).

The energy range of the instrument is split into a total of 88 levels, the first 16 of which are spaced linearly over the energy range 0.59 eV - 9.45 eV and the rest from 9.45 eV are equally spaced logarithmically by a factor of 1.165. During each energy sweep the instrument first measures particles with high energies, and then systematically lower energies until the full energy range is covered. In order

to vary the azimuthal angle resolution of the instrument there are 3 sweep modes all of which can be used by either sensor. The Low, Medium and High Angular Resolution (LAR, MAR and HAR) measurements have 60 levels, 16 sweeps/spin and 22.5° resolution, 60 levels, 32 sweeps/spin and 11.25° resolution and 30 levels, 63 sweeps/spin and 5.625° resolution respectively (*Johnstone et al.*, 1997).

3.2 ACE

The ACE spacecraft was launched in August 1997 by a Delta II 7920 - 8 into an L1 Lissajous orbit. Its position means that it is constantly in the ambient solar wind.

3.2.1 The Magnetic Field Experiment (MAG)

The Magnetic Field Experiment (MAG) is a pair of tri-axial fluxgate magnetometers, measuring the magnetic field in ranges from $\pm 4\ nT$ to $\pm 65,536\ nT$. The identical magnetometers, located 4.16 m from the centre of the spacecraft, are mounted on two separate booms. These booms are mounted on the Y and -Y solar panels. It supplies 3 dimensional magnetic field data for resolutions of 3, 4 and 6 vectors/s in a continuous data stream and 24 vectors/s in snapshot memory. In this thesis we use the 1 second resolution magnetic field (*Smith et al.*, 1998).

3.2.2 Solar Wind Electron Proton Alpha Monitor (SWEPAM)

The Solar Wind Electron Proton Alpha Monitor (SWEPAM) experiment aboard the ACE spacecraft provides ion and suprathermal electron distribution functions.

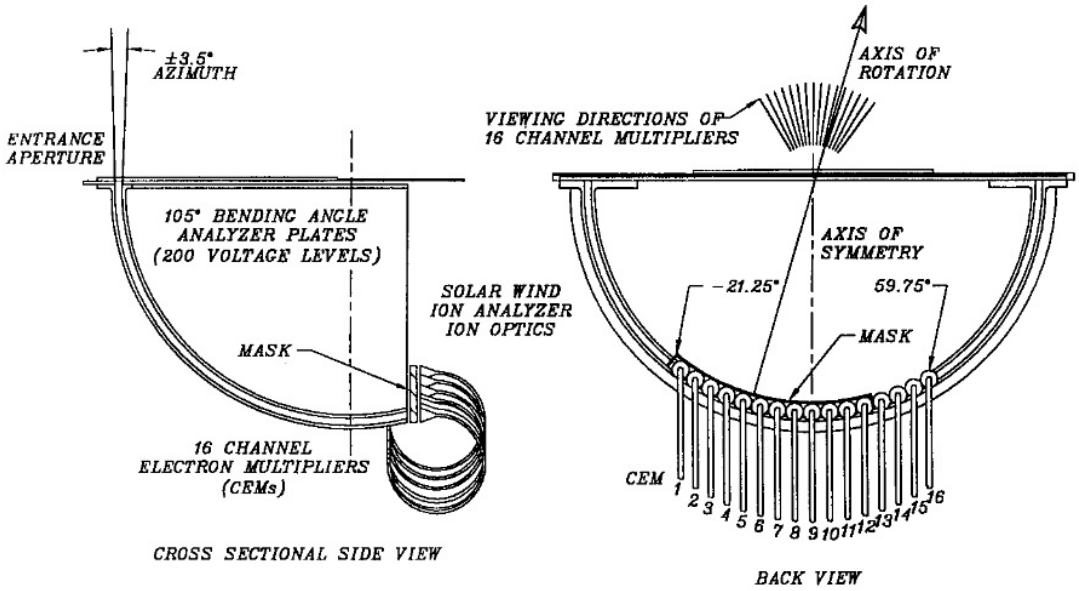

Figure 3.4: The cross sectional side view (left) and the back view (right) of the ion SWEPAM instrument on the ACE spacecraft. Ions enter in through the entrance aperture and, if they are within the energy range and azimuthal angle range being measured, they will be detected by the Channel Electron Multipliers (CEM) (*McComas et al.*, 1998).

It measures in the energy range of 0.26 KeV - 36 KeV for protons and 1.6 eV - 1350 eV for electrons. The data is obtained at a time resolution of 64 s (*McComas et al.*, 1998).

The ion instrument is a spherical electrostatic analyser as shown in Figure 3.4. The ions enter the instrument through the entrance aperture. The inner plate inside the instrument has a high negative voltage and so will deflect the incoming ions. For the ion to be deflected onto the Channel Electron Multipliers (and thus detected) they must be within a certain energy per charge range and within a certain azimuthal angular range (which is determined by what the instrument is measuring at the time). The tolerance on the energy per change is about 5% and the azimuthal angle is between $(3 - 4.5\%)$ (*McComas et al.*, 1998). In this thesis we use the ion distribution function at a cadence of 64 s.

3.3 Wind

3.3.1 Wind Orbit

The Wind spacecraft was launched on the 1st November 1994. It is currently situated in a halo orbit around the Lagrange point and was in this position for the period of time that the Wind spacecraft was used in this thesis. From this vantage point the Wind spacecraft can observe the ambient solar wind.

3.3.2 Magnetic Field Investigation (MFI)

The Magnetic Field Investigation aboard the Wind spacecraft consists of a pair of tri-axial fluxgate magnetometers fixed 8m away from the spacecraft on a 12m boom. It measures 3D magnetic field data at 10.87 vector samples/s as standard, in ranges from $\pm 4\ nT$ and $\pm 65,536\ nT$ (*Lepping et al.*, 1995). For this thesis we data is the 3 second resolution data.

3.3.3 3D Plasma and Energetic Particle Instrument (3D Plasma)

The 3D plasma instrument is a collection of six sensors: two electron (EESA) and two ion (OESA) electrostatic sensors and two solid state telescopes (SST). The electrostatic analysers cover the energy range from 3 eV to 30 keV with angular resolution of $22.5 \times 36°$. The telescopes measure electrons up to 400 keV and protons to 6 MeV and have a resolution of 3 seconds (*Lin et al.*, 1995). For this thesis, the 3 second resolution data is used.

3.4 Geocentric Solar Ecliptic (GSE) Co-ordinate System

We download the data from the Cluster spacecraft in the Geocentric Solar Ecliptic (GSE) co-ordinate system (*Hapgood*, 1992). This system is based on the positions of the Earth relative to the Sun, the X direction is the vector pointing from the Earth to the Sun, the Z direction is the ecliptic north pole and the Y direction makes up the right handed co-ordinate set (which points dawnward).

3.5 Basic Structural Analysis Techniques

This thesis details a number of investigations which involve the determination of the basic structure associated with the reconnection events in order to determine e.g., the orientation of the current sheets and the velocity of the reconnection exhausts. The techniques used throughout the rest of the thesis are outlined in this section.

3.5.1 Minimum Variance

When analysing 3 dimensional data it is often useful to rotate it into a co-ordinate system with the direction of maximum variance as one of the vectors. This makes it possible to analyse changes more easily as the majority of the fluctuations in the data set are in one direction. The minimum variance technique (*Sonnerup et al.*, 1967, 1998), finds the direction of minimum change in a vector quantity. A magnetic field is divergenceless, thus the component of the field normal to an idealised current sheet should be constant and thus corresponds to the minimum variance direction. When using real data it will be necessary to take into account

any deviations from the ideal case. These could include 2D or 3D internal structures (for example fluctuations in the normal direction), temporal changes in the normal direction due to spacecraft transversal time, random and systematic errors.

The minimum variance technique is the determination of $\mathbf{n}$ by the minimisation of σ where:

$$\sigma^2 = \frac{1}{M}\sum_{m=1}^{M} |(\mathbf{B}^{(m)} - \langle \mathbf{B} \rangle) \cdot \mathbf{n}|^2 \tag{3.1}$$

where M is an integer, m = 1,2,3...M, and

$$\langle \mathbf{B} \rangle = \frac{1}{M}\sum_{m=1}^{M} \mathbf{B}^{(m)} \tag{3.2}$$

with the minimisation condition that $|\mathbf{n}|^2 = 1$. It is then necessary to find the solution of the 3 homogenous equations:

$$\frac{\partial}{\partial n_x}(\sigma^2 - \lambda_1(\mathbf{n}^2 - 1)) = 0 \tag{3.3}$$

$$\frac{\partial}{\partial n_y}(\sigma^2 - \lambda_2(\mathbf{n}^2 - 1)) = 0 \tag{3.4}$$

$$\frac{\partial}{\partial n_z}(\sigma^2 - \lambda_3(\mathbf{n}^2 - 1)) = 0 \tag{3.5}$$

In order to determine the value of λ these can be written in the form:

$$\sum_{\nu=1}^{3} \mathbf{M}^B_{\mu\nu}\mathbf{n}_\nu = \lambda \mathbf{n}_\mu \tag{3.6}$$

where $\mu, \nu = 1, 2, 3$ are Cartesian components and

$$\mathbf{M}^B_{\mu\nu} \equiv \langle \mathbf{B}_\mu \mathbf{B}_\nu \rangle - \langle \mathbf{B}_\mu \rangle \langle \mathbf{B}_\nu \rangle \tag{3.7}$$

There are three allowed values for λ from Equation 3.6: λ_1, λ_2 and λ_3 are the eigenvalues of the minimum, intermediate and maximum variance directions in order of increasing magnitude. In this thesis we shall use the labels N, M, L for the minimum, intermediate, and maximum variance directions respectively. The directions are well-defined if the ratio of two consecutive eigenvalues (for example $\frac{\lambda_{int}}{\lambda_{min}}$) > 10 (*Sonnerup et al.*, 1967, 1998).

Figure 3.5 illustrates an idealised case of how the minimum, intermediate and maximum eigenvectors relate to each other if all the eigenvectors are well-defined.

Panel a) shows an arc shape as there is variation in both the maximum and intermediate directions, but more in the maximum variance direction than the intermediate. Panel b) and c) show straight lines, as the minimum variance direction in the ideal case has no variation. Panel d) shows the data in the maximum, intermediate and minimum variance directions. Here it is possible to see that the most variation is in the maximum variance direction and there is no variation in the minimum variance direction.

However, there are situations where the intermediate and minimum variance directions will be degenerate: $\lambda_1 \sim \lambda_2$ and therefore the equivalent eigenvectors are not well-defined. In such a case it is not possible to accurately distinguish a minimum variance direction. This is because essentially all of the variation is in one direction, along the current sheet. In this case the minimum variance analysis will appear as in Figure 3.6.

It is also possible for the maximum and intermediate directions to be poorly defined: if $\lambda_2 \sim \lambda_3$. In situations were not all of the direction vectors are well defined it becomes necessary to use other techniques for determining a useful co-ordinate system for a data. It is still possible to identify reconnection events where the variance directions are not well defined, but further analysis techniques need to be more sophisticated.

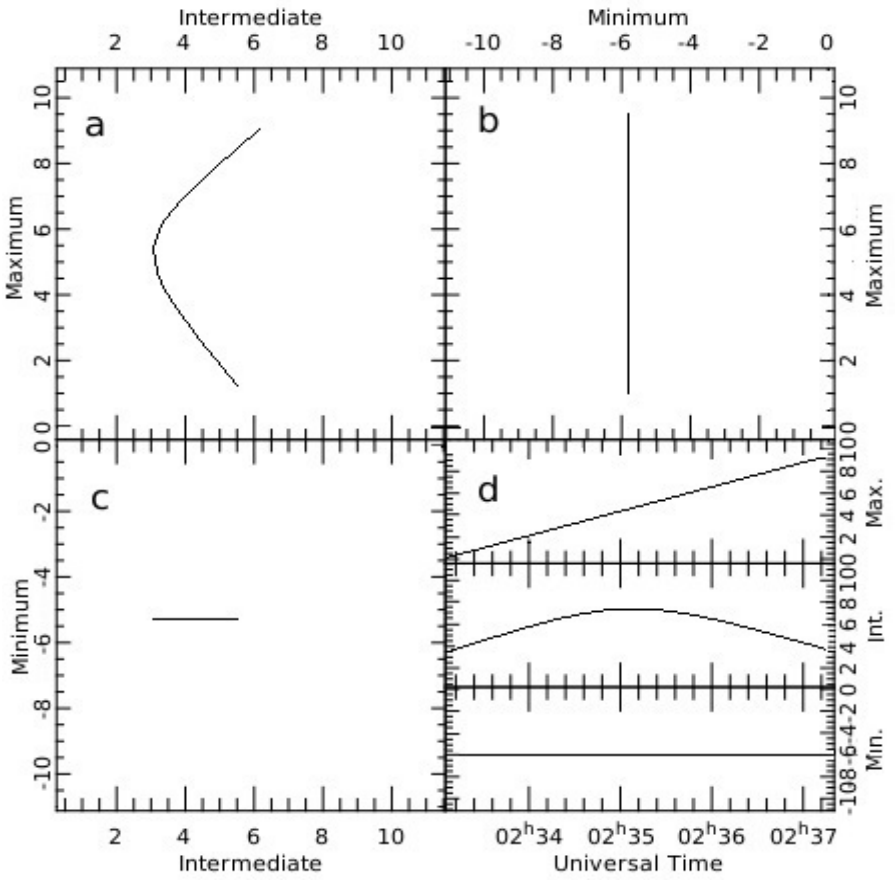

Figure 3.5: Figure shows the results of a minimum variance analysis conducted over an ideal set of data where the minimum and maximum variance directions are both well defined. The maximum variance direction vs. the intermediate variance direction in the panel a), the maximum variance direction vs. the minimum variance direction in panel b) and the minimum variance direction vs. the intermediate variance direction in panel c). Panel d) shows the data in the maximum, intermediate and minimum variance direction going from the top to the bottom panel.

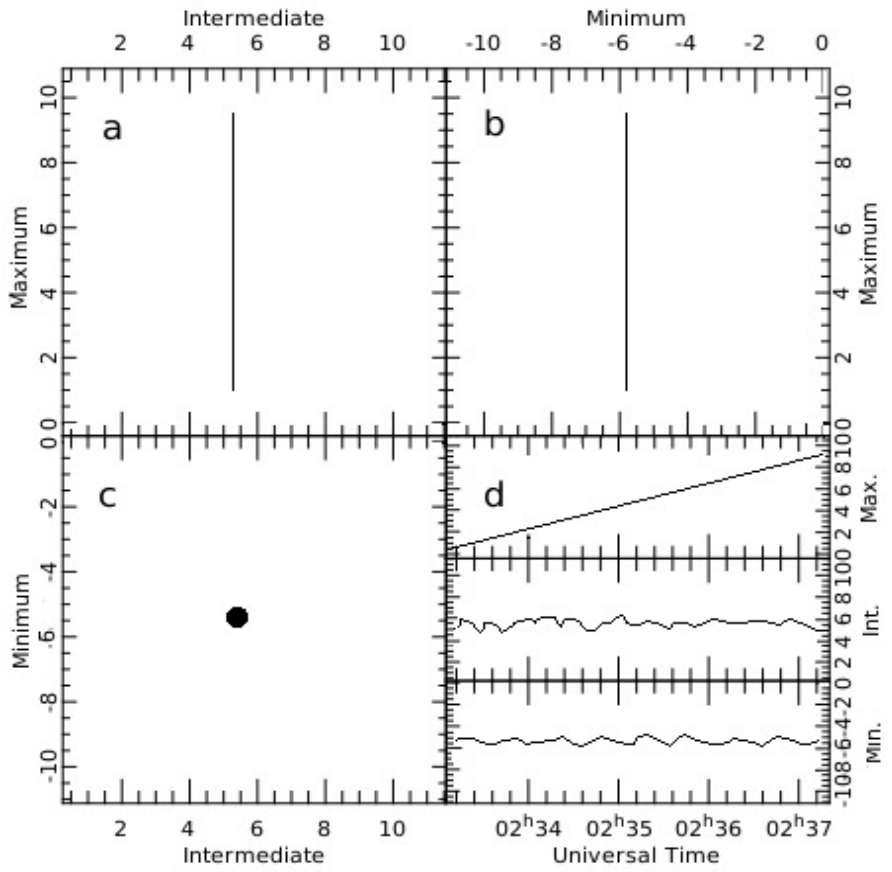

Figure 3.6: Figure shows an idealised current sheet in which all the variance is in one direction (the maximum variance direction). In this case we are considering that the current sheet was formed between two anti-parallel field lines. The maximum variance direction vs. the intermediate variance direction are shown in panel a), the maximum variance direction vs. the minimum variance direction in panel b) and the minimum variance direction vs. the intermediate variance direction in panel c). Panel d) shows the data in the maximum, intermediate and minimum variance direction going from the top to the bottom panel.

3.5.2 Timing Analysis

With a set of 4 spacecraft it is also possible to find the normal direction vector of a discontinuity that passes over the spacecraft, along with its velocity in the normal direction, by using the following relation (*Paschmann and Daly*, 1998):

$$(\mathbf{r}_\alpha - \mathbf{r}_1)\hat{\mathbf{n}} = V(t_\alpha - t_1) \tag{3.8}$$

where α is an integer between 1 and 4 that denotes the spacecraft number, $\mathbf{r}$ is the spacecraft position, $\hat{\mathbf{n}}$ is the normal direction vector of the discontinuity, V is the speed of the discontinuity and t is the time at which the discontinuity reaches the spacecraft. We also assume that the discontinuity is planar, travelling at constant speed, and the Cluster spacecraft are in an approximate tetrahedral formation. For this method it is necessary to know the average distances between the spacecraft over the crossing and the times at which each spacecraft encountered the discontinuity.

For timing analysis it is initially necessary to find the positions of the spacecraft relative to one reference spacecraft. Over the typical duration of a discontinuity the distance between Cluster spacecraft will fluctuate, though only to a very small degree, and therefore it is necessary to take an average of the spacecraft positions over the period where the spacecraft is traversing the discontinuity.

It is also necessary to find the relative times at which each spacecraft encountered a given discontinuity. In order to find the time difference between Cluster 1 encountering the discontinuity and the other 3 spacecraft, it is necessary to correlate the magnetic field data between pairs of spacecraft. The time lag at the point of maximum correlation is equivalent to the time difference between the spacecraft

encounters. In order to ensure the most accurate results the correlation analysis should be done using the magnetic field data in the maximum variance direction.

Using the position and timing it is possible to find the normal direction vector of the current sheet and the speed in this direction. By multiplying the inverse of the position matrix with the timing matrix $\hat{\mathbf{n}}/V$ could be found. The equation $V = 1/((x^2 + y^2 + z^2))^{0.5}$ where $\hat{\mathbf{n}}/V = [x, y, z]$ allows us to find V and thus $\hat{\mathbf{n}}$.

3.5.3 Determining the Solar Wind Rest Frame and Exhaust Flow Enhancement

In this thesis we investigate magnetic reconnection exhausts as described in Section 1.8 and Chapter 2. A simple picture of magnetic reconnection in the solar wind is as described by *Gosling et al.* (2005); a reconnection exhaust directed between two bounding current sheets. In order to test whether the exhaust flow enhancement is directed between the current sheets, the orientation of the two current sheets and the velocity of the exhaust must be determined.

In order to find the exhaust flow enhancement we must first find the solar wind rest frame. The average solar wind velocity at either side of the exhaust determines what we will consider to be the solar wind rest frame in this thesis. The residual solar wind velocity, after subtraction of the rest frame velocity, is the reconnection exhaust flow enhancement.

3.5.4 Walén Test

A common test used on discontinuities, to check they are rotational discontinuities, is the Walén test (*Paschmann et al.*, 2013). It can provide strong evidence

for magnetic reconnection events. The Walén relation in the spacecraft frame of reference is given by:

$$\Delta \mathbf{v} = \pm \Delta \mathbf{V}_A \tag{3.9}$$

where Δ is the change across the discontinuity, $\mathbf{v}$ is the plasma velocity, $\mathbf{V}_A$ is the local Alfvén velocity. Alfvén velocity should be corrected for the effects of pressure anisotropy so:

$$\mathbf{V}_A = \mathbf{B}[\frac{(1-\alpha)}{\mu_0 \rho}]^{0.5} \tag{3.10}$$

where $\alpha = \frac{(p_\parallel - p_\perp)\mu_0}{B^2}$.

How well the data agrees with the Walén relation depends on the ratio:

$$R = \frac{\Delta \mathbf{v}}{\Delta \mathbf{V}_A} \tag{3.11}$$

and also the angle, θ, between $\Delta \mathbf{v}$ and $\Delta \mathbf{V}_A$. In the ideal case $R = \pm 1$ and $\theta = 0$ where a positive R indicates that the change in plasma velocity and Alfvén speed are correlated and a negative correlation indicates that they are anti-correlated.

As, in this thesis, we will be dealing with real data it is highly unlikely that any discontinuity will perfectly agree with the Walén relation. Thus we determine that values of R between 0.5 - 0.8 and 1.2 - 2 weakly satisfy the Walén relation and R values between 0.8 - 1.2 strongly satisfy the Walén relation.

The De Hoffmann-Teller (dHT) frame is an appropriate reference frame from which to conduct an assessment of the Walén relation (*Paschmann et al.*, 2013). The dHT frame is the frame of reference in which the electric field, **E'** vanishes:

$$\mathbf{E}' = \mathbf{E} + \mathbf{V}_{HT} \times \mathbf{B} = 0 \tag{3.12}$$

where $\mathbf{V}_{HT}$ is the dHT frame velocity with respect to the observer frame. In the dHT frame, the plasma velocity should be aligned with the magnetic field

(as the plasma is frozen-in to the magnetic field) either side of the discontinuity (*Paschmann et al.*, 2013).

3.5.5 Natural Co-ordinate Frame

It is useful to establish a natural reference frame in order to put any reconnection events in a more readily understandable context. Such a reference frame can aid in the determination of the structure and dynamics of the events we are investigating. In this section we will detail a method used for finding an appropriate co-ordinate system to use when studying individual magnetic reconnection events.

We conduct a minimum variance analysis (using the minimum variance analysis technique described in Section 3.5.1) over the whole event for each of the 4 Cluster spacecraft individually. Thus we have a set of eigenvectors and their associated eigenvalues λ for minimum, intermediate and maximum variance directions for each of the spacecraft.

The 'mean maximum variance' direction across an event is found by taking a weighted average of the variance analysis results from each of the spacecraft. The weight used is given by the ratio of the maximum and intermediate eigenvectors. Thus for the 'natural' reference frame we use the 'mean maximum variance' direction $\mathbf{E}_{max}$, given by:

$$\mathbf{E}_{max} = \frac{M}{|M|} \tag{3.13}$$

where M is given by:

$$M = \frac{\sum_{i=1}^{4} \frac{\lambda_{maxi}}{\lambda_{inti}} \mathbf{E}_{maxi}}{\sum_{i=1}^{4} \frac{\lambda_{maxi}}{\lambda_{inti}}} \tag{3.14}$$

where subscripts i refer to the spacecraft number, max and int refer to the maximum and intermediate variance directions, and λ is the eigenvalue. The 'mean minimum variance' direction is found similarly using the following equation

to get an estimate for the direction:

$$\mathbf{E}_{min} = \frac{m}{|m|} \tag{3.15}$$

where m is given by:

$$m = \frac{\sum_{i=1}^{4} \frac{\lambda_{inti}}{\lambda_{mini}} \mathbf{E}_{mini}}{\sum_{i=1}^{4} \frac{\lambda_{inti}}{\lambda_{mini}}} \tag{3.16}$$

and then rotating $\mathbf{E}_{min}$ to find $\mathbf{E}'_{min}$ which is orthogonal to $\mathbf{E}_{max}$ by using:

$$\mathbf{E}'_{min} = \mathbf{E}_{max} \times (\mathbf{E}_{min} \times \mathbf{E}_{max}) \tag{3.17}$$

The final co-ordinate, taken to be the 'mean intermediate variance' direction completes the right handed set:

$$\mathbf{E}_{int} = -\mathbf{E}'_{min} \times \mathbf{E}_{max} \tag{3.18}$$

The complete rotational matrix which transforms the data into the natural co-ordinate system is then:

$$M_{NAT} = \begin{pmatrix} \mathbf{E}_{min} \\ \mathbf{E}_{int} \\ \mathbf{E}_{max} \end{pmatrix}$$

Chapter 4

Small Scale Reconnection in the Solar Wind

Previous studies of magnetic reconnection in the solar wind have concluded that, in this environment, reconnection is large scale and non-patchy in nature. For example, *Phan et al.* (2006) described a reconnection event that was observed by the ACE, Wind and Cluster spacecraft. Due to the positions of these spacecraft at the points of observation, the associated structures were deemed to extend at least $390R_E$ along the X-line. The time taken between the initial observations at ACE and the final observations of the reconnection event at Wind was approximately 2.5 hours. As the observations showed similar properties at ACE and Wind, it was concluded that the event was large-scale and non-patchy in both space and time.

A statistical study by *Phan et al.* (2009) found 51 events observed by the ACE spacecraft and found that 50 of those events were also detected by the Wind spacecraft. They made predictions of the arrival time of the event at Wind based on the orientation of the event at ACE and the speed of the solar wind and compared their predictions with observations. Figure 2.14 shows the predictions vs. the

observed time lags. The line of best fit has a gradient of 0.94 with a correlation co-efficient of 0.98 and led *Phan et al.* (2009) to conclude that reconnection in the solar wind in general is large-scale and non-patchy.

In this chapter we test the validity of this large-scale steady structure conclusion. We analyse a case study of a reconnection event which contains temporal and/or spatial changes which are smaller in scale than the distances between the Cluster spacecraft. In Section 4.1 we look at the relative positions of the Cluster, ACE and Wind spacecraft with respect to the Earth and to each other, in Section 4.2 we look at the plasma and magnetic field observations for each Cluster spacecraft, in Section 4.3 we check that the characteristics of the event are consistent with it being a reconnection event, in Section 4.4 we look at the data observed at ACE and Wind at the times that the reconnection event is predicted to cross them, in Section 4.5 we interpret and discuss our results and in Section 4.6 we draw our conclusions.

4.1 Spacecraft Positions

In this chapter we will consider observations by Cluster, ACE and Wind. On the 2nd March 2006 16:38:00 UT, the 4 Cluster spacecraft were located in the solar wind in a tetrahedral formation with inter-spacecraft separations of $\sim 10,000\ km$. Cluster 1 was located at [17, 8, -3] R_E in the GSE co-ordinate frame (see Section 3.4). The ACE spacecraft was located at [188, 30, -5] R_E at the time of this event. The position of the Wind spacecraft at the time of observation was [165, -95, -5] R_E. Figure 4.1 panels a) and b) show the large-scale separations of the spacecraft projected onto the GSE XY and XZ planes. The ACE and Wind spacecraft are widely separated ($>$ 100 R_E) in the Y direction but closer together in the X

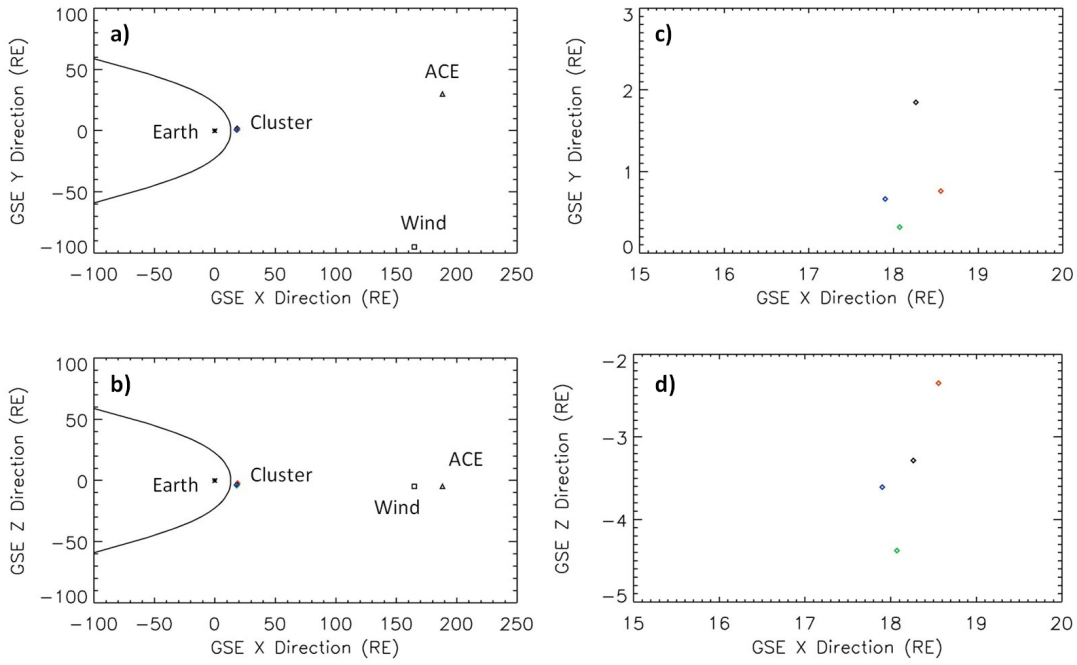

Figure 4.1: The positions of the ACE, Wind and the 4 Cluster spacecraft relative to the Earth and each other. In this image the spacecraft positions are denoted by diamonds; black for C1, red for C2, green for C3 and blue for C4. ACE is denoted by a black triangle and Wind by a black square. The Earth is indicated by the black star and the black curve shows the nominal position of the Earth's bow shock. Panel a) shows the spacecraft in the X Y plane in GSE co-ordinates relative to the Earth and the Earth's bow shock and panel b) shows the positions of ACE, Wind and the 4 Cluster spacecraft in the X Z plane. Panels c) and d) are an expansion of the region around the Cluster spacecraft to show clearly the relative distances from each other.

(23 R_E) and Z (0 R_E) directions. Both ACE and Wind are separated from the Cluster tetrahedron by over 150 R_E in the X direction. Figure 4.1 panels c) and d) show the relative positions of the 4 Cluster spacecraft. In the XY plane the Cluster spacecraft are situated such that Cluster 2, 3 and 4 are approximately equally separated but spacecraft 1 is situated further in the +Y direction. In the XZ plane the Cluster spacecraft are approximately aligned in the Z direction with the Cluster 2 spacecraft the furthest in the +Z direction and Cluster 3 at the other extreme.

4.2 Cluster Observations

On the 2nd March 2006 between 16:37:00 UT and 16:40:00 UT all four of the Cluster spacecraft were in the solar wind, consistent with the locations shown in Figure 4.1. Figure 4.2 shows data from this 3 minute interval, in particular the magnetic field and plasma parameters observed by Cluster 1. From top to bottom, Figure 4.2 shows a) the total magnetic field strength; b) the 3 components of the magnetic field in GSE co-ordinates; c) the total ion velocity; d) the 3 components of the ion velocity in GSE co-ordinates, e) the ion density; f) the ion temperature; g) the ion β; h) the Alfvén speed; and i) the ion temperature anisotropy (defined here as $A_p = \frac{T_{para}}{T_{perp}} - 1$). In panels b) and d) the x, y and z GSE components of the vector quantities are indicated by red, green and blue respectively, as indicated in the key. Note that in Figure 4.2 d) we have added 400 $km\ s^{-1}$ to the x-component (red trace) of velocity to facilitate a comparison between the variations in all three velocity components.

Three significant magnetic field rotations, predominately in the B_{xGSE} component (red trace) of the magnetic field, were observed and are evident in panel b). The vertical dashed lines on Figure 4.2 indicate the start of each of these magnetic field rotations. This is consistent with the spacecraft crossing three distinct current sheets. The rotations will hereafter be referred to as current sheet 1 (CS1) for the 26° rotation in B field direction occurring at 16:38:17 UT, current sheet 2 (CS2) for the 43° rotation occurring at 16:38:40 UT and current sheet 3 (CS3) for the 13° rotation at 16:39:00 UT. The total magnetic field rotation over all three current sheets (i.e. between upstream and downstream regions) is 68°.

Figure 4.2 panel c) shows that the event occurs during a period of slow solar wind (400 $km\ s^{-1}$). Panel c) shows a total ion velocity increase of $\sim 20\ km\ s^{-1}$

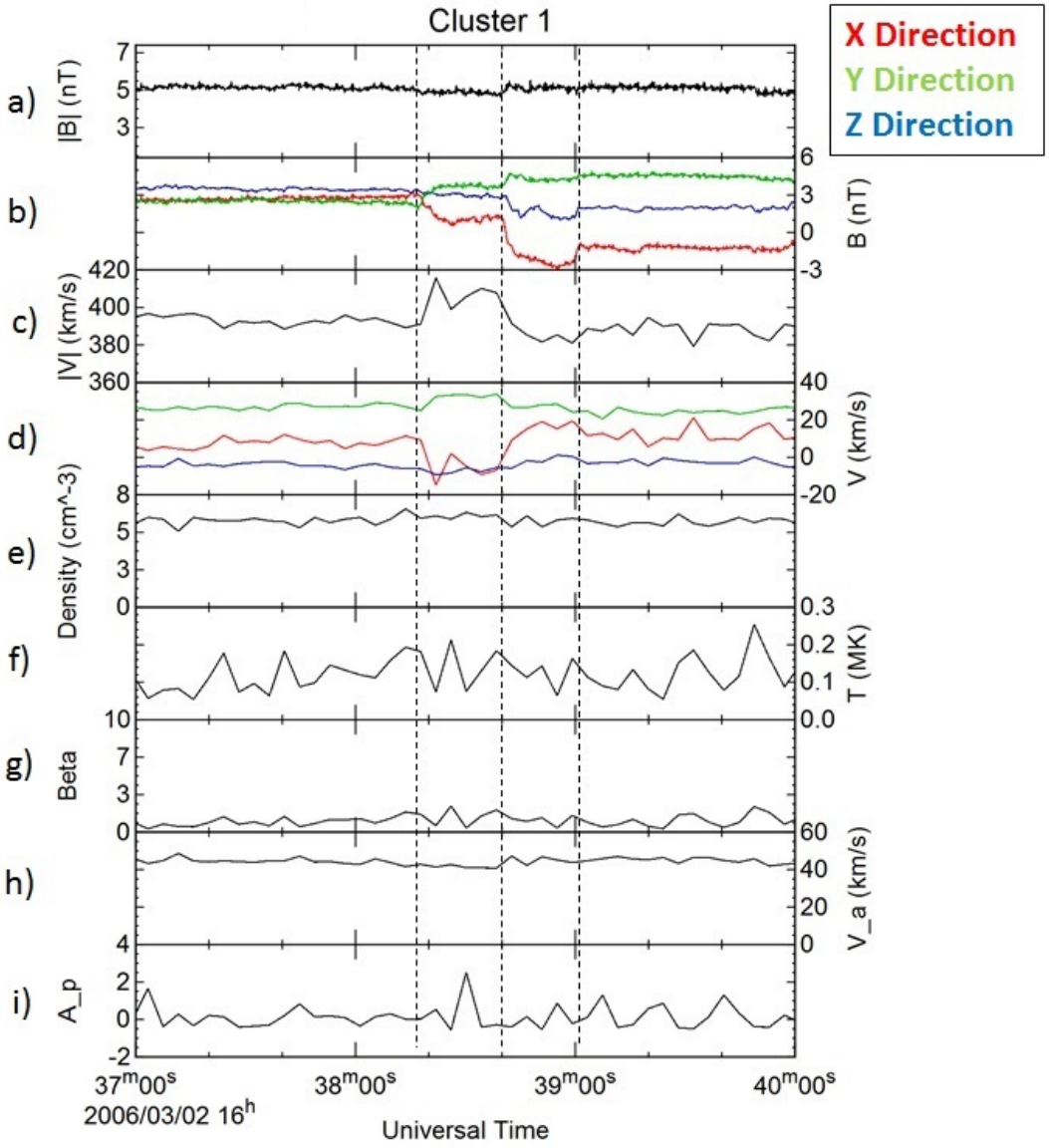

Figure 4.2: Solar wind and magnetic field data obtained by Cluster 1 over a 3 minute interval, from 16:37:00 UT to 16:40:00 UT, on the 2nd March 2006. Starting from the top the panels show; the total magnetic field strength, the magnetic field strength in the GSE co-ordinate directions B_x (red), B_y (green) and B_z (blue), the total ion velocity, the ion velocity in the GSE co-ordinate directions v_x +400 $km\ s^{-1}$ (red), v_y (green) and v_z (blue), the ion density, temperature, β, Alfvén velocity and the ion temperature anisotropy (given by $A_p = \frac{T_{para}}{T_{perp}} - 1$). The black vertical dashed lines show the start of each of the 3 magnetic field rotations.

between the first two magnetic field rotations which, from examination of panel d), occurs predominately in the B_{xGSE} direction. It should be noted that the largest changes in both magnetic field and ion velocity are in the x_{GSE} direction. These changes are anti-correlated over CS1 and correlated over CS2. This feature is characteristic of current sheets bounding a reconnection exhaust (*Gosling et al.*, 2005). There is no significant change in ion velocity across CS3.

Panel e) of Figure 4.2, shows that there is no discernible difference in the ion density in the regions either side of the exhaust, as had been reported in some previous studies (e.g. *Teh et al.* (2009)). The ion temperature (shown in panel f)) also does not show any significant variation over the event, though a temperature increase is often seen in the reconnection events reported by *Gosling et al.* (2005). The ion β (panel g)) over the event remains steady; $\beta \sim 1$. There have been reports of a slight increase in ion β during some reconnection events, e.g., *Gosling et al.* (2006a), but this is not apparent here.

The Alfvén velocity, shown in panel h), throughout the event remains approximately constant at 45 $km\ s^{-1}$. This is expected given that there are no large changes in the magnetic field strength or plasma density across the event. There is, however, a large spike, from approximately 0 to 2, in the ion temperature anisotropy (panel i) between the first two magnetic field rotations, as compared to values on either side of the reconnection event. Therefore, the temperature of the ions parallel to the magnetic field appears to be greater than that perpendicular to the magnetic field within the exhaust region. This conclusion must be treated with caution, as it is based on a single data point. However this observation would be consistent with reconnection accelerating ions along the magnetic field direction and has been reported in previous studies (*Gosling et al.*, 2005).

Figure 4.3 shows the differential energy flux of electrons in the solar wind for pitch angles $0 - 180°$ as seen by the Cluster 1 PEACE instrument over the event. the view is of 180° because the graph is symmetrical about the vertical axis and thus it is only necessary to display one half. The data is divided into segments of a circle each representing a specific energy and pitch angle. The colour of the segment indicates the relative number of electrons found in that segment with red the highest number and purple the lowest number. The blank white spaces indicate areas where no data was taken. The data include a correction to the electron energies to account for the spacecraft potential. On the left hand half of each panel is the pitch angle distribution observed at 16:38:05 - 16:38:07 UT, before the spacecraft encounters the event.The right hand half shows 8 subsequent intervals covering the event (these intervals have separations which range from $4 - 8s$ depending on the PEACE data available), with the final panel showing the data observed at 16:38:54 - 16:38:56 UT. This is so a direct comparison can be made between the distribution before the magnetic reconnection event and the distribution at points over the event. There is a peak in electron differential energy flux observed at electron energies of around 20 eV, in particular between the pitch angles $90 - 180°$ for each of the distributions shown indicated by the black circles. However, there is a large drop-out of half the maximum flux of these electrons at 16:38:44 UT (panel f) indicated by the blue circle on panel f)), just after the spacecraft crossed CS2, indicating that a transition into a different plasma region has indeed occurred. There are no significant changes in the differential energy flux of electrons over CS1 (between panels b) and c)) but there does appear to be a reversal of the beam between CS2 and CS3 (panels g) and h) indicated by the red circles).

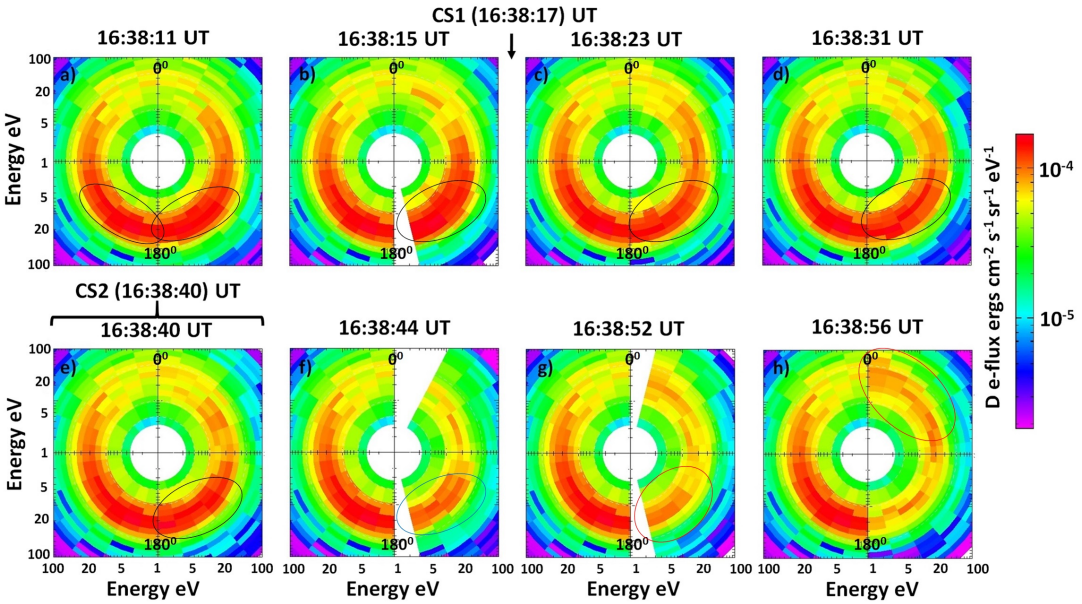

Figure 4.3: PEACE pitch angle distribution data over the event. The left hand side of each graph shows the distribution at 16:38:05 - 16:38:07 UT and the right hand side shows subsequent times with the last at 16:38:56 - 16:38:58 UT. The times above each panel indicate the start time of the sweep. The electrons are binned by pitch angle, the colour indicates the differential energy flux as indicated by the colour bar.

Figure 4.4 shows the field and plasma parameters observed by Cluster 3, presented in the same format as Figure 4.2. Cluster 1 and 3 are only minimally separated ($< 0.5\ R_E$) in the X direction but are more widely separated in the Y and Z directions ($> 1\ R_E$ in both cases). Cluster 3 also observed three magnetic field rotations similar to Cluster 1. The rotations are predominately in the B_{xGSE} and the rotation angle of the field in CS1 and CS2 is comparable to that seen by Cluster 1; Cluster 1 observes rotations of 26° and 43° and Cluster 3 observes 25° and 39° for CS1 and CS2 respectively. The third rotation at 16:38:50 UT is 7°, which is half of that seen at Cluster 1 (13°). Cluster 3 also observed an ion velocity increase of $\sim 20 kms^{-1}$ predominately in the v_{xGSE} direction, between CS1 and CS2, again similar to that observed by Cluster 1. The density, temperature, plasma β and Alfvén speed showed no large change during the event, as was the case when observed at Cluster 1. The sharp increase in temperature anisotropy seen in the Cluster 1 data is smaller at Cluster 3, but this is perhaps a more reliable measurement as there are 2 data points rather than 1. The PEACE instrument was not operational for Cluster 3 during this event and so it was not possible to observe the nature of the variations of the electron population at this spacecraft. However, from the CIS and FGM observations it is clear that Cluster 3 passed through the same set of current sheets.

Neither the CIS nor the PEACE instruments were operating on Cluster 2 or 4 at the time of this event. However it is still possible to examine the FGM data from each of these two spacecraft and compare to Cluster 1 and 3. Figure 4.5 shows the magnetic field data for each of the 4 Cluster spacecraft rotated into a reference frame that minimises the changes in one direction and maximises them in another orthogonal direction. This natural co-ordinate system is based on the

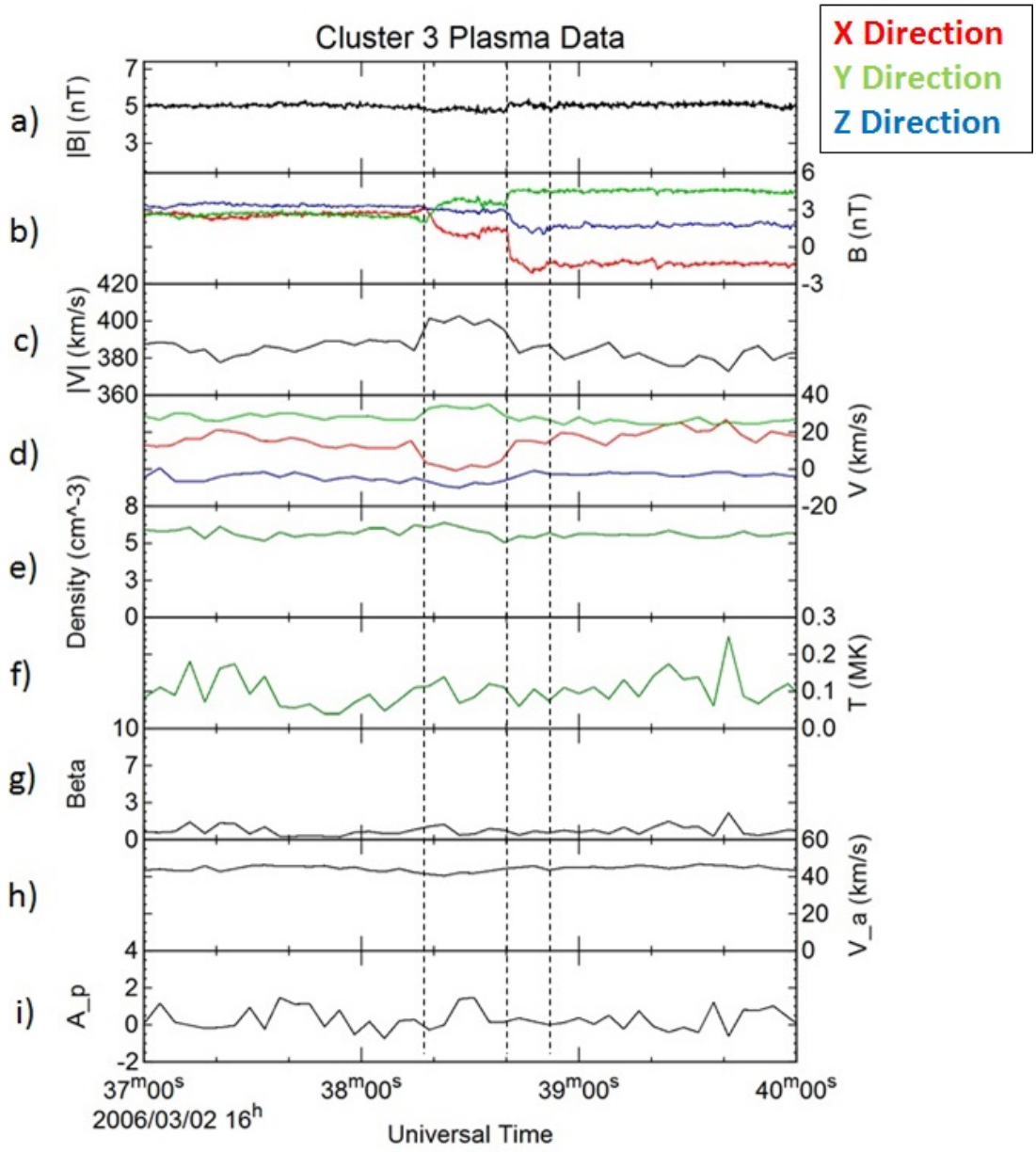

Figure 4.4: Solar wind and magnetic field data obtained by Cluster 3 over a 3 minute interval over the event on the 2nd March 2006 from 16:37:00 UT to 16:40:00 UT. This figure follows the same format as Figure 4.2.

mean weighted minimum variance analysis, described in Section 3.5.5 and with the inputs detailed in Table 4.1. The appropriate rotational matrix from the GSE co-ordinate system is given by the following matrix:

$$\begin{pmatrix} L \\ M \\ N \end{pmatrix} = \begin{pmatrix} 0.849, & -0.414, & 0.328 \\ 0.262, & -0.868, & -0.418 \\ -0.458, & -0.269, & 0.849 \end{pmatrix} \begin{pmatrix} X \\ Y \\ Z \end{pmatrix} GSE$$

The total field strength at each of the 4 Cluster spacecraft and the 3 components of the magnetic field vector transformed into this natural reference frame for the event are shown in Figure 4.5. In this natural co-ordinate frame, the field components in the mean minimum variance direction (N) are shown in red, the mean intermediate variance direction in green (M) and the mean maximum variance direction in blue (L). Panels a) and b) show the total and component magnetic field data respectively for C1 panels c) and d) for Cluster 2 and so on for all 4 Cluster spacecraft.

The full vertical dashed line indicates the start time of the first magnetic field rotation seen by Cluster 1. The vertical dashed lines on panels c) and d), e) and f), and g) and h) which cover individual spacecraft data, show the time at which that spacecraft observed the beginning of the first magnetic field rotation. The lag between these times and the Cluster 1 start time is indicated in seconds on each $|\mathbf{B}|$ panel. It can be seen that Cluster 3 encountered the event first, 0.1 s before Cluster 1. Cluster 4 observed the event 16.6 s after Cluster 1 and Cluster 2 35.5 s after Cluster 1. These values are determined as the time lag providing the maximum correlation between Cluster 1 magnetic field and the magnetic field of Cluster 2, 3 and 4 respectively. In each case the analysis used the component of magnetic field in the mean maximum variance direction, and returned a correlation

coefficient > 0.95 with a p value of < 0.01, indicating a high level of correlation between spacecraft observations.

The Cluster 4 spacecraft observes the 3 current sheets (rotations in the L direction) which appear similar to those observed at Cluster 1 and 3 but ~ 16.6 seconds later. However the Cluster 2 spacecraft does not observe these sharp current sheets. Instead it observes a more monotonic gradual rotation in the magnetic field beginning 35.5 seconds after the Cluster 1 encounter. The overall change in magnetic field direction is comparable between Cluster 2 and 4 with a total angle change of $\sim 45°$ for both spacecraft. Cluster 2 also observes some fluctuations after the main rotation has finished. These are in the same component direction (L) and so Cluster 2 may also have encountered the third current sheet. Recall that Cluster 2 is situated further in the +Z direction than the other 3 spacecraft.

Cluster spacecraft 1, 3 and 4 see 3 clear magnetic field rotations which are comparable spatially and temporally. The first current sheet rotates over 36° for Cluster 1 and 3, and 16° for Cluster 4. The time between current sheet 1 and 2 is 22 s for Cluster 1 and 3 and 18 s for Cluster 4. The rotations over the second current sheet are 44° for Cluster 1, 32° for Cluster 3 and 42° for Cluster 4. For Cluster 1 the third rotation is 18°, for Cluster 3 the rotation is 7° and for Cluster 4 15°. There are 20 s and 26 s between sheet 2 and 3 for Cluster 1 and 4 respectively, which is larger that the time difference observed at Cluster 3 (10 s). Thus, while there are small differences in the timing and level of rotation for each spacecraft, they all appear to be observing the same structure. Cluster 2 however, does not see the same magnetic field configuration as the other 3 spacecraft despite the distance between spacecraft being small in comparison to the inferred size of reconnection structures that have previously been documented (*Phan et al.*, 2006; *Gosling*, 2010,

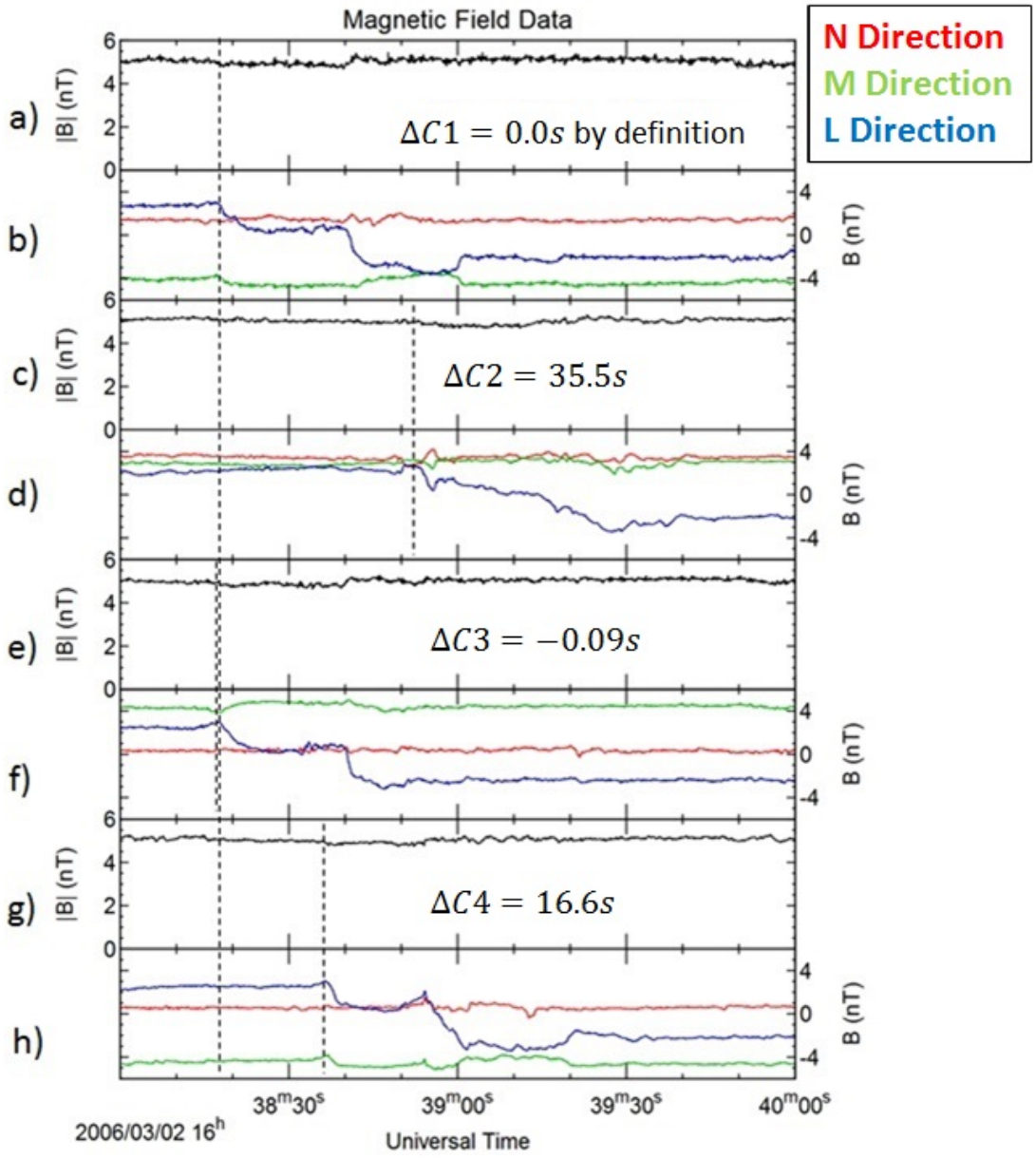

Figure 4.5: Magnetic field data for each of the four Cluster spacecraft over the event in the derived natural reference frame. The black vertical dashed lines indicate the time of observation of the initial magnetic field rotation for each of the Cluster spacecraft. The time lag between each spacecraft observing this rotation is given on each panel. It can be seen that there are 3 distinct steps of magnetic field rotation for Cluster 1, 3 and 4, whereas the magnetic field at Cluster 2 shows a gradual magnetic field rotation over the same time period.

	Time frame h:m:s UT	**Variance**	**Direction Vector**	λ	λ Rat.
C1	16:38:10 - 16:38:50	**Minimum:**	-0.404, -0.280, 0.871	0.037	3
-	-	**Intermediate:**	-0.235, -0.888, -0.395	0.109	30
-	-	**Maximum:**	0.884, -0.365, 0.292	3.3	
C2	16:38:46 - 16:39:26	**Minimum:**	-0.113, 0.469, 0.876	0.026	3
-	-	**Intermediate:**	-0.614, -0.726, 0.310	0.076	29
-	-	**Maximum:**	0.781, -0.502, 0.370	2.19	
C3	16:38:10 - 16:38:50	**Minimum:**	-0.508, -0.490, 0.708	0.011	9
-	-	**Intermediate:**	-0.124, -0.772, -0.623	0.093	35
-	-	**Maximum:**	0.852, -0.405, 0.332	3.27	
C4	16:38:27 - 16:39:07	**Minimum:**	-0.432, -0.258, 0.864	0.037	3
-	-	**Intermediate:**	-0.249, -0.887, -0.390	0.114	31
-	-	**Maximum:**	0.867, -0.384, 0.318	3.54	

Table 4.1: The results of the minimum variance analysis observed at each of the 4 spacecraft for the 2nd March 2006 event for the full crossing. The minimum, intermediate and maximum variance directions and the eigenvalues associated with each of these vectors (λ) and their ratios (λ Rat.) are given.

2011).

4.3 Evidence for Reconnection

A quantitative test of whether the above observations agree with typical predications for reconnection is the Walén test (*Paschmann et al.*, 2013, and the references therein). The Walén relation is satisfied when the change in plasma flow velocity over a discontinuity is equal to the change in the Alfvén velocity. If the Walén relation is satisfied, it indicates the likely presence of Alfvén waves and/or rotational discontinuities. It is also approximately satisfied for intermediate and 'switch-off' slow shocks which are sometimes associated with reconnection (*Nykyri et al.*, 2003). In the De Hoffman-Teller (dHT) frame (see Section 3.5.4) the Walén relation is satisfied if:

$$v_i - v_{HTi} = \pm V_{Ai} \tag{4.1}$$

where the subscript i refers to the components in GSE x, y and z direction, v_i are the components of the ion velocity (in GSE), v_{HTi} are the components of the velocity of the dHT frame (in GSE) and V_A is the local Alfvén velocity in the field aligned direction (*Paschmann et al.*, 2013).

The results of the Walén test in this instance should provide a positive correlation between the magnetic field and ion velocity on the leading edge and a negative correlation on the trailing edge of the event. In this chapter we plot the left hand side of Equation 4.1 vs. the right hand side and find the gradient of the line of best fit. If the Walén relation is perfectly satisfied the gradient of the line of best fit should equal 1, however for real world data we will consider gradients between 0.5 - 0.8 and 1.2 - 2 as weakly satisfying the Walén relation and gradients between 0.8 and 1.2 as strongly satisfying the Walén relation (*Sonnerup et al.*, 1990).

Figure 4.6 shows the plots of the left hand side of Equation 4.1 vs. the right hand side for the 3 current sheets observed by Cluster 1 and Cluster 3. The black line indicates the best fit slope as found by orthogonal regression analysis and the red line indicates the linear best fit line. The details of the Walén relation, the T-test and its significance are shown in Table 4.2. For both Cluster 1 and 3 CS1 strongly satisfies the Walén relation and CS2 and CS3 are weakly satisfying. However each of the slopes are highly correlated with the best fit lines with the student T-test determining that each is significant to the 1 % level (except CS3 as seen by Cluster 3 which is only significant to the $< 5\%$ level). It should also be noted that the Walén test is more strongly satisfied for the discontinuities as encountered by Cluster 1 than by Cluster 3. The results of the Walén test indicate that the plasma observed between CS1 and CS2 is consistent with a set of current sheets associated with reconnection. We note that it was not possible to perform the Walén test for Cluster 2 and 4 due to a lack of ion data.

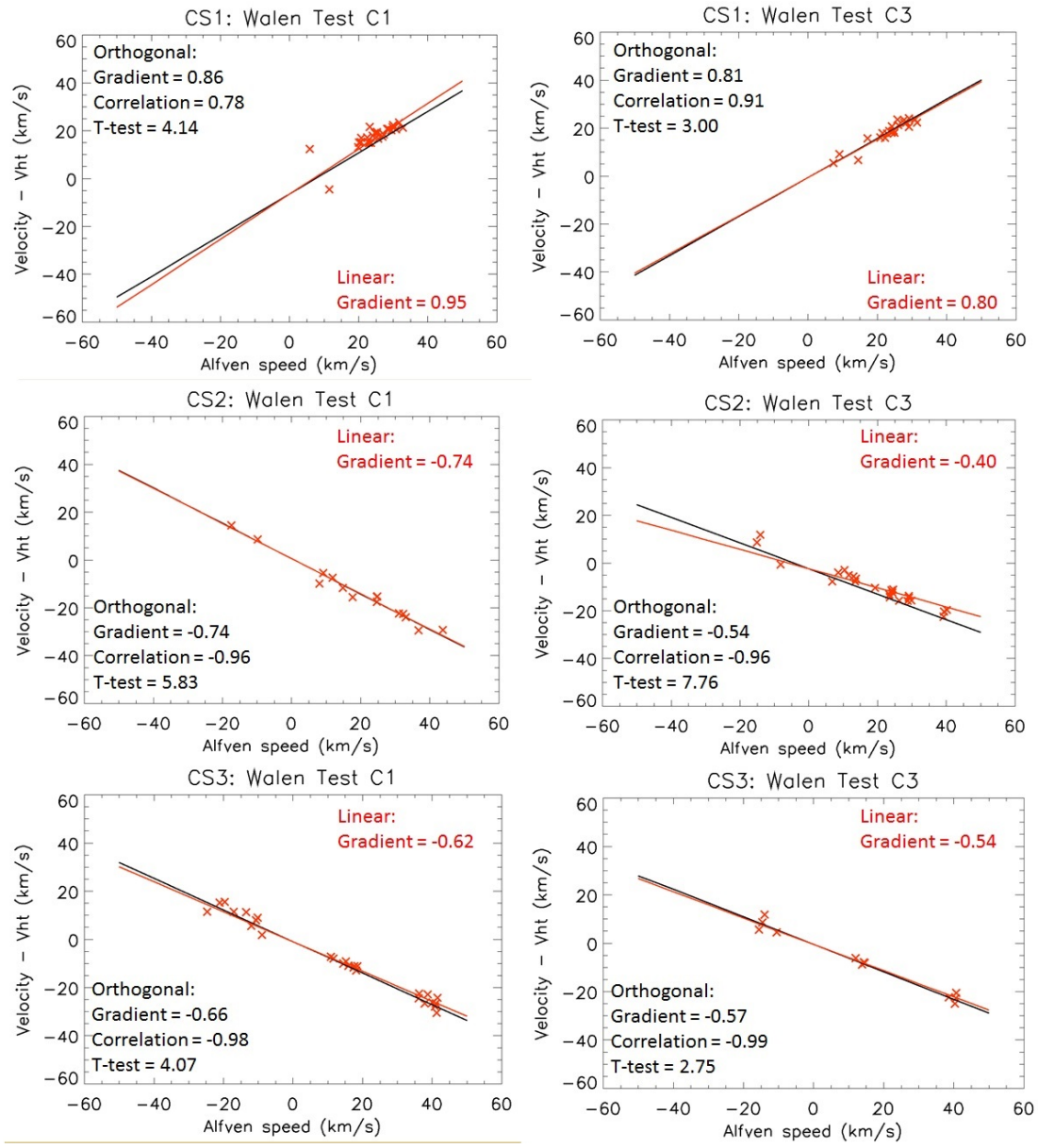

Figure 4.6: The Walén test results over the three discontinuities observed by C1 and C3. The black diagonal line indicates the gradient of the orthogonal regression analysis best fit slope and the red line indicates the linear best fit line. The gradient of both of the lines is indicated on each of the figures and the correlation and t-test result for each data set are also shown.

SC	CS	Start (h:m:s)	End (h:m:s)	V_{HT} $(km\ s^{-1})$	Int.	Gr.	Corr.	n	t.	sig.
C1	1	16:37:50	16:38:30	[-410, 12.1, -26.6]	-3.8	0.86	0.71	27	4.1	1.2E-4
C1	2	16:38:30	16:38:50	[-399, 56.2, 10.0]	-0.22	-0.76	-0.96	15	5.8	2.9E-6
C1	3	16:38:45	16:39:20	[-396, 51.1, 8.5]	-0.84	-0.66	-0.98	27	4.1	1.6E-4
C3	1	16:38:00	16:38:30	[-407, 11.0, -27.9]	0.57	0.81	0.91	24	3.0	0.00434
C3	2	16:38:20	16:38:50	[-394, 48.9, 4.4]	-2.45	-0.54	-0.96	24	7.8	6.6E-10
C3	3	16:38:45	16:39:00	[-391, 49.1, 5.57]	-0.47	-0.57	-0.99	12	2.8	0.0117

Table 4.2: Walén test results for both C1 and C3. The table contains the start and end times of each of the tests, the velocity of the De Hoffmann Teller frame, the intercept, gradient, and correlation coefficient of the best fit line of each of the Walén tests, the number of points, n, the value of the student T-test and its significance.

In order to determine the relative orientation and structure of the reconnection event we now attempt to accurately determine the orientation of each of the individual current sheets, and the outflow. This is in order to make a comparison between this reconnection event and the standard picture of reconnection in the solar wind. Using the relative positions of the spacecraft and the time lag between current sheet encounters it is possible to find an estimate for the normal direction vector of the discontinuity, under the assumption that the sheets are planar and non-rotating during the period of observation.

In order to determine the overall normal direction vector of the event using the timing method we use the following equation (*Schwartz*, 1998):

$$(\mathbf{r}_\alpha - \mathbf{r}_1) \cdot \hat{\mathbf{n}} = V(t_\alpha - t_1) \tag{4.2}$$

where $(\mathbf{r}_\alpha - \mathbf{r}_1)$ is the relative positions of the Cluster spacecraft in the GSE co-ordinate system (with Cluster 3 as the reference spacecraft), $\hat{\mathbf{n}}$ is the normal direction vector, V is the speed of the discontinuity and $(t_\alpha - t_1)$ is the time lag at the point of maximum correlation over the whole event (with Cluster 3 as the reference spacecraft). The normal direction vector for the whole event was found to be = [-0.528, -0.447, 0.722] in the GSE frame with the structure moving at a speed of $178 km\ s^{-1}$. This is only 13° away from the minimum variance direction in the natural co-ordinate frame (-0.458, -0.269, 0.849) and thus we can be confident that the reference frame is reliable. The projection of the average background solar wind velocity $(-384, 27, -2)\ km\ s^{-1}$ onto this timing-derived vector gives a speed of 189 $km\ s^{-1}$, which is consistent with speed found using the timing analysis. Note also that the projection of the solar wind velocity on the minimum variance direction in our natural co-ordinate frame is 167 $km\ s^{-1}$, which is also consistent

with the speed found using the timing analysis.

The timing analysis technique was also implemented over the individual current sheets. From this it was determined that the normal direction vector and speed of CS1 was [-0.615, -0.414, 0.671] and 163 $km\ s^{-1}$ and for CS2 they were $[-0.431, -0.478, -0.765]$ and 201 $km\ s^{-1}$. The solar wind projection onto the CS1 normal direction vector gives a speed of 228 $km\ s^{-1}$ and the projection onto the CS2 normal direction is 150 $km\ s^{-1}$. From this it appears that CS1 is moving slower while CS2 is moving faster in the direction normal to the current sheets than the corresponding speed of the solar wind.

The orientation and configuration of each of the current sheets that bound the magnetic reconnection event can also be determined with some confidence simply by using the magnetic field data. We again use the minimum variance technique (as described in 3.5.1) (*Sonnerup et al.*, 1967) to determine the individual orientation of the current sheets observed in this event. These results are presented in Appendix A. We note that several of the minimum variance directions for the individual current sheets are not well-defined (with λ ratios < 5) so some caution needs to be assumed in drawing conclusions from these results. Cluster 4 is the only spacecraft with minimum variance results reliable enough for both sheets CS1 and CS2 if we use the definition of a well-defined direction being that with a ratio of > 10 (*Paschmann and Daly*, 1998).

To accurately determine the structure of the event we can use a combination of the timing and the minimum variance techniques. The minimum variance directions are not well-defined but the maximum variance directions are. Thus we can reliably use the maximum variance direction when finding the orientation of the current sheets but not the minimum. We use the normal direction vector found

by the timing analysis in order to orientate the normal direction vectors for each current sheet for each spacecraft by using:

$$\mathbf{E}'_{min_{ij}} = \mathbf{E}_{max_{ij}} \times (\mathbf{E}_{timing} \times \mathbf{E}_{max_{ij}}) \tag{4.3}$$

Where the subscript i stands for the spacecraft number, 1-4, and the subscript j stands for the current sheet number 1, 2. The third co-ordinate direction vector was found using the cross product of $\mathbf{E}'_{min_{ij}}$ and $\mathbf{E}_{maxij}$ as shown in Section 3.5.1.

This analysis resulted in the set of individual normal directions (in GSE co-ordinates) to the current sheet shown in Table 4.3, which indicate that each of the current sheet normals are predominantly in the Z GSE direction with the exception of CS2 for Cluster 2. Each of these new 'fixed' normals were found to be within 10° of the timing normal except CS2 for Cluster 2. We also present the angle between the two sheets CS1 and CS2 in Table 4.3 by calculating the angle between the two current sheet normals. The angles between the current sheet normals for spacecraft 1,3, and 4 are very small ($\sim 5°$) but the angles for Cluster 2 is much larger (33°). Furthermore, by taking the cross product of these two values, the normals for sheets CS1 and CS2, the direction of the X-line can be inferred; under the large scale assumption, the X line will be orthogonal to the normals of both current sheets.

The exhaust velocity vectors were also transformed into the natural reference frame. The average solar wind velocity on either side of the event was subtracted from the total ion velocity to leave a residual flow velocity in the reference frame moving with the solar wind. In GSE co-ordinates, this background velocity is given by: (-384, 27, -2) $km\ s^{-1}$. This gives a residual velocity of (-17, 6, -6) $km\ s^{-1}$. This vector is 83° and 86° away from the normal direction vector of the whole

S/C	n̂ CS1 (GSE)	n̂ CS2 (GSE)	A °	X-line Direction
C1	-0.446, -0.480, 0.722	-0.519, -0.454, 0.723	4	0.266, 0.720, 0.641
C2	-0.589, -0.407, 0.692	-0.725, -0.04, 0.425	33	0.404, 0.699, 0.590
C3	-0.503, -0.459, 0.732	-0.430, -0.521, 0.726	6	0.506, 0.530, 0.680
C4	-0.479, -0.469, 0.740	-0.565, -0.410, 0.713	6	0.354, 0.697, 0.624

Table 4.3: Details of the event from the point of view of each spacecraft (S/C). Table includes the normal direction vector of each of the current sheets determined using a combination of the timing analysis and minimum variance methods. It also presents the angle (A) between the two current sheets and the X-line direction.

event found by timing analysis and minimum variance analysis on the magnetic field respectively, which is consistent with the expectations of a reconnection event geometry.

Figure 4.7 shows a 2D representation of the crossing of Cluster 1 and 3 through the reconnection event in the natural co-ordinate system and the solar wind rest frame. Here the X-line direction (determined from the cross product of CS1 and CS2 sheet normals) is directed out of the page, the normal direction of the natural co-ordinate system is along the horizontal axis and the vertical axis shows the direction that makes an orthogonal right-handed set. The black arrows indicate the measured magnetic field vectors and the red arrows are the residual ion velocity vectors. The magnetic field has been interpolated onto the ion velocity time series. CS1 and CS2 are indicated by the green and blue lines respectively. The grey arrow is the spacecraft trajectory through the exhaust at the negative residual velocity (from right to left). The residual ion velocity is the total ion velocity minus the background solar wind velocity. Point (0,0) is the position at the first ion velocity and magnetic field measurement. This figure illustrates the magnetic field clearly rotates over each current sheet for both spacecraft. The residual ion velocity is much greater inside the exhaust region and it is directed away from the

direction of the inferred reconnection site. From the geometry of these figures, the Cluster spacecraft encounter the reconnection event very close to the reconnection site ($\sim 2 \times 10^4$ km or approximately 3 R_E) assuming that the normal direction vectors are accurate and the sheets are planar in nature.

Unfortunately there is no CIS data available for Cluster 2 and 4 which means that it is not possible to generate a complete picture of the event from the perspective of all 4 spacecraft.

4.4 ACE and Wind Observations

ACE and Wind were both in the solar wind at the time of this event but located at relatively large distances from Cluster (see Section 4.1). These spacecraft have often been used to study magnetic reconnection in the solar wind (*Phan et al.*, 2009). We use the derived speed and orientation of the current sheet CS1 and CS2 at Cluster to estimate when these sheets should have passed over ACE and Wind, assuming that, on the global scale, they remain large scale planar structures travelling with the same solar wind velocity.

The predictions are shown in Table 4.4. Note that even the small angle between CS1 and CS2 normals results in a significant time difference between arrival of these 2 current sheets at ACE and Wind. In particular, we predict that the crossing duration between these sheets for ACE would be 4 minutes and Wind would be 10 minutes. This assumes that the current sheets remain large scale, planar and non-rotational over the large separation scales between these spacecraft. Figure 4.8 shows the 3 components of the magnetic field in GSE co-ordinates and the total ion velocity for the ACE, Wind and Cluster 1 spacecraft over the times when we predict they should have observed the event. The red bars highlight the

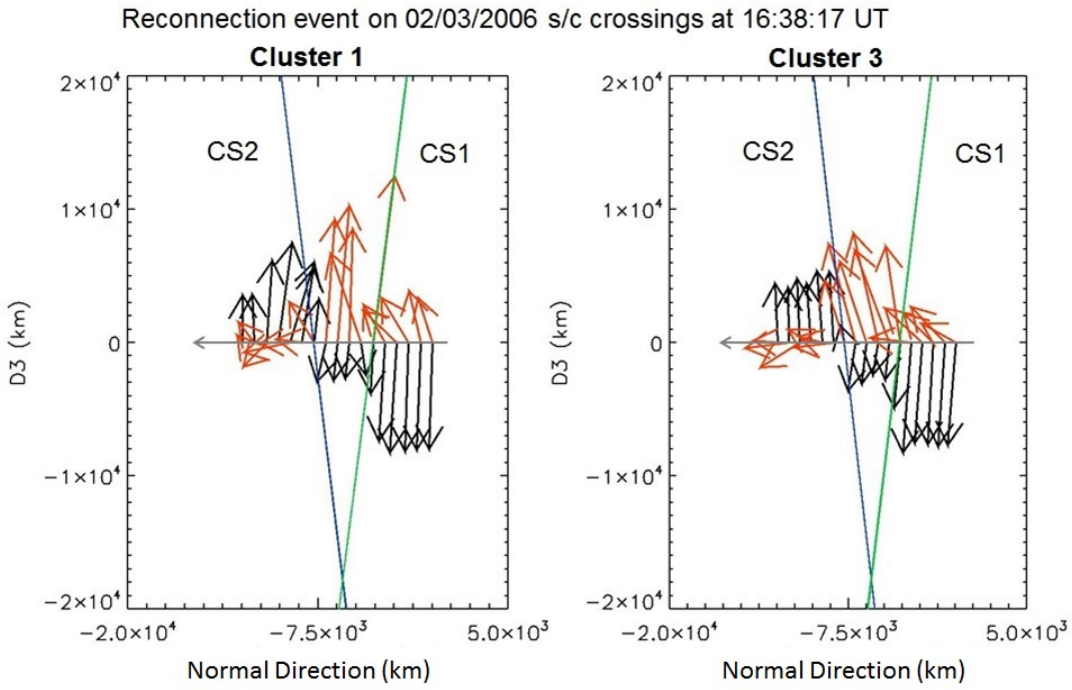

Figure 4.7: The geometry of the crossings of Cluster spacecraft 1 and 3 over the event. The X-line direction is out of the page, the normal direction is plotted on the horizontal axis and the direction that makes up a right handed set is along the vertical axis in each panel. The green and blue solid lines indicate CS1 and CS2 respectively, the black arrows show the magnetic field vectors and the red arrows show the residual ion velocity vectors after a background velocity has been subtracted. The grey arrow shows the motion of the spacecraft. A magnetic field rotation over each of the current sheets for each of the spacecraft and an increase in ion velocity between the two current sheets in the direction away from the x point is observed. The ion velocity measurements are not available for spacecraft 2 and 4, hence similar plots cannot be constructed for these spacecraft data.

Spacecraft	**Predicted Time Lag /s**	**Time Lag /s** (at max. cor.)	**Maximum Correlation**
Cluster 1	0.0	0.0	1.0
Cluster 2	32	35.5	0.960
Cluster 3	-5	-0.09	0.974
Cluster 4	13	16.6	0.979
ACE	CS1: -3100, CS2:-2800	-4592	0.964
Wind	CS1:-1200, CS2: - 600	-1904	0.887

Table 4.4: The predicted and correlated time lags between a spacecraft and Cluster 1.

regions where the current sheets were predicted to occur and the black dashed lines indicate the point of maximum correlation between the magnetic field data based on analysis in Table 4.4.

There are no similar structures at the predicted times (highlighted by the red bars on Figure 4.8) for either the ACE or Wind data, even within a error margin of ± 10 mins. Thus we did a cross correlation analysis on the ACE and Wind data with the Cluster data to see whether there were any similar structures in the data within a few hours of the predicted time. Table 4.4 also shows the time lags found using the maximum cross correlation analysis on the magnetic field in the maximum variance direction for each spacecraft. This cross correlation returns a maximum correlation at a time lag that is longer than predicted. For ACE we get a maximum correlation of 0.96 at a time of 4590 seconds (50% longer than the average predicted time $\sim 3000\ s$) before the encounter at Cluster 1 and for Wind a maximum correlation of 0.89 at a time of 1904 seconds (more than double the average predicted time of 900 s) before the Cluster encounter (highlighted by the black dashed lines on Figure 4.8). At these times there are features that look similar to the features seen at Cluster (as expected if the correlation coefficient is

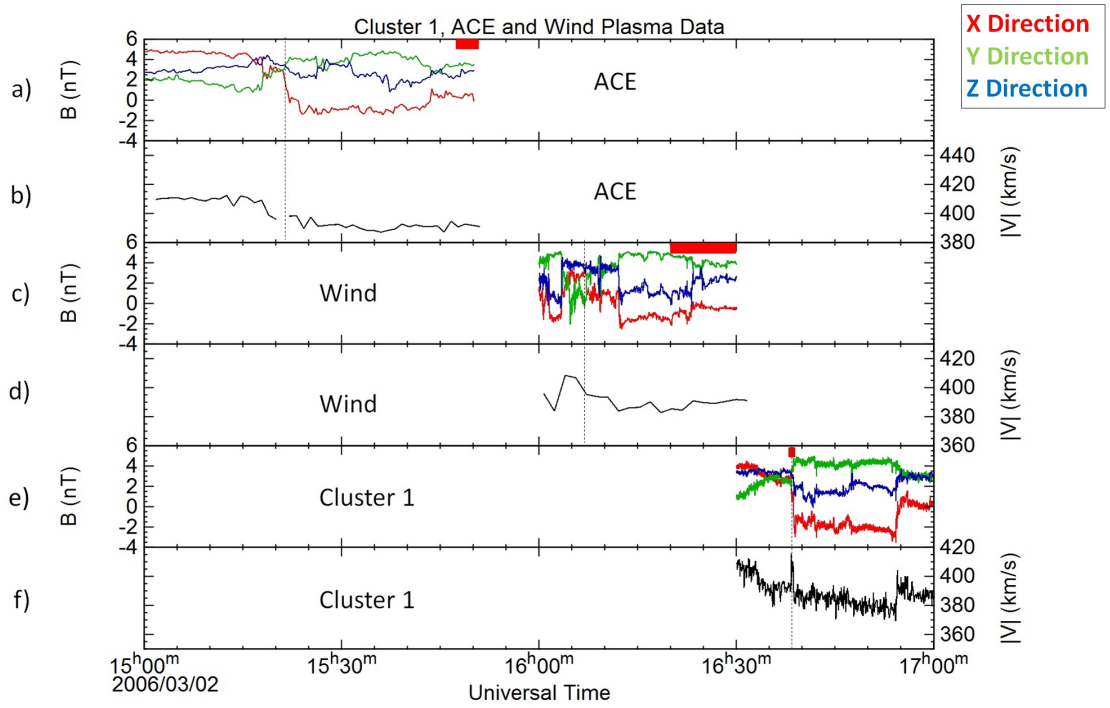

Figure 4.8: The magnetic field and ion velocity data for the ACE, Wind, and Cluster spacecraft over the periods that they were predicted to have encountered the event assuming that the current sheets remain planar and move with the same solar wind velocity. For each spacecraft the upper panel shows the 3 components of the magnetic field and the lower panel shows the total ion velocity. The red bars at the top of panels a), c) and e) indicate the predicted time duration of the event in each case and the black dashed lines indicate the time lag at maximum correlation.

high), namely a magnetic field rotation predominately in the x-direction in GSE co-ordinates, which appears in two step-like stages.

A minimum variance analysis was done over the rotations found at the time of maximum correlation for ACE and Wind, the results of which are shown in Table 4.5 along with the angle between the vector and the equivalent in the natural co-ordinate frame (e.g. the angle between the minimum variance direction and the n direction). The ACE and Wind minimum variance results for the CS1 are however not similar to that of the Cluster spacecraft. For example if we compare the maximum variance direction (well defined in each case) for ACE and Wind we find that each of the direction vectors is at an angle greater than 30° from the L direction of the natural co-ordinate frame. However the equivalent angle for CS2 is very close for ACE (9°) and quite close for Wind (18°). Thus despite the possible identification of the event by cross correlation analysis, the minimum variance analysis for the ACE and Wind spacecraft is not consistent with the interpretation that the current sheets are planar over large distances, unless the current sheets have significantly rotated.

There is no evidence of any ion velocity enhancement at ACE at either the predicted time or at the time lag of maximum correlation and thus there is no evidence that there is magnetic reconnection taking place at this spacecraft. There is, however, an increase in ion velocity just before the time lag at maximum correlation, indicating that reconnection may be occurring at the Wind spacecraft.

S/C	Time frame, h:m:s UT		Direction Vector	λ	ratios	A
ACE	CS1: 15:17:40 - 15:18:10	**Min:**	-0.029, -0.464, 0.885	0.00959	3	27°
		Int:	-0.648, -0.665, -0.371	0.0271		56°
		Max:	0.761, -0.584, -0.281	1.9	70	37°
Wind	CS1 :16:07:00 - 16:07:20	**Min:**	0.712, 0.592, 0.377	0.0131	3	99°
		Int:	0.219, 0.322, -0.921	0.042		81°
		Max:	-0.667, 0.738, 0.100	2.39	57	33°
ACE	CS2 : 15:20:55 - 15:22:25	**Min:**	0.279, 0.878, 0.390	0.00559	6	92°
		Int:	-0.314, -0.300, 0.901	0.036		79°
		Max:	0.907, -0.374, 0.192	1.68	47	9°
Wind	CS2: 16:11:58 - 16:12:15	**Min:**	-0.358, 0.546, 0.785	0.0121	5	48°
		Int:	0.626, 0.742 -0.239	0.065		59°
		Max:	-0.693, 0.389, -0.607	3.13	48	18°

Table 4.5: The minimum variance analysis for CS1 and CS2 for the ACE and Wind spacecraft (S/C), the minimum, intermediate and maximum variance directions, the eigenvalues associated with each of these vectors are given as well as the angle between that vector and the equivalent vector in the natural co-ordinate frame.

4.5 Interpretation and Discussion

The observations and analysis presented are consistent with a magnetic reconnection event being encountered by the Cluster spacecraft. The Cluster 1 and 3 data show magnetic field and ion velocity changes that are consistent with previous studies of similar events (*Gosling et al.*, 2005). There is a bifurcated, or even trifurcated, magnetic field reversal region, within which there is a significant increase in ion velocity directed between the two main current sheets in both cases. The changes in the magnetic field and ion velocity are anti-correlated over the leading edge of the exhaust and correlated on the trailing edge, a feature of reconnection initially indicated by *Gosling et al.* (2005).

The spacecraft, in particular Cluster 1, observed small plasma $\Delta\beta$ values (< 0.2 for both spacecraft) across the event. This is consistent with reconnection occurring for a magnetic shear which is fairly small (in this case 63°) as the plasma $\Delta\beta$ is expected to be small in order for magnetic reconnection to occur (*Phan et al.*, 2010).

The Alfvén speed on either side of the exhaust is approximately 45 $km\ s^{-1}$, which is typical of the solar wind (*Mullan et al.*, 2006). The exhaust jet in the frame of reference of the solar wind is travelling at speeds of approximately 20 $km\ s^{-1}$, approximately half of the exterior Alfvén speed, with respect to the reference frame of the event, which suggests that not all of the available magnetic energy is being converted into plasma bulk flow velocity (*Yamada et al.*, 2014).

The Walén test results for the Cluster spacecraft show that the leading and trailing discontinuities weakly satisfy the Walén relation in the positive and negative sense respectively. This is expected from a reconnection event where the plasma flows into the exhaust region from either side of the event. A weakly sat-

isfying trend would indicate the presence of intermediate and slow mode shocks (*Sonnerup et al.*, 1990). *Petschek* (1964) discussed the presence of slow mode shocks on the boundaries of magnetic reconnection events, so these are expected results.

It is logical to abduct that the CS1 is the boundary of the ion outflow and CS3 is the ion boundary on the other side as the ion velocity increase is completely encompassed in these times thus logically CS2 is the central current sheet.

The results of the timing analysis show that CS1 is moving slower and CS2 faster than expected in the normal direction to the current sheets, which implies that they are moving closer together in the solar wind reference frame. This could be indicative of a few physical processes, for example a slowing magnetic reconnection rate would cause the current sheets to move closer together (*Owen and Cowley*, 1987b). If this is the case, the reconnection rate could be slowing down / turning off which might suggest that the current sheets had started to merge when reached by Cluster 2, which could explain the lack of two clear rotations at that spacecraft.

A comparison between the magnetic field data collected by the four spacecraft, shows significant spatial and/or temporal changes over scales that are of order that of the Cluster spacecraft tetrahedron formation. The most significant difference in the magnetic field over the event is that between Cluster 2 and the other three Cluster spacecraft, as is evident in Figure 4.5. While Cluster 2 does show an overall magnetic field rotation that is comparable in size to that observed by the other spacecraft, it does not observe the distinctive sharp rotations of magnetic field. This suggests that the event itself is either a relatively small-scale event, a statement that is corroborated by the crossing time of the event ($\sim 30\ s$), or that

the reconnection event is very short lived (< 60 s between the first encounter by Cluster 1 and the final encounter by Cluster 2).

By assuming the current sheets are moving with the solar wind, are large scale and non-rotating, the time at which the event would have passed the spacecraft ACE and Wind was predicted. Figure 4.8 shows that there is no similar magnetic field structure at the predicted times, indicated by the red bar. However a cross - correlation analysis determined that there were similar features in the ACE and Wind data rather earlier (25 minutes earlier at ACE and 13 minutes earlier at Wind) than predicted. This data shows there are two current sheets at ACE and Wind that follow a similar magnetic field rotation to the ones found at Cluster, but do not necessarily have the same orientation. There is no distinct ion velocity increase between the two at ACE, thus it appears unlikely that magnetic reconnection is active here. However there is an increase in ion velocity at approximately the same time as the time lag at maximum correlation at Wind and so reconnection could be active here.

In order to determine the orientation of the current sheets a minimum variance analysis was done. CS2 at ACE and wind have a similar orientation to the sheets found at Cluster, but CS1 for ACE and Wind do not. It seems likely that the current sheets are not the same current sheets as seen at Cluster, unless the sheets have rotated significantly or are curved over large distances. A rotation of the current sheets could also account for the difference between the observed and predicted time between the sheets being detected at ACE and Wind. As both spacecraft are > 100 R_E away from Cluster in the -X direction it could be that these current sheets are simply not planar over such large scales. If the reconnection exhaust is significantly asymmetric the current sheets might not have the

same orientation as a Cluster and ACE. Another alternative would be that Wind crosses the reconnection exhaust on the other side of the X-line and so the sheets are not in the same orientation as at Cluster.

It appears that clear reconnection outflows are seen only at Cluster, though there is some indication that a reconnection outflow is seen at Wind as well. This suggests that magnetic reconnection could have been initiated between the time of observation of the ACE and Wind spacecraft encounters. Previous studies have suggested that magnetic reconnection in the solar wind is fundamentally large scale ($\sim$ 100 R_E) and non-patchy (*Phan et al.*, 2006). In this study we have shown evidence that reconnection is variable on small temporal ($< 60s$) and/or spatial scales ($\sim 10,000\ km$). This is indicated by the differences in the magnetic field between Cluster 1, 3 and 4 and Cluster 2; Cluster 2 witnessed a gradual magnetic field rotation whereas the other 3 Cluster spacecraft observed two distinct magnetic field rotations. Also the differences in the Walén test results from Cluster 1 and 3, showed that the Walén test was better satisfied at Cluster 1 than Cluster 3, which in itself suggests that the event was evolving. The current sheets also appeared to be moving together which could be indicative of the reconnection rate slowing down. Despite the multi-spacecraft observations, it was not possible to determine whether the differences between spacecraft are spatial or temporal in nature, possible explanations include: rotating current sheets, current sheets moving relative to each other and, reconnection turning on between spacecraft.

4.6 Conclusion of Case Study

We have shown evidence of a magnetic reconnection event that exhibits large differences in the magnetic field structure over distances that are smaller than the

Cluster spacecraft separation. This result raises questions about our current understanding of magnetic reconnection in the solar wind. While large-scale, steady state events are evident in the solar wind, other small scale, transient events are also clearly possible. Multi-spacecraft observations of such events could help shed light on the triggers for the start and end of reconnection in the solar wind environment.

In this study we found:

- Small differences in the structure of the magnetic field between the 4 Cluster spacecraft suggesting that the reconnection has evolved over distances and times smaller than that between the Cluster spacecraft.

- The speeds of each of the current sheets at Cluster suggested that they were moving towards each other in the rest frame of the solar wind consistent with a reducing reconnection rate.

- Larger differences in the structure of the magnetic field between Cluster and the spacecraft ACE and Wind which suggests evolution on a large scale.

- It is possible that the reconnection associated structure is rotating in the solar wind frame and the ACE and Wind spacecraft do not observe exactly the same orientations for the current sheets.

Chapter 5

Reconnection Structures in the Solar Wind and a Comparison with Theory

5.1 Introduction

The current prevailing understanding of reconnection in the solar wind is as described in the model of *Gosling et al.* (2005a); a bifurcated current sheet bounds the reconnection exhaust, as discussed in Chapter 2. However, there are other models of reconnection outflow structure that suggest that the outflow region may be more complex than this simple bifurcated current sheet model assumes.

The Petschek model (*Petschek*, 1964) of reconnection has been generalised over time to include situations where the inflow conditions are asymmetric (with the Petschek solution as a special case).

For example, *Semenov et al* (1983) presented a two dimensional model of reconnection in which the inflow magnetic field strength and/or plasma density are

asymmetric. This is expanded on in *Heyn et al.* (1985) who devised a generalised structure for the reconnection outflow region shown in Figure 2.5. The structure of the reconnection layers shown are dependent on the ratios of the inflow parameters on either side of the structure. The structure of such reconnection events, as shown in Figure 2.5, take the form: $AS^{-}(R^{-})C\tilde{S}^{-}$ where A is a rotational wave (or Alfvén wave), S is a slow shock wave, R is a slow expansion fan, C is a contact discontinuity and $\tilde{S}$ is a slow shock wave on the opposite inflow side. The brackets indicate that the slow shock wave can be replaced by the slow expansion fan in the very asymmetric case. For $\nu > \nu_{ACS}$ there is a slow shock solution ($AS^{-}C\tilde{S}^{-}$) and for $\nu < \nu_{ACS}$ the solution is a rarefaction wave ($AR^{-}C\tilde{S}^{-}$) where

$$v_{ACS} = \frac{(\mu-1)^2}{4}\frac{\gamma(\beta+1)+(2-\gamma)\mu}{\gamma(\beta+1)-(\mu+1)+(2-\gamma)\mu} \tag{5.1}$$

In this case $v = \tilde{\rho}_0/\rho_0$, $\mu = \tilde{B}_0/B_0$, $\beta = \frac{8\pi p_0}{B_0^2}$, and $\gamma = \frac{c_p}{c_v}$ where ρ is the density, B_0 is the magnetic field, p_0 is the gas pressure and γ is the ratio of specific heats; ˜ indicates which inflow side is being referred to. The side that the rotation Alfvén wave appears is dependent on ratio of the inflow Alfvén speeds. If, for example, the inflow on the leading side is greater than that of the trailing side, the rotational Alfvén waves (A) should appear downstream of the slow mode shocks (S, i.e at the trailing edge) as shown in Figure 5.1. If there is only a slight asymmetry between the inflows the slow mode shocks will be of switch-off type (*Heyn et al.*, 1985).

In this chapter we first present a new concept for the structure of a reconnection exhaust region and apply it to an existing theoretical treatment, Section 5.2. We then test against three case studies of events that were observed in the solar wind, Sections 5.4 - 5.6. In Section 5.7 we discuss the results and in Section 5.8 draw our conclusions.

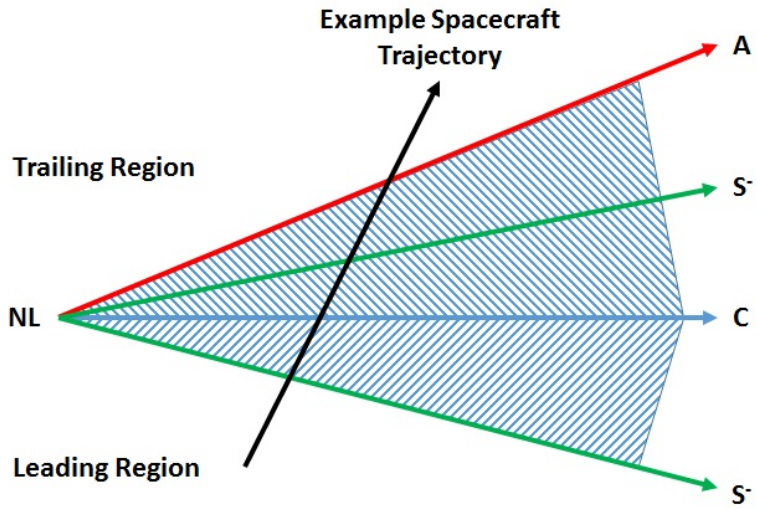

Figure 5.1: Figure shows an example of the Heyn model where the inflow velocity on the trailing side is slightly greater that of the leading side. 'A' (red arrowed line) represents a rotational Alfvén wave, '$\tilde{S}$' and 'S' (green arrowed lines) the slow mode shocks on the leading and trailing sides respectively and 'C' (the blue arrowed line) the contact discontinuity. The black arrow indicates an example spacecraft trajectory. The blue shaded areas indicate the reconnection outflows on either side of the contact discontinuity.

5.2 New Concept for the Reconnection Exhaust Region

In Figure 5.2 we present a sketch which illustrates a new concept for the possible boundaries that we believe could be present within a generalised reconnection event. Figure 5.2 also shows a graphical representation of some parameters we believe are relevant to the analysis of such events, which we present later in this chapter. In Figure 5.2, the original current sheet is shown by the horizontal red dashed line. The blue shaded areas either side of the original current sheet represent the regions that would contain the outflow ions (travelling at speeds v_{01} and v_{02}) and the red shaded areas show areas into which the outflow electrons could expand. This region extends further from the original current sheet than the region occupied by ions as the electrons are able to stream away from the current sheet along reconnected field lines much faster than the ions. In principle, the fastest moving electrons may form a layer which extends out as far as the most recently reconnected field line, or the magnetic separatrix, which in this figure are represented by the thick red arrowed lines. The angles between the separatrix and the original current sheet are defined as θ_1 and θ_2 and between the ion outflow boundary and the original current sheet ϕ_1 and ϕ_2. The exterior ion flows on either side of the event are defined as V_{in1} and V_{in2} with densities of n_1 and n_2.

In principle, there will be a gradient in the plasma populations at each of the boundaries between the regions defined above. These gradients may create a diamagnetic current sheet co-located at the boundary, and thus the magnetic field could change strength and/or rotate over each of the boundaries. An example spacecraft trajectory across such a reconnection event is represented by the black

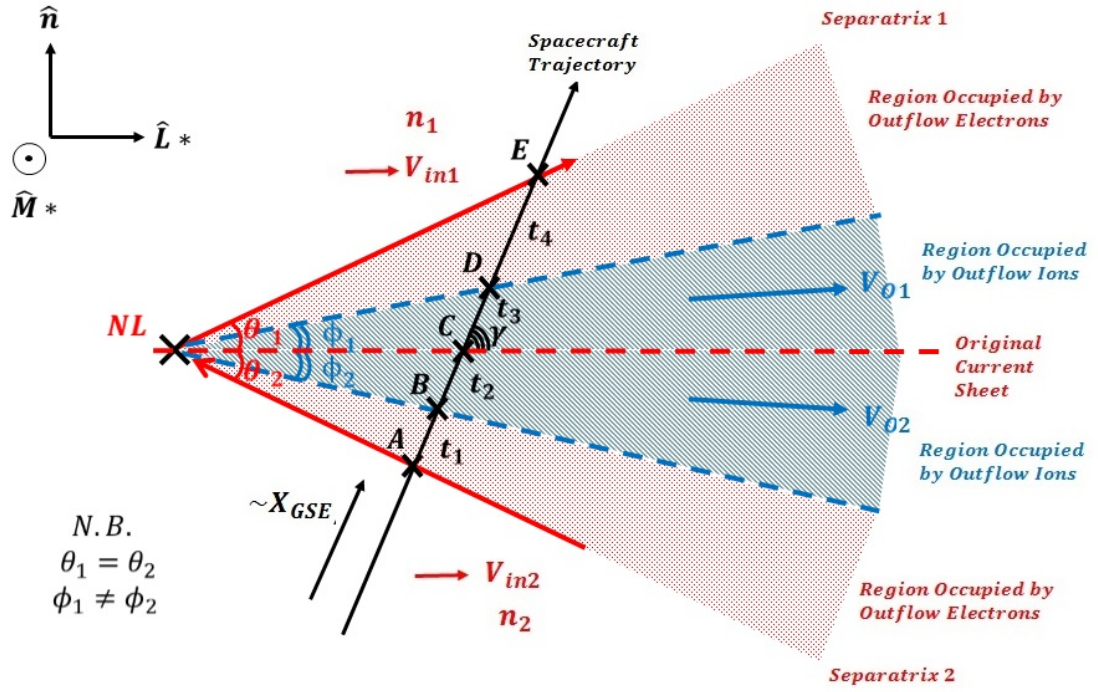

Figure 5.2: A sketch of possible boundaries associated with a magnetic reconnection exhaust outflow in the solar wind. The co-ordinate system assumed is such that the bounding separatrix (the thick red arrows bounding the red shaded area - the region occupied by the outflow electrons) are symmetrical about the original current sheet (red dashed line). This means that the angle between the original current sheet and the two separatrices are equal: $\theta_1 = \theta_2$. The blue shaded area shows the region occupied by the outflow ions. These regions on either side of the original current sheet will contain the reconnection outflows (V_{O1} and V_{O2}). The boundaries of these regions (indicated by the blue dashed lines) will form different angles with the original current sheet ($\phi_1 \neq \phi_2$). The electron outflow region (red shaded area) extends further towards the separatrix, as the electrons are moving at higher speeds than the ions. The magnetic field can potentially rotate across each of the boundaries (shown by the thin red arrows) due to the gradient in plasma properties across the boundary leading to a diamagnetic depression of the field strength. If a spacecraft were to pass through the region, for example along a trajectory represented by the black arrow, it could encounter up to 5 distinct boundaries (at A, B, C, D and E) which encompass the 4 layers. The relative time spent in each of these regions is dependent on the angle between the spacecraft trajectory and the original current sheet γ, as well as the angles subtended by the separatrixes and plasma boundaries. At either side of the event we have an external ion inflow velocity V_{in1} and V_{in2} with densities of n_1 and n_2.

arrow (in the solar wind context this direction should be approximately similar to the X direction in GSE co-ordinates as the structure should be carried past spacecraft with the solar wind velocity). The angle between the spacecraft trajectory and the original current sheet is given by parameter γ. Given the above arguments, a spacecraft travelling along such a trajectory could potentially see current sheets at points A, B, C, D, and E, depending on the field and plasma conditions within and around the event and/or the nature of the gradients in the plasma properties. A current sheet at C will be detected if the original current sheet is not completely eliminated by the diamagnetic effects of the heated outflow ions in the reconnection process and a weak gradient persists. We expect there will be current sheets at B and D if the heated ion outflows do have a diamagnetic effect (if this is the case it will reduce any rotation around C), and at A and E if the electron outflows also drive a diamagnetic effect.

The electron outflow could be observed indirectly by the observations of current sheets that are outside the ion outflow. But they could also be observed more directly by looking at changes in the differential energy flux of electrons over all pitch angles, as there may be a change in the distribution of electrons over the boundaries. This would be most apparent in situations where the reconnection changes the topology of field lines between open, closed and disconnected field lines due to the direction (or absence of in the case of disconnected field lines) of the strahl electrons as discussed in *Gosling et al.* (2005a). For the remainder of this thesis we shall be considering the indirect observations of the current sheets at the boundary of the electron outflow region.

The co-ordinate system employed in this analysis is indicated in the top right of the figure. Here, n is the direction of minimum variance of the magnetic field

over the whole event, which we can assume in an ideal case to be representative of the average normal direction to the system of current sheets, since $\nabla \cdot B = 0$ implies $B_n = constant$. In order to apply an existing analysis to this concept, in this Chapter M* and L* are chosen such that the magnetic field on either side of the event are equal and opposite in the L* direction. With regards to a minimum variance analysis, the L* direction should be similar to the direction of the magnetic field in the maximum variance direction (but not necessarily exactly the same due to the possible presence of guide fields) as it identifies the reversing component of the magnetic field across the current system. In this framework we expect $\theta_1 = \theta_2$ since the field lines defining the separatrix have $B_{N1} = B_{N2}$ and $B_{L*1} = -B_{L*2}$. Note however that $\phi_1 \neq \phi_2$ necessarily.

Figure 5.3 shows some examples of an idealised reproductions of the field and plasma flow variations that might be observed during crossings of possible reconnection structures consistent with some or all of the current sheets identified in Figure 5.2. Panel (i) shows the example where all 5 boundaries form current sheets, and thus magnetic field rotations are visible at all, and there are differences between the two outflows. In this scenario both the ion outflow and the electron outflow show a diamagnetic effect and the original current sheet is still detectable. Panel (ii) shows the case which is consistent with the typical Gosling sketch of reconnection in the solar wind. In this panel we show the case in which the original current sheet has been completely destroyed (hence no rotation at C) and the electrons are considered to have little or no diamagnetic effect on the magnetic field (at A or E). Also in this case there is a single outflow speed, $v_{01} = v_{02}$.

Panels (iii) and (iv) show examples where there is a detectable outflow on only one side of the original current sheet. This situation may arise if the differences in

inflow conditions on either side of the current sheets mean that the plasma from one side dominates in the interaction and stress balance at the original current sheet. If this plasma is largely transmitted though the current sheet it will appear as an accelerated outflow on the other side, but there may be an absence of a flow through in the other direction. Panel (iii) shows the example with visible current sheets at B, C, and D. This will thus appear as though there is a Gosling style reconnection event with another current sheet nearby (as is for example seen in Chapter 4 in the Cluster 1 data, see Figure 4.2). In contrast, panel (iv) shows no rotation at point D, in which case it would appear in the data to look similar to that of panel (ii) but perhaps of relatively shorter duration. If there were a small reconnection outflow between C and D (such that there is no diamagnetic effect at D) the structure may appear as though the changes in the ion properties occur somewhat outside the major current sheet boundaries (we will consider a case study like this later in the chapter, see Figure 5.7).

Panels (v) and (vi) show scenarios where a change may be seen in one of the variables but not in the other. Panel (v) shows a situation where the rotation at C is apparent but the outflow speeds are the same on both sides of the current sheet whereas Panel (vi) shows a scenario where there is no apparent change in the magnetic field over the current sheet at C but there are two different outflow speeds.

The above examples illustrate that there may be a large variety of reconnection structures possible, dependent on the individual reconnection event characteristics.

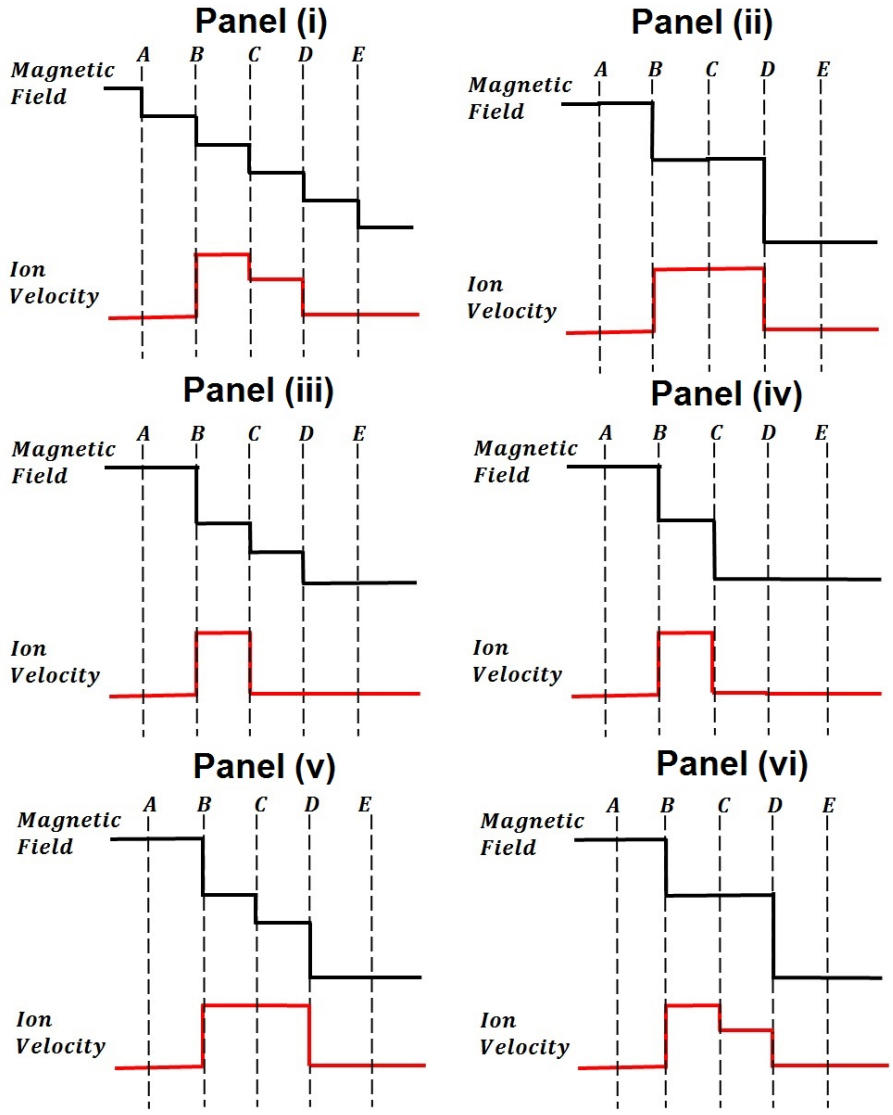

Figure 5.3: Representative examples of reconnection outflows and current sheet structure. In each panel the black trace represents the variation of the transverse component of the magnetic field to the current sheet, while the red trace represents the variation in ion flow velocity. Panel (i) shows the result if all possible current sheets and gradients in ion flows occur. Panel (ii) shows the result which is in keeping with the Gosling model (only rotations at B and C and equal outflows). Panel (iii) shows an example where there are rotations are seen and B, C, and D but only at outflow between B and C is large enough to be detected. Panel (iv) shows a similar situation but in this case there is also no detectable field rotation at D. Panel (v) shows a situation where there are rotations at B, C, and D but the outflows are similar in strength. Panel (vi) shows an example where the magnetic field is the same as in the Gosling model but the outflows are different. This is not an exhaustive set, many variations on these themes are possible.

5.3 Quantified Testing of the Concepts

In order to make the concept introduced in the previous section more quantified, we apply some analytical results from previous studies. In this chapter we describe an adaptation of a mathematical model of magnetic reconnection to the concepts introduced in the previous section. We then apply this model to three case studies in which we use the inflow conditions surrounding a magnetic reconnection event in the solar wind as inputs for this model and test the model output against the observations.

In Chapter 2 we reviewed the *Owen and Cowley* (1987a) model of reconnection and described how it uses the inflow conditions to predict the outflow conditions and structures. The model we will apply and test in this chapter is the one described in *Owen and Cowley* (1987a). This model includes the effects of asymmetries on either side of the current sheet. Although this model was originally developed for the case of the magnetotail reconnection, and thus has some limitations in its application to the solar wind case (particularly the assumption of equal and opposite external fields), it does address the effects of asymmetry in the ion outflows on either side of a reconnecting current sheet; and also it thus implicitly includes the possibility of multiple reconnection layers.

5.3.1 Application of the Owen and Cowley Model

Figure 5.2 shows our general set up to which we can apply the principles set out in the *Owen and Cowley* (1987b) model adapted for the solar wind context, hereafter known as OC87. Note that this figure is drawn to represent the rest frame of the neutral line. Magnetic-reconnection-related structures in the solar wind are likely to be frozen into the solar wind plasma flow and so largely moving with the solar

wind. The velocity of the neutral line in the spacecraft frame is thus likely to be comparable to the average solar wind velocity. The OC87 analysis assumes that in the rest frame of a neutral line in the solar wind, the outflow velocities can be found using the, assumed uniform, background magnetic field strength, B, the density at either side of the reconnection event (n_1 and n_2) and the residual inflow speeds (v_{I1} and v_{I2}) where subscripts 1 and 2 indicate the leading and trailing side of the exhaust respectively. We separate the leading and trailing sides of the event to account for any asymmetry between the two sides. Under these assumptions, the following equations from OC87 predict the set of outflow speeds:

$$v_{O1} = 2R - v_{IM} - \frac{n_1}{n_1 + n_2}\Delta v_I \tag{5.2}$$

$$v_{O2} = 2R - v_{IM} + \frac{n_2}{n_1 + n_2}\Delta v_I \tag{5.3}$$

where:

$$R = \sqrt{\frac{B^2}{\mu_0 m_i (n_1 + n_2)} - \frac{n_1 n_2 (v_{I1} - v_{I2})^2}{(n_1 + n_2)^2}} \tag{5.4}$$

$$v_{IM} = \frac{(n_1 v_{I1} + n_2 v_{I2})}{(n_1 + n_2)} \tag{5.5}$$

$$\Delta v_I = v_{I1} - v_{I2} \tag{5.6}$$

The angles between the reconnected field lines and the current sheet are represented by $\theta = \theta_1 = \theta_2$:

$$\theta \sim sin\theta = \frac{|B_{min}|}{B} = \frac{E_y}{v_F B} = \frac{B_n}{B_{L*}} \tag{5.7}$$

Where $v_F = R - v_{IM}$. The magnetic and electric fields are those outside of the event. θ will be the same on both sides of the original current sheet as long as the co-ordinate system is as defined and shown in Figure 5.2. The angle between the outflow boundary and the central current sheet is then given by:

$$\phi \simeq (1 - \frac{v_F}{v_0})\theta \tag{5.8}$$

The angle ϕ tends to θ with increasing outflow speed; it will vary in the different ion outflow layers due to differences in v_0, the field aligned flow, between layers (Equations 5.2 and 5.3). Thus we can use the inflow conditions to estimate the relative width of the outflow layers at the point of spacecraft crossing (the absolute width of the event is dependent on the distance from the neutral line, which is not generally known) by extracting the following observables: the residual inflow velocity in the neutral line rest frame on either side of the event; the density of the plasma on either side of the event and the background magnetic field strength (ignoring the guide field components). These values substituted into the above equations will give predictions of the outflow speeds, and thus relative layer widths, which we can test against observations.

Note that a single spacecraft travelling through a reconnection event will likely not pass at a normal incidence. Thus we also need to determine the overall geometry of an event to: remove the solar wind flow; identify a natural co-ordinate frame; rotate this frame so that it is comparable to the OC87 co-ordinate system; identify the trajectory of the spacecraft through the structure in this co-ordinate system.

If we compare the original Owen and Cowley model to our concept sketched in Figure 5.2 and the subsequent outflow structures in Figure 5.3, we have a ready explanation for the current sheets at B, C and D defined by angles ϕ_1 and ϕ_2 and

A and E defined by angle θ. Note however that our concept assumes that there is a diamagnetic effect associated with the edge of the outflow ion region and possibly the edge of an electron outflow region (equivalent to the separatrix). However, this diamagnetic effect is not explicitly included in the OC87 analysis (see *Beyene* (2013) for treatment of this effect in the OC87 type analysis). We assume also that the original current sheet is still apparent in observations (unlike *Gosling et al.*, 2005).

5.3.2 Extracting Specific Observables

In order to compare the predictions of the Owen and Cowley model with actual events detected in the solar wind, it is necessary to determine whether an event is a reconnection event, determine the structure of the event in a relevant co-ordinate system for analysis, find the inflow quantities in that co-ordinate system and determine the predictions from the application of the model.

First, the magnetic field and ion velocity data returned by a spacecraft are analysed to determine whether the event exhibits the two main features of a reconnection event: an overall magnetic field rotation coincident with an increase in ion velocity.

Once all the magnetic field rotations have been identified it is then possible to conduct a Walén test over each one to determine whether the observations are consistent with a reconnection event. Typically in the Gosling picture of the solar wind we would expect to observe two current sheets bounding the reconnection exhaust that both obey the Walén relation. However as we are testing a hypothesis that includes the possibility of multiple current sheets, we must anticipate the possibility that a given event will have more than 2 current sheets. Details on how

to conduct a Walén test are given in Section 3.5.4.

Once an event has been diagnosed as a likely reconnection event, a natural co-ordinate system for the event must be found. We again use the method described in Section 3.5.5, in order to provide a frame in which to work that is appropriate for the event. A minimum variance analysis over each of the magnetic field rotations is also used to find the normal direction vector of each of the current sheets, following the method described in Section 3.5.1.

Then, in order to simplify the analysis and to consider those parameters which are most relevant to the assumptions made in OC87, we also further rotate the analysis co-ordinate system around the average normal direction to the current sheets in order to work in a frame of reference that has equal anti-parallel magnetic field components in the inflow region on either side of the event, as shown in Figure 5.2. We rotate the natural co-ordinate frame around the normal direction, $\hat{\mathbf{n}}$, so that the magnetic field in the new $\hat{\mathbf{L}}$* direction has an equal and opposite magnitude at either side of the event. Figure 5.4 shows the basic structure of the event and how we rotate it to identify the anti-parallel fields. Here we have the natural co-ordinate frame with the normal direction vector out of the paper. The directions of the magnetic field on either side of the event are given by the red lines labelled $\mathbf{c_1}$ and $\mathbf{c_2}$. Their relative magnitude is indicated by their relative length. We wish to find the direction vector '$\mathbf{a}$' such that the projection of the field lines $\mathbf{c_1}$ and $\mathbf{c_2}$ onto '$\mathbf{a}$' are equal and opposite. In this frame we know the vectors $\mathbf{c_1}$ and $\mathbf{c_2}$ and we know the direction of $\mathbf{b_1}$ and $\mathbf{b_2}$ as $\mathbf{c_1} + \mathbf{c_2} = \mathbf{b_1} + \mathbf{b_2}$. We can then find the value of α by:

$$cos\alpha = \frac{(\mathbf{b_1} + \mathbf{b_2}).\mathbf{c_1}}{|\mathbf{b_1} + \mathbf{b_2}||\mathbf{c_1}|} \tag{5.9}$$

and thus a can be found using $\mathbf{a} = \mathbf{c_1} cos\alpha$. Then in order to rotate the frame we

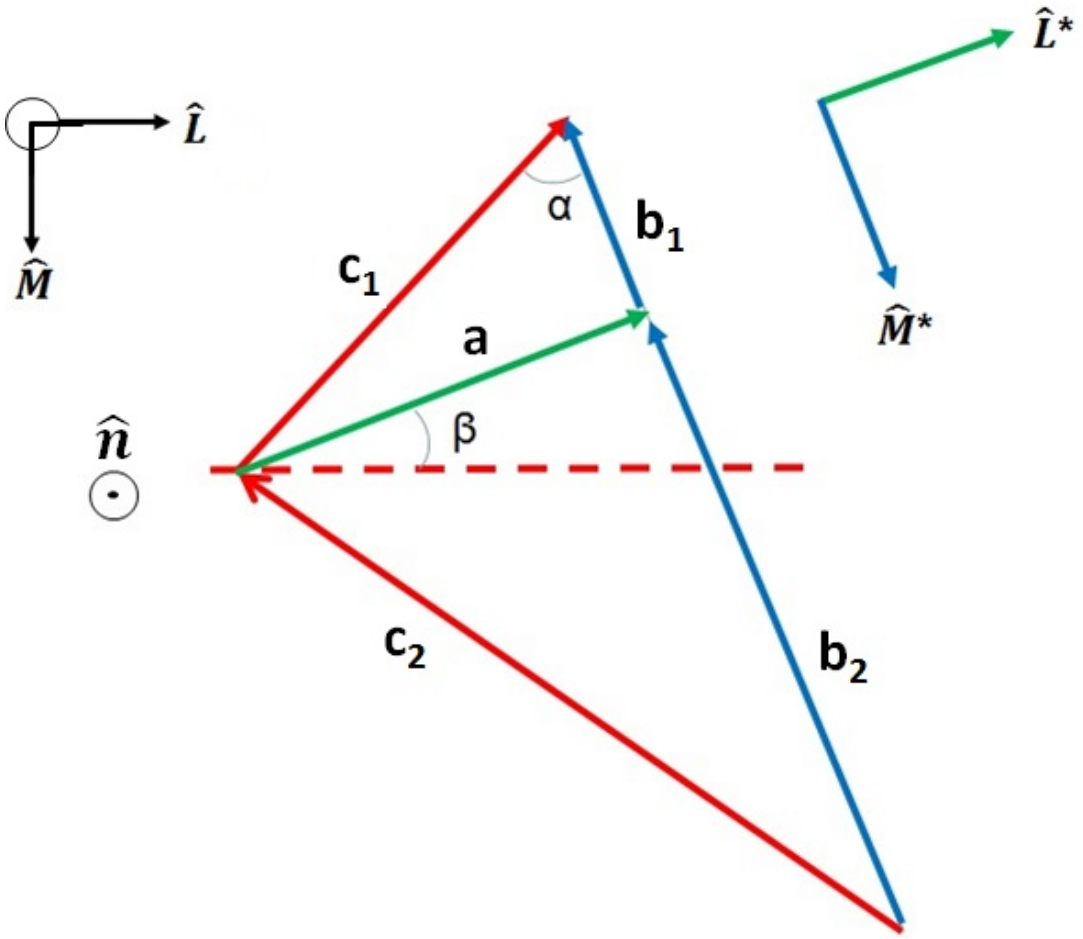

Figure 5.4: Rotating the natural co-ordinate frame defined in Chapter 4 to ensure that the fields appear equal and anti-parallel. The original co-ordinate system ($\hat{\mathbf{n}}$, $\hat{\mathbf{L}}$ and $\hat{\mathbf{M}}$ where $\hat{\mathbf{n}}$ is the minimum variance direction - also normal direction vector in the natural co-ordinate frame, $\hat{\mathbf{L}}$ is the maximum variance direction and $\hat{\mathbf{M}}$ is the intermediate variance direction) is given in the top left hand corner with the normal direction vector out of the page. $\mathbf{c_1}$ and $\mathbf{c_2}$ are the magnetic fields vectors on either side of the event (their length indicates an example of their relative magnitude). Line '**a**' indicates the direction in which the projections of $\mathbf{c_1}$ and $\mathbf{c_2}$ are anti-parallel. The new co-ordinate directions are given in the top right corner.

must find the value of β and rotate each direction by this angle.

$$cos\beta = \frac{\mathbf{a}.\hat{\mathbf{L}}}{|\mathbf{a}||\hat{\mathbf{L}}|} \tag{5.10}$$

where $\hat{\mathbf{L}}$ is the maximum variance direction vector. Thus $\mathbf{L}* = \mathbf{L}cos\beta - \mathbf{M}sin\beta$ and $\mathbf{M}* = \mathbf{L}sin\beta + \mathbf{M}cos\beta$ using the 2d rotation matrix:

$$\begin{pmatrix} cos\beta & -sin\beta \\ sin\beta & cos\beta \end{pmatrix}$$

The required observables we need to input into the Owen and Cowley model analysis are the inflow residual velocity, V_{L*}, on either side of the event, the density on either side of the event and the strength of the background magnetic field in the L*N plane. We use these observables in the neutral line (NL) frame of reference. This means that in order to find the residual inflow velocity we must first find an average of the background solar wind velocity and subtract that from the velocity data for the whole event. The inflow velocities, densities and magnetic field are taken from an average over a short time ($\sim 12\ s$) on either side of the event.

The resulting variables are then used as inputs to equations 5.2 to 5.8. The outputs v_{O1}, v_{O2} can be compared directly with the outflow ion velocities over the event. The angles given by equation 5.7 and 5.8 cannot be directly compared with the raw data. Instead we can compare the ratios of the time it takes the spacecraft to cross each distinct layer observed/predicted within the event.

Figure 5.5 shows the basic geometry of a spacecraft travelling through an event. The relative time spent in each layer (t_2 and t_3) of the reconnection event will depend on the angle of the spacecraft trajectory to the event γ. The relative times, t_2 and t_3 one would expect the spacecraft take to travel is given by the following equations:

$$t_3 = \frac{Asin\phi_1}{sin(\gamma - \phi_1)} \tag{5.11}$$

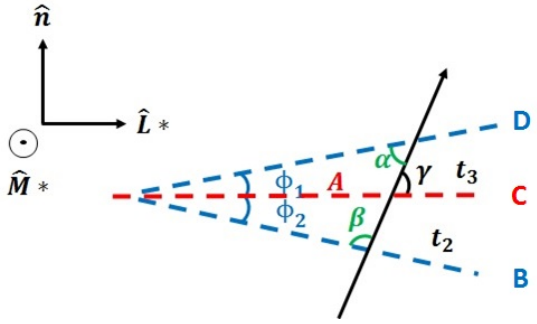

Figure 5.5: The geometry of a spacecraft passing through a reconnection event (black arrow) in the OC87 co-ordinate system. The dashed lines indicate points B, C and D where is most likely to be able to determine the boundaries. 'A' indicates the distance between the X-line and the point at which the spacecraft crosses the current sheet at C. Using this geometry we can find a ratio of the times t_2 and t_3 taken for the spacecraft to pass over regions.

$$t_2 = \frac{A sin\phi_2}{sin(180 - \phi_2 - \gamma)} \tag{5.12}$$

thus the ratio:

$$\frac{t_3}{t_2} = \frac{sin\phi_1}{sin\phi_2} \cdot \frac{sin(180 - \phi_2 - \gamma)}{sin(\gamma - \phi_1)} = \frac{sin\phi_1}{sin\phi_2} \cdot \frac{sin(\phi_2 + \gamma)}{sin(\gamma - \phi_1)} \tag{5.13}$$

Since A will be an unknown in most cases it is only possible to determine $\frac{t_3}{t_2}$. However if there are only 2 current sheets whose orientation can be accurately determined it is possible so determine the value of A (as in Chapter 4), assuming the current sheets are planar over those distances.

A comparison between the values we predict on the right hand side of Equation 5.13 and those observed (left hand side) will give an indication as to whether this model accurately describes magnetic reconnection structures in the solar wind.

5.3.3 Comparing Input Values

The accuracy of the predicted outflows is highly dependent on an accurate determination of the inflow characteristics in the rest frame of the solar wind. Table 5.1 shows the differences in the predicted outflows over a variety of inflow speeds

V_{in1}	10	10	-10	-10	20	20	-20	-20	50	-50	25	10
V_{in2}	10	-10	10	-10	20	-20	20	-20	50	-50	30	50
V_{01}	54	51	71	74	44	30	70	84	14	114	39	40
V_{02}	54	71	51	74	44	70	30	84	14	114	34	-0.4

Table 5.1: Testing the velocity inflow values with the magnetic field fixed at 8nT and a density on either side of 15 particles cm^{-3}.

(the background magnetic field and the density of the plasma at either side of the event are fixed at 8nT and 15 particles cm^{-3} respectively). Table 5.1 shows that if the two input values are equal then the outputs will be of equal value, but different input values can lead to quite different outflow speeds and the more different the inflows the more different the outflows. For example, with inflow values of $v_{in1} = 10$ and $v_{in2} = -10$, which are equal and opposite we see output speeds of 51 $km\ s^{-1}$ on side 1 and 71 $km\ s^{-1}$ on side 2 and with inflows of $v_{in1} = 20$ and $v_{in2} = -20$ we see output speeds of 70 $km\ s^{-1}$ on side 1 and 30 $km\ s^{-1}$ on side 2. The larger the value of the input speeds in the positive direction (the direction shown in Figure 5.2) the smaller the output speeds. Note that the last case has essentially no output for one of the outflows (V_{02}).

5.4 Case Study 1: 7th February 2006

5.4.1 Spacecraft Positions

We will test the predictions of the above model for an event observed on the 7th February 2006, where the Cluster spacecraft were located in the solar wind in an approximately tetrahedral formation around the location [17, 7.5, 5.5] R_E in GSE co-ordinates, as shown in Figure 5.6. On the left hand side the two panels show the position of the Cluster spacecraft (C1 in black, C2 in red, C3 in green, and C4

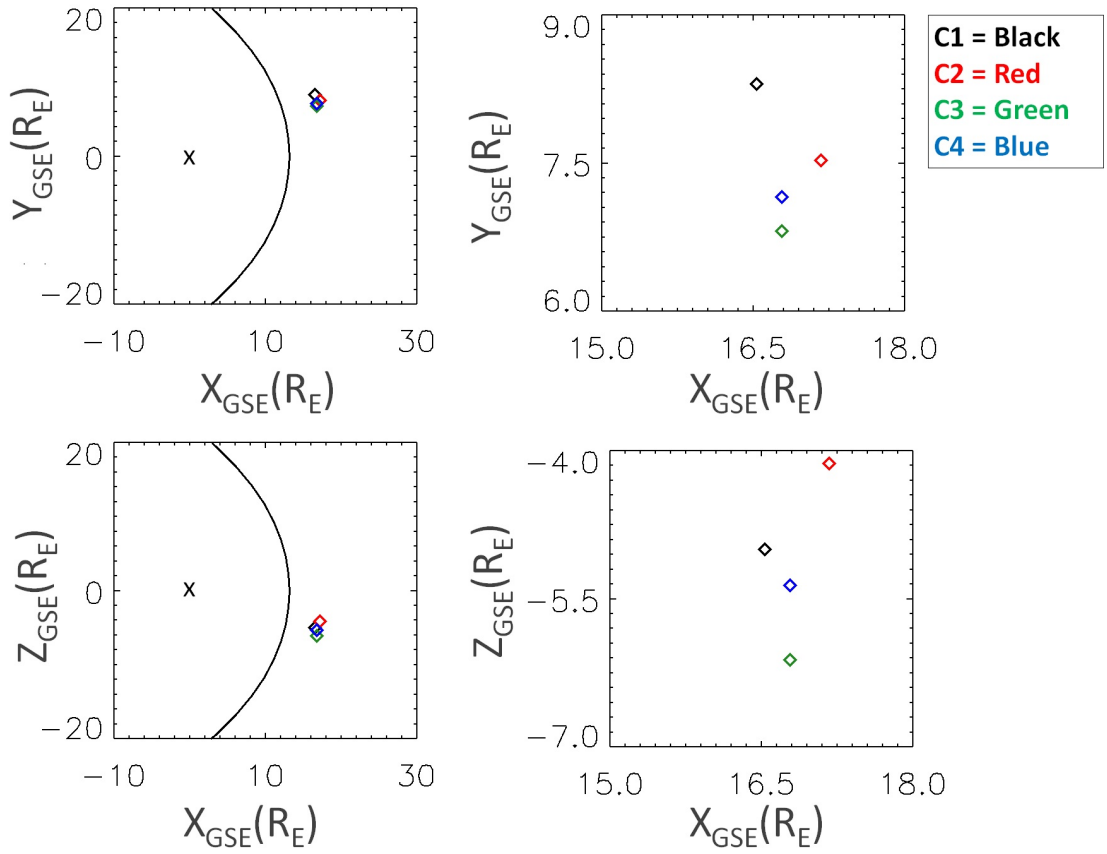

Figure 5.6: The positions of the Cluster spacecraft at the time of the case study 1 event are shown GSE co-ordinates. On the left hand side the top picture shows the spacecraft positions in the Y and X co-ordinate directions in GSE with Cluster 1 in black, Cluster 2 in red, Cluster 3 in green and Cluster 4 in blue. The bottom left panel shows the spacecraft in the Z and X co-ordinate directions. The Earth is shown by an 'x' and the Earth's bow shock is represented by the black curve. The right hand side shows an expansion of the area around the Cluster spacecraft.

in blue) with respect to the Earth ('x') and the Earth's bow shock (black curve) in the X-Y and X-Z directions in the GSE co-ordinate system. The two right hand panels show a zoom in on the Cluster positions. Cluster 2 and 1 are at the two extremes in the X direction. Cluster 1 and 3 are at the two extremes in the Y direction, and Cluster 2 and 3 in the Z direction. The tetrahedral formation means that the Cluster spacecraft are in a near optimum arrangement for observing events in the solar wind.

5.4.2 Cluster Spacecraft Observations

On the 7th February 2006, between 00:52:00 UT and 00:55:00 UT, the four Cluster spacecraft encountered an event. Figure 5.7 shows plasma and magnetic field data from this 3 minute interval, as observed by the Cluster 1 spacecraft. From the top, Figure 5.7 shows a) the total magnetic field strength, b) the magnetic field components in the GSE co-ordinate system, c) total ion velocity, d) ion velocity in GSE components (here the x direction is shown as $x + 300\ km\ s^{-1}$ in order to make a clearer comparison between each component) and e) ion density. The vertical green dashed line indicates the start of the changes in the ion velocity, the vertical black dashed lines indicate the starting point of the first two magnetic field rotations and the vertical red dashed line indicates the point at which the magnetic field strength returns to the ambient solar wind level. The black dashed horizontal lines on panels a), c) and e) indicate changes in the levels of the variables. In panels b) and d) the X, Y, and Z GSE components of the vector quantities are indicated by red, green and blue respectively.

Two significant magnetic field rotations are evident in panel b) most prominently in the Z direction. Magnetic field rotations are consistent with the spacecraft crossing current sheets. These current sheets bound a dip in the total magnetic field strength, a reduction in the ion velocity, and an increase in the ion density. The total magnetic field strength decreases from a background strength of 7.5 nT to 4 nT, a 47% decrease. The black horizontal dashed lines on panel a) show 3 different levels of magnetic field strength, the lowest is between the two magnetic field rotations, the highest is the background level and the middle is the level between the last rotation and the red line.

The change in ion velocity is approximately 20 $km\ s^{-1}$ mostly in the + Z

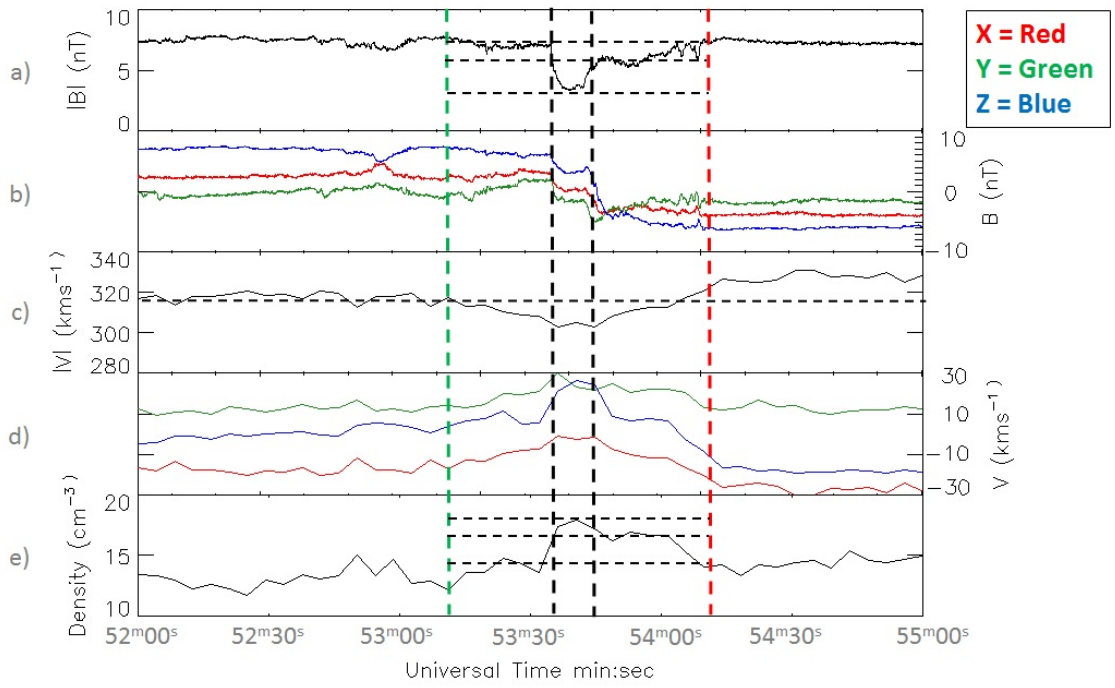

Figure 5.7: Magnetic field and plasma data obtained by the Cluster 1 spacecraft over a period of 3 minutes on the 7th February 2006 from 00:52:00 UT to 00:55:00 UT. Panel a) shows the total magnetic field strength, b) shows the magnetic field in the GSE co-ordinate directions x (red), y (green) and z (blue), c) shows the total ion velocity, d) the ion velocity in the GSE co-ordinate directions x +300 $km\ s^{-1}$ (red), y (green) and z (blue), and e) the ion density. The green vertical line indicates the start of the ion velocity changes, black vertical lines show the magnetic field rotations and the red line indicates the point at which the magnetic field returns to a background level. The black dashed horizontal lines indicate changes in the levels of magnetic field strength, ion velocity and density in panels a), c) and e) respectively.

direction, as seen in panel d). The total ion velocity, $|V|$, drops approximately 15 $km\ s^{-1}$ which is shown in panel c) (this is due to a reduction of the magnitude of the velocity in the X direction). The black horizontal dotted line in panel c) shows that the background solar wind speed is lower before the event encounter than after. The ion density, shown in panel e) increases 30% from 13 cm^{-3} to 18 cm^{-3} from the background density to the maximum density between the two current sheets.

It is shown in Figure 5.7 that these changes in the ions and magnetic field persist after the two magnetic field rotations have passed, continuing until the red line, at a smaller deviation from the background. During this period the magnetic field strength is lower than the background field, which can be seen in panel (a), the magnetic field of each component is still settling and there is noise particularly in the Y direction, panel (b), and the ion density is still higher than the background density after the event, panel (e). There is some asymmetry between the ion density on the leading and trailing sides of the event; the trailing side is approximately 20% increase from 12.5 cm^{-3} to 15 cm^{-3}. The black horizontal dotted lines show the different density levels, the background level, the maximum density is between the rotations and the intermediate density between the second rotation and the red line.

Figure 5.8 shows the magnetic field and plasma parameters observed during the event by Cluster 3, presented in the same format as Figure 5.7. Note Cluster 1 and 3 are separated by a distance of $< 1\ R_E$ in the X direction, $\sim 1.5\ R_E$ in the Y direction and $\sim 1.1\ R_E$ in the Z direction.

Similarly to Cluster 1, Cluster 3 observes two magnetic field rotations mainly in the Z direction. These magnetic field rotations are again indicative of the

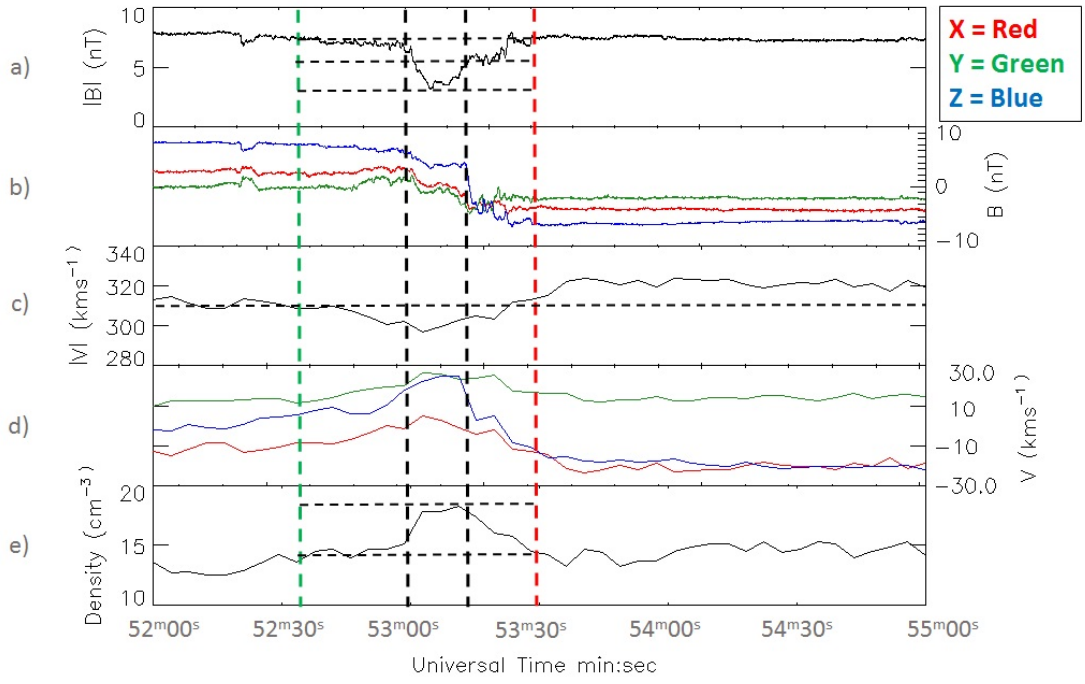

Figure 5.8: Magnetic field and plasma data obtained by the Cluster 3 spacecraft over a period of 3 minutes on the 7th February 2006 from 00:52:00 UT to 00:55:00 UT. Panel a) shows the total magnetic field strength, b) shows the magnetic field in the GSE co-ordinate directions x (red), y (green) and z (blue), c) shows the total ion velocity, d) the ion velocity in the GSE co-ordinate directions x +300 $km\ s{-}1$ (red), y (green) and z (blue), and e) the ion density. The vertical green dashed line indicates the point at which the ion velocity starts to change, the vertical black dashed lines show the magnetic field rotations and the vertical red dashed line indicates the point at which the magnetic field returns to a background level. The black horizontal lines indicate different levels of the magnetic field strength, total ion velocity and ion density in panels a), c) and e) respectively.

spacecraft crossing current sheets. These current sheets bound a large decrease in magnetic field strength from 8 nT to 4 nT (highlighted by the lowest and highest black horizontal lines in panel a)) the magnetic field returns to an intermediate level between the second magnetic field rotation and the red line. The change in ion velocity of 20 $km\ s^{-1}$ during the event is also predominantly in the +Z direction. The difference between the background ion velocity before and after the event is approximately 10 $km\ s^{-1}$ and is highlighted by the black horizontal line in panel c). There is also an increase in ion density from 13 cm^{-3} to 18 cm^{-3}. Cluster 3 does not observe the consistent intermediate density between the second current sheet and the red line; instead the density gradually drops back down to the background level during this period of time. The green line indicates the start of the changes in the ion velocity and also the changes in density.

Cluster 3 also observes a disturbance continuation, to a lesser extent, after the second current sheet has passed, the latest extent of which is marked by the red line.

Figure 5.9 shows the total magnetic field and the magnetic field in the GSE co-ordinate directions X (red), Y (green), and Z (blue) for the Cluster 2 and Cluster 4 spacecraft. The CIS instruments on both these spacecraft were not in operation at the time of this event and so the ion velocity and ion density are not available. As with Cluster 1 and 3, Cluster 2 and 4 observe magnetic field rotations as indicated by the vertical black lines. In this case Cluster 4 observes two magnetic field rotations, and Cluster 2 appears to observe three. Between these rotations there is a significant magnetic field decrease. Again the magnetic field decrease continues to a lesser extent after the second magnetic field rotation has passed.

Figure 5.10 shows Cluster 2 magnetic field and differential energy flux (DEF)

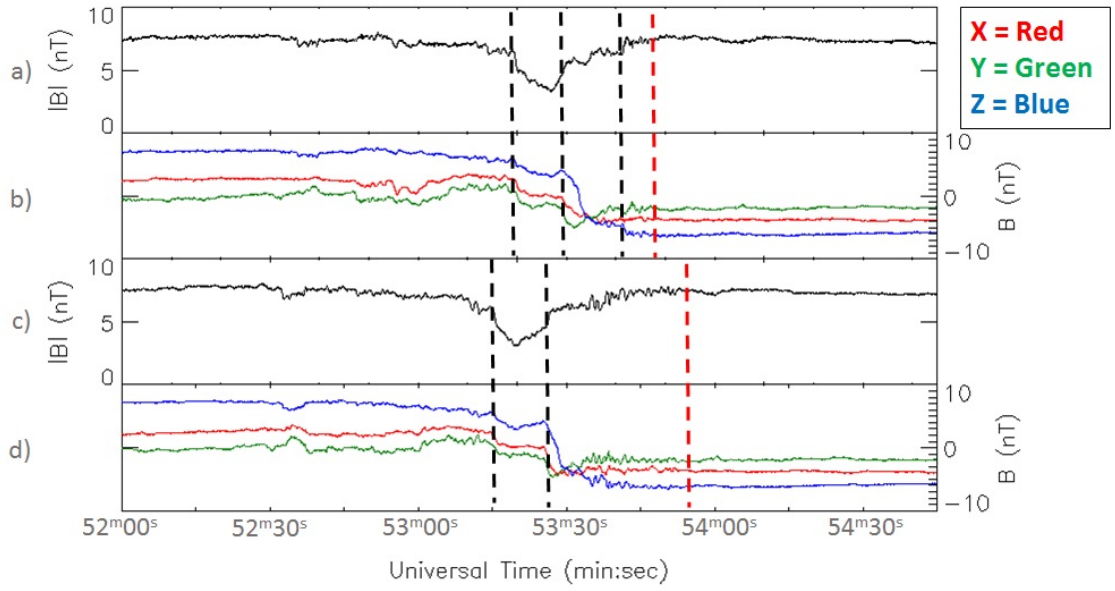

Figure 5.9: The total magnetic field strength and the magnetic field strength in GSE co-ordinate directions x (red), y (green) and z (blue) for the Cluster 2 and Cluster 4 spacecraft. The black vertical lines indicate the magnetic field rotations and the red line indicates the point at which the magnetic field returns to the background level.

of the electron populations as a function of energy and pitch angle over a 90 second period over the event. Only the Cluster 2 data is available for the time period of this case study. The plots show the DEF over the pitch angles $0° - 180°$. On the left hand side of the DEF plots is a time slice before the event taken at a time indicated by the red dashed line on the magnetic field panels. The right hand side of the DEF plots show subsequent time slices recorded at the times indicated by the black dashed lines. The maximum of the electron differential energy flux is seen at energies of approximately 15 eV. Just before the spacecraft encounters the first dip in magnetic field strength (panel a)) there is a strong drop out of these electron fluxes. However they then increase after the magnetic field strength has begun to dip (panels b), c) and d)). Panels b)-d) show that there is a peak in the differential energy flux of these electrons between $0° - 90°$, as indicated by the black ovals, which switches to $90° - 180°$ for panels e)-h). Between the points d)

and e) the spacecraft has started to move over the second current sheet and thus it would be expected that the directions of the electrons may change depending on the connectivity of the magnetic field. In fact panel d) appears to have two peaks, one around 180° and the other around 0°. The disturbance in electron observations may give an indication of the full extent of the separatrix layer.

5.4.3 Evidence for Reconnection

This section provides evidence that the case study that occurred on the 7th February 2006, as presented above, is indeed a reconnection event.

The Walén test is first performed over each of the discontinuities observed by spacecraft 1 and 3. In order to be considered a reconnection event the discontinuities should satisfy the Walén relation. As in Chapter 4, the Walén relation will be considered weakly satisfied for slopes of gradient between 0.5 - 0.8 and 1.2 - 2 and strongly satisfied for slopes with gradients between 0.8 - 1.2. It was not possible to do the Walén test for spacecraft 2 and 4 due to the lack of ion velocity data.

Figure 5.11 shows the results of the Walén test over the leading and trailing discontinuity for Cluster 1 in the left two panels and for Cluster 3 in the right two panels. Table 5.2 shows the time periods over which each of the tests was performed, as well as the velocities of the De Hoffmann Teller frame derived in each case. Table 5.2 also provides details of the orthogonal best fit for the Walén test results shown in Figure 5.11, including the intercept, gradient, correlation coefficient (C.C.) and student T-test. Each frame shows the ion velocity in the De Hoffmann Teller frame on the vertical axis and the Alfvén velocity on the horizontal axis. The black line indicates a best fit line as found by the orthogonal regression analysis technique. We consider the orthogonal regression line when discussing the

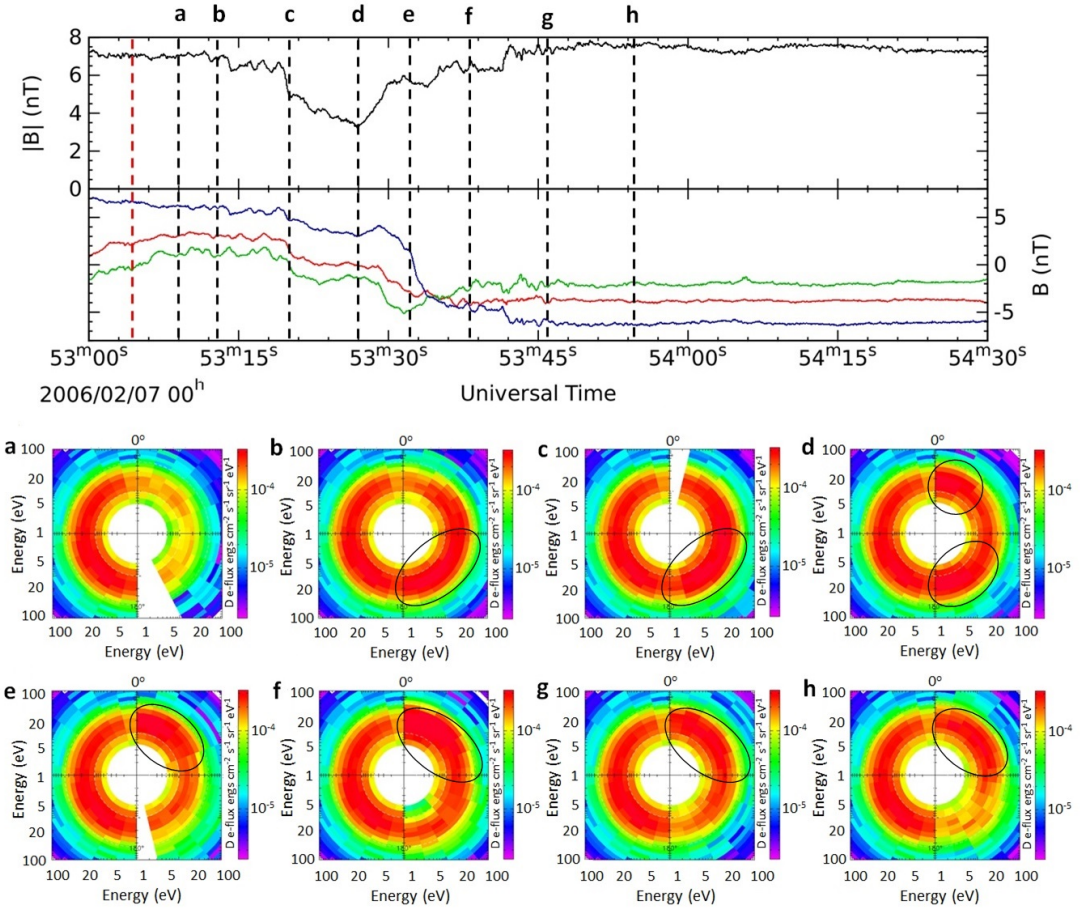

Figure 5.10: The magnetic field and differential energy flux of electrons for pitch angles 0-180 as seen by Cluster 2. The top two panels show the total and GSE co-ordinate components of the magnetic field over a period of 90 seconds. The bottom two panels show the differential energy flux of electrons over pitch angles 0-180 for time slices over the event (labelled by the black dashed lines on the figure) the left hand side of each plot shows the data at 00:53:05 UT indicated by the red dashed line on the magnetic field panels. The right hand side show subsequent time slices labelled by the black lines on the magnetic field plot. The black ovals indicate the peaks of differential energy flux.

correlation and slope as this line of best fit takes into account errors in both the horizontal and vertical direction rather than just in the vertical direction as is the case with a linear best fit line, for example.

It can be seen that there is a negative slope for the leading edge and a positive slope for the trailing edge. This is as expected, as the ion velocity and Alfvén speed changes will be correlated on one edge of a reconnection exhaust and anti-correlated on the other.

Sheet	**Start - End (hr: min: sec)**	**VHT**	**Int.**	**Slope**	**C. C.**	T-Test
1 (C1)	00:53:28 - 00:53:40	-297.7, 26.7, 24.0	0.12	-0.534	-0.973	0.0003
2 (C1)	00:53:40 - 00:54:20	-302.4, 24.8, 21.1	0.64	0.871	0.882	0.17
1 (C3)	00:52:48 - 00:53:13	-296.1, 21.7, 24.5	1.59	-0.504	-0.895	0.000004
2 (C3)	00:53:08 - 00:53:35	-296.7, 25.7, 17.0	0.567	0.800	0.952	0.515

Table 5.2: The De-Hoffman Teller frame and the Walén test analysis for each current sheet for both spacecraft. The time boundaries are the time periods over which the tests were performed, VHT is the velocity in the De Hoffmann - Teller frame, the intercept, gradient, correlation coefficient (C.C.), and T-test refer to the best fit line of the Walén test.

It can be seen that the gradients of the best fit lines over the first current sheet can be considered to be weakly satisfying the Walén relation. The gradients of the best fit lines over the second current sheet strongly satisfy the Walén relation. However, the results from the first current sheet for each spacecraft are statistically significant to the 1% level while those for the second current sheet are not. This is likely due to the small number of points available for analysis due to the short duration of this event. It would be preferable to have an event with a large number of points to ensure a statistically significant result. However this is often not possible in the solar wind, as for this event, as the structures convect past the spacecraft very quickly. Nevertheless, these results appear to be consistent with this indeed being a reconnection event.

5.4.4 Structure of the Event

A suitable reference frame based on the minimum variance technique was created in order to study the event in context. Here we took a weighted average of the minimum variance results for the magnetic field vectors observed at each of the 4 spacecraft over the whole event (as described previously in Section 3.5.5); the minimum variance technique yields 3 vectors in the direction of minimum, intermediate and maximum change and their associated eigenvalues (λ). The minimum variance results for the magnetic field data from each of the spacecraft are shown in Table 5.3. A weighted average is obtained by using the technique described in Section 3.5.5.

It can be seen that the minimum variance directions over the whole event for each spacecraft are very similar to each other; all are within a 15 degree cone. In addition, the results are very well defined (ratio $>$ 10), the lowest value for

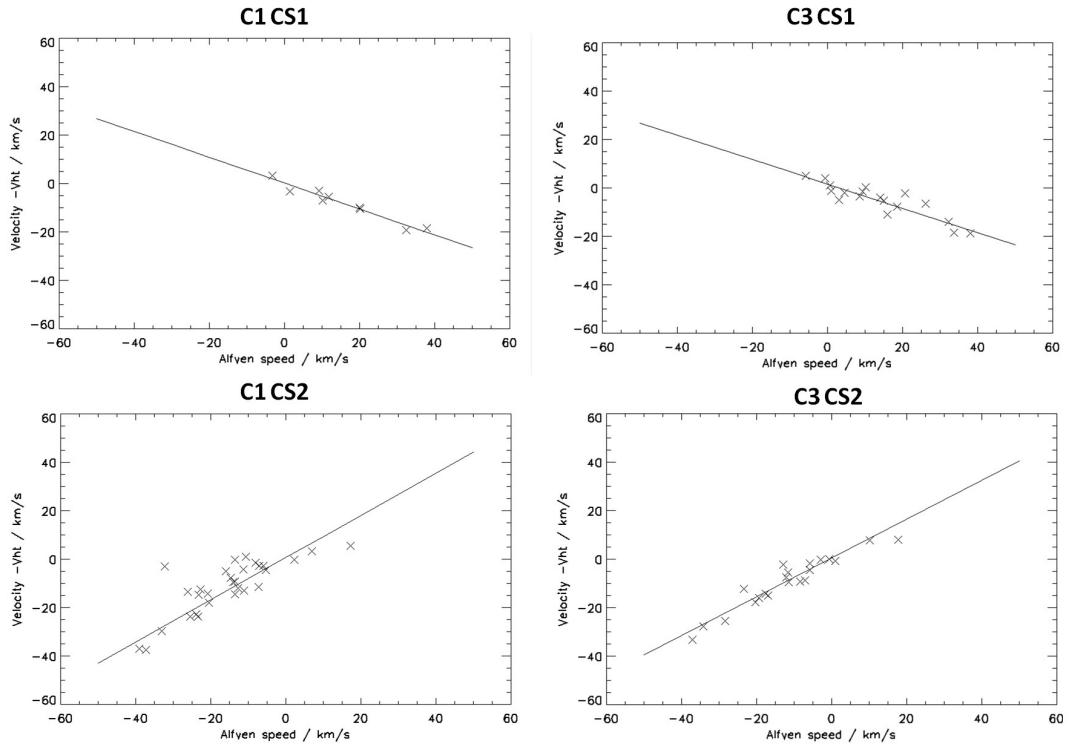

Figure 5.11: Walén test results over both current sheets for the event that occurred on the 7th February 2006 for data taken by Cluster 1 and 3. The panels on the left hand side indicate the Walén test results for Cluster 1 and on the right hand side, for Cluster 3.

S/C	Time frame (mm:ss)		**Direction Vector**	λ	λ **Rat.**
C1	53:33 - 53:52	**Minimum:**	-0.851, 0.402, 0.338	0.0384	44.8
		Intermediate:	0.181, 0.828, -0.530	1.72	11.45
		Maximum:	-0.493, -0.390, -0.778	19.7	
C2	53:15 - 53:39	**Minimum:**	-0.803, 0.509, 0.311	0.0778	28.9
		Intermediate:	0.309, 0.801, -0.512	2.25	8.93
		Maximum:	-0.510, -0.315, -0.800	20.1	
C3	53:00 - 53:18	**Minimum:**	0.734, -0.658, -0.170	0.0489	32.3
		Intermediate:	-0.448, -0.658, 0.607	1.58	10.1
		Maximum:	-0.511, -0.369, -0.776	16	
C4	53:12 - 53:31	**Minimum:**	-0.746, 0.612, 0.262	0.0266	42.9
		Intermediate:	0.329, 0.681, -0.654	1.14	11.6
		Maximum:	-0.579, -0.402, -0.710	13.2	

Table 5.3: The minimum variance analysis over the whole event, for each of the 4 Cluster spacecraft (S/C). The maximum, intermediate and minimum variance direction vectors are given, their corresponding eigenvalues, λ and the λ ratios between the minimum and intermediate directions and between the intermediate and maximum directions.

λ (between the minimum and intermediate variance directions) is 28.9. Thus we infer, by weighted average, the natural co-ordinate system is given by a rotation from GSE given by the matrix:

$$\begin{pmatrix} N \\ M \\ L \end{pmatrix} = \begin{pmatrix} -0.819 & 0.561 & 0.286 \\ 0.345 & 0.830 & -0.640 \\ -0.559 & -0.399 & -0.818 \end{pmatrix} \begin{pmatrix} X \\ Y \\ Z \end{pmatrix} GSE$$

The results of minimum variance analysis on the two current sheets separately are shown in Tables 5.4 and 5.5 in the same format as Table 5.3.

Using the weighted average technique that we used to find the natural co-ordinate frame of the event, we find the normal direction of the current sheets as an average of the spacecraft minimum variance results CS1 = [-0.800, 0.492, 0.341] and CS2 = [-0.824, 0.495, 0.274]. These results are both within 10° of the result obtained for the full event.

Another way of finding the structure of the event is to use the 4 spacecraft timing analysis technique, as described in Section 3.5.2. This can thus be used as a test of the accuracy of the natural co-ordinate system. The 3×3 matrix $(\mathbf{r}_\alpha - \mathbf{r}_1)$ is given by the distance from Cluster 2, 3 and 4 to the reference spacecraft, Cluster 1 and $(t_\alpha - t_1)$ is the time difference at maximum correlation (over the whole event) between Cluster 2, 3 and 4 relative to the reference spacecraft Cluster 1. These values are given in Table 5.6. Thus we determine the normal direction of the event is given by $\hat{\mathbf{n}} = [-0.826, 0.441, 0.351]$ and the speed at which it travels: $v = 257\ km\ s^{-1}$. The timing normal direction vector is within 5° of the minimum variance direction found by the Cluster 1 and Cluster 3 spacecraft, thus we can be very confident of its accuracy.

S/C	Time frame (mm:ss)		**Direction Vector**	λ	λ **Rat.**
C1	53:35 - 53:40	**Minimum:**	-0.840, 0.284, 0.462	0.01	9.06
		Intermediate:	-0.159, 0.686, -0.710	0.0906	38.9
		Maximum:	-0.519, -0.670, -0.531	3.52	
C2	53:17 - 53:25	**Minimum:**	-0.777, 0.544, 0.315	0.00764	13.7
		Intermediate:	0.023, 0.526, -0.850	0.105	35.7
		Maximum:	-0.628, -0.654, -0.421	3.75	
C3	53:00 - 53:39	**Minimum:**	-0.739, 0.563, 0.370	0.00625	24
		Intermediate:	0.051, 0.595, -0.802	0.15	18.9
		Maximum:	-0.671, -0.574, -0.468	2.84	
C4	53:12 - 53:21	**Minimum:**	-0.773, 0.574, 0.270	0.0168	7.38
		Intermediate:	0.165, 0.593, -0.788	0.124	22.1
		Maximum:	-0.613, -0.565, -0.553	2.74	

Table 5.4: The minimum variance analysis for current sheet 1, for each of the 4 Cluster spacecraft (S/C). The maximum, intermediate and minimum variance direction vectors are given, their corresponding eigenvalues, λ and the λ ratios between the minimum and intermediate directions and between the intermediate and maximum directions.

S/C	Time frame (mm:ss)		Direction Vector	λ	λ Rat.
C1	53:43 - 53:50	**Minimum:**	-0.857, 0.368, 0.362	0.0574	21.8
		Intermediate:	0.292, 0.924, -0.247	1.25	9.04
		Maximum:	-0.425, -0.106, -0.899	11.3	
C2	53:27 - 53:37	**Minimum:**	-0.844, 0.462, 0.273	0.0672	21.1
		Intermediate:	0.413, 0.884, -0.220	1.42	8.87
		Maximum:	-0.343, -0.073, -0.936	12.6	
C3	53:13 - 53:18	**Minimum:**	-0.786, 0.587, 0.195	0.063	14.2
		Intermediate:	0.583, 0.808, -0.082	0.899	12.3
		Maximum:	-0.206, 0.050, -0.977	11.1	
C4	53:23 - 53:31	**Minimum:**	-0.718, 0.651, 0.248	0.03	47
		Intermediate:	0.511, 0.734, -0.448	1.41	9.0
		Maximum:	-0.474, -0.195, -0.859	12.7	

Table 5.5: The minimum variance analysis for current sheet 2, for each of the 4 Cluster spacecraft (S/C). The maximum, intermediate and minimum variance direction vectors are given, their corresponding eigenvalues, λ and the λ ratios between the minimum and intermediate directions and between the intermediate and maximum directions.

Spacecraft	**Time Lag /s**	**Maximum Correlation**	**Distance from ref. (C1) /km**
Cluster 1	0.0	1.0	0, 0, 0
Cluster 2	-14.2	0.990	4110, -4870, 5518.5
Cluster 3	-31.3	0.984	1615, -9487.1, -7124.3
Cluster 4	-18.8	0.989	987, -7210.6, -2305

Table 5.6: Time lag between Cluster spacecraft and spacecraft 1 Event 7/2/2006.

5.4.5 Removing the Solar Wind Flow

Removing the solar wind flow from the event so that only the residual velocity remains is fraught with potential causes of error. In the solar wind the background velocity is of the order of 300 $km\ s^{-1}$ while the residual reconnection inflow is of the order of 20 $km\ s^{-1}$ or less. This means that any error in determining the background solar wind velocity will have a significant impact on the determined residual solar wind flow. However, in order to determine the background solar wind flow we take an average of the solar wind velocity before and after the event. This is only possible for spacecraft 1 and 3 as the CIS instrument is not operational for spacecraft 2 and 4 during this time.

For Cluster 1 we use an average of the solar wind velocity between 0:52:30 UT - 00:53:00 UT and 00:54:30 UT - 00:55:00 UT and for Cluster 3 00:52:00 UT - 00:53:00 UT and 00:53:30 UT - 00:54:00 UT. This is to ensure that the average is taken from points close to the reconnection event, without being inside the reconnection event itself. This leads to background solar wind flows of $[-322.7, 12.5, -8.6]\ km\ s^{-1}$ and $[-315.6, 13.3, -8.31]\ km\ s^{-1}$ for Cluster 1 and 3 respectively (in the GSE co-ordinate system; after the background has been removed we rotate the frame into the OC87 frame).

As a check we will compare the speed of the background solar wind flow that we have just determined with the speed of the direction normal of the event ($257\ km\ s^{-1}$). We are making the assumption that the magnetic reconnection event is being carried along by the solar wind. The angle between the normal direction of the event and the x direction is 34° and thus the solar wind speed in the x direction must be $\frac{257}{cos(34)} = 311\ km\ s^{-1}$. The difference between the background solar wind speed and the speed in the x direction found by the timing analysis is

less than 5% and thus we can say that the two are consistent.

By subtracting the solar wind background flows we can see any enhancements of the flow. Figure 5.12 shows the crossings of the four spacecraft with the event with the maximum variance direction, L, on the horizontal axis and the minimum variance direction on the vertical axis. The black lines indicate the current sheets (determined using the normal direction and by the position of the Cluster 1 spacecraft when the sheets was encountered and extrapolating the position using the solar wind speed), the black arrows indicate the magnetic field vector (the size of the vectors indicate their relative magnitude), the red arrows indicate the ion velocity enhancement over the event (the size of the vectors indicate their relative magnitude). Data from the CIS instrument is only available on Cluster 1 and 3. The data from Cluster 1 and 3 indicate an ion velocity enhancement that is directed between the two current sheets. However the ion velocity enhancement appears to continue outside of the two current sheets, as was seen in Figures 5.7, 5.8 and 5.9.

It should also be noted that Cluster 4 appears to observe the event from the opposite side of the reconnection site from the other 3 spacecraft. The orientation of the current sheets is determined by making the assumption that the minimum variance direction of the magnetic field across the current sheet is synonymous with the normal direction vector of the current sheet. The angles between the current sheet normals and the natural co-ordinate frame normal are very small ($< 10^{\circ}$) and so a small error could mean that the extrapolated current sheet structure has the X line on the incorrect side of the spacecraft. The Cluster 4 spacecraft is situated in the middle of the spacecraft formation and so we would expect that it would observe the same structure as the other 3 spacecraft, and so it is not possible

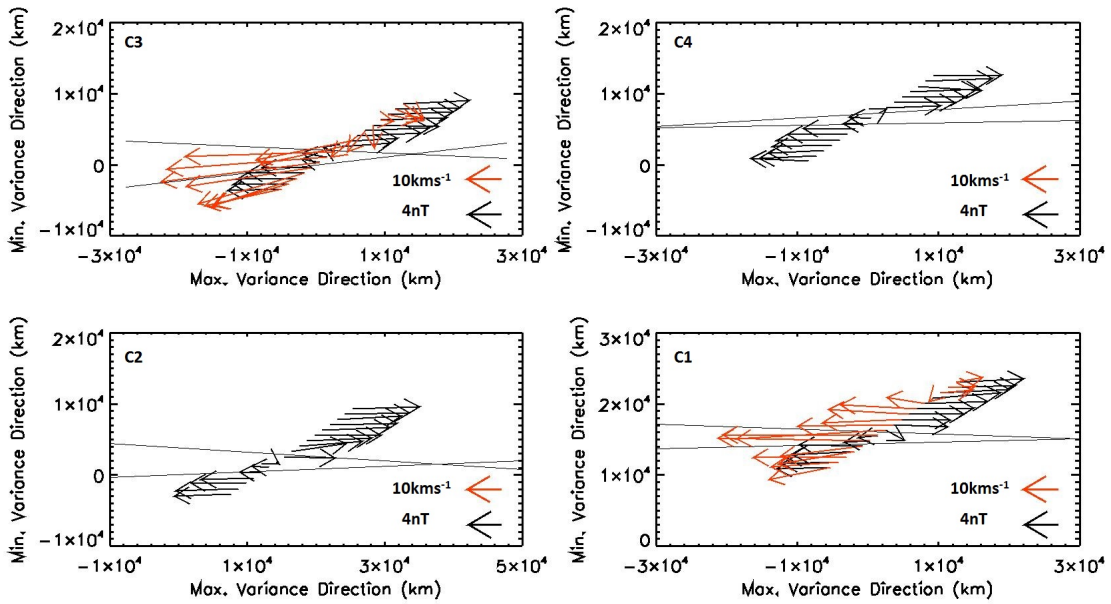

Figure 5.12: Cluster crossings of the event in order of spacecraft encounter. The top left is Cluster 3, the top right Cluster 4, bottom left Cluster 2 and bottom right Cluster 1. The black lines indicate the current sheets, the black arrows the magnetic field and the red arrows the ion velocity enhancement (total ion velocity - background). The length of the arrows indicates the relative magnitude of the vector.

to conclusively prove that the Cluster 4 spacecraft observed the event from the opposite side of the X line from Cluster 1, 2, and 4.

We then rotate the event into the OC87 frame so that the magnetic field in the L* direction is equal and opposite on each side of the event. In this case study the value of the angle of rotation β is 146° and 151° for the data at Cluster 1 and 3 respectively.

5.4.6 Derive the Inflow Quantities

The input variables for the OC87 model are the inflow velocities (in the L* direction) and densities, and the magnetic field strength (in the L* direction). The inflow quantities are determined by taking an average of the data over short time

Cluster 1	Input Variable	Value (L* direction)
v_{1L*}	v_{I1}	18.0 $km\ s^{-1}$
v_{2L*}	v_{I2}	$-9.0\ km\ s^{-1}$
Density (inflow side 1)	n_1	13.6 cm^{-3}
Density (inflow side 2)	n_2	14.2 cm^{-3}
B_{L*}	B	7.6 nT
Angle between spacecraft and event normal	γ	129°
Cluster 3	**Input Variable**	**Value (L* direction)**
v_{1L*}	v_{I1}	19.6 $km\ s^{-1}$
v_{2L*}	v_{I2}	$-9.7\ km\ s^{-1}$
Density (inflow side 1)	n_1	14.6 cm^{-3}
Density (inflow side 2)	n_2	13.2 cm^{-3}
B_{L*}	B	7.6 nT
Angle between spacecraft and event normal	γ	124°

Table 5.7: Derived inflow quantities for the Cluster 1 and Cluster 3 spacecraft for case study 1.

periods on either side of the exhaust. For Cluster 1 the time frames are 00:53:20-00:53:30 UT and 00:54:00 - 00:54:10 UT and for Cluster 3, 00:52:50-00:53:00 UT and 00:53:20 - 00:53:30 UT for the leading and trailing side of the exhaust respectively. For the inflow velocity we use the residual velocity remaining after subtracting the background solar wind flow. All the inflow quantities are in the OC87 reference frame, and are given in Table 5.7 along with the angle between the spacecraft trajectory and the normal direction to the reconnection event γ.

The inflows are similar but not identical for the Cluster 1 and 3 spacecraft. The inflow densities on either side of the event are approximately equal but the inflow velocities on either side of the event are in opposite directions.

Variable	Cluster 1	Cluster 3
v_{0E1}	39 $km\ s^{-1}$	34 $km\ s^{-1}$
v_{0E2}	67 $km\ s^{-1}$	64 $km\ s^{-1}$
$\frac{t_3}{t_2}$ ratios	1.65	1.83

Table 5.8: Predicted outflows for case study 1.

5.4.7 Predictions

We input the values found in the previous section into Equations 5.2 - 5.8 to obtain predictions for the outflow speeds; v_{0E1} and v_{OE2} and the ratio of the time the spacecraft is predicted to spend in each outflow $\frac{t_3}{t_2}$. The results are shown in Table 5.8. The predicted outputs for the reconnection event are comparable between spacecraft, though not identical.

The velocities predicted for the two outflows, v_{0E1} and v_{OE2}, have very different speeds. The model predicts that the outflow on the leading side of the event has a lower speed (39 $km\ s^{-1}$ for Cluster 1 and 34 $km\ s^{-1}$ for Cluster 3) than the outflow on the trailing side (67 $km\ s^{-1}$ for Cluster 1 and 64 $km\ s^{-1}$ for Cluster 3). The predictions for Cluster 1 are very similar to the predictions for Cluster 3.

The ratio of the relative times the spacecraft is predicted to spend in the two sections of the ion outflow t_2 (leading) and t_3 (trailing) are 1.65 for Cluster 1 and 1.83 for Cluster 3, meaning that the Cluster spacecraft is expected to spend a larger amount of time in the trailing side of the exhaust than the leading side.

5.4.8 Comparisons with model

The reconnection exhaust speed observed by the Cluster 1 and 3 spacecraft is of the order 20 $km\ s^{-1}$ between the two current sheets. Cluster 1 and 3 also observe a smaller reconnection exhaust speed of $\sim 10\ km\ s^{-1}$ after the second current sheet

has passed. It must be noted that the exact speeds of the outflow exhaust are hard to calculate accurately due to the different background speeds on the leading and trailing side and because the residual solar wind flow is less than 10% of the background flow. This means that small errors in calculating the background flow can translate to large inaccuracies in the determination of the inflow and outflow velocities.

These observed outflow velocities are smaller than that predicted by the Owen and Cowley model: the leading side has predicted speeds of 39 $km\ s^{-1}$ for Cluster 1 and 34 $km\ s^{-1}$ for Cluster 3 and the trailing side; 67 $km\ s^{-1}$ for Cluster 1 and 64 $km\ s^{-1}$ for Cluster 3. The predictions made by the OC87 will be maximum outflow values thus we would expect the observed speeds to be lower. The model neglects the possibility that not all the magnetic energy available is converted to outflow kinetic energy. The OC87 model predicts that the two exhaust speeds will be different, which is what is observed at Cluster 1 and 3, however it predicts that the exhaust on the trailing edge side should have a larger speed than that on the leading edge side and the observations show the ion velocity enhancement is reduced between the second current sheet and the point that the solar wind conditions return to the background level (see Figure 5.7). Though depending on whether the majority of particles are reflected or transmitted at the central current sheet it could have the reverse result.

Using Equation 5.13 we can predict the ratio of the amount of time that the Cluster spacecraft spends in each region of the reconnection exhaust. In this case we predict the ratio to be $t_3/t_2 = 1.65$ for Cluster 1 and $t_3/t_2 = 1.83$ for Cluster 3. This predicts that the Cluster spacecraft should spend more time in the trailing side than the leading side. For the Cluster 1 and 3 spacecraft the amount of time

that the two outflow speeds were observed appears to be approximately the same if we compare the length of time the Cluster spacecraft spends at the two increased levels of density (see Figure 5.7).

For this case study the approximate Alfvén speed is 44 $km\ s^{-1}$. The actual outflows are in the region of 20 $km\ s^{-1}$, and the predicted outflows are between $34 - 67\ km\ s^{-1}$. This means that some of the predicted outflow speeds (the V_{OE2} predictions) are larger than the Alfvén speed of the region.

5.5 Case Study 2: 2nd February 2002

For the second case study we will use a reconnection event that occurred on the 2nd February 2002. This particular event has been studied previously and is shown to have a large scale structure (*Phan et al.*, 2006; *Teh et al.*, 2009). At the time of this event the Cluster spacecraft are in their most closely situated formation (maximum 550 km apart).

5.5.1 Spacecraft Positions

In this particular study the spacecraft are situated very closely together as is shown in the matrix below:

$$\begin{pmatrix} \mathbf{r}_1 - \mathbf{r}_3 \\ \mathbf{r}_2 - \mathbf{r}_3 \\ \mathbf{r}_4 - \mathbf{r}_3 \end{pmatrix} = \begin{pmatrix} -401 & -270 & 235 \\ 239 & 73 & -299 \\ 25 & 49 & -99 \end{pmatrix} km$$

This matrix shows the distance in GSE co-ordinates (in km) between each Cluster spacecraft and Cluster 3. It is possible to see here that the spacecraft are well within 1000 km of each other. The event itself extends at least 390 R_E

along the X line (*Phan et al.*, 2006), and so we expect that the Cluster spacecraft should essentially see identical slices through the event as the Cluster spacecraft separation is less than 1% of the total event size.

Figure 5.13 shows the Cluster spacecraft positions located in the solar wind around the location [14, 10, 5]R_E in GSE co-ordinates. In each panel the 'X' indicates the position of the Earth, the curved black line shows the position of the Earth's bow shock and the Cluster spacecraft are represented by black, red, green and blue diamonds for spacecraft 1, 2, 3, and 4 respectively. The two panels on the left show the position of the Cluster spacecraft with respect to the Earth and the Earth's bow shock in the X-Y and X-Z directions. The two panels on the right show a zoom in on the Cluster positions. Cluster 1 and 2 are at the two extremes in the X, Y and Z direction, and the Cluster 3 and 4 spacecraft are located in the middle very close together (< 100 km in any direction). The spacecraft are not magnetically connected to the foreshock.

5.5.2 Cluster Spacecraft Observations

The Cluster spacecraft are very close together in this event, which means that it is more likely that the spacecraft see very similar magnetic field strengths and rotations. Data from the Cluster 3 spacecraft is shown in Figure 5.14 with the total magnetic field strength in panel a), the magnetic field components in GSE co-ordinates (with x in red, y in green and z in blue) in panel b), the total ion velocity in panel c), the x component of ion velocity in panel d), the y and z components of ion velocity in panel e), density in panel f) and total ion pressure g). The two black vertical dashed lines indicate the start of the two distinct magnetic field rotations.

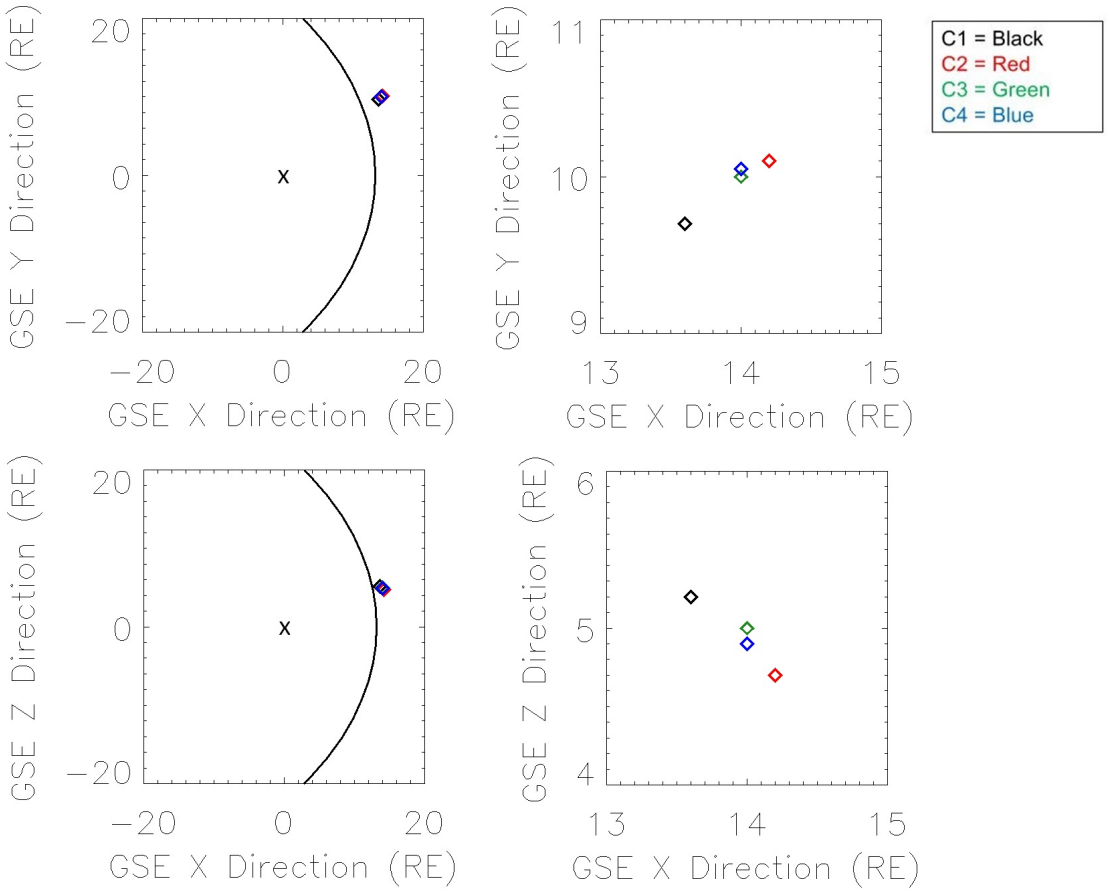

Figure 5.13: The positions of the Cluster spacecraft on the 2nd February 2002. The two left hand panels show the positions of the Cluster spacecraft (diamonds) in the XY and XZ directions in the GSE co-ordinate system. The right hand panels show a zoom-in of the area around the Cluster spacecraft. The black 'X' is Earth and the black curve is the Earth's bowshock and the Cluster spacecraft 1, 2, 3, and 4 are represented by the colours black, red, green, and blue.

In panel a) it is shown that there is a reduction in the magnetic field strength of 4 nT from 12 nT to 8 nT. This reduction is mostly encompassed within the time between the two magnetic field rotations, indicative of current sheets, which are shown in panel b). It should be noted that while the change in total magnetic field strength on the trailing edge of the reconnection event is sharp, this is not the case at the leading edge where a gradual reduction in magnetic field strength is observed. In fact, on the leading edge, a reduction in magnetic field strength is observed before there is any indication of a magnetic field rotation.

Panel c) shows that there is an increase in the total ion velocity that displays similar changes to the magnetic field strength. This increase in ion velocity is $\sim 40\ km\ s^{-1}$ as measured from the background on the leading side. It must be noted that the background velocity on the trailing side of the event is $\sim 20\ km\ s^{-1}$ greater than the background on the leading edge. Panels d) and e) show that the ion velocity enhancement, indicative of a reconnection exhaust, is predominately in the -z direction in GSE co-ordinates ($\sim 40\ km\ s^{-1}$), but there is also a significant component in the -x direction ($\sim 40\ km\ s^{-1}$ if measured from the leading edge and $10\ km\ s^{-1}$ if measured from the trailing end).

Panel f) shows that there is a distinct density increase during the exhaust of approximately 7 cm^{-3} (from the leading edge). The density is not symmetrical on either side with the trailing edge being approximately 15 cm^{-3} higher than that on the leading edge.

Panel g) shows ion pressure in nPa. There is an increase in pressure during the exhaust of 0.04 nPa also bounded by the current sheets.

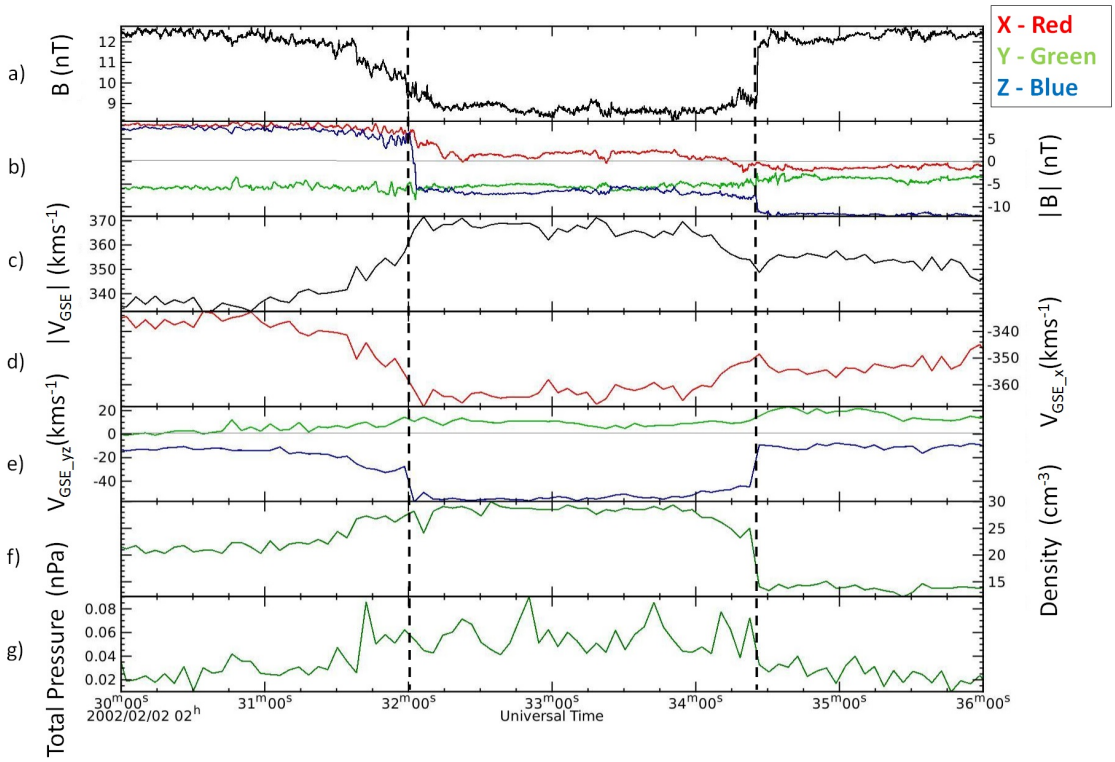

Figure 5.14: Data from the Cluster 3 spacecraft over the event. The panel a) shows the total magnetic field strength, panel b) shows the magnetic field strength in GSE co-ordinates, panel c) the total ion velocity, panels d) (x component) and e) (y and z components) show the ion velocity in GSE co-ordinates, panel f) shows the particle density and panel g) shows the pressure. The black vertical dashed lines indicate the start of the two magnetic field rotations.

5.5.3 Evidence For Reconnection

As in the previous case studies we perform a Walén test over each of the discontinuities to test that it is consistent with the expectations of a reconnection event. As has been the case for all previous analyses, the Walén relation will be considered weakly satisfied for slopes of gradient between 0.5 - 0.8 and 1.2 - 2 and strongly satisfied for slopes with gradients between 0.8 - 1.2. It was not possible to do the Walén test for spacecraft 2 and 4 due to the lack of ion velocity data.

Figure 5.15 shows the Walén test results for Cluster 1 on the left hand side with CS1 on the top left and CS2 on the bottom left. The Walén tests for Cluster 3 are on the right hand side. The line of best fit here is a result of an orthogonal regression analysis. These results appear to be consistent with this event being a reconnection event.

Table 5.9 shows the De-Hoffman Teller frame, the intercept and slope of the Walén analysis, the correlation co-efficient and the results of the student T-test. It can be seen here that for both of the spacecraft the results for CS1 strongly satisfy the Walén relation whereas CS2 is only weakly satisfying. In each case the correlation coefficient is > 0.9.

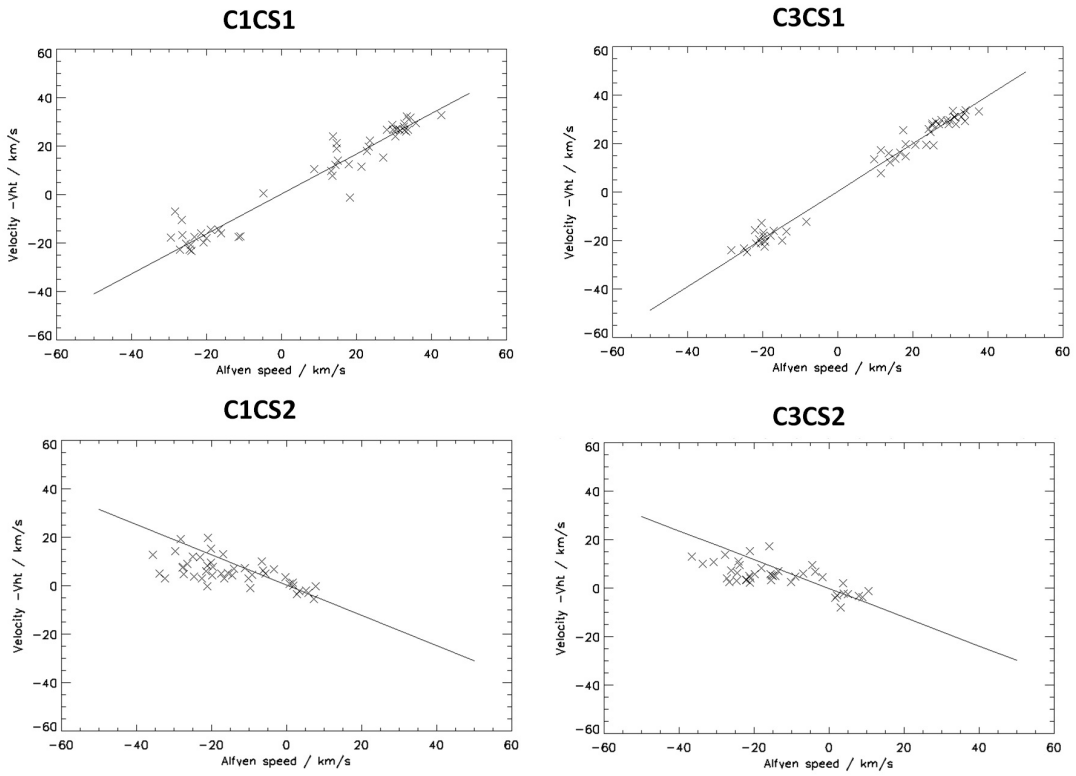

Figure 5.15: Walén test results over both current sheets for the event that occurred on the 2nd February 2002 for data taken by Cluster 1 and 3. The left hand side panels show the Walén tests for Cluster 1 over sheets C1 and C2 and the right hand side shows the Walén tests for Cluster 3.

Sheet	**Time Boundaries (UT)**	**VHT**	**Int.**	**Grad.**	**C.C.**	T-Test
1 (C1)	02:31:00 - 02:32:10	-374, 25, -42	0.3	0.828	0.964	0.884
2 (C1)	02:33:40 - 02:24:50	-366, 3, -56	0.19	-0.645	0.915	0.117×10^{-13}
1 (C3)	02:31:00 - 02:32:10	-369, 26, -44	-1.36	0.942	0.98	0.937
2 (C3)	02:33:40 - 02:34:40	-357, 5, -56	-0.69	-0.67	0.91	0.117×10^{-9}

Table 5.9: The De-Hoffman Teller frame and the Walén test analysis for each current sheet for the event on 2nd February 2002.

The same analysis was conducted in *Teh et al.* (2009) yielding very similar results; the correlation coefficients for both sheets at Cluster had a magnitude of > 0.95. The gradient was found to be 0.698 for sheet 1 and -0.776 for sheet 2 which both weakly satisfy the Walén relation and thus we can be confident that this has been correctly identified as a reconnection event.

5.5.4 Structure of Event

We determine a natural co-ordinate frame of reference for the event using a weighted average of the minimum variance analysis shown in Table 5.10. The minimum variance analysis for the individual current sheets is shown in Tables 5.11 and 5.12. Thus we have the normal direction vectors current sheet 1 as [0.686, -0.28, -0.189] and for sheet 2 it is [0.890, -0.230, 0.007].

In this case the X-line direction was found to be $= [0.169, -0.985, -0.036]$ (in GSE co-ordinates), which is found be taking the cross product of the normal direction vectors of the two current sheets. If we compare this to the X line direction found in the *Teh et al.* (2009) analysis, where the X-line was calculated to be in the $[0.428, -0.832, -0.353]$ (in GSE co-ordinates), we find that the angle between the two directions is 25°. Given that in the *Teh et al.* (2009) analysis they are considering the results from ACE and Wind in addition to the Cluster spacecraft we can consider these to be the same result within error.

The natural co-ordinate frame is given by the rotation matrix:

$$\begin{pmatrix} N \\ M \\ L \end{pmatrix} = \begin{pmatrix} -0.677 & -0.678 & 0.289 \\ -0.597 & 0.735 & 0.325 \\ -0.432 & 0.047 & -0.901 \end{pmatrix} \begin{pmatrix} X \\ Y \\ Z \end{pmatrix} GSE$$

S/C	Time frame (mm:ss)		**Direction Vector**	λ	λ **Rat.**
C1	31:00 - 34:45	**Minimum:**	-0.707, -0.638, 0.306	0.313	2.01
		Intermediate:	-0.561, 0.769, 0.307	0.63	76.7
		Maximum:	-0.431, 0.046, -0.901	48.3	
C2	30:58 - 34:43	**Minimum:**	-0.732, -0.605, 0.315	0.308	1.99
		Intermediate:	-0.529, 0.794, 0.300	0.613	78.6
		Maximum:	-0.429, 0.055, -0.901	48.2	
C3	31:01-34:46	**Minimum:**	-0.572, -0.786, 0.236	0.356	1.89
		Intermediate:	-0.696, 0.617, 0.367	0.674	72.0
		Maximum:	-0.434, 0.046, -0.900	48.5	
C4	31:00 - 34:45	**Minimum:**	-0.637, -0.722, 0.272	0.322	1.93
		Intermediate:	-0.639, 0.691, 0.339	0.620	78.1
		Maximum:	-0.432, 0.042, -0.901	48.4	

Table 5.10: The minimum variance analysis over the whole event, for each of the 4 Cluster spacecraft (S/C). The maximum, intermediate and minimum variance direction vectors are given, their corresponding eigenvalues, λ and the λ ratios between the minimum and intermediate directions and between the intermediate and maximum directions.

S/C	Time frame (mm:ss)		Direction Vector	λ	λ Rat.
C1	32:02 - 32:04	**Minimum:**	0.64, 0.768, 0.018	0.0038	20.8
		Intermediate:	0.743, -0.612, -0.271	0.079	62.4
		Maximum:	-0.198, 0.187, -0.962	4.93	
C2	32:04 - 32:06	**Minimum:**	0.615 -0.714, -0.334	0.0306	11.3
		Intermediate:	-0.611, -0.7, 0.371	0.345	15.0
		Maximum:	-0.499, -0.024, -0.866	5.19	
C3	32:00 - 32:03	**Minimum:**	0.722, 0.646, -0.248	0.359	3.1
		Intermediate:	0.667, -0.745, -0.0	1.11	16.7
		Maximum:	-0.184, -0.165, -0.969	18.5	
C4	32:02 - 32:03	**Minimum:**	0.899, -0.414, -0.145	0.0386	9.6
		Intermediate:	-0.386, -0.903, 0.188	0.369	22.7
		Maximum:	-0.209, -0.113, -0.971	8.37	

Table 5.11: The minimum variance analysis for the event that occurred on the 2nd February 2002: Sheet 1.

S/C	Time frame (mm:ss)		Direction Vector	λ	λ Rat.
C1	34:25 - 34:26	**Minimum:**	0.842, 0.011, 0.539	0.00103	3.5
		Intermediate:	-0.436, 0.602, 0.669	0.00356	387
		Maximum:	-0.317, -0.798, 0.512	1.38	
C2	34:26 - 34:27	**Minimum:**	0.812, -0.375, -0.446	0.00865	2.4
		Intermediate:	0.562, 0.299, 0.771	0.0204	95.1
		Maximum:	-0.159, -0.877, 0.454	1.94	
C3	34:24 - 34:25	**Minimum:**	0.985, -0.163, -0.051	0.00149	
		Intermediate:	0.154, 0.723, 0.674	0.223	149.7
		Maximum:	-0.073, -0.672, 0.737	1.57	7.04
C4	34:24 - 34:26	**Minimum:**	0.919, -0.393, -0.013	0.00489	61.3
		Intermediate:	0.304, 0.689, 0.658	0.3	7.1
		Maximum:	-0.250, -0.609, 0.753	2.13	

Table 5.12: The minimum variance analysis for the event that occurred on the 2nd February 2002: Sheet 2.

Spacecraft	**Sheet 1: Time Lag /s**	**Sheet 2: Time Lag /s**	**Distance from ref. (C3) /km**
Cluster 1	1.02	0.62	-410, -270, 235
Cluster 2	3.03	1.78	239, 73, -299
Cluster 3	0	0	0, 0, 0
Cluster 4	0.758	0.508	25, 49, -99

Table 5.13: Time lag between a Cluster spacecraft and spacecraft 1 Event 7/2/2006.

	Speed	Direction
Sheet 1	241 $km\ s^{-1}$	-0.986**x**, -0.169 **y**, -0.00471**z**
Sheet 2	301 $km\ s^{-1}$	-0.969**x**, -0.160**y**, -0.187**z**

Table 5.14: Results of the timing analysis: the speed and direction of the two current sheets

We also use the timing method to estimate the normal direction vector of the current sheets and the speed in this direction. To accomplish this we take the time lag between spacecraft at the point of maximum correlation. Table 5.13 shows the time lag in seconds for each of the current sheets at the point of maximum correlation between that spacecraft and Cluster 3 (hence why the timelag for Cluster 3 is 0). Table 5.13 also shows the distance (in GSE co-ordinates in km) that each spacecraft is from Cluster spacecraft 3. Each of the time lags are less than 5 seconds indicating that the spacecraft encountered each of the current sheets at almost the same time in the order Cluster 3, 4, 1, and finally 2.

The speed and orientation for each current sheet (CS1 and CS2) found using the timing analysis method, are shown in Table 5.14. Here we can see that the speeds of each of the current sheets is quite different, though the normal direction vectors are very similar. Here current sheet 1 is determined to be travelling at a speed of 241 $km\ s^{-1}$ and current sheet 2 at 301 $km\ s^{-1}$.

5.5.5 Removing the solar wind

It is only possible to find a background solar wind flow for Cluster 1 and 3 as the CIS instrument is not operational for Cluster 2 and 4 during this event. The times over which the background solar wind speed is found are as follows for both Cluster 1 and 3: the leading side is calculated between 02:29:00 - 02:30:00 UT and the trailing side between 02:36:00 - 02:37:00 UT. This leads to the average background solar wind velocity as [-347, 6, -10] $km\ s^{-1}$ for Cluster 1 and [-339, 7.5, -11] $km\ s^{-1}$ for Cluster 3 (in the GSE co-ordinate system; after the background has been removed we rotate the frame into the OC87 frame).

We then rotate the event into the OC87 frame so that the magnetic field in the L* direction is equal and opposite on each side of the event. In this case study the value of the angle of rotation β is 146° and 149° for the data at Cluster 1 and 3 respectively.

5.5.6 Derive the inflow quantities

The inputs are the average found from the times 02:31:00 UT - 02:31:30 UT and 02:34:40 UT and 02:35:10 UT for input sides 1 and 2 respectively for both the Cluster 1 and 3 spacecraft. This gives the input values as shown in Table 5.15. All the inflow quantities are given in the OC87 frame.

The inflows for the Cluster 1 and Cluster 3 spacecraft are very similar to each other, as would be expected for spacecraft that are situated so close together when observing such a large event. In this case study the inflows on either side are very different with the inflow speed on the trailing edge ($V_{2L*} = -22.0\ km\ s^{-1}$ for Cluster 1 and $V_{2L*} = -17.3$ for Cluster 3) being much larger than that for the leading edge ($V_{1L*} = 2.0\ km\ s^{-1}$ for Cluster 1 and $V_{1L*} = 2.0\ km\ s^{-1}$ for Cluster 3).

Cluster 1	Input Variable	Value (L* direction)
v_{1L*}	v_{I1}	2.0 $km\ s^{-1}$
v_{2L*}	v_{I2}	$-22.0\ km\ s^{-1}$
Density (inflow side 1)	n_1	18.9 cm^{-3}
Density (inflow side 2)	n_2	13.0 cm^{-3}
B_{L*}	B	9.3 nT
Angle between spacecraft and event normal	γ	134°
Cluster 3	Input Variable	Value (L* direction)
v_{1L*}	v_{I1}	$-1.8\ km\ s^{-1}$
v_{2L*}	v_{I2}	$-17.3\ km\ s^{-1}$
Density (inflow side 1)	n_1	22.7 cm^{-3}
Density (inflow side 2)	n_2	14.4 cm^{-3}
B_{L*}	B	9.5 nT
Angle between spacecraft and event normal	γ	134°

Table 5.15: Derived inflow quantities for the Cluster 1 and Cluster 3 spacecraft for case study 2.

Variable	Cluster 1	Cluster 3
v_{0E1}	61 $km\ s^{-1}$	65 $km\ s^{-1}$
v_{0E2}	85 $km\ s^{-1}$	80 $km\ s^{-1}$
$\frac{t_3}{t_2}$ ratios	1.02	1.02

Table 5.16: Predicted outflows for case study 2.

The densities on either side of the event are also quite asymmetric with the plasma on the leading side ($n_1 = 18.9\ cm^{-3}$ for Cluster 1 and $n_1 = 22.7\ cm^{-3}$ for Cluster 3) being much more dense than the plasma on the trailing side ($n_2 = 13.0\ cm^{-3}$ for Cluster 1 and $n_1 = 14.4\ cm^{-3}$ for Cluster 3). It should also be noted that the densities at Cluster 3 are greater than that at Cluster 1, particularly on inflow side 1. On the inflow side 1 the density is 20% higher at Cluster 3 than Cluster 1.

5.5.7 Predictions

Using the inflow parameters described in Section 5.5.6 we then make predictions on the output parameters. The predictions are given in Table 5.16.

The reconnection outflows predicted for the OC87 have slightly different speeds for the leading and trailing sides. For both Cluster 1 and 3 the outflow predicted for v_{0E1}, 61 $km\ s^{-1}$ and 65 $km\ s^{-1}$ respectively, is less than that predicted for v_{0E2}, 85 $km\ s^{-1}$ and 80 $km\ s^{-1}$ respectively.

The ratio of the relative times the spacecraft is predicted to spend in the two sections of the ion outflow is $t_3/t_2 = 1.02$ for Cluster 1 and 3, meaning that each Cluster spacecraft is expected to spend an equal amount of time in the leading and trailing side of the exhaust.

5.5.8 Comparisons with model

The observed speed of the exhaust is $\sim 40\ km\ s^{-1}$ between the two current sheets. There is no evidence for a third current sheet or outflows of different speeds, which were predicted by the OC87 model (Cluster 1: $v_{0E1} = 61\ km\ s^{-1}$ and $v_{0E2} = 85\ km\ s^{-1}$ and Cluster 3: $v_{0E1} = 65\ km\ s^{-1}$ and $v_{0E2} = 80\ km\ s^{-1}$). The Cluster reconnection exhaust observations are also smaller than the predictions produced by the OC87 model. The observations of the outflow speed are a minimum of 50% of the speed of the predicted outflow.

For this case study $t_3/t_2 = 1$. In this case study there is no distinct central current sheet so it is not possible to compare this with observations.

For this case study the approximate Alfvén speed is $\sim 72\ km\ s^{-1}$. The actual outflows are in the region of $40\ km\ s^{-1}$, and the predicted outflows are between $61 - 85\ km\ s^{-1}$. This means that some of the predicted outflow speeds are larger than the Alfvén speed of the region and the observed outflows are $\sim 55\%$ of the Alfvén speed.

5.6 Case Study 3: 2nd March 2006

Finally we test the OC87 model using the case study from Chapter 4. The structure and orientation of the event had already been determined in Chapter 4 along with the evidence that it is a reconnection event.

5.6.1 Event Overview

As we have considered this event in a previous chapter the spacecraft positions have already been described in Section 4.1, the Cluster spacecraft observations

(including the minimum variance analysis) in Section 4.2 and the evidence for reconnection in Section 4.3. We rotate the data from the natural co-ordinate system used in Chapter 4 and rotate into the OC87 frame to complete the analysis here. The angle of rotation from the natural frame to the OC87 frame, β is 45° and 50° for Cluster 1 and 3 respectively

5.6.2 Removing the solar wind

The background solar wind velocity was found by taking an average of the solar wind from times at either side of the exhaust. In this case the average was taken between 16:37:30 UT - 16:38:00 UT and 16:39:30 UT - 16:40:00 UT for both spacecraft. For Cluster 1 the background solar wind velocity was found to be $[-388.8, 26.2, -3.1]\ km\ s^{-1}$ and for Cluster 3 it was found to be $[-382.4, 27.4, -2.85]\ km\ s^{-1}$ (as in Chapter 4).

5.6.3 Derive the inflow quantities

The inputs are the average found from the times 16:38:00 UT - 16:38:10 UT and 16:39:00 UT and 16:39:10 UT for input sides 1 and 2 respectively. This gives the input values as shown in Table 5.17 all in the OC87 frame.

5.6.4 Predictions

Using the inflow parameters we then make predictions on the output parameters. The predictions are given in Table 5.18.

The reconnection outflows have similar speeds for V_{0E1} and V_{0E2} but the predictions are more similar and smaller for Cluster 1 ($V_{0E1} = 32\ km\ s^{-1}$ and $V_{0E2} = 29\ km\ s^{-1}$) than Cluster 3 ($V_{0E1} = 40\ km\ s^{-1}$ and $V_{0E2} = 34\ km\ s^{-1}$). In

Cluster 1	Input Variable	Value (L* direction)
v_{1L*}	v_{I1}	$-1.3\ km\ s^{-1}$
v_{2L*}	v_{I2}	$2.4\ km\ s^{-1}$
Density (inflow side 1)	n_1	$7.0\ cm^{-3}$
Density (inflow side 2)	n_2	$6.5\ cm^{-3}$
B_{L*}	B	$2.6\ nT$
Angle between spacecraft and event normal	γ	136°
Cluster 3	**Input Variable**	**Value (L* direction)**
v_{1L*}	v_{I1}	$-4.5\ km\ s^{-1}$
v_{2L*}	v_{I2}	$0.8\ km\ s^{-1}$
Density (inflow side 1)	n_1	$5.9\ cm^{-3}$
Density (inflow side 2)	n_2	$5.8\ cm^{-3}$
B_{L*}	B	$2.8\ nT$
Angle between spacecraft and event normal	γ	135°

Table 5.17: Derived inflow quantities for the Cluster 1 and Cluster 3 spacecraft for case study 3.

Variable	Cluster 1	Cluster 3
v_{0E1}	$32\ km\ s^{-1}$	$40\ km\ s^{-1}$
v_{0E2}	$29\ km\ s^{-1}$	$34\ km\ s^{-1}$
$\frac{t_3}{t_2}$ ratios	1.00	0.98

Table 5.18: Predicted outflows for case study 3.

both cases V_{0E1} is the larger of the two outflows.

The ratio $t_3/t_2 \simeq 1$ for both the Cluster 1 and Cluster 3 spacecraft and therefore we expect that the Cluster spacecraft will spend an approximately equal amount of time in the two outflow regions.

5.6.5 Comparisons with Model

The observed outflow speed for this case study is $\sim 20\ km\ s^{-1}$. There appear to be 3 current sheets (as highlighted in Figures 4.2 and 4.4.) The outflow is only apparent between the first two current sheets as the total ion velocity has returned to approximately the background speed after the second current sheet has passed. The OC87 predictions for the outflow are larger than that observed (ranging between $29\ km\ s^{-1} - 40\ km\ s^{-1}$). The outflow speeds are between $50-69\%$ of the predicted values.

The amount of time that each spacecraft is predicted to spend in each outflow is approximately equal. In this case study the 3 observed current sheets are approximately equal for Cluster 1 but for Cluster 3 the time between current sheets 1 and 2 is double that of the time between 2 and 3.

For this case study the approximate Alfvén speed is $\sim 41\ km\ s^{-1}$. The actual outflows are in the region of $20\ km\ s^{-1}$, and the predicted outflows are between $29 - 40\ km\ s^{-1}$.

5.7 Interpretation and Discussion

In this chapter we have compared the observations of three case studies with the model devised by *Owen and Cowley* (1987b). In each of the case studies the predicted values for the outflow speeds were larger than that observed but of the

same order of magnitude.

In the first case study the predictions for the outflow speeds were found to be between 34 $km\ s^{-1}$ to 67 $km\ s^{-1}$ whereas the observed outflows were found to be $\sim 20\ km\ s^{-1}$. The other two case studies were also found to predict larger values for the outflow velocities that were actually observed. In the second case study the predictions for the outflows are between 61 $km\ s^{-1} - 85\ km\ s^{-1}$ in comparison with the observed flow which is $\sim 40\ km\ s^{-1}$. The final case study has much lower predicted values than the other case studies, between 29 $km\ s^{-1} - 40\ km\ s^{-1}$. This is more similar to the outflow speeds which are $\sim 20\ km\ s^{-1}$. The general trend of the predictions follows the observations as the case study with the highest observed exhaust has the greatest predicted speeds. Each of these observed outflows is much lower than the predictions. This is because the predictions are maximum values and assume all available magnetic energy is converted to kinetic energy of the outflow. In order to improve the model it would be necessary to make an estimate of the percentage of available magnetic energy that is liberated by reconnection.

Theoretical models of reconnection often overestimate the outflow speeds of reconnection events in the solar wind, as seen in the following studies: (*Sonnerup et al.*, 1981; *Gosling et al.*, 2006b; *Phan el al.*, 2013). In these studies the actual observed outflows were found to be on average 75% of the predicted outflows. The observations of the outflow exhausts for these case studies are approximately $40\% - 70\%$ of the predicted outflows. The OC87 model did appear to predict outflow speeds that were similar to, and sometimes slightly greater than, the Alfvén speeds for the region.

The relative time that the spacecraft was predicted to be in each of the reconnection outflows, the ratio t_3/t_2, for the first case study was 1.65 for Cluster 1 and

1.83 for Cluster 3. This meant that the spacecraft were predicted to spend more time in the trailing side outflow than the leading side outflow. The observations of density for Cluster 1 suggested that the spacecraft spent approximately equal amounts of time in each outflow. For the other cases studies the predicted ratio was approximately 1. It was not possible to test for case study 2 as a third current sheet and/or two distinct exhausts are not apparent, however for the third case study Cluster 1 did observe an equal time difference between the first and second current sheets and the second and third current sheets. Cluster 3 observed a longer period of time in the leading side than the trailing side.

5.8 Conclusion

For the first case study we have provided evidence for a magnetic reconnection event that occurs in the solar wind seen by the Cluster spacecraft. In this event the typical reconnection exhaust characteristics continue after the double magnetic field rotation has passed and there are some small perturbations in the magnetic field after the two rotations. Cluster 2 witnesses what appears to be a third current sheets during the reconnection exhaust leading to the conclusion that the current sheet structure may be trifurcated in this case. The other 3 spacecraft results also suggest the magnetic reconnection event has a more complicated magnetic field structure and may in fact be bound by more than two current sheets.

Using the Owen and Cowley model to predict the outflows and compare with the observed outflows we find that the outflow predictions are greater but of the same order of magnitude as that observed by the spacecraft. The predictions are close to the Alfvén speed in the solar wind which suggests that the amended predictions could indicate a maximum outflow speed.

We conclude that the Owen and Cowley model makes outflow predictions that are of the same order of magnitude as the observed outflows but some further predictions e.g. a difference in the outflow speeds for the two outflows are not observed. This could be due to the fact that we are potentially measuring inflow particles in the outflow which makes the observed outflows appear smaller and the model does not take into account any heating of the plasma.

The Heyn model might be a suitable framework within which to continue this research as it includes up to 4 discontinuities; depending on the input parameters.

Chapter 6

Statistical Survey of Magnetic Reconnection Events in the Solar Wind

In the previous two chapters we have shown that there are examples of magnetic reconnection events in the solar wind that are not consistent with the prevailing Gosling picture. It can thus be inferred that magnetic reconnection in the solar wind may result in a variety of more complex structures. In Chapter 4 we looked at the evolution of a magnetic reconnection event over timescales and distances similar to the Cluster spacecraft separation. In Chapter 5 we applied reconnection models which were derived from those developed for the magnetotail in order to interpret more generally the signatures of reconnection in the solar wind, and we have found events that are more complex than the Gosling picture. In this chapter we explore the structure of reconnection outflow regions and the prevailing conditions in which such structures are observed in more detail, using a statistical survey of events detected by the Cluster spacecraft. By producing a statistical

survey, we address a number of key science questions including:

1. What, if any, are the prevailing solar wind conditions which support reconnection events in the solar wind? Are events typically associated with a particular range of solar wind speed, magnetic field and/or density? Magnetic reconnection occurs in many contexts, but the solar wind offers one of the largest scale and boundary free environments for directly observing these events. Determining the typical solar wind parameters in which these events occur could help to determine how these events are formed.

2. Where does the energy for the outflow exhaust originate? What is the observed relationship between the outflow velocity and the Alfvén speed? How is the input energy partitioned between the kinetic energy and temperature of the outflow? Theoretical models of reconnection predict the outflow at speeds of approximately the Alfvén speed (e.g., *Parker*, 1963; *Petschek*, 1964). However, previous analysis of events has indicated that the outflow speed can be significantly less (50 - 75%) of the Alfvén speed (e.g., *Sonnerup et al.*, 1981; *Phan el al.*, 2013; *Gosling et al.*, 2006b). What outflow speed is typically the case in the solar wind, and why?

3. How many distinct current sheets does reconnection typically generate in the solar wind? The Gosling model of reconnection (*Gosling et al.*, 2005) predicts a single exhaust bounded by 2 current sheets, but in Chapters 4 and 5 we have reported the potential for up to 5 current sheets to be apparent.

4. Does magnetic reconnection in the solar wind show evidence of evolution with time? Previous studies have suggested that reconnection events in the solar wind are usually large scale and have little temporal or spatial variation

(*Phan et al.*, 2006; *Gosling*, 2010, 2011). In Chapter 4 we presented a case study of an event in which there was temporal and/or spatial evolution of the reconnection event structure. Are there significant numbers of other events with a similar character? Is structural evolution a typical or more unusual feature of magnetic reconnection events in the solar wind?

In order to systematically find reconnection events in the solar wind to address these questions we construct an automated algorithm which selects reconnection events based on a specific set of criteria. These criteria are based on the characteristics of clear reconnection events in the published literature. In Section 6.1 we describe the functionality of the algorithm. In Section 6.2 we test a variety of threshold values. In Section 6.3 we discuss the limitations of the algorithm. In Section 6.4 we then analyse the events found using the algorithm in order to answer the above science questions and in Section 6.5 we discuss the results and draw conclusions.

6.1 Algorithm for Finding Reconnection Events

We have developed an algorithm designed to find reconnection events within the Cluster spacecraft data set that fulfil a set of criteria. The following section describes how the algorithm is constructed in order to produce a list of candidate reconnection events. We describe the basis of the algorithm using an example time period that runs from 22:00:00 UT to 23:00:00 UT on the 23rd February 2002, as we have visually determined that there is a reconnection event in this period.

In order to determine whether a given time period of data contains a candidate event, we must identify some changes in variables that we consider to be indicative of the passage of a magnetic reconnection event past the spacecraft. It is essential,

for statistical purposes, to maximise the number of true events while simultaneously minimising the number of false positives, and so a number of thresholds are defined taking this into account. In this algorithm we have several thresholds for variations to extract the reconnection events within a given period of data. A key for each of the thresholds used and associated values and units is given in Table 6.1

For this study we need to select data periods for which the Cluster 1 spacecraft is outside of the Earth's bowshock. We use the *Chao et al.* (2002) model for the Earth's bow shock. In this model we use the average values for the parameters cited in this paper to determine the size and shape of the bowshock, thus the bowshock size is considered fixed. However we have included an additional margin of error, the threshold parameter BS (R_E), to account for the fluctuations in the bow shock position during different solar wind conditions. Whilst this means that some data will be discarded that would have been appropriate for use, it is more important to ensure that all the data used in the algorithm was recorded in the ambient solar wind and not influenced by bow shock physics.

One of the primary indications for reconnection is a magnetic field rotation bounding, or associated with, an increase in ion velocity (*Parker*, 1963; *Gosling et al.*, 2005). Thus we must initially find clear indications of magnetic field rotations. It is then necessary to determine what is an appropriate minimum rotation that constitutes a potential magnetic reconnection event. This is the purpose of the magnetic field rotation threshold, BT (°).

The other major indicator for a magnetic reconnection event is the observation of a potential reconnection exhaust. Therefore we set a threshold limit for the minimum change in ion velocity over the time span of a potential event, VT

Var.	Details	Var.	Details
BS	In this algorithm we model the Earth's bowshock as having a fixed size and shape. This threshold is an additional distance upstream from the model of Earth's bowshock that the Cluster spacecraft must be for the data to be included in the algorithm. **Value: 3** R_E	**BT**	Minimum magnetic field rotation threshold. **Value: 80°**
CD	The maximum current density over each event should be greater than this value. **Value:** $40nA\ m^{-2}$.	**DT**	CIS instrument lower limit threshold for the density of the plasma. **Value: 1** cm^{-3}
ED1	The maximum time allowed for an event. Above this value an event is discarded. **Value:** 1000 s	**ED2**	The minimum duration of an event; to ensure there are enough data points to analyse effectively. **Value:** 60 s
FS	Foreshock threshold: the maximum percentage of magnetic field data points in a candidate event where the Cluster spacecraft is connected to the bowshock before a potential event is discarded. **Value: 45** %	**GP**	Number of points over which we determine the magnetic field angle change. **Value:** 100
GS	The number of points in a gap between two 'accepted' points above which it is considered to be separate current sheets. **Value:** 5	**MV**	The threshold for the difference in the magnetic field component in the maximum variance direction between the start and end of the event. **Value:** 6 nT
SM	The number of points over which the data is smoothed. **Value:** 1	**VT**	Minimum change in ion velocity. **Value:** 20 $km\ s^{-1}$

Table 6.1: A list of each of the thresholds used in this algorithm (alphabetical order) and their final assigned value and unit.

$(km\ s^{-1})$.

As stated above, in the algorithm we consider rotations in the magnetic field to be indicative of current sheets. We do not consider the angle change between consecutive points in the magnetic field data, instead we consider an overall angle change over a range of points, the number of which is determined by the threshold, GP (points). This is to eliminate fluctuations due to background noise or high frequency waves. For each data point 'n' we determine the change in the unit magnetic field vector direction between points $n - \frac{gp}{2}$ and $n + \frac{gp}{2}$. This is illustrated by Figure 6.1. This figure shows a section of illustratory magnetic field data. Point 'n' is highlighted by the black arrow. The algorithm determines the angle between the magnetic field direction vectors that are at a time period defined by $\pm\frac{gp}{2}$ away of either side of the tested point. We then move onto point $n + 1$ and continue.

The temporal resolution of the magnetic field used is 4s. This means that, for an event that lasts longer than 60s (the minimum timespan threshold ED2, means events of a shorter duration are discarded) there will be at least 15 data points. It is quite likely that not all of these data points will be over the chosen thresholds and we require a way to classify whether non-consecutive data points satisfying the criteria are part of the same event or not. For example in the case of a large event where there are two current sheets bounding an exhaust, the magnetic field data between the current sheets may not satisfy the rotation criteria as there is often only minimal magnetic field rotation between current sheets. For this we use a threshold, GS, (points). If, as in the example, we have two distinct current sheets which satisfy the criteria but there are a couple of points between them that do not, the two rotations will be considered separate potential events if the number of non-satisfing points is greater than GS and part of the same event otherwise.

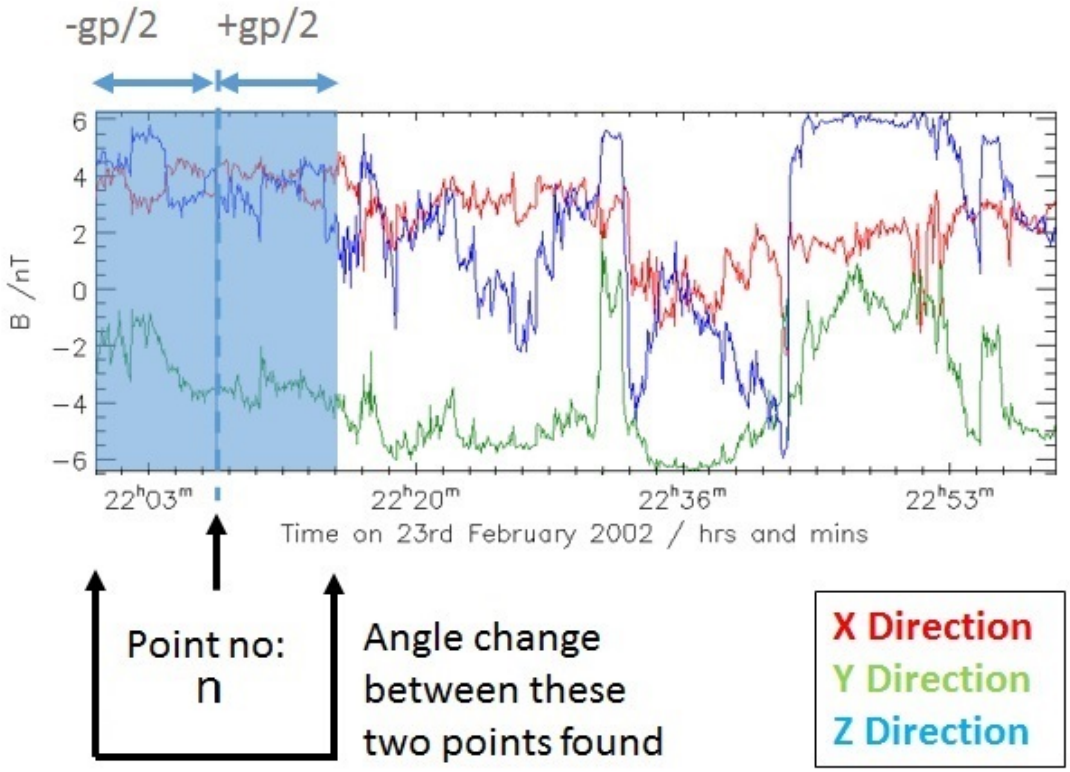

Figure 6.1: An example of finding the magnetic field rotation over a given time period, gp. The data shown is magnetic field data in GSE co-ordinates x (red), y (green) and z (blue). The point, n, that is being tested is highlighted by the vertical black arrow. The angle change between the magnetic field vectors that are $-gp/2$ and $+gp/2$ either side of the testing point is found.

In order to try and minimise the amount of background fluctuations and noise in the magnetic field data, we introduce a smoothing factor. This factor is the number of data points over which the smoothing will be done. Smoothing the data does mean that any sharp changes will be much less apparent. The level of smoothing is determined by the smoothing value, SM (points).

Reconnection events may have wide ranging durations, and in any automated algorithm, upper and lower bounds of what we will consider an event must be chosen. This choice dictates the scale of the reconnection events that can be identified. The lower time criteria ED2, (seconds) ensures that there must be several data points within each selected reconnection event so that there is sufficient data for study. This does mean that smaller events or events which traverse the spacecraft at high speed will be discarded from the analysis. The upper time frame, ED1, (seconds) is to discard any data sets over large periods of time as they often contain large data gaps. If there is no data for a specific time period then the data is set as a null value.

The foreshock threshold, FS, (%) is the maximum percentage of allowed points within a candidate event period where the Cluster 1 spacecraft can be magnetically connected to the bowshock before an event is discarded. This is to ensure that the events that we are analysing are not significantly affected by foreshock processes and that we are not picking up foreshock events.

In any reconnection event there should be a large difference between the magnetic field in the maximum variance direction at the start and end of the event (as the majority of the change will be in the maximum variance direction). The minimum acceptable difference is described by MV (nT).

The current density ($nA\ m^{-2}$) over the events is found using the following

equation:

$$\frac{dBmax}{dn} = \mu_0 j \tag{6.1}$$

where dBmax is the magnetic field in the maximum variance direction, dn is the distance travelled in the direction normal to the event and j is the current density. We use the assumption that the minimum variance direction in the magnetic field is equivalent to the normal direction of the current sheet which can be further considered to be 1-dimensional: it extends essentially unvaryingly in distances tangential to the current sheet which are large compared to the distance across it. We estimate dn by dividing the solar wind speed in the minimum variance direction by the number of data points per second.

Thus for a candidate time period to be considered an event, the maximum current density over the event should be larger than the threshold, CS.

The Cluster CIS instruments have lower limit values of density below which the values are not reliable. *Dandouras et al.* (2015) states that the lower limit for meaningful densities for HIA is $0.01 - 0.02$ particles cm^{-3}. At the lower limit the counting statistics are insufficient to allow for reliable calculation of any higher order moments, for example the ion velocity. It is important in this study that the ion velocity measurements are accurate as we are looking for very small changes in comparison to the background. Thus an instrumental threshold, DT (particles cm^{-3}) is set.

6.1.1 Structure of Algorithm

In the example time period there is a reconnection event, originally found using a visual search of the data. Initially 4s magnetic field and ephemeris, and ion velocity data, collected by the FGM and CIS instruments respectively, are downloaded from

the Cluster Science Archive.

Both the FGM and ephemeris data are then interpolated onto the ion velocity time points, such that all the data is now on a common timebase. Figure 6.2 shows the GSE components of the magnetic field in panel a) and ion velocity in panel b) downloaded directly from the Cluster Science Archive for the example time period. Panel a) shows the magnetic field components in GSE (x direction in red, y direction in green, and z direction in blue - this colour scheme will be implemented throughout the rest of the Chapter). Several very distinct magnetic field rotations are observed, which are highlighted by the black arrows. Panel b) of Figure 6.2 shows the ion velocity components in GSE in which, again, there are a few significant deviations from the background as indicated by the red arrows which are generally coincident with the magnetic field rotations. The next stage of the algorithm determines which (if any) of these magnetic field rotations and ion velocity changes satisfy the criteria.

6.1.2 Verifying that Cluster is in the Pristine Solar Wind

For the initial part of the algorithm we determine the periods where the Cluster spacecraft are in the solar wind. For this we use a model of the Earth's bow shock position from *Chao et al.* (2002) which is as follows:

$$r = r_0(\frac{1+\epsilon}{1+\epsilon cos\theta})^{\alpha} \tag{6.2}$$

where r_0 is the sub-solar bowshock standoff distance, α is a parameter representing the level of tail flaring, ϵ is a parameter that represents the eccentricity of the bowshock and r and θ are the polar co-ordinates describing the bow shock surface in the ecliptic plane. This model assumes a rotational symmetry around the Earth-Sun line. This is the bowshock threshold. For this model α and r_0 are given by

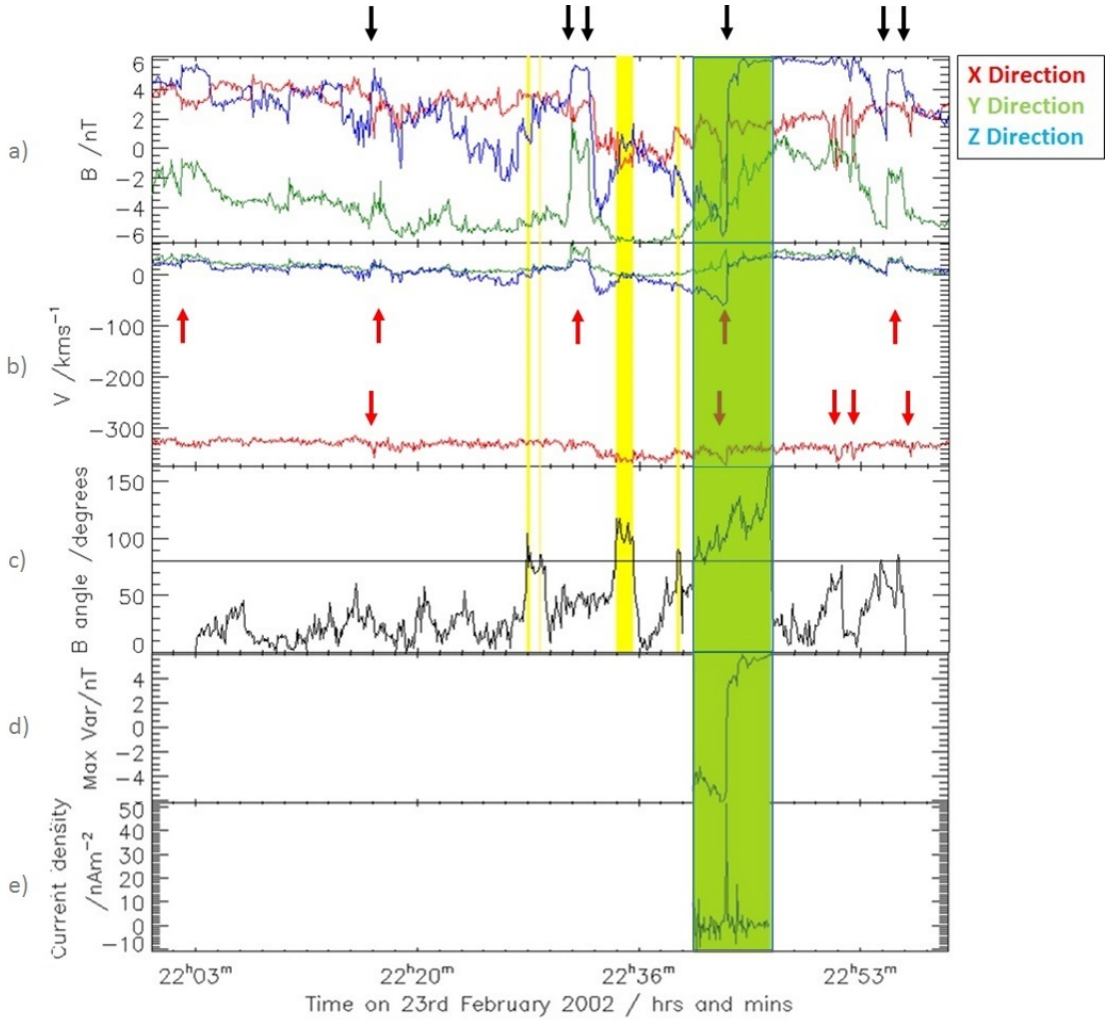

Figure 6.2: Figure showing the data downloaded from the Cluster Science Archive, the angle change in ° of the magnetic field over 'GP', the magnetic field in the maximum variance direction, and the current density. Panel a) shows the magnetic field data in GSE components, Panel b) shows the ion velocity data (also in GSE components), panel c) shows the angle change of the magnetic field, panel d) shows the magnetic field in the maximum variance direction, and panel e) shows the current density. The black arrows indicate large magnetic field rotations and the red arrows indicate deviations in the ion velocity. The yellow boxes indicate the current sheets found by the algorithm and the orange box shows the reconnection event found by the algorithm.

the following equations:

$$\alpha = a_5(1 + a_6 B_z)(1 + a_7 D_p)(1 + a_{10} ln(1 + \beta))(1 + a_1 4 M_m s) \tag{6.3}$$

$$r_0 = a_1(1 + a_3 B_z)(1 + a_9 \beta)(1 + a_4 \frac{((a_8 - 1)M_m s^2 + 2)}{((a_8 + 1)M_m s^2)}) D_p^{-1/a_{11}} \tag{6.4}$$

$$\epsilon = 1.029 \tag{6.5}$$

Where B_z is the IMF north-south component, D_p is the dynamic pressure of the upstream solar wind, β is the solar wind plasma β and M_{Ms} is the magnetosonic mach number. For each of the variables listed in equations 6.2, 6.3 and 6.4, *Chao et al.* (2002) found their average values to be:

$$B_z = -0.35, D_p = 2.48, \beta = 2.08, M_{Ms} = 6.96, a1 = 11.1266, a3 = -0.0005,$$
$$a_4 = 2.5966, a_5 = 0.8182, a_6 = -0.017, a_7 = -0.0122, a_8 = 1.3007, a_9 = -0.0049,$$
$$a_{10} = -0.0328, a_{11} = 6.047, a_{14} = -0.002, a_{12} = 1.029 \tag{6.6}$$

Using the spacecraft position data we can determine the angle θ and the distance away from the Earth, d:

$$\theta = sin^{-1}(\frac{\sqrt{(p_y^2 + p_z^2)}}{\sqrt{(p_x^2 + p_y^2 + p_z^2)}}) \tag{6.7}$$

$$d = \sqrt{p_x^2 + p_y^2 + p_z^2} \tag{6.8}$$

where p_x, p_y and p_z are the positions of the Cluster spacecraft in GSE co-ordinates.

In our algorithm we used these long-term average values for the standoff distance and the level of tail flaring and thus we added an additional distance, BS, to r to provide a margin to ensure that the Cluster spacecraft were definitely in the ambient solar wind. Substituting θ into Equation 6.2 we then discard any

data points for which $d < r + BS$ to ensure that the data in a candidate event is definitely recorded outside the Earth's bowshock and in the solar wind.

In the example shown in Figure 6.2 all of the data is recorded outside of the bowshock and so no data is discarded.

It is further expected that there may be measurement points during an event for which the spacecraft is magnetically connected to the bowshock. This arises since Cluster is very close to Earth and thus there can only be a narrow range of IMF vectors that are not connected. In addition, during a reconnection event the magnetic field is expected to rotate significantly, making it very likely that some of these magnetic field vectors will connect to the bowshock.

We must then consider how likely or how much connectivity to the Earth's bowshock may affect the results of an analysis of a reconnection event. *Sibeck et al* (2004) showed that while kinetic processes like foreshock cavities can introduce perturbation and structure to the solar wind just upstream of the Earth's magnetosphere, the effects diminish very rapidly with increasing distance from the bowshock, thus the additional margin of error 'BS' should ensure that the spacecraft is sufficiently far away from bowshock to avoid these effects.

The main remaining effects would be in the form of foreshock cavities which produce high fluxes of energetic ions moving back upstream along the field, and cause depressed plasma density and depressed magnetic field strength. In the case study described by *Sibeck et al* (2004), it was found that the plasma flux or pressure variations were due to the density fluctuations rather than velocity fluctuations which suggests that the main changes would be seen in the density and magnetic field data, which could potentially be misconstrued as a reconnection event, if the thresholds are not strict enough.

We have implemented a maximum threshold, the maximum percentage of points in the candidate event for which the spacecraft may be connected to the bowshock before the event is considered too connected and discarded.

6.1.3 Determining Magnetic Field Rotations

In the next stage we derive the angle changes of the magnetic field direction over a specified time-range, GP.

Next, we define a threshold for a minimum rotation: BT. Panel c) of Figure 6.2 shows a graph of the angle change in the magnetic field along with a horizontal line showing the threshold. We do not consider periods if there are not at least 2 consecutive data points that exceed the criteria to minimise effects from noise. We can see that there are several instances where the angle change exceeds the threshold, most notably between 16:00:00 - 16:16:00 UT.

6.1.4 Selecting Potential Events

Magnetic reconnection events often have multiple current sheets. This means that it is possible that between current sheets of the same magnetic reconnection event there could be some data points that do not fit the criteria and thus the two current sheets are separated and labelled as two separate events. A solution to this problem is to introduce a limit, GS, whereby if two periods of data that satisfy the reconnection criteria are sufficiently close together, they will be considered as one reconnection event.

Figure 6.2 highlights these potential events with the vertical yellow shaded bars. In this case there are 5 periods of data identified that we will test in the rest of the algorithm.

6.1.5 Implementing the Exhaust Threshold

A list of potential events is now available; a threshold based on the ion velocity is now applied. We identify changes in ion velocity based the following summation of the changes in the components:

$$\delta V_T = \sqrt{\delta V_X^2 + \delta V_Y^2 + \delta V_Z^2} \tag{6.9}$$

Where V_T is the total velocity change, and δV_i where i is X, Y and Z which are the changes in components of velocity in GSE.

The green vertical band in Figure 6.2 shows the result of this second cut through of the data, indicating the current sheet that also passed the ion velocity threshold. Thus all but one of the current sheets which passed the field rotation threshold are eliminated after application of this threshold in this example.

We then implement the limits on the event duration; any events falling outside the minimum and maximum will be discarded, which is to ensure that short events with too few data points to study are not included. In this example the potential event identified by the orange bar is well within the time boundaries.

6.1.6 Implementing Minimum Variance and Current Thresholds

We now transform the magnetic field into the frame defined by a minimum variance analysis (see Section 3.5.1). For each of the potential events, a minimum variance analysis is conducted over the time frame identified above. The spin resolution data is then rotated into this the minimum variance analysis (MVA) frame.

In this MVA frame we also estimate the current density. We keep the potential event if the difference between the maximum and minimum current density is

greater than the current density threshold, CD.

The start and end of the minimum variance analysis is the start and end times of the event which include a 'buffer' at either side of the event. Thus the minimum variance analysis will not return a completely accurate minimum variance time. However as the magnetic reconnection events found are the larger events the direction found is accurate enough to use as a threshold and to estimate a current density (but wouldn't be accurate enough to extrapolate any further information from).

6.1.7 Implementing Maximum Variance Direction and Foreshock Thresholds

The difference between the magnetic field in the maximum variance direction at the start and end of the event must be greater than MV. This is an additional threshold to the rotation threshold, BT, as it ensures that the magnitude of the magnetic field change, not just the angle change, is large.

At this point we also apply the threshold that ensures that the magnetic field is not connected to the foreshock. This threshold is implemented here in order to reduce the amount of computational power the algorithm uses.

The candidate event highlighted by the orange bar in Figure 6.2 has both a change in the maximum variance direction that is greater than the MV threshold (6 nT) and a % of points where the spacecraft is connected that is lower than the FS threshold (45%).

Thus this is a good candidate event, and the algorithm adds the start and end times of the event found to the list of events, along with the event characteristics and the prevailing solar wind conditions, on which in depth analysis can be later

conducted.

6.2 Testing the Algorithm

In order to determine the optimum values for the above thresholds it was necessary to test a variety of thresholds on a limited data set and check the outcome. For this algorithm we prioritise that the events found must be clear reconnection events and thus in the iteration reported here this may necessitate the omission of many of the smaller and/or more ambiguous events. For each test we have used the algorithm on Cluster data over the months January to April in 2003. Each candidate event found was then visually inspected to verify whether it was an event and given one of the labels: 'Yes', 'No' or 'Maybe'. The percentage of candidate events that were definitely events, labelled 'Yes', gave an idea of how effective a given set of thresholds are.

Tables 6.2 to 6.5 show the results of each test of the thresholds. The final selected boundaries for the work in the rest of this chapter are the ones described in Threshold Test 30. These were chosen as this set returns a large number of candidate events for which a high percentage, on visual inspection, are concluded to be true events. For these thresholds the number of false positives are minimised.

In the following sections 6.2.1 - 6.2.11 we describe how we determined each threshold value.

Another method to find the most optimum set of thresholds could have been to use a multi-variate regression analysis (A utilised in *Milan et al.*, 2012). However as this requires substantially more computing power than the above method it was not utilised in this study.

6.2.1 Current Density Threshold

In this algorithm we use a threshold of 40 $nA\ m^{-2}$ for the minimum current density, this was found from testing a variety of thresholds as is shown in Table 6.2, tests 2-4. Although a slightly higher percentage of true events are found using a threshold of 50 $nA\ m^{-2}$ in Test 3, the threshold greatly reduces the number of candidate events found in comparison with Test 4.

6.2.2 Maximum Variance Direction Threshold

Tests 5 and 6 show a testing of the maximum variance direction threshold, and from this we put a limit that the difference between the start and end value must be at least 6 nT as this gives the best percentage for correct positives (comparing Test 4 with 5 and 6).

6.2.3 Foreshock Threshold

It was found that the vast majority of events had a least one point where the Cluster spacecraft was magnetically connected to the bow shock, including some reconnection events used in previous analyses e.g., the event described in *Phan et al.* (2006).

Thus it was not practical to eliminate all events that have at least one point connected to the foreshock. Instead a maximum percentage of connected points was established as a threshold (45%). This was obtained by testing relative values for the foreshock threshold (see Table 6.2 and 6.3, tests 7 to 10).

	T 1	T 2	T 3	T 4	T 5	T 6	T 7
BS	3	3	3	3	3	3	3
SM	1	1	1	1	1	1	1
GP	100	100	100	100	100	100	100
BT	80	80	80	80	80	80	80
GS	5	5	5	5	5	5	5
VT	20	20	20	20	20	20	20
ED 1	5000	5000	5000	5000	5000	5000	5000
ED 2	60	60	60	60	60	60	60
FS	50	50	50	50	50	50	**75**
MV	6	6	6	6	**4**	**8**	6
CD	25	**30**	**50**	**40**	40	40	40
DT	1	1	1	1	1	1	1
Positives	46	38	13	23	25	15	31
Yes	30	27	10	17	17	11	23
No	11	10	3	5	7	3	6
Maybe	5	1	0	1	1	1	2
% Yes	65%	71%	77%	74%	68%	73%	74%
% No	24%	26%	23%	22%	28%	20%	19%

Table 6.2: A table of the tests 1 -7 threshold values and the results on running the algorithm over the 2003 data. The bold type indicates a value has been changed and is the value subject to testing.

6.2.4 Limits for the Duration of Potential Events

The lower limit used in this case is 60 s, as it means that the shortest events will have at least 15 data points within them. A lower limit of 120 s was also tested but it did not improve the ratio of correct positives (test 11, Table 6.3). The maximum time is 1000 s (Test 12), this is much longer than any reconnection event previously reported or found in this study and so should not result in discarding any true events. A value of 5000 s was also initially tested but as the values were so much higher than the event durations there was no difference between the two thresholds.

6.2.5 Ion Velocity Change Threshold

From previous analysis of reconnection in the solar wind we expect exhaust velocity is usually of the order of 20 $km\ s^{-1}$ (*Gosling et al.*, 2005; *Phan et al.*, 2006). Thus we tested the range of 15 $km\ s^{-1} - 25\ km\ s^{-1}$ (Tests 13 and 14, Table 6.3). It was determined that the value of 20 $km\ s^{-1}$ returned the best results and so we set this as the VT threshold.

6.2.6 Gap Size Threshold

The threshold, GS, is set at 5 data points, from the results of tests 15 and 16 on Table 6.4. Test 15, which uses a GS value of 2 points returns significantly fewer events and Test 16, which uses a GS value of 10 returns a lower percentage of false positives, than Test 12 ($GS = 5$ and all other values are the same).

	T 8	T 9	T 10	T 11	T 12	T 13	T 14
BS	3	3	3	3	3	3	3
SM	1	1	1	1	1	1	1
GP	100	100	100	100	100	100	100
BT	80	80	80	80	80	80	80
GS	5	5	5	5	5	5	5
VT	20	20	20	20	20	**15**	**25**
ED 1	5000	5000	5000	5000	**1000**	1000	1000
ED 2	60	60	60	**120**	60	60	60
FS	**25**	**40**	**45**	45	45	45	45
MV	6	6	6	6	6	6	6
CD	40	40	40	40	40	40	40
DT	1	1	1	1	1	1	1
Positives	8	12	17	14	17	19	13
Yes	6	10	14	11	14	15	10
No	2	2	3	3	3	3	3
Maybe	0	0	0	0	0	1	0
% Yes	75%	83%	82%	79%	82%	79%	77%
% No	25%	17%	18%	21%	18%	16%	23%

Table 6.3: A table of the tests 8 - 14 for threshold values and the results on running the algorithm over the 2003 data.The bold type indicates a value has been changed and is the value subject to testing.

6.2.7 Minimum Magnetic Field Rotation Threshold

We have considered the minimum magnetic field rotation thresholds 70°, 80°, and 90°, as shown in Tests 17 and 18 in Table 6.4 (comparing with Test 12 where $BT = 80°$ and all other values are the same). From this it was found that a minimum magnetic field rotation of 80° gave the best results, as a minimum rotation of 70% reduces the percentage of false positives and a minimum rotation of 90% returns fewer candidate events. The magnetic field rotation threshold must be large as smaller thresholds give a much larger percentage of false positives. In previous iterations of the algorithm using rotation thresholds of less than 50° meant that most of the magnetic field data would be flagged up as current sheets and discerning actual reconnection events from the false positives required a visual inspection of the data. As the intention was to create a fully automatic algorithm having a higher rotation threshold was chosen.

6.2.8 Duration over which the Angle Change is Determined

Table 6.4 shows how GP was determined. Comparing the values in Tests 19-25 where the value of GP was between 50 and 200 points respectively it is possible to see the advantage of using the value 100 points as we have a higher number of correct positives, see Test 30. Tests 19 - 22, with GP values < 100 points show a much larger increase in the number of false positives found; reducing the reliability of the algorithm. Tests 23 - 25, with GP values > 100 points also have an increase of false positives and return a lower number of candidate events.

	T 15	T 16	T 17	T 18	T 19	T 20	T 21	T 22
BS	3	3	3	3	3	3	3	3
SM	1	1	1	1	1	1	1	1
GP	100	100	100	100	**50**	**75**	**80**	**90**
BT	80	80	**70**	**90**	80	80	80	80
GS	**2**	**10**	5	5	5	5	5	5
VT	20	20	20	20	20	20	20	20
ED 1	1000	1000	1000	1000	1000	1000	1000	1000
ED 2	60	60	60	60	60	60	60	60
FS	45	45	45	45	45	45	45	45
MV	6	6	6	6	6	6	6	6
CD	40	40	40	40	40	40	40	40
DT	1	1	1	1	1	1	1	1
Positives	7	19	23	8	20	16	12	22
Yes	5	13	14	5	9	12	8	12
No	1	6	8	3	11	3	2	10
Maybe	1	0	1	0	1	1	2	0
% Yes	71%	68%	61%	63%	43%	75%	67%	55%
% No	14%	32%	35%	38%	52%	19%	17%	45%

Table 6.4: A table of the tests 15 - 22 for threshold values and the results on running the algorithm over the 2003 data. The bold type indicates a value has been changed and is the value subject to testing.

6.2.9 Smoothing of the Magnetic Field and Ion Velocity Data

Table 6.5 shows tests for the value of smoothing (Tests 26 and 27). In the final analysis we have set the smoothing value to be 1 (i.e. no smoothing) as many reconnection events were being discarded with higher values for smoothing.

6.2.10 Bowshock Threshold

We tested bowshock values of 2 R_E (Test 28, Table 6.5). It was found that while a threshold of 2 R_E yielded a lot of results there was a much higher percentage of false positives when you compare it with tests in which 3 R_E was used (e.g Test 30). The bowshock threshold was set at 3 R_E.

6.2.11 Minimum Solar Wind Density

A conservative threshold is set at the density of the plasma $n_i = 1$ particle/cm^3 above which ion moments are considered reliable (*Dandouras et al.*, 2015). We did additionally test a threshold of 0.1 particles cm^{-3} (test 29, Table 6.5) but this was found to greatly increase the number of false positives in comparison with Test 30 (*Dandouras et al.*, 2015).

6.3 Limitations of the Algorithm

The strategy of looking for reconnection events in the solar wind with an automated algorithm raises several issues and caveats. The signatures of reconnection in the magnetic field and ion velocity data can be small in comparison to the level of random background fluctuations and, in the case of the ion velocity, very small in

	T 23	T 24	T 25	T 26	T 27	T 28	T 29	T 30
BS	3	3	3	3	3	**2**	3	3
SM	1	1	1	**2**	**5**	1	1	1
GP	**110**	**150**	**200**	100	100	100	100	100
BT	80	80	80	80	80	80	80	80
GS	5	5	5	5	5	5	5	5
VT	20	20	20	20	20	20	20	20
ED 1	1000	1000	1000	1000	1000	1000	1000	1000
ED 2	60	60	60	60	60	60	60	60
FS	45	45	45	45	45	45	45	45
MV	6	6	6	6	6	6	6	6
CD	40	40	40	40	40	40	40	40
DT	1	1	1	1	1	1	**0.1**	1
Positives	13	19	18	11	2	87	72	17
Yes	10	12	12	8	0	49	46	14
No	3	4	4	3	2	37	26	3
Maybe	0	3	2	0	0	1	0	0
% Yes	77%	63%	67%	73%	0%	56%	64%	82%
% No	23%	21%	22%	27%	100%	43%	38%	17%

Table 6.5: A table of the tests 23-30 for threshold values and the results on running the algorithm over the 2003 data. The bold type indicates a value has been changed and is the value subject to testing.

comparison to the bulk solar wind flow. In addition to this, the fluctuations and background noise in the solar wind vary considerably over time, making it difficult to account for. This has meant that strict thresholds often rule out events that may be selected after case by case human analysis.

Additionally we have had to set strict criteria on what we are looking for and what we will accept as a reconnection event, in order to minimise the number of false positive results. This means that we will have selected reconnection events that have a particular set of characteristics and it is possible that this set will not be a completely representative subset of all events. For example, using these thresholds with this algorithm we will not to select any events that rotate less than 80°, although we know these exist (*Phan et al.*, 2010).

The algorithm presented in this chapter is at least a great demonstration of the potential of using an algorithm for automatically finding and analysing events in the solar wind. Development of an algorithm that successfully finds all or a large majority of events whilst also excluding anything that is not an event may require a lot more time and potentially have to incorporate other methods, such as machine learning (e.g., *Colak and Oahwaji*, 2009).

However we can still obtain many valuable results from the event list produced. The event list (Tables B.2 - B.17, Appendix B) contains more than 300 events, and so we can make statistical conclusions about these large events in the solar wind. As these events have a sufficient number of data points to analyse fully they will also be good candidates for any case studies.

6.3.1 Event List Analysis

In this sub-section we consider the event list selected using the algorithm and listed in Appendix B. For each of the events we have determined several characteristics which will enable us to sort the events. For each event we have determined: the average solar wind speed, the average background magnetic field strength, the average solar wind density, the average Alfvén speed, the duration of the event, the temperature increase over the exhaust, the magnetic field rotation and the Exhaust speed (all listed in Appendix B). The magnetic field rotation and the exhaust speed have values that are limited by the algorithm, the magnetic field rotations are a minimum of 80° and the exhaust speeds are greater than 20 $km\ s^{-1}$ by selection.

As we will show later in this Chapter there are often events that appear during periods of unusual solar wind conditions or have features that are very different from the average. In this section we shall 'flag' events which are deemed to have unusual features and test if some of these features are interlinked. For example, we have a few events in our list which occur during periods of very low solar wind speed, some events with a large temperature change, and some events with a unusually high exhaust speed. We flag up each of the individual irregularities. We check whether the same events are flagged up for different conditions, as this could indicate a false positive result. The outlying parameters that we shall flag are as follows:

(a) Solar wind speeds below 250 $km\ s^{-1}$

(b) Exhaust speeds above 200 $km\ s^{-1}$

(c) Temperature changes greater than 2 MK

Outlier type	a	b	c	d	e	f	g
Number of events	11	32	4	8	27	26	30

Table 6.6: The number of the different types of outlier

Total number of outliers per event	0	1	2	3	4
Number of events	245	66	20	8	2

Table 6.7: The number of events with a given number of 'flags'.

(d) Time lags greater than 50 s at the point of maximum correlation (for the magnetic field data in the maximum variance direction) between the Cluster spacecraft.

(e) Maximum correlations (between spacecraft using the magnetic field in the maximum variance direction) of less than 0.5

(f) Current densities over 500 $nA\ m^{-2}$

(g) Number of sheets > 5

Here we have established a list of 7 variables that, if they go beyond a given limit will be considered an outlier. Table 6.6 shows the number of events that were found with each type of outlier. There were 32 events with an exhaust speed of over 200 $km\ s^{-1}$ (outlier b) which is the most populous outlier. There are 4 events with an increase in temperature greater than 2MK, the lowest number of outliers for a characteristic.

From Table 6.7 we see that there are 10 events that have 3 or more flags. However most of the outliers occur singly, i.e., most events that have an outlying characteristic only have one. These events would be good candidates for future case studies.

6.4 Survey Analysis

In this section we analyse the survey results. In Section 6.4.1 we look at the number of events found in each year. In Sections 6.4.2 - 6.4.5 we analyse data relevant to each of the science questions stated at the beginning of this Chapter and in Section 6.5 we discuss the results.

6.4.1 Initial Survey Results

Using the thresholds described in Section 6.2, the algorithm was applied to the Cluster 1 data from 2001 - 2011 inclusive. This produced a total of 341 events that satisfy the criteria and pass all the thresholds. A visual inspection of the data returns the same percentage of correctly identified positives as Test 30. These events are listed in Appendix B. These tables list the start and end time of each of the events selected along with details about each of the event, e.g. the background solar wind speed, magnetic field strength. We will refer back to this list during the rest of this Chapter.

The number of events found per year per relative available data is shown in Figure 6.3. The Cluster spacecraft spends varying amounts of time in the ambient solar wind each year depending on its orbit and thus it is necessary to take into account the amount of ambient solar wind data available from Cluster from each year to make a fair comparison. There is a wide range in the absolute number of events found each year, with 2004, 2007 and 2008 being the most abundant years and 2001, 2003 and 2006 begin the years with the fewest reconnection events. The difference between these more barren years and the most abundant years (in terms of relative reconnection events found) is more than twofold, which suggests that there may be a physical reason why we observe more events at certain times than

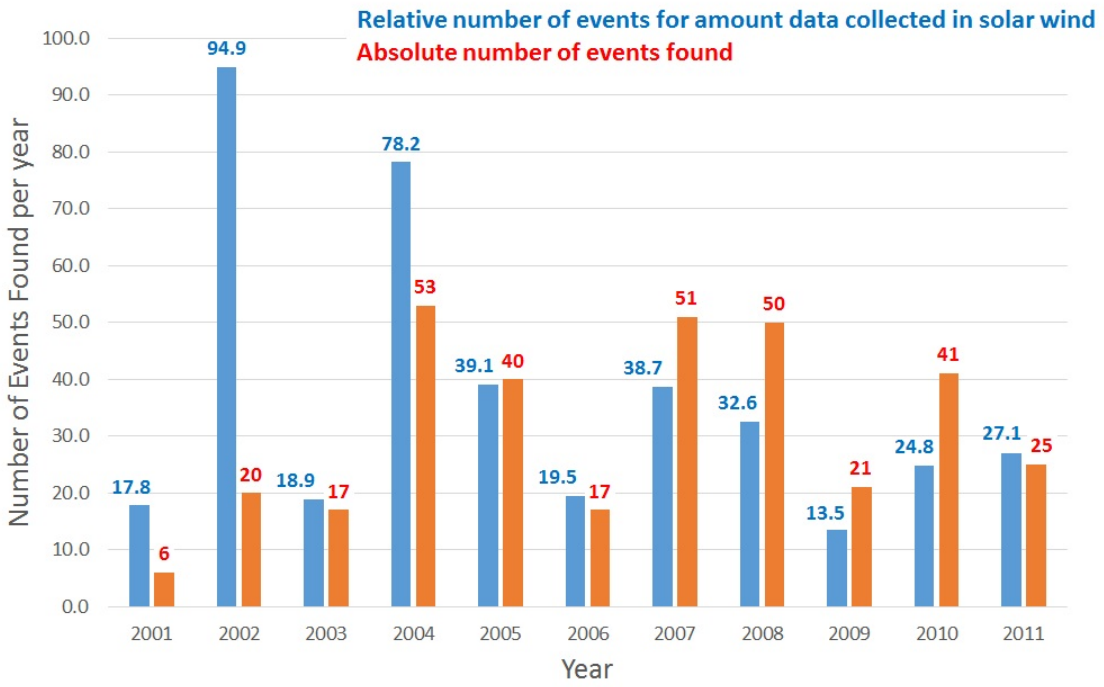

Figure 6.3: The number of reconnection events found each year. The orange data set shows the absolute number of events found in that year, whereas the blue data set shows the amount of events found relative to the amount of time that the Cluster spacecraft spent in the ambient solar wind that year.

others. We also observe that there is a large difference in the number of events found per year after accounting for the amount of time spent in the solar wind. In particular we notice that in 2002 (where there was the least data available) we see a lot of events. In the next section we compare the number of events found per year with some of the solar and solar wind parameters e.g. solar activity (as represented by average yearly sunspot count), solar wind speed, solar wind density, interplanetary magnetic field strength, and also distance of the Cluster spacecraft from Earth. We test the data set for any possible correlations between the variables.

6.4.2 What are the Typical Solar Wind Conditions of Reconnection Events?

The first science question that we consider is 'What are the typical solar wind conditions during magnetic reconnection events?'. In particular we consider whether some solar wind conditions are more conducive to magnetic reconnection events than others. There have been a few previous studies that have considered the dependence of solar wind reconnection on the surrounding plasma conditions (e.g. *Phan et al.* (2010)). Our study is both large in scale as we have a large number of events (341) and spread over a large timespan (over 10 years) and thus we can be confident about the validity of the results.

In this section we present the yearly trends of solar wind variables and whether there is a correlation between them and the number of events found that year. We look for correlations between the values of the average solar wind velocity, average magnetic field strength, average solar wind density and average Alfvén speed within the selected events and compare the distributions of these variables with the average distributions for these variables in the solar wind. We look at the distribution of the size of the magnetic field rotations, the exhaust speeds and the maximum value for current density over each of the selected events.

As shown in Figure 6.3 there is a big difference between the maximum number of reconnection events found in a year (53, 2004) and the minimum number found in a year (6, 2001). We first consider the long term variability of solar wind conditions (e.g. over the solar cycle) as a possible explanation for the varying event numbers in different years.

We determine the average values for the solar wind characteristics as seen by the Cluster spacecraft during its time in the pristine solar wind. The data is taken

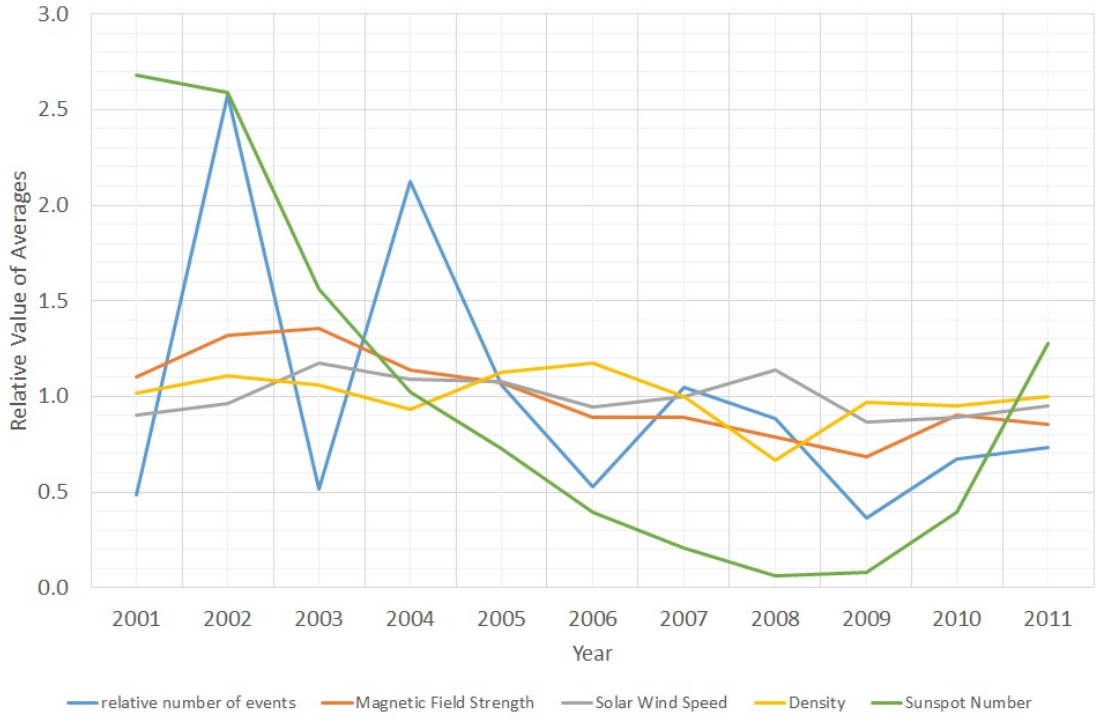

Figure 6.4: A graphs showing the yearly trends of the variables: Number of events per year per available data, average magnetic field strength, average solar wind speed, average density and the yearly average sunspot number. The relative average is the yearly average/total average.

during periods of time where the Cluster spacecraft is outside the bowshock as determined by *Chao et al.* (2002) with a margin of error of 4 R_E. We take an average of the magnetic field strength, the solar wind speed and the solar wind density for each year using data. Additionally we obtain the yearly average sunspot numbers (SILSO: Sunspot Index and Long-term Solar Observations).

Figure 6.4 shows the relative value of averages over the number of reconnection events each year (light blue), the average background magnetic field strength (red), the average background solar wind speed (grey), average background plasma density (yellow), and the yearly average sunspot number (green) for the years 2001 - 2011. In this case the 'relative value of the average' is the average for that year divided by the average of all the years combined.

Figure 6.5 shows the formal correlation between the number of events per

Parameter	R	p-value	Significant?
Magnetic Field Strength	0.509	0.11	No
Solar Wind Speed	0.210	0.54	No
Density	0.067	0.84	No
Sunspot Number	0.362	0.27	No

Table 6.8: Table of statistical significance of yearly average correlations

year per available data and the following variables: yearly average magnetic field strength, yearly average solar wind speed, yearly average density and yearly sunspot average. In order to determine whether these correlations are statistically significant we will consider the statistical test; the p-value, which we will determine using the Pearson (r) score and the number of points. We will consider p values of < 0.05 to be statistically significant. A p-value of 0.05 means that there is only a 5% probability that a given correlation could have occurred by chance if the values were not correlated. Table 6.8 shows the R, and p values of each of the 4 correlations and whether the correlation statistically significant. The n value is always 11 as this is the number of years we are testing.

In Figure 6.5 the top two panels show the magnetic field strength, and the the solar wind velocities, and the bottom two panels show solar wind densities and the yearly average sunspot number respectively. Each of these figures show only extremely weak correlations. The correlations of the number of events with these variables were not found to be significant, shown in Table 6.8.

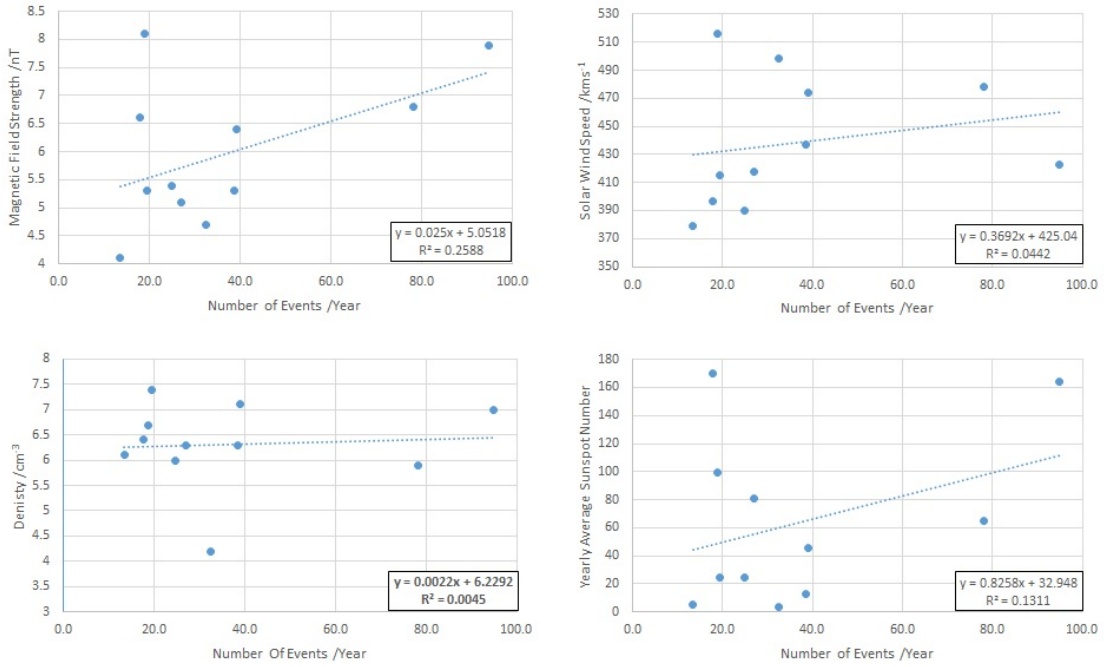

Figure 6.5: Correlation between the number of events per year per available data and yearly average magnetic field strength (top left), yearly average solar wind speed (top right), yearly average density (bottom left) and the yearly average sunspot number (bottom right).

We now consider solar wind characteristics that were occurring during the reconnection events found by the algorithm. Figure 6.6 shows a set of 4 histograms detailing the average values of solar wind speed, magnetic field strength, plasma number density and the Alfvén speed during each event. The solar wind speed shows a distribution around the solar wind speed mean of $491 \pm 137\ km\ s^{-1}$. The magnetic field strength ranges from 3nT to approximately 36nT with the majority of events occurring at a background magnetic field of $8.1 \pm 4.8\ nT$ where 4.8 nT is one standard deviation. The plasma densities during the events are predominately small, the majority (68%) of events occur when the solar wind density is 5.5 ± 5 particles cm^{-3} where 5 particles cm^{-3} is 1 standard deviation. The final panel shows a histogram of the Alfvén speeds over each of the events. As there is a wide spread ($\sim 20 - 500\ km\ s^{-1}$) in the maximum and minimum Alfvén speed the figure also shows a zoom in on the speeds between $0 - 150\ km\ s^{-1}$. The Alfvén speeds have a mean of $97 \pm 85\ km\ s^{-1}$, but there are a few events with Alfvén speeds up to 500 $km\ s^{-1}$.

Figure 6.7 shows the scatterplots and correlations between the 4 variables solar wind speed, magnetic field strength, density and Alfvén speed. The top two panels show magnetic field strength vs wind speed and density vs wind speed respectively. For both of these panels the R value is very low ($|R| < 0.2$) which suggests that the correlation between the variables is very weak. This is to be expected as these variables are not known to be dependent on each other in any way.

In the bottom left panel it appears that there are two populations the Alfvén speeds at low solar wind speed are highly variable and Alfvén speeds relating to solar wind speeds greater than 350 $km\ s^{-1}$ appear to show a very weak slightly positive correlation, though the R value is very low ($R = 0.1$). The line of best

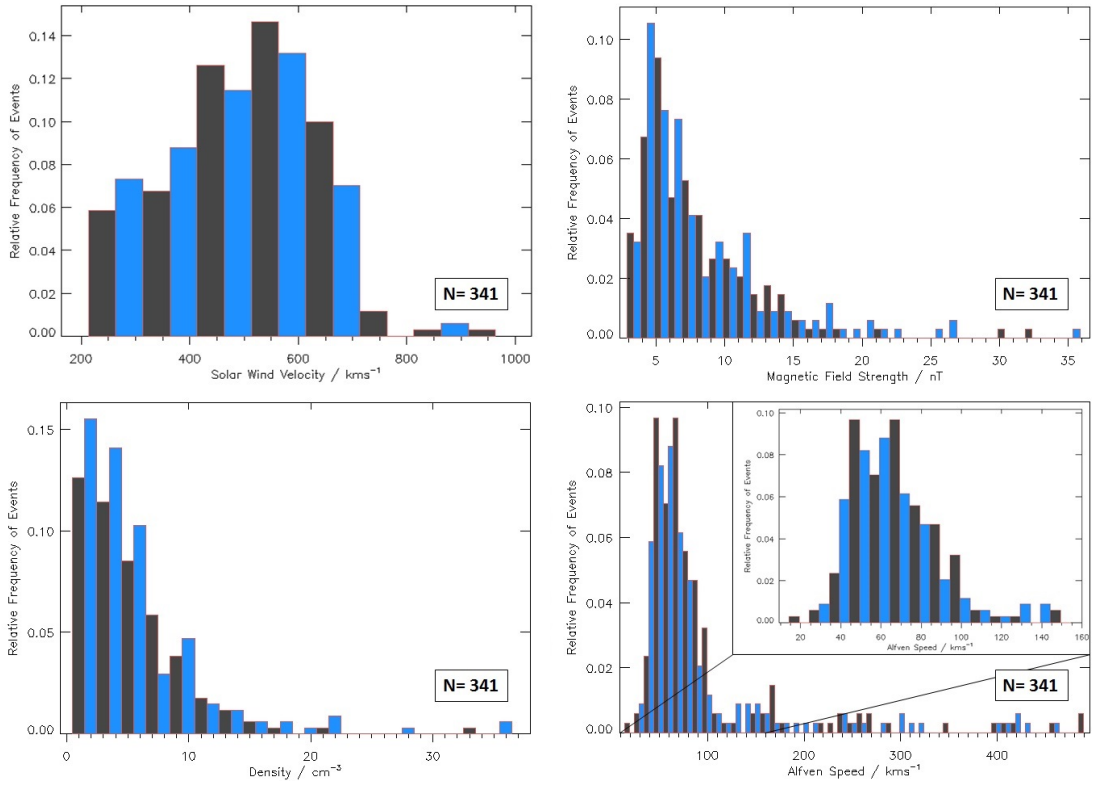

Figure 6.6: The four panels show histograms of some of solar wind averaged parameters during the selected reconnection events. The top left shows a histogram of background solar wind speed (bin size 50 $km\ s^{-1}$), the top right panel shows the overall magnetic field strength over the event (bin size 0.5 nT), the bottom left shows the average number density of the plasma during these events (bin size 1 particle $cm^{-}3$) and the bottom right panel shows the average Alfvén speed of each event (bin size 5 $km\ s^{-1}$). The inset in the Alfvén speed histogram shows a zoom in between $15 - 150\ km\ s^{-1}$, it has a binsize of 5 $km\ s^{-1}$.

fit for the bottom left panel only includes the data where the solar wind speed is $> 350\ km\ s^{-1}$. What gives rise to these two separate populations? The two parameters that Alfvén speed are dependent on is the magnetic field strength and the ion density. Observing the top left hand panel, it can be observed that the magnetic field strength at solar wind speeds lower than $400\ km\ s^{-1}$ is more variable than at higher solar wind speeds. Whereas the density is lowest and least variable at solar wind speeds below $400\ km\ s^{-1}$. This means that the Alfvén speed at solar wind speeds below $400\ km\ s^{-1}$ will be on average higher (due to the low plasma density) and more variable (due to the most highly variable magnetic field strength). The bottom right panel shows the average solar wind density vs magnetic field strength. Here $R = 0.305$ and $n = 341$ which gives us $p < 0.05$ and so this has a statistically significant weak positive correlation. It also appears that the spread in the density is larger with greater field strength.

We also compare the solar wind conditions during our events, shown in Figure 6.6, with the average solar wind conditions encountered by the Cluster spacecraft.

First comparing the solar wind speed, we note that the average of the distribution of the pristine solar wind speed ($438\ km\ s^{-1}$) is slightly lower than that of the selected reconnection events (average: $491\ km\ s^{-1}$). The spread of data is slightly wider in the selected events (standard deviation: $137\ km\ s^{-1}$) than in the pristine solar wind ($108\ km\ s^{-1}$). We also note that there appears to be a disproportionately high number of events in the slow solar wind than is expected given the fraction of the time that Cluster spends in the slow solar wind. The average magnetic field strength for the selected reconnection events is much higher and with a wider spread ($8.1 \pm 4.8\ nT$) than the distribution of magnetic field

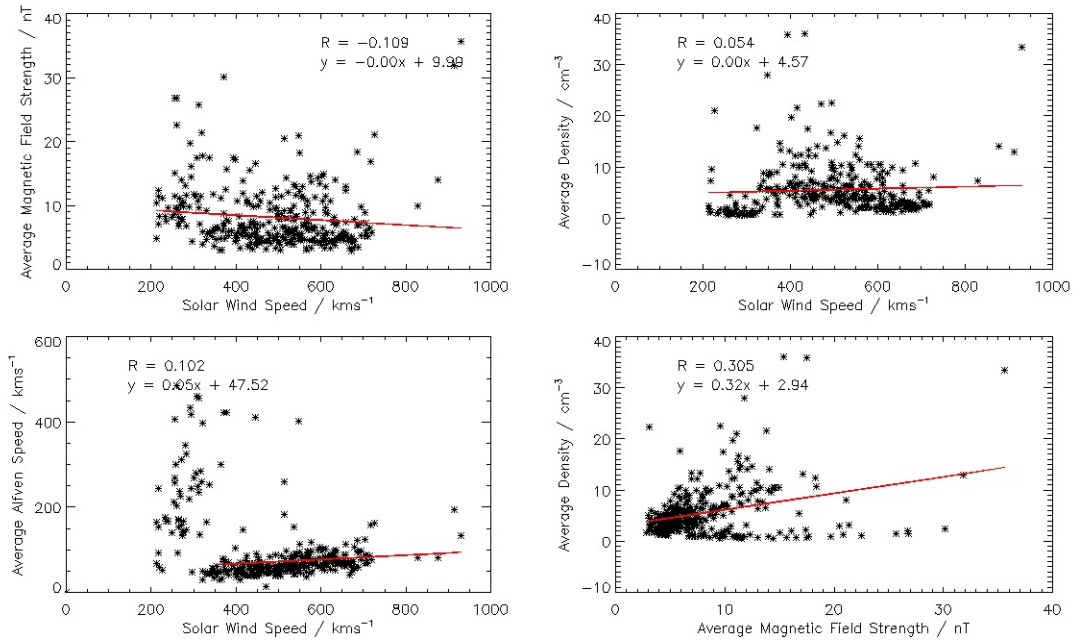

Figure 6.7: Correlations between the basic solar wind parameters: Solar wind speed, magnetic field strength, density and Alfvén speed. Each panel includes a linear line of best fit, the equation of the line of best fit and it's R value. The bottom left panel, which contains the correlation between the average Alfvén speed and the solar wind speed shows the line of best fit for the solar wind speeds $> 350\ km\ s^{-1}$.

strengths in the pristine solar wind ($5.34 \pm 3.0\ nT$). The density graphs have very similar averages and spreads for the selected reconnection events and the pristine solar wind (5.5 ± 5.0 particles cm^3) and (6.0 ± 4.4 particles cm^3). The bottom right panel of Figure 6.8 shows the distribution of Alfvén speeds in the pristine solar wind (average: 76 $km\ s^{-1}$, standard deviation 49 $km\ s^{-1}$) has a lower average and narrower spread than the selected events (average: 97 $km\ s^{-1}$, standard deviation 85 $km\ s^{-1}$).

We now compare the results of the correlations of the solar wind parameters at the reconnection events (shown in Figure 6.7) with the same correlations for the ambient solar wind values (shown in Figure 6.9). While the range of values for each of the parameters in the ambient solar wind is larger than that of the solar wind conditions found during the reconnection events, the shapes of the graphs are

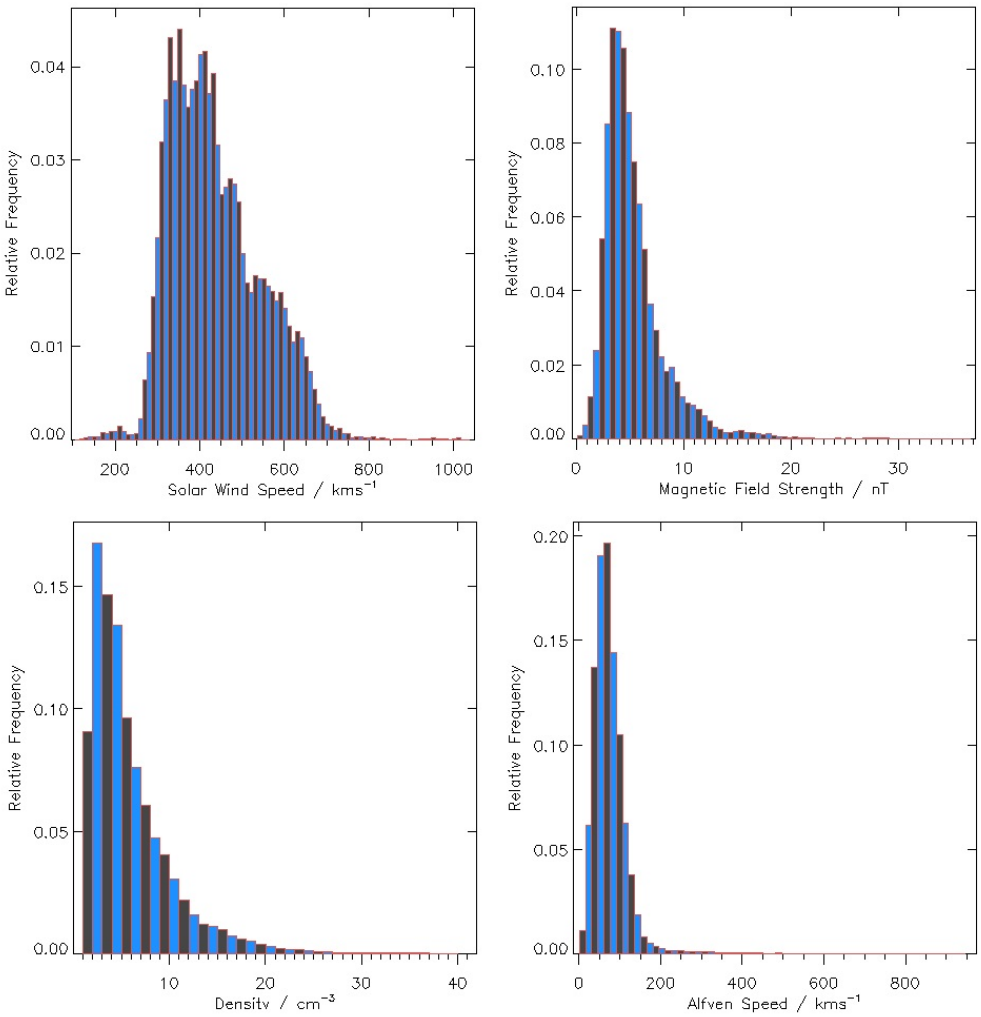

Figure 6.8: The average solar wind conditions over the period of time that Cluster was in the pristine solar wind between January and April between 2001-2011. Solar wind speed (top left, binsize: 15 $km\ s^{-1}$), Magnetic field strength (top right, binsize: 0.5 nT), density (bottom left, binsize: 1 particle cm^{-3}), Alfvén Speed (bottom right, binsize: 15 $km\ s^{-1}$).

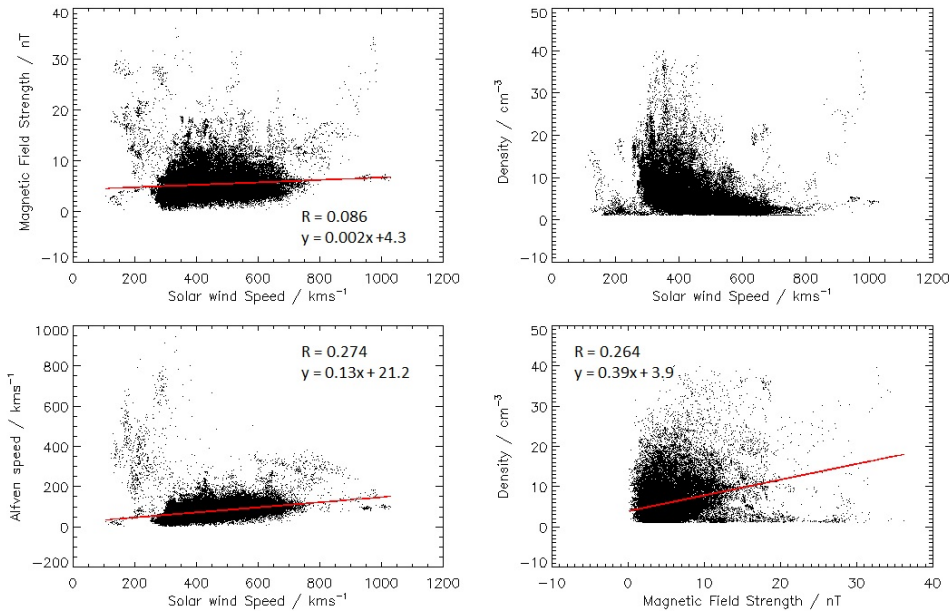

Figure 6.9: Correlations between the ambient solar wind parameters; solar wind speed, magnetic field strength, density, Alfvén speed. All but the top left panel (showing solar wind speed vs. density) include a linear line of best fit, the equation of the line of best fit and its R value.

very similar. The panel of particular interest here is the bottom left panel showing Alfvén speed vs the solar wind speed. The ambient solar wind shows the same high variation of Alfvén speeds in low solar wind speed plasma as was seen in the reconnection solar wind conditions suggesting that this population is part of the normal solar wind. Similarly the bottom right panel showing the B populations; a constant very low density population and another population that has a very weak correlation with magnetic field strength.

The overall distribution of magnetic field rotations within the selected events is shown in Figure 6.10. This is the rotation in the magnetic field from the start to the end of the event. The magnetic field rotations in the selected events have an average of $148 \pm 21\ nT$. From the algorithm the magnetic field rotation over an event must be a minimum of 80°. This means that for this study we will be omitting any events with a smaller rotation which we know exist (*Phan et al.*,

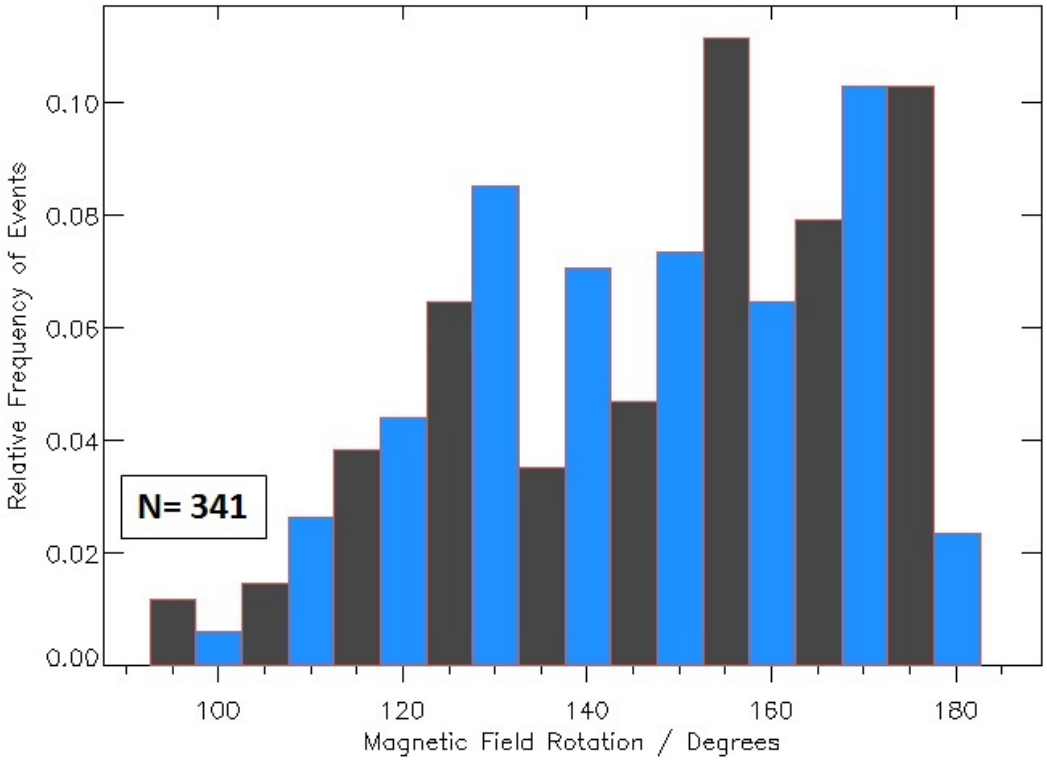

Figure 6.10: The distribution of magnetic field rotations over the duration of the selected events (bin size: 5°). The algorithm applies a cutoff threshold and so no events with a magnetic field rotation $< 80°$ are selected.

2010).

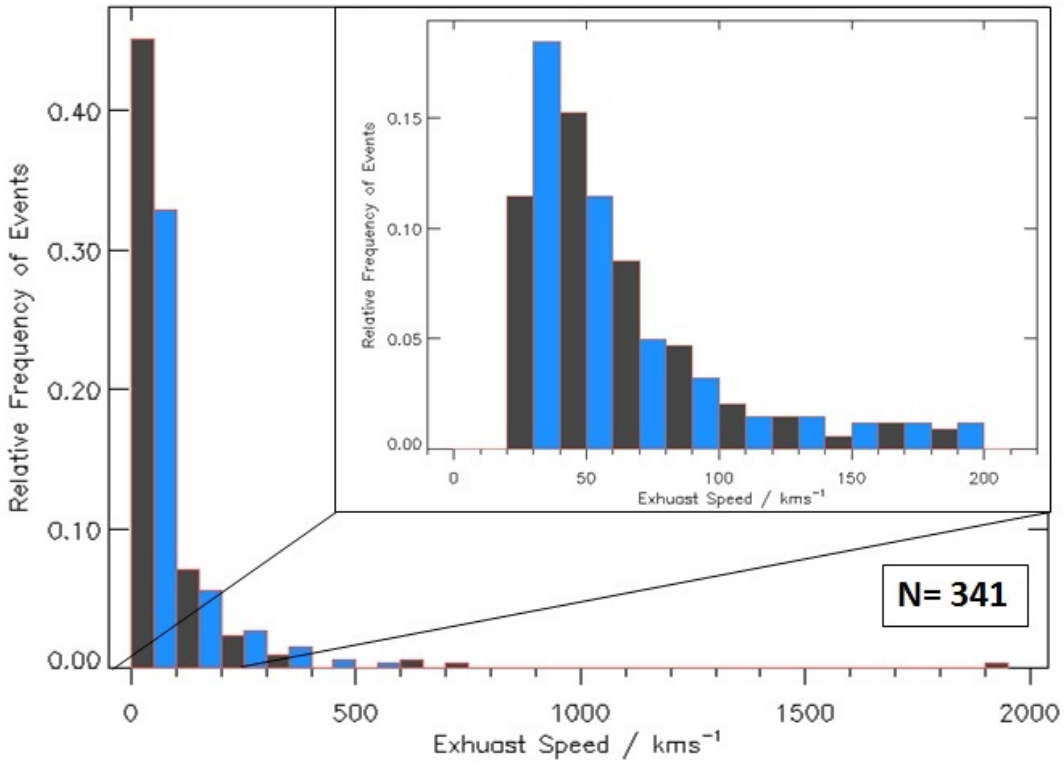

Figure 6.11: The distribution of peak exhaust speeds of each of the selected events. The main panel shows all the selected events which have a peak exhaust speed ranging from $20 - 2000\ km\ s^{-1}$ (bin size: $50\ km\ s^{-1}$). The zoom in plot shows exhaust speeds between 0 and $200\ km\ s^{-1}$. The algorithm does not select events with a peak reconnection exhaust speed that is $< 20\ km\ s^{-1}$.

The distribution of the peak speed of the reconnection exhaust found during each of the events is shown in Figure 6.11. The main panel shows all of the exhausts which are all below $500\ km\ s^{-1}$ with the exception of 5 events. The event with an outflow measured at $\sim 2000\ km\ s^{-1}$ is unlikely to be a reconnection exhaust. The zoom in panel shows the same data for peak exhausts speeds between 0 and $200\ km\ s^{-1}$. The mean peak speed is $94\ km\ s^{-1}$ and the standard deviation is $139\ km\ s^{-1}$. This is approximately as expected as the mean of the Alfvén speeds is very similar ($97\ km\ s^{-1}$). The algorithm only selects events with a peak speed of at least $20\ km\ s^{-1}$. In the next section we will discuss in more detail the energy budget of the outflow exhaust.

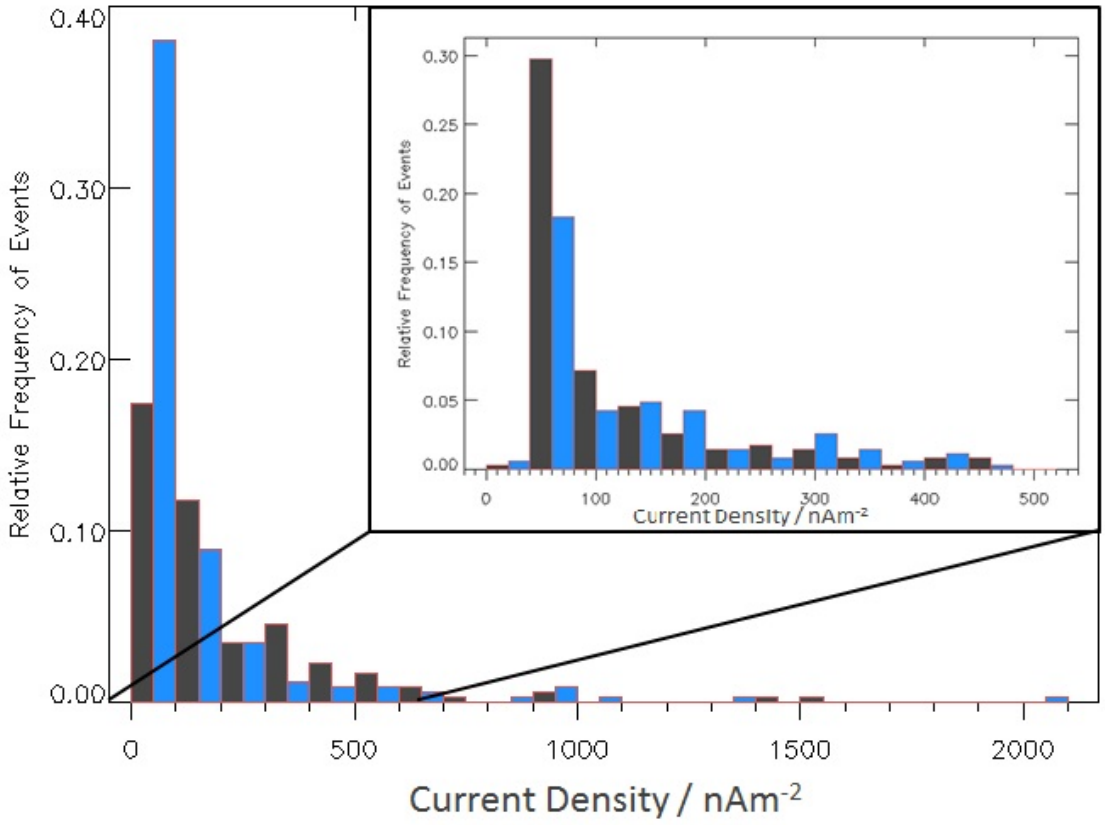

Figure 6.12: The figure and insert showing histograms of the distribution of maximum current densities of the selected events. The zoom window shows the events with maximum currents densities below 500 $nA\ m^{-2}$. The bin size for the main graph is 50 $nA\ m^{-2}$, for the zoom in graph 20 $nA\ m^{-2}$.

For each event the maximum value for the current density is also recorded. The maximum current density that occurs during the selected events is shown in Figure 6.12. There are a couple of instances where the current density is very high and so there is a zoom window to highlight the more typical range below 500 $nA\ m^{-2}$.

6.4.3 What Determines the Outflow Exhaust Speed?

In this section we compare the speed of the exhausts with that predicted by theory (*Parker*, 1963; *Petschek*, 1964) and measured observationally (*Sonnerup et al.*, 1981; *Phan el al.*, 2013). We also use our statistical survey to consider the nature of energy partitioning in the exhaust. We use our event list to make a comparison between observations and theory, to try and determine how the energy of the inflow exhaust is distributed in the outflow.

The Sweet-Parker reconnection picture predicts an outflow speed that is approximately equivalent to the Alfvén speed. Thus determining the speed at which the Alfvén waves will propagate along the boundary (the separatrix), essentially allowing the reconnected magnetic field lines to recoil away from the reconnection site. Away from the ion diffusion region, the plasma is frozen-in to the magnetic field and is carried along with it, hence, in theory, the plasma also travels at the Alfvén speed (*Parker*, 1963; *Petschek*, 1964).

Previous observational studies have shown however that this is not necessarily the case. For example *Gosling et al.* (2006b) studied reconnection events observed by the Helios spacecraft and found that the reconnection exhausts, while the same order of magnitude as the Alfvén speed, tended to be approximately $0.75V_A$ on average. This means that we must also consider that the energy available to release by reconnection does not all necessarily go into kinetic energy of the exhaust. Thus we will also explicitly consider whether some of the energy is directed into heating the exhaust plasma.

The main source of energy that we consider is the exterior magnetic field. The Alfvén speed in the exterior region gives us an idea of how much magnetic energy density is available to accelerate particle populations of a given number

density n. If a particle population trapped in a reconnection process is accelerated to the Alfvén speed this means that all the available magnetic energy has been converted to kinetic energy, as is shown in Equations 6.10, 6.11, where V_a is the Alfvén speed, B is the inflow magnetic field strength, ρ is the plasma density, μ_0 is the permeability of free space, n is the number of particles and m is the particle mass. Equation 6.11 shows that the kinetic energy (we are assuming that, in the rest frame of the solar wind, the particles have 0 kinetic energy) of a particle population of number density n, travelling at the Alfvén speed is equal to that of the magnetic energy in a cubic meter. Thus in this study we shall compare the exhaust speed with the Alfvén speed, in order to determine the percentage of energy converted to kinetic energy.

$$V_A = \frac{B}{\sqrt{\rho\mu_0}} = \frac{B}{\sqrt{nm\mu_0}} \tag{6.10}$$

$$\frac{1}{2}mV_A^2 * n = \frac{B^2}{2\mu_0} \tag{6.11}$$

Figure 6.13 shows the ratio of the exhaust speed over the Alfvén speed for all our selected events. From previous analysis (*Parker*, 1963; *Petschek*, 1964) we would expect that the range would be approximately between 0 and 1 (as theory predicts that the maximum outflow speed should be comparable to V_A). However we find that there is a wide range of V/V_A estimates which range between 0 and 10. The distribution has a mean of 1.04 and a median of 0.80. Thus we find $\sim 70\%$ of the reconnection events in our survey have an outflow speed that is less than the Alfvén speed.

Whilst the majority of reconnection events have ratios that are below 1 there is a significant number (30%) where the ratio is higher. Much of this may be due to errors in the determination of the Alfvén speed. A correct determination of Alfvén speed is dependent on correct measurements of the ion density and magnetic field

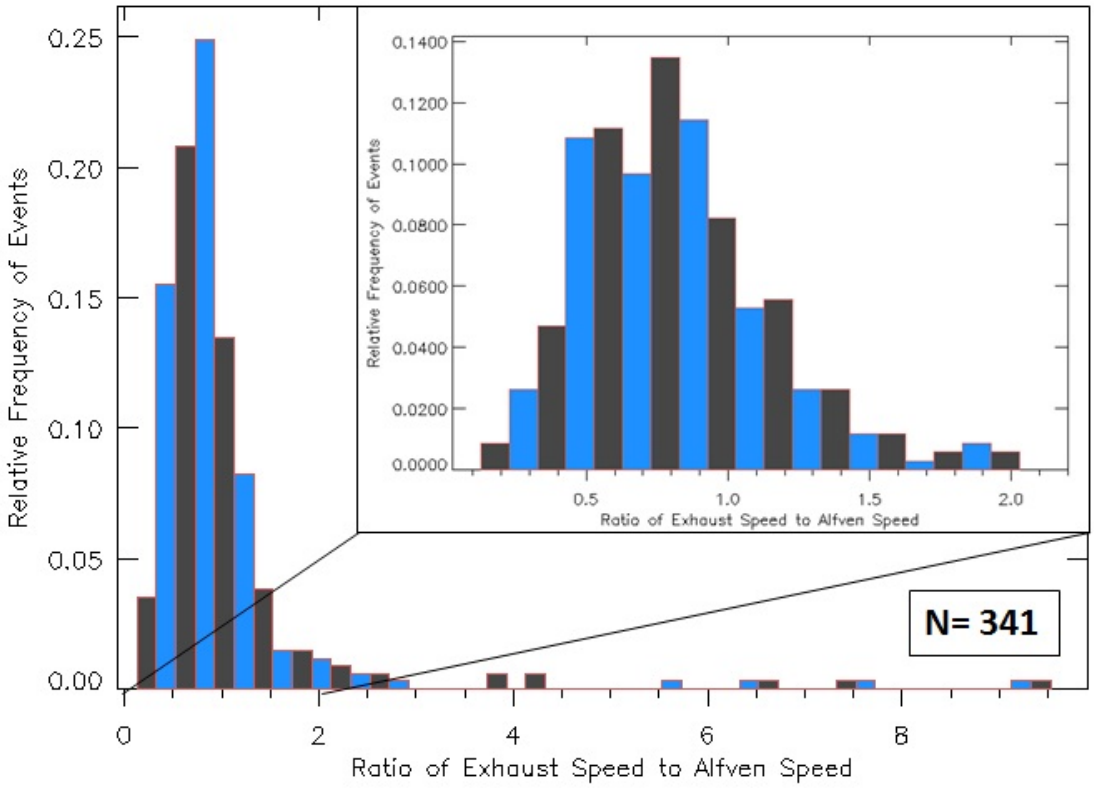

Figure 6.13: The distribution of the ratio of the reconnection exhaust speed over the Alfvén speed. The large graph shows the full range and the zoom shows the range between 0 - 2.0. The bin size for the main graph is 0.2 and for the zoom in graph it is 0.1.

strength, thus small errors in these measurements will lead to errors in the Alfvén speed measurements. However there are more reconnection events with a ratio above 1 than would be likely due to identification error alone. Some of these reconnection events found have solar wind conditions that are outside the 'normal' range, for instance there are examples of reconnection events occurring in very low solar wind speed.

During reconnection, magnetic energy is transferred to exhaust kinetic energy, but, as many events do not have a 100% conversion of magnetic energy to plasma kinetic energy, there may also be heating of the plasma. Thus we now consider whether the plasma in the reconnection exhaust is heated, i.e. whether there is a increase in temperature observed during the reconnection exhaust.

Figure 6.14 shows the maximum temperature change between the temperature in the exhaust and the temperature of the background plasma. The majority of events show very little temperature change, and are therefore clustered around the 0 mark.

Most of the temperature changes shown in Figure 6.14 are within the range expected in the solar wind (the average solar wind temperature is approximately $0.35 \pm 0.31\ MK$ during the periods where Cluster are in the solar wind). There are two instances of temperature changes over 5 MK one of which corresponds to a fast exhaust of ($> 200\ km\ s^{-1}$). Given that the temperature range in the solar wind found by Cluster is between 0-2 MK, we have flagged these points in the event list in Appendix B.

The average and the mode change in temperature during the exhaust is zero and the temperature measurements show both slight heating and cooling. Thus there is no evidence that the energy is going into plasma heating. Slight fluctuations in

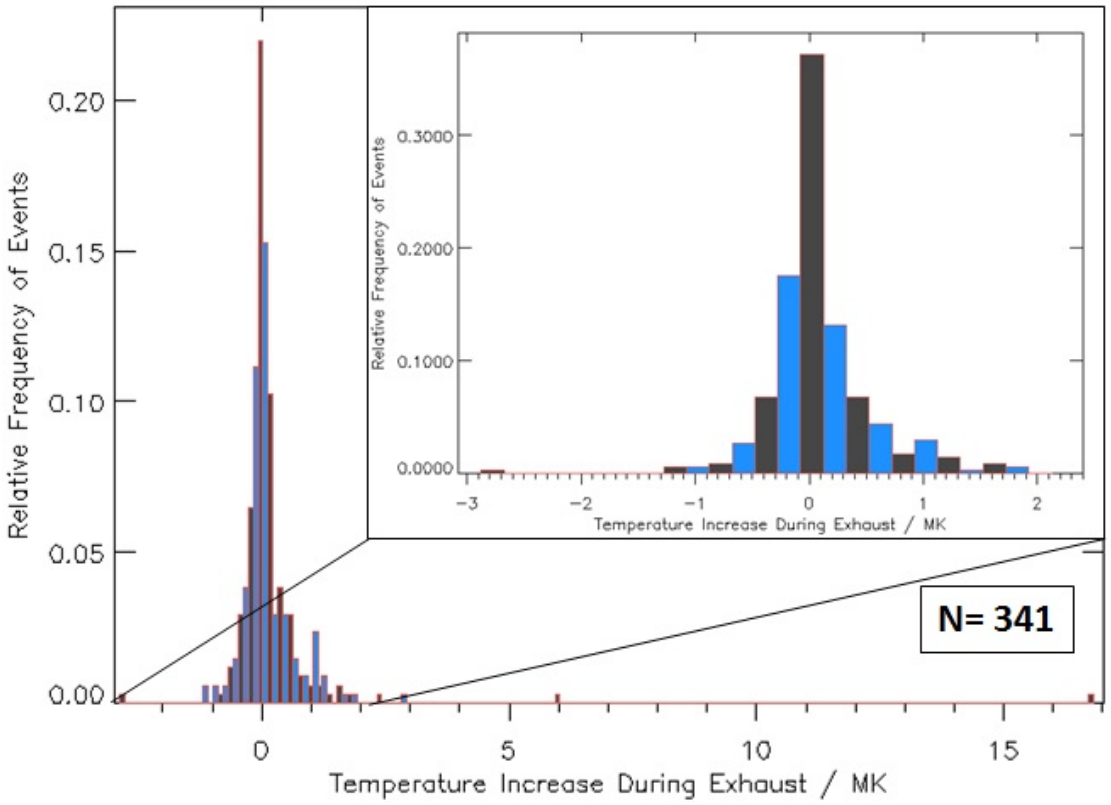

Figure 6.14: The change between the background temperature and the temperature during the exhaust. The main panel shows all the data with a binsize of 0.01 MK and the zoom in shows the range between $-3-2.5$ MK with a binsize of 0.02 MK.

the temperature along with any errors in temperature measurements could account for the events with small temperature changes. It must also be noted that the Cluster spacecraft is most likely sampling exhaust plasma which is remote from the reconnection site and so the background conditions may be different, leading to observations that are not necessarily consistent with what is occurring at the reconnection site.

6.4.4 Structure of Reconnection Current Sheets in the Solar Wind

Previous models and studies of reconnection have suggested a range of possible configurations for current sheet structure. For example, early idealised reconnection pictures are of a single reconnecting current sheet (e.g., *Parker*, 1963). However in the solar wind the reconnection picture is of a bifurcated current sheet structure with an exhaust directed between the sheets (e.g., *Gosling et al.*, 2005). In the context of the magnetopause there are observations of up to 5 discontinuities (*Heyn et al.*, 1985) and in Chapter 5 we discussed how reconnection events with different inflow characteristics could give rise to reconnection with structures of up to 5 current sheets. In this section we determine how many distinct current sheets can be identified in the solar wind reconnection events in our survey database. In this section we want to compare the structures that we have found from the statistical analysis with the list of possibilities that we discussed in Chapter 5 (see Figure 5.2).

Figure 6.15 shows the distribution of the number of current sheets found in each event in our database. These current sheets have been visually determined from the data. The > 5 sheet events are those that seem to have a number of waves in the event and thus it is difficult to determine what is a current sheet and what is a wave.

Figure 6.15 shows a predominance of events with a single current sheet, which make up more than half of the selected events. There are also many events that have a 2 and 3 current sheet structure. Relatively few events have 4 or 5 current sheets. Within the events that have one current sheet there are some events where there appears to be one current sheet that traverses over the spacecraft very slowly,

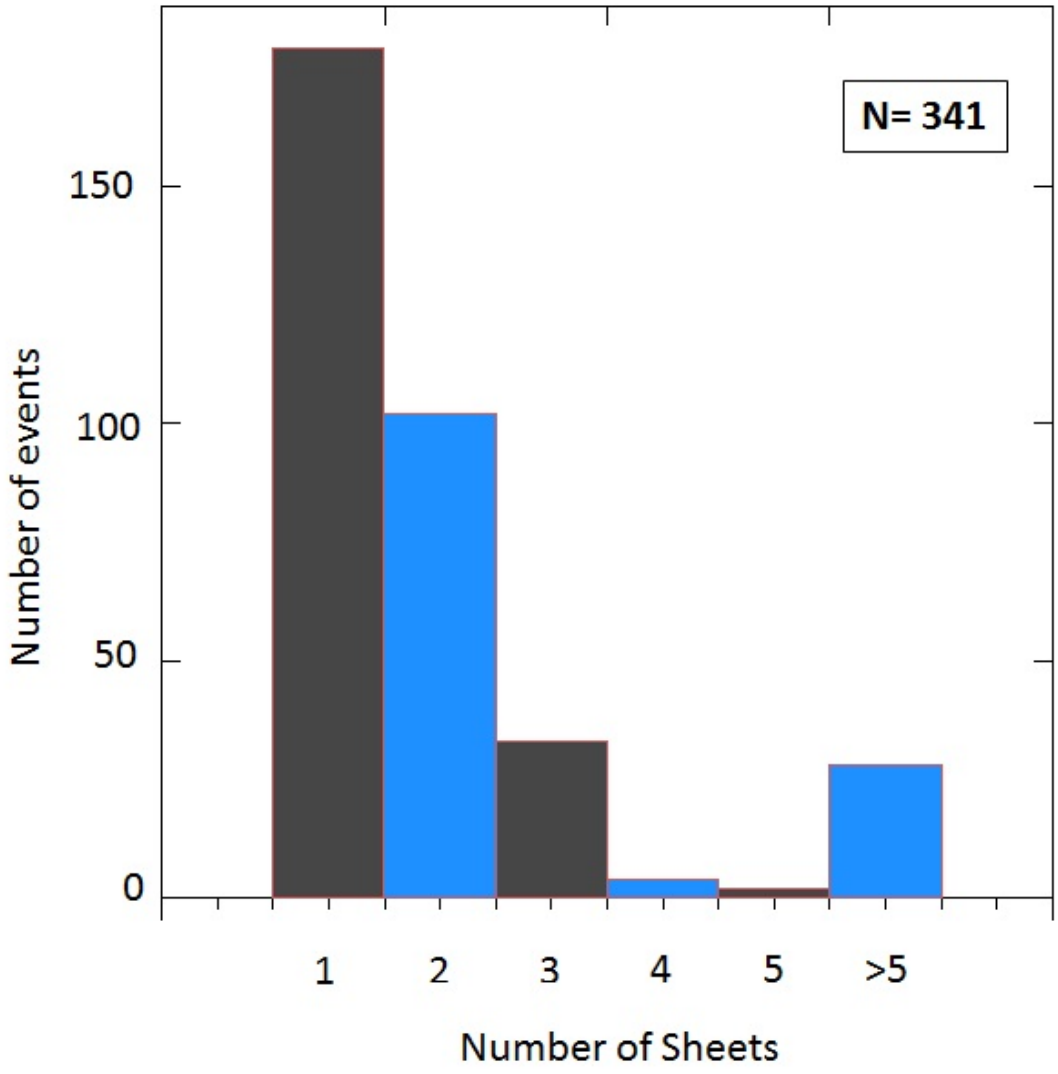

Figure 6.15: Histogram of the number of current sheets found in each event.

rather than the more typical events where the sheets appear as very sharp rotations in the magnetic field.

It must be noted that the number of identified current sheets are a minimum value within the event as the temporal resolution of 4s may not be small enough to pick out the smallest sheets that occur. For example at least 6 points are needed in order to identify a set of 3 current sheets which (for 4s resolution data) is a timespan of 20 s.

As an aside we now present the findings of some case studies made using the above statistical analysis of current sheet structure in reconnection events. We compare our theoretical model in Chapter 5 (see Figures 5.2 and 5.3) with event case studies which have been identified as 3, 4 and 5 current sheet structures.

Initially we will consider those events with 3 current sheets which can be compared with panels (iii) and panel (v) in Figure 5.3, which shows possible magnetic field and ion outflow exhaust structures for reconnection events. There are 5 possible points where magnetic field rotations could occur (labelled A, B, C, D, and E), with various outflows possible in the regions between B and D. For the example in panel (iii) it is possible for the exhaust to be either between B and C (as it is shown in the figure), or between C and D. We name the three possible structures as structure χ (for panel (iii) with the exhaust between B and C, and current sheets at B, C, and D) structure ϕ (for panel (iii) with the exhaust between C and D, and current sheets at B, C, and D), and structure ω (for panel (v) with an exhaust between B and D, and current sheets between B, C, and D).

Table 6.9 shows the number of events in each of the above categories. There were examples for each of the types of structures. The structure in which there were reconnection exhausts between all 3 current sheets were found to be the most

likely structure, however there were also many events that had an exhaust between only two of the current sheets. An example of each is shown in Figure 6.16.

In Figure 6.16 we show two examples of the magnetic reconnection structures that were described above. Each figure shows the magnetic field in GSE components with the current sheets highlighted in the yellow boxes on the top panel (with the x direction in red, the y direction in green, and the z direction in blue), and the ion velocity in the bottom panel (also in GSE co-ordinates), with the reconnection exhaust(s) highlighted by the yellow boxes.

Figure 6.16a) shows an example where the reconnection exhaust is directed between only two of the three current sheets and Figure 6.16b) shows an example where there is an exhaust between all the current sheets, where the exhausts are similar in strength and direction.

Figure 6.16a) shows the three current sheets indicated by the magnetic field rotations in predominately the x direction. The bottom top panel shows a clear increase in ion velocity ($\sim$ 30 $km\ s^{-1}$) in the x direction between the first two current sheets.

Figure 6.16b) shows the three current sheets highlighted are predominately shown by rotations in the y direction of the magnetic field. The increase in ion velocity is ($\sim$ 50 $km\ s^{-1}$) in the y direction and ($\sim$ 20 $km\ s^{-1}$) in the z direction. The ion velocity conditions on either side of the exhaust are different with a higher speed (an increase of approximately 20 $km\ s^{-1}$) on the trailing edge.

There are a few reconnection events that exhibit more complex structures and have 4 or 5 current sheets within the event. Figure 6.17 is the same structure as Figure 6.16 and shows a event that has 4 current sheets highlighted by the yellow boxes in the top panel. In the bottom panel we see that there are two

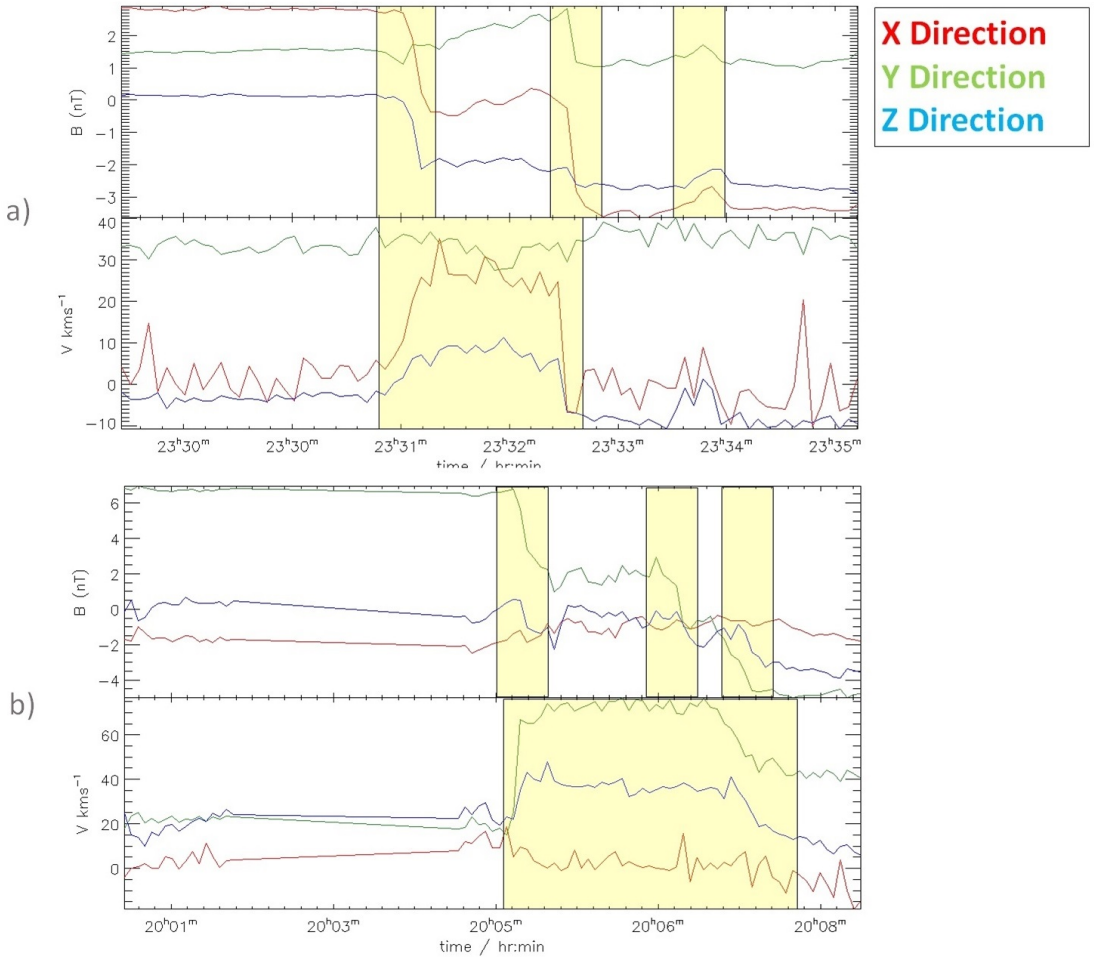

Figure 6.16: Two examples of magnetic reconnection events with 3 current sheets. In each of the figures the top panel shows the magnetic field data in the GSE co-ordinate system with the x direction in red, the y direction in green and the z direction in blue, the yellow panels highlight the presence of current sheets. The bottom panel shows the ion velocity in the same co-ordinate system, the yellow panels indicate the reconnection exhausts. In Figure a) the reconnection exhaust is located between the first two current sheets. In Figure b) the magnetic reconnection exhaust appears as an approximately constant speed encompassing all 3 sheets. In order to view the change in ion velocity in each component on the same graph we removed the background V_x.

Type of structure	χ	ϕ	ω equal	ω unequal
Number of events	3	4 (5)	2	7

Table 6.9: How the magnetic reconnection events that have 3 current sheets are structured. χ represents a panel (iii)-like structure with the exhaust between B and C, and current sheets at B, C, and D, ϕ represents a panel (iii)-like with the exhaust between C and D, and current sheets at B, C, and D, and ω represents a panel (v)-like structure with exhaust between B and D, and current sheets between B, C, and D.

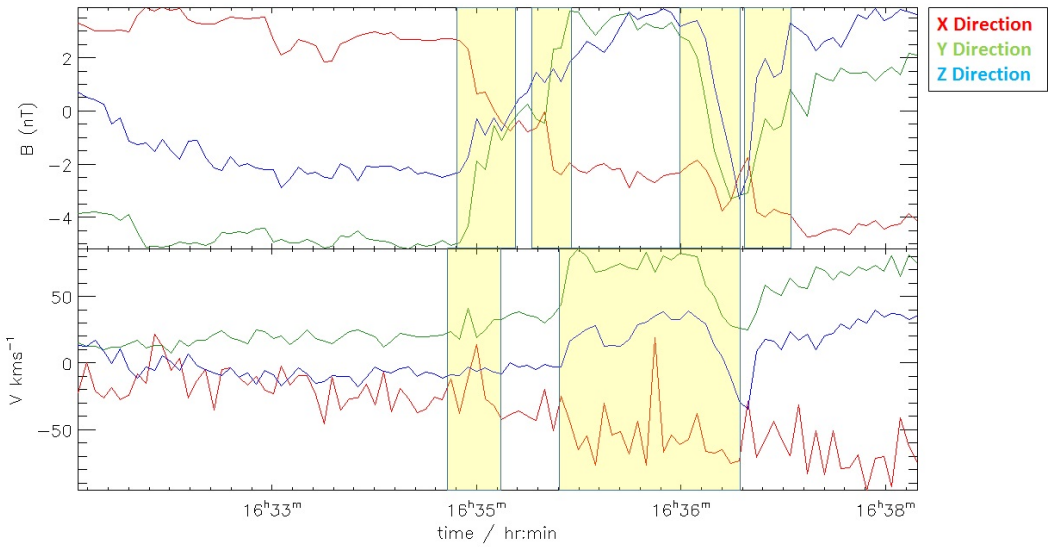

Figure 6.17: An example of a magnetic reconnection event with 4 current sheets. In this case the reconnection exhaust is split into two jets (highlighted in the bottom panel). In order to view the change in ion velocity over the event we have removed the background velocity in the X direction.

instances where the ion velocity deviates from the background. The first instance is coincident with the first highlighted current sheet and the second is between the second and third current sheet. In the second ion velocity enhancement there is a consistent outflow in the y direction but there is also a short sharp increase in the x direction in the middle of this outflow. It is a possibility there is more than one reconnection event here that happen to be very close together.

Figure 6.18 is in the same format as Figure 6.17 and shows an example of an

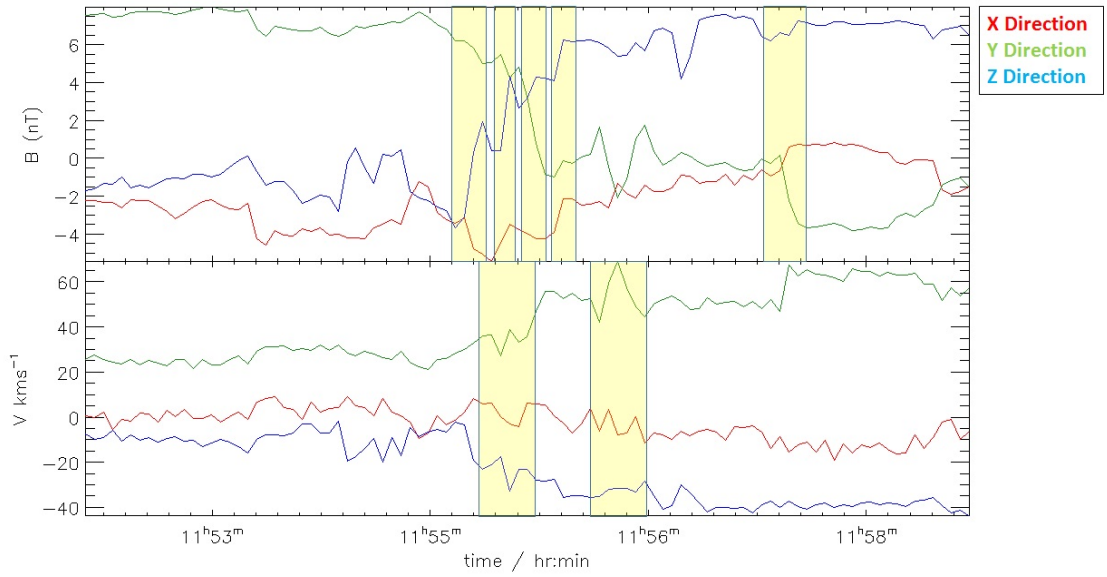

Figure 6.18: An example of a magnetic reconnection event with 5 current sheets in the structure. The top panel shows the magnetic field in GSE co-ordinates and the bottom panel shows the ion velocity, again in GSE co-ordinates. In order to view the change in ion velocity over the event the first data point in the ion velocity in the X direction is added to the X component over the whole event.

event that has 5 current sheets. Here the exhaust jets are very small. The second jet is approximately 20 $km\ s^{-1}$ and located between the last two current sheets.

In summary, the Gosling picture of a reconnection exhaust bounded by two rotations is not always apposite. It is shown here that there are large numbers of events exhibit only 1 rotation and many that are 3 rotations. There are also a few events with a 4 and 5 current sheet structure. Also one must note that the number of current sheets is a minimum as the temporal resolution of the data can only pick out separate current sheets that are more than 4s apart. It appears that there are examples of all the possible 3 current sheet structures as predicted by Figure 6.16 in Chapter 5. There is thus a wide range of magnetic reconnection event structures in the solar wind.

6.4.5 Evolution of Reconnection Events with Time and/or in Space

In this section we will address the science question 'How do reconnection events evolve over time and/or space?'. Previous studies have suggested that reconnection in the solar wind is usually large scale in 3 dimensions (of the order of at least a few R_E) and non-patchy. In other words, magnetic reconnection is not considered to change structurally over short periods of time ($\sim$ minutes) (*Phan et al.*, 2006; *Gosling*, 2010, 2011). For example, *Phan et al.* (2006) discussed a reconnection X line that is at least 390 R_E in length which was seen by the ACE, Cluster and Wind spacecraft. The time delay between the ACE and Wind spacecraft encountering the event was approximately 2 hours, the spatial distance between the spacecraft was of order 390 R_E and *Phan et al.* (2006) determined that there was no structural change worthy of note.

In Chapter 4 we demonstrate that this was not true for a case study in which the reconnection current sheets changed over time-scales and/or distances that were smaller than the differences between the Cluster spacecraft tetrahedron. The Cluster spacecraft, over the course of their lifetime, change their relative separation, but at their most distant they are 10,000km ($< 2\ R_E$) away from each other, which is much smaller than the scales assumed for solar wind reconnection events on the basis of earlier studies.

In this section we will use our survey event list to determine whether reconnection events in the solar wind are observed by all 4 Cluster spacecraft and, if so, how similar are the observed reconnection signatures to each other i.e., whether there is often evidence that reconnection events evolve over the timescales and/or distances between spacecraft.

In order to test whether at least some reconnection events evolve in space and/or time, we initially use spin resolution Cluster (4s) magnetic field data from the Cluster Science Archive for each of the 4 spacecraft for each of the identified events.

For each of the spacecraft we conduct a minimum variance analysis on the magnetic field data and rotate the magnetic fields into this frame of reference. This magnetic field data is then interpolated onto a common time base, that of the Cluster 1 spacecraft.

We then find the correlation between the component of the magnetic field in the maximum variance direction between each of the pairs of spacecraft over a range of time lags. From this analysis we obtain the time lag between spacecraft for each of the pairs of spacecraft for every event and the value of the maximum correlation.

Figure 6.19 and 6.20 show the time lag at maximum correlation and the value of the maximum correlation found between the Cluster 2 and the Cluster 1 spacecraft.

For the Cluster 2 spacecraft correlated with the Cluster 1 spacecraft we can see that for 67% of the events the time lag at the point of maximum correlation is between 0 and 4 s. Thus it appears that in almost all cases a reconnection event is swept past at great speed (and not at an oblique angle to the spacecraft formation), the events are witnessed by the spacecraft at almost the same time and unchanged.

There are however some events that have a timelag at the point of maximum correlation that is much larger. In this case the timelags can be up to approximately $\pm$ 50 s. Those events with time lags greater than 50 s are quite rare and make up approximately 4% of the total number of events. As the distances be-

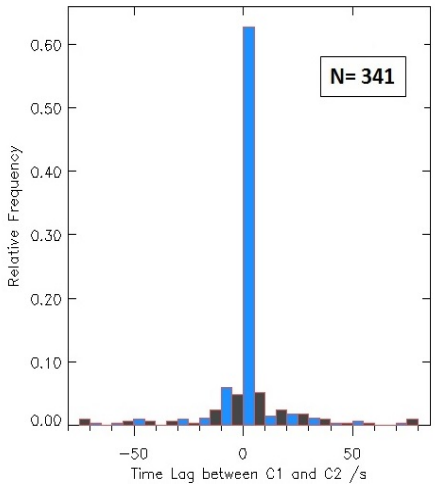

Figure 6.19: Histogram of the time lag at the point of maximum correlation between the Cluster 2 and Cluster 1 spacecraft. Binsize = 4 s

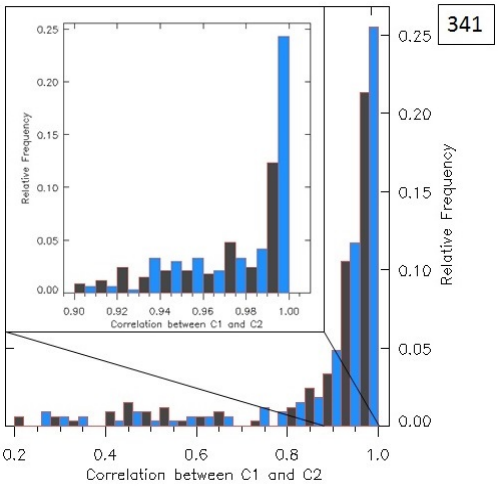

Figure 6.20: Histogram of the value of maximum correlation for each of the events between the Cluster 2 and the Cluster 1 spacecraft. Binsize = 0.05 s

tween Cluster spacecraft are at maximum approximately $10,000\ km$ apart and the average solar wind speed is ($\sim 450\ km\ s^{-1}$) the largest time-lags should be of the order 22 s, assuming that the reconnection event passes over the spacecraft in the direction approximately normal to the current sheets of the event. This means that these large time lag events, if they are observations of the same event, must have passed over the spacecraft very obliquely. It is possible that the different Cluster spacecraft are not observing the same reconnection event and there are two similar rotations of the magnetic field within 60 s of each other.

In Figure 6.20 we see that most of the events ($> 75\%$) of the events have a correlation that is greater than 0.9. There are 25 events (7%) with a value of maximum correlation that is lower than 0.5.

We also consider the same graphs for the correlation and timelags between Cluster 3 and Cluster 1 and also Cluster 4 and Cluster 1. These are shown in Figures 6.21, 6.22, 6.23 and 6.24.

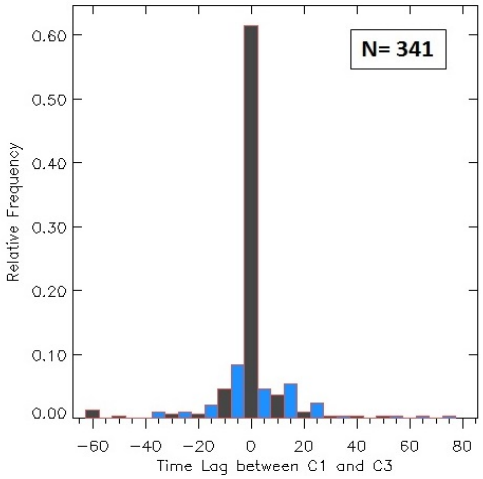

Figure 6.21: Histogram of the average time lag at the point of maximum correlation between the Cluster 3 and Cluster 1 spacecraft

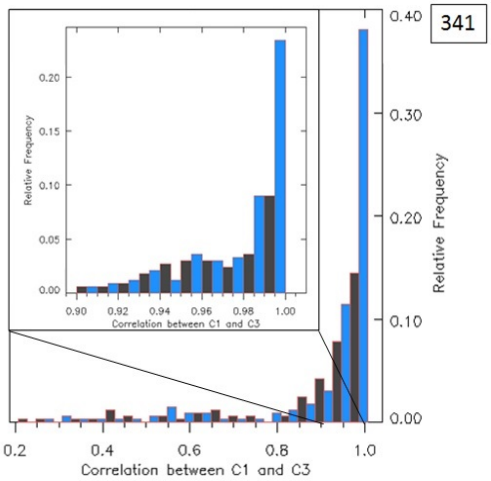

Figure 6.22: Histogram of the value of maximum correlation for each of the events between the Cluster 3 and the Cluster 1 spacecraft

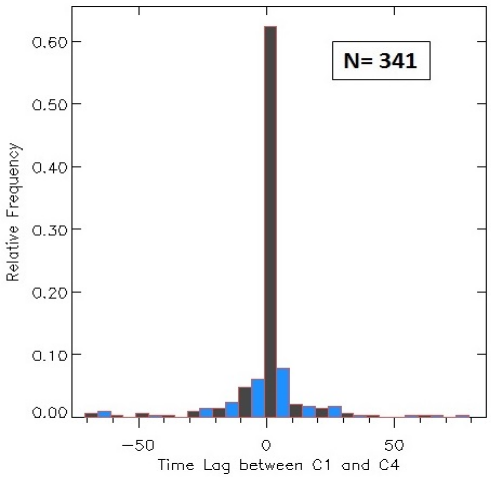

Figure 6.23: Histogram of the average time lag at the point of maximum correlation between the Cluster 4 and Cluster 1 spacecraft

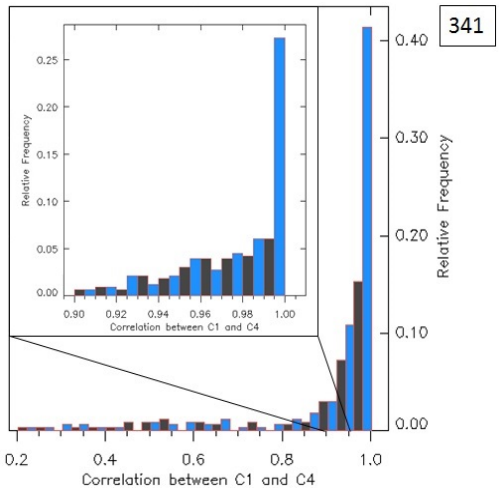

Figure 6.24: Histogram of the value of maximum correlation for each of the events between the Cluster 4 and the Cluster 1 spacecraft

Figures 6.21, 6.22, 6.23 and 6.24 show similar results to the equivalent graphs for the Cluster 3 and 4 spacecraft. As all these Figures show very similar results we do not show the equivalent graphs for the correlations between C2-C3, C2-C4, and, C3-C4.

Cluster 3 and 4 show that the average time lag is again predominantly close

to 0 with over 75% of the events with a timelag $\lesssim 4$ s. They also show very high correlations with over 75% of the events having a maximum correlation of over 0.90, which means that the overall shape of the magnetic field change is the same for both spacecraft.

In Chapter 4 we showed an example of an event in which the magnetic field data for the 4 Cluster spacecraft had a highly correlated general structure (> 0.95 for each spacecraft) but did show smaller scale changes over time-scales and distances of order of the distance between spacecraft.

In order to quantify these small scale changes we introduce an 'evolution index'. This index is devised as follows: each of the 4 spacecraft magnetic field data sets (in the minimum variance frame) are shifted in accordance with the timelag at maximum correlation. We take the average of the spacecraft data sets to determine an average maximum variance data set. We then find the difference between each point in the average data set and the corresponding point in each of the spacecraft data sets, sum the results and divide by the number of points. Thus we obtain an evolution index for each of the spacecraft for each of the events. We average the spacecraft evolution indexes to determine the evolution index for each event. The events with the lowest evolution index are likely to have very little temporal and/or spatial change between the spacecraft observing the reconnection event, whereas events with greatest evolution indices are likely to have the most change between spacecraft. It is not possible to determine a strict numerical value to what can be considered a 'low' index before the evolution index has been tested on the event list and the resultant evolution index values compared with a visual inspection of the events.

Figure 6.25 shows a histogram of the evolution indices for Cluster 1 in panel a),

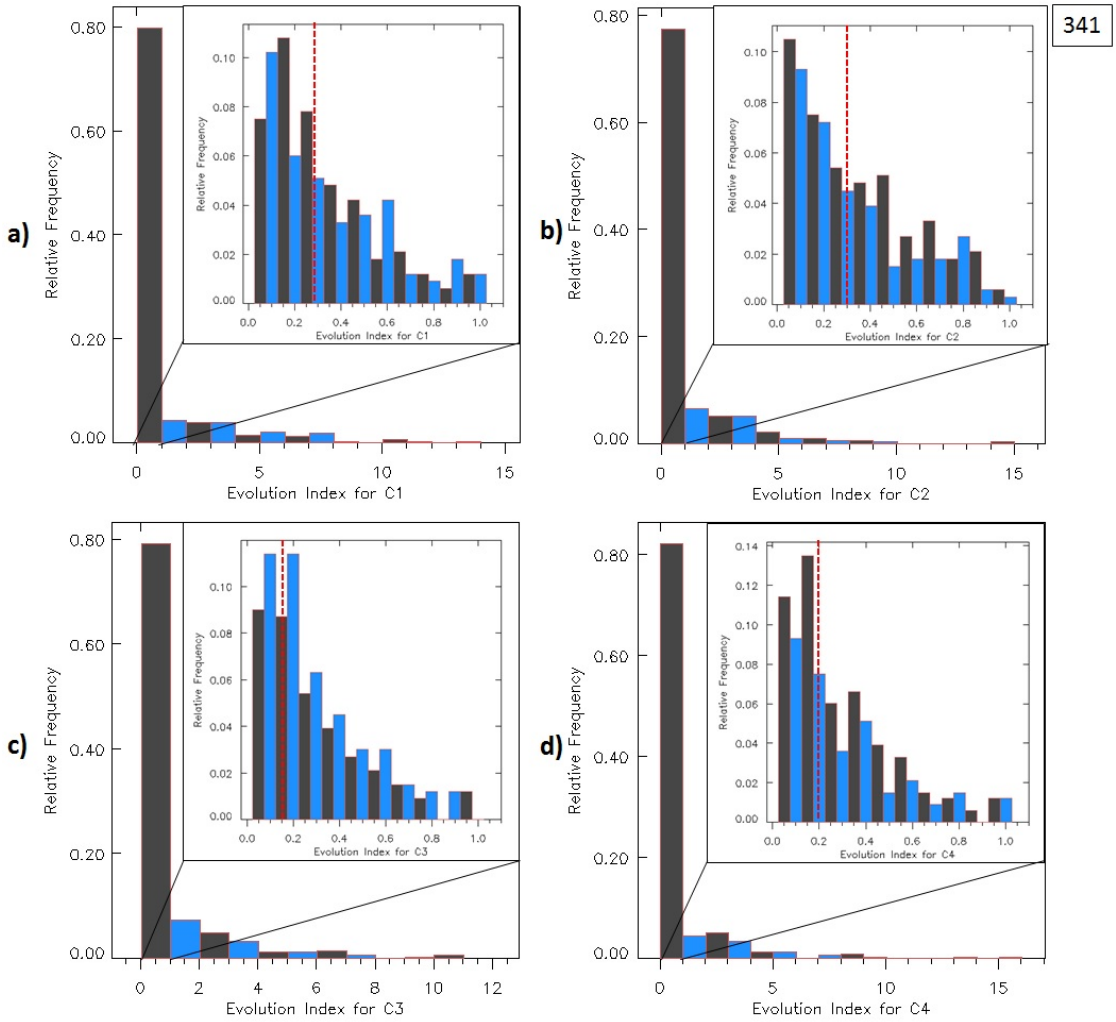

Figure 6.25: The evolution index for each of the Cluster spacecraft with Cluster 1 in panel a), Cluster 2 in panel b), Cluster 3 in panel c) and Cluster 4 in panel d). In the main panel the binsize is 1. The zoom in for each panel shows the evolution indices from 0-1 with a binsize of 0.05. The red dashed line shows the evolution index for the magnetic reconnection event that was described in Chapter 4.

Cluster 2 in panel b), Cluster 3 in panel c) and Cluster 4 in panel d). The zoom in for each of the panels shows the histogram for indices between 0 and 1 as in the main plot $> 75\%$ of the indices are < 1. The red line on the zoom in panel shows the evolution index for the magnetic reconnection event we described in Chapter 4.

Figure 6.25 shows that $> 75\%$ of events each spacecraft have an evolution index that is < 1. The magnetic reconnection event that we described in Chapter 4 have

indices of 0.28, 0.30, 0.18 and 0.20 for Cluster 1, 2, 3 and 4 respectively. This puts each of the indices in the smallest 40% so this is not an event that has a particularly large evolution index in comparison to the other reconnection events in this statistical survey.

Figure 6.26 shows a histogram of the evolution indices for all the events in the event list. Figure 6.26 shows that the majority of the events have a evolution index close to 0, on the low end of the spectrum, with relatively few events with higher indices.

The event described in Chapter 4 has an index value of 0.96 which is in the lowest 40% of values. Note: the changes in the Chapter 4 event are small but easy to distinguish via a visual inspection of the magnetic field data.

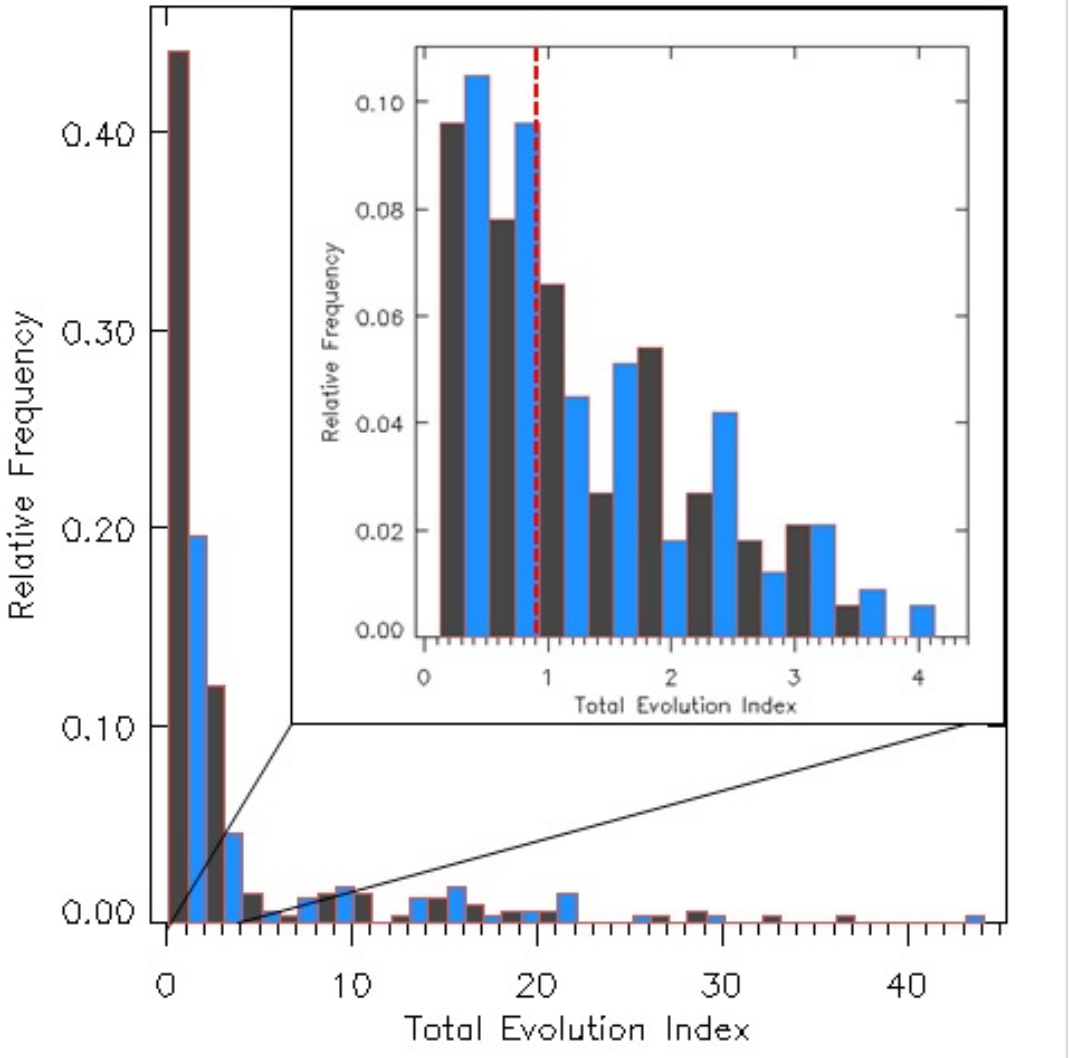

Figure 6.26: Histogram showing the total evolution index for each of the events; the total of the individual spacecraft indices for an event. The main panel shows the full range of evolution indices from 0 - 44, with a binsize of 1. The zoom in shows the evolution indices between 0-4 as $> 75\%$ of events have an index value of < 4. The binsize in this case is 0.2. The red dashed line shows the total evolution index for the Chapter 4 reconnection event.

6.5 Discussion of Survey

In this Chapter we have detailed the results of a statistical survey and compared them to current theories and previous (case and statistical) studies (e.g., *Sonnerup et al.*, 1981; *Gosling et al.*, 2005; *Phan et al.*, 2006).

Our automated algorithm requires the specification of thresholds which naturally have some impact on the characteristics of the reconnection events selected for study. Thus the thresholds may include some events that are not reconnection events and discard others that should, as is the case with any automated method. However the event list has returned a large number of events, which, when examined visually are good candidates for reconnection events with a minimised number of false positives.

There are a few events in the list that occur in solar and solar wind conditions, or have characteristics that are outside what is considered to be the normal range. While this does not necessarily imply anything about their validity as events, it does suggest that these events would be worthy of a further case study (which is beyond the scope of this study). The event list in Appendix B labels a reconnection event with a letter tag corresponding to the unusual condition that is present (if any) as we described in Section 6.3. In Section 6.3.1 we found that 28% of events were present where at least one of the solar conditions was outside the 'normal' range (see Section 6.3). Of these events 68% only had one outlying condition and a further 21% had two. The remaining reconnection events (10 events), where there were three or more outlying conditions, would be the most likely candidates for interesting case studies in the future, assuming they are not false positives.

In Section 6.4.2 we compared the average solar and solar wind conditions with the conditions during the events. The average values for the solar wind speed and

its standard deviation are 491 ± 137 $km\ s^{-1}$ and 438 ± 108 $km\ s^{-1}$ and for the solar wind density, 5.5 ± 5.0 particles cm^{-3} and 6.0 ± 4.4 particles cm^{-3}, for the reconnection events and the ambient solar wind conditions respectively and thus the average values are relatively similar. But the average background magnetic field strength for reconnection events is much higher (8.1 ± 4.8 nT) than that of the average ambient solar wind (5.4 ± 3.0 nT). One possibility is that reconnection is more likely in higher strength magnetic fields, or possibly that higher magnetic field strengths make it easier for an event to pass the threshold criteria of the algorithm as it implies a higher Alfvén speed and thus a potentially higher outflow exhaust. It would mean that a smaller rotation of the field would result in a higher absolute change in magnetic field strength. There does not appear to be an overall correlation between the number of events found and the average solar wind density or solar wind speed however there does appear to be a larger number of events in slow solar wind speed than we would expect given the fraction of the time that the Cluster spacecraft spends in the slow solar wind. We did not find a conclusive reason as to why some of the years yielded many more events than others, but it would appear to be a combination of solar wind conditions, as the reconnection events do occur in regions of higher magnetic field strength and in slower solar wind speed.

The correlations between the number of events per year and the solar and solar wind characteristic yearly averages are weak and none returned a statistically significant result. The lack of significance could be attributed to the low number of points as we only have data for 11 years. Possibly a longer study could produce results of greater significance.

Note also that some of the Alfvén speeds are very high. A combination of high

magnetic field strengths (30 nT) and a low density (2 particles cm^{-3}) could yield a Alfvén speed of around 500 $km\ s^{-1}$, so these high values are still valid.

Field rotation and exhaust speed distributions will have cutoffs due to algorithm thresholds. For example, the magnetic field rotations are limited to that greater than 80° and exhaust speed to that greater than 20 $km\ s^{-1}$ so we must be aware of this when making any conclusions about these characteristics of the events.

The thresholds for minimum field rotation and the change in the maximum variance directions are both absolute values. This means that events with a larger background field are more likely to be picked out as an 80° rotation will produce a larger absolute change than events which have a smaller background field. Thus in future iterations it would be better to move to a more flexible threshold.

One such threshold could be a percentage change in the magnetic field rotation. This method also comes with drawbacks, for example a percentage change will always return some candidate events which means that there will be a significant number of false positives from this threshold which will need to be filtered out later in the algorithm. The reverse problem is also an issue as periods of time with a lot of events will mean that some of the events will not pass the percentage threshold and so will be discarded.

There is a high amount of variability in the current density between events. This suggests that there is a wide range of current sheet thicknesses contained in the events that are found by the algorithm. This is because a thin current sheet will give a high current density for a given degree rotation, whereas a more broad sheet with the same degree rotation will have a lower current density.

In Section 6.4.3 we found that the ratio of the exhaust to the Alfvén speed is mostly below 1 and thus not all magnetic energy available is completely transferred

to kinetic energy of the exhaust in most cases as predicted by theory. For instances that the outflow speed is less than the Alfvén speed, it is possible that energy has already been extracted from this process closer to the reconnection site. If magnetic reconnection events in the solar wind are over large scales, spacecraft may encounter exhausts at distances that are far away from the point of reconnection and so it is possible that some of the energy could have already been lost to other processes in the interim or that the surrounding conditions are different.

In this algorithm it was not possible to accurately determine the distance between the spacecraft and the reconnection site as it requires a highly accurate determination of the orientation of 2 current sheets. With accurate orientations it would be possible to use the geometry as described in Chapter 4 to determine the distance between the spacecraft crossing and the reconnection X line.

The average temperature increase during the exhaust is near 0 which suggests that for most events energy does not go into heating the plasma. We consider the following:

$$\frac{B_{IN}^2}{2\mu_0} = \frac{1}{2}nm\Delta V^2 + nk\Delta T + \frac{B_{OUT}^2}{2\mu_0} \tag{6.12}$$

where ΔV is the change in ion velocity (the outflow exhaust speed) and ΔT is the change in ion temperature between the inflow and outflow plasma. The left hand side is the total magnetic energy density available before reconnection occurs. On the right hand side of the equation the first term is the kinetic energy gained by the plasma, the second term is the energy associated with the increase in temperature of the plasma and the last term is the remaining magnetic energy left in the outflow.

The magnetic energy in the outflow will always be non-zero. Thus if the outflow velocity of the plasma is less than the Alfvén speed and it is not being appreciably heated then it is likely that there is a significant amount of energy that was not

liberated from the magnetic field during reconnection.

It should also be noted that many statistical surveys of magnetic reconnection events find that the observed outflow is less than that predicted. An early example of this is described in *Sonnerup et al.* (1981). In this instance the exhaust values relative to the prediction have a ratio that ranges from 0.6 -1.2 with a mean value of 0.8. A more recent example is *Phan el al.* (2013), whereby the authors found that the range of the exhaust/prediction ratio is between 0.23 -1.28 with a mean of 0.66 and a median value of 0.6. These ranges are very similar to the ranges of the ratios in this study and support the conclusion that, usually, reconnection does not convert all of the available reconnection energy to kinetic energy in the exhaust.

However, there are some events with a V/V_A ratio greater than 1. A significant number of events ($\sim$ 35), 10% of the total number of events have an exhaust Alfvén speed ratio that is greater than 1.5. As we have stated in the testing phase it was not possible to completely extract all the non-events using the automatic algorithm, for the 2003 data we had a true positive outcome of around 83% this could account for at least some of these events having ratios that are outside of the typical range.

There are a wide range of magnetic reconnection event structures in the solar wind. The Gosling picture of reconnection is an exhaust bound by two current sheets. However this study shows that there are large numbers of events that have only 1 current sheet and many that have 3 current sheets or more.

In our analysis of reconnection structures with 3 current sheets we found that these were comparable to those structures we described in Chapter 5. We found examples of reconnection events where the reconnection exhaust was directed be-

tween one or both sets of current sheets. Again this suggests that the structures in the solar wind can be very complex.

We found that the majority of events have overall a general structural stability over the timescales and distances of the Cluster spacecraft. We can conclude this as over 75% of the events had correlation coefficients between magnetic field measurements at individual spacecraft that was greater than 0.9. This does not necessarily mean that there is not small scale fluctuation in the structure as the reconnection event described in Chapter 4 had correlation coefficients between the magnetic field data between each spacecraft of > 0.95 and did exhibit small-scale (Cluster spacecraft separation) structural variation.

We introduced an evolution index to quantify the level of similarity between the magnetic field data on each of the 4 spacecraft. It was found while the evolution index range was between 0-15 for each spacecraft (see Figure 6.25), $> 75\%$ of events had an evolution index < 1. Similarly with the total evolution index $> 75\%$ of the events have an index < 4.

The total evolution index of the Chapter 4 event is 0.96 which is in the lower 40% of values. This event had clear visual evidence of changes in the magnetic field data between spacecraft. The individual evolution indices for Cluster 1, 2, 3 and 4 were 0.28, 0.30, 0.18 and 0.20. As described in Chapter 4, the Cluster 2 spacecraft does not observe the 2 distinct current sheets that are observed by the other 3 spacecraft and, as expected, the evolution index for Cluster 2 is the largest value here. This potentially means that $> 60\%$ of events observe changes between spacecraft of a similar magnitude to this event.

Karimabadi et al. (2010) discussed the possibility of fossil sites: where the reconnection has ceased to occur but the remnants of the reconnection exhaust

are still visible, and observed by the spacecraft. This means that estimates of the Alfvén speed and available magnetic energy may not be an accurate representation of what was available at the point of reconnection. Thus events where we witness an outflow velocity that is higher than the local Alfvén speed, or a temperature decrease during the exhaust could be examples of this.

6.6 Conclusion of Survey

In conclusion in this study:

- We designed an algorithm that automatically extracts reconnection events in the solar wind using the magnetic field and ion velocity data from the Cluster 1 spacecraft.

- We looked at the number of events found per year between the years 2001-2011. We could not draw any strong conclusions about why each year returned a different number of reconnection events. As we noted earlier, there are more events in the slow solar wind (at solar wind speeds $\sim 200\ km\ s^{-1}$) than would be expected given the amount of time that the Cluster spacecraft encounter such speeds, and how rare these speeds are in the solar wind (*McGregor et al.*, 2011).

- We determined that the average solar wind speed and density during the reconnection events was the same as that for the ambient solar wind but the background magnetic field strength was higher for the reconnection events (ambient average $5.34 \pm 3.0\ nT$ and event average $8.1 \pm 4.8\ nT$). Reconnection events with a higher background field strength are more likely to be picked up by the algorithm, because an equivalent angle change in magnetic field

yields a higher absolute change in the magnetic field components for a high background magnetic field strength than a lower strength, which makes the change easier to discern from noise. As such in future iterations of such an algorithm a percentage change of the magnetic field may be a good way of being able to find reconnection events in lower background magnetic field conditions.

- We found that the speed of the reconnection exhaust is usually lower than the Alfvén speed (median of V/V_A : 0.80). Most events did not show any evidence of heating (the mode value is 0 and $> 50\%$ of the results were between a $-0.2 \leqslant nk\Delta T \leqslant -0.2$ change) so it was determined that the reconnection exhausts had lower speeds due to not all the available magnetic energy being liberated and is non-local. For the events that had exhaust speeds that were higher than the Alfvén speed we concluded that the reconnection X-line was far away from the spacecraft and the magnetic field conditions at the reconnection site were different from the point of observation, e.g., the Alfvén speed at the X-line is higher, which would mean more energy was available.

- The reconnection events found had a variety of structures, the most common being a single current sheet structure. We also found many events that have 3 or more current sheets and so we concluded that reconnection is often more complex than the Gosling picture which has a bifurcated current sheet structure.

- A comparison of the reconnection events as observed by each of the spacecraft showed that, for $> 75\%$ of events, the magnetic field is correlated to > 0.9.

- The evolution index for the Chapter 4 reconnection event was in the lowest 40% of events (with a value of 0.96). This suggests that the majority of events observe some temporal or spatial differences over length and timescales that are smaller than the distances between spacecraft.

Chapter 7

Conclusions and Future work

The motivation for this work was to further understand the mechanism for reconnection using the solar wind environment. This environment is ideal for studying reconnection as related structures are swept past the spacecraft at high speeds and the solar wind does not have the limiting and fluctuating boundary conditions that are generally present in most other environments where reconnection is observed.

From our analysis our stand-out conclusion is that reconnection in the solar wind (and indeed any environment) is more complex than the simple models that have been created to help describe it. In order for us to have a complete understanding of the basic mechanism behind magnetic reconnection, a large scale survey of magnetic reconnection events in multiple environments must be undertaken.

In Chapter 4 we analysed a case study of an event that exhibited small-scale differences in structure over times/distances that were smaller than the time-scales and/or distances between Cluster spacecraft. In this case study, the magnetic field data for Cluster 2 did not show the distinct magnetic field reversals indicative of current sheets that were seen by the other 3 Cluster spacecraft (though it did observe a overall magnetic field rotation of similar magnitude). From this we

conclude that reconnection can evolve over spatial and/or temporal scales of order $\lesssim 10,000\ km$, in contrast to conclusions from earlier works.

The main questions that arise from this conclusion are: how prevalent are reconnection events that evolve over such small time-scales/ length-scales? What is causing the reconnection event to evolve? Is it typical for an event that current sheets will be apparent at one spacecraft but not at another?

In order to extend this work we can utilise both case and statistical studies of reconnection events in the solar wind. The analysis of further case studies of magnetic reconnection events in the solar wind using the 4 point measurement capability of the Cluster spacecraft to observe changes would help us to see whether there were any commonalities between events that observed change, and whether it is possible to detect a trigger for the evolution. The use of a statistical study would enable us to answer the question of the prevalence of evolution in events in the solar wind. This work was begun in Chapter 6, where we introduced the concept of an evolution index, describing the difference in the magnetic field observed by each spacecraft.

In Chapter 4 we also determined that the current sheets were moving towards each other. In the OC87 model a slowing reconnection rate would produce current sheets that appeared to move closer together (*Owen and Cowley*, 1987a). Also in Chapter 4 we found that some similar features to the event found at Cluster were also observed at ACE and Wind. These current sheets were not at the time or orientation predicted by extrapolation of the orientation and speed of the sheets found at Cluster. This suggests, if this is indeed the same event, that reconnection events in the solar wind can change significantly over time, possibly including rotating. To further work in this area, we would need large-scale case studies

where events were observed by at least 4 spacecraft, preferably spacecraft that are as far apart as Cluster, ACE, and Wind, in order to see how the relative movement of the current sheets changed over time.

In Chapter 5 we devised a new picture of reconnection which for the first time includes a variety of observable outcomes based on the characteristics of the plasma on either side of the structure and whether or not the outflow ions and electrons show a diamagnetic effect. This model has 5 possible current sheets within the reconnection structure (depending on the reconnection event characteristics), which may or may not be observable within a given event. Thus we concluded that it was possible to have a wide variety of observed structures for magnetic reconnection events in the solar wind.

This conclusion was further strengthened by the results in Chapter 6, where we looked at the number of current sheets in each of the selected reconnection events and found evidence of reconnection events exhibiting between 1-5 current sheets. The logical next step is to determine the reason for each event having the number of current sheets that it does. We can compare each of the reconnection structures found with Figures 5.2 and 5.3 and look for correlations between the characteristics of events with the same number of sheets.

In Chapter 5 we also compared a mathematical model (OC87) with observations of three case studies. It was found that the mathematical model overestimated the outflow speeds but was of the same order of magnitude. It did not correctly predict the relative strength of the two outflows but it was partially successful in predicting the relative times that the Cluster spacecraft spends in each outflow region. In order to further this work we will modify the existing mathematical model for predicting the outflow and structure of events based on the observables outside

so that it is more accurate. For example, developing the model to account for 3 dimensional structure variations would be advantageous as all real events exist in 3 dimensions.

In Chapter 6 we used an automatic method to obtain a list of reconnection events in the solar wind observed by the Cluster 1 spacecraft. From this we were able to draw the following conclusions: reconnection events in the solar wind appear to occur in higher magnetic field strengths than the average solar wind conditions. The ion velocity outflow is usually less than the Alfvén speed and the net change in temperature is usually near zero, which for these events suggests that not all the available magnetic energy is liberated to flow kinetic energy by reconnection but that the outflow plasma is also not generally heated. For the instances where the outflow ion velocity is greater than the Alfvén speed we concluded that we may be observing an event where the reconnection X - line is far from the spacecraft and in different solar wind conditions (where the Alfvén speed is higher) so the Alfvén speed at the point of observation is not an accurate estimate of the available magnetic energy. This is potentially a caveat for any of the events. We determined that almost half of the identified reconnection events only had a single current sheet and that there were a few events with 2-5 current sheets, which lead to the conclusion that reconnection events can have a variety of structures (as we theorised in Chapter 5).

In Chapter 6 we also looked at the evolution of events by creating an evolution index that determined the difference between the magnetic field data observed by each of the 4 Cluster spacecraft and the average of the 4 data sets. This determined that most of the events are on the low end of the scale (total evolution index ranges between 0-44 but $> 75\%$ of events have a total index value < 4). We

found that the case study reconnection event in Chapter 4 has a relatively low total evolution index of 0.96 (60% of the events have a higher total index value). This suggests that either most of the reconnection events are highly variable and evolve significantly or that it is not possible for the index to determine small differences between spacecraft where the overall structure is similar (in this case the Cluster 2 spacecraft did observe an overall rotation that was the same as the other 3 spacecraft but it did not discern any individual current sheets).

In order to improve the functionality of the evolution index it would be first necessary to eliminate any data that is not part of the reconnection event. The inclusion of too many 'background' data points may lead to the evolution index being underestimated. Another improvement would be to be able to discern whether the majority of the change was observed at one spacecraft in particular or whether there was a gradual change seen by all 4. It would also be advantageous to look at the time span between the changes. For example, looking at the time differences over which the spacecraft encounter the event in order to answer the question of whether the spacecraft that is most separated from the others see the largest changes.

The selection algorithm described in Chapter 6 is a demonstration of a systematic approach to finding events in the solar wind. The algorithm can be improved in many ways.

For example, the parameters and thresholds in the current version of the algorithm place limitations on the reconnection events that can be found. For instance the magnetic field rotation has a minimum threshold of 80° and so any events with a smaller overall field rotation will be discarded. It would be highly advantageous for a future version of this algorithm to not have such strict thresholds as we know

that magnetic reconnection events with much smaller magnetic field rotations exist (*Phan et al.*, 2010).

One way of accounting for this would be to have the threshold level change depending on the background solar wind conditions, as the present thresholds are high to account for high variability in the background. It would also be an improvement to introduce machine learning into the program to further refine it.

Further, it would be advantageous for the algorithm to be able to pick out more characteristics for each of the events automatically. For example, having a strong definition of what constitutes the start and end time of an event would make it easier to determine the exact duration of an event and identify the relevant inflows on either side of the event. Another example would be the automatic identification of individual current sheets in the event.

In Chapter 6 we highlighted several events that had characteristics, or existed in solar wind conditions that were different from what is usually seen. Case studies based around some of these more eccentric events would certainly help further our understanding both of the structure and dynamics of events and also the various conditions in which they appear.

We mentioned that in the case of events with an exhaust speed less than that of the Alfvén speed, that not all of the apparently available magnetic energy was liberated to the plasma by reconnection. We can test this theory by measuring the difference between the background magnetic field strength and the magnetic field strength during the event. If the remaining energy plus the kinetic energy add up to the total initial magnetic energy then we have accounted for all the energy in that event.

The energy not converted to kinetic energy could have either been converted

to other forms, for example we discussed the possibility that it could have been converted to a heating of the plasma, though we did not find any evidence for this in Chapter 6. It could be that the remaining energy is in the magnetic field in the outflow region, if the magnetic field strength is non-zero in the outflow then there will be some finite magnetic field energy.

Appendix A

Minimum Variance Analysis

Tables A.1, A.2 and A.3 show the minimum variance analysis for each of the Cluster spacecraft over each of the current sheets, CS1, CS2, and CS3 respectively for the event analysed in Chapter 4. Here it can be seen that the maximum variance directions for each current sheet are well defined but the minimum variance direction is not. Thus it is not possible to rely on the minimum variance technique alone to determine the structure of the event. By combining the minimum variance analysis with the timing analysis we can get a much more accurate picture of the current sheet orientations, this is described in Chapters 3 and 4.

S/C	Time frame (mm:ss)		Direction Vector	λ	λ Rat.
C1	38:16 - 38:23	**Minimum:**	0.004, 0.197, 0.980	0.00338	4
		Intermediate:	-0.663, -0.733, 0.150	0.0126	63
		Maximum:	0.748, -0.651, 0.128	0.791	
C2	38:52 - 38:56	**Minimum:**	0.882, 0.468, 0.059	0.00244	2
		Intermediate:	0.301, -0.463, -0.834	0.0471	219
		Maximum:	-0.363, 0.753, -0.549	1.03	
C3	38:17 - 38:25	**Minimum:**	0.074, 0.164, 0.984	0.00138	3
		Intermediate:	-0.599, -0.781, 0.175	0.00476	173
		Maximum:	0.797, -0.602, 0.040	0.823	
C4	38:36 - 38:44	**Minimum:**	0.004, 0.227, 0.974	0.000848	5
		Intermediate:	0.711, 0.684, -0.162	0.00405	222
		Maximum:	-0.703, 0.693, -0.159	0.901	

Table A.1: The minimum variance analysis for CS1, the minimum, intermediate and maximum variance directions and the eigenvalues associated with each of these vectors are given.

S/C	Time frame h:m:s UT		Direction Vector	λ	λ Rat.
C1	38:38 - 38:45	**Minimum:**	0.345, 0.928, -0.144	0.0202	3
		Intermediate:	-0.290, 0.251, 0.923	0.0589	
		Maximum:	0.893, -0.277, 0.356	2.01	34
C2	39:19 - 39:28	**Minimum:**	-0.156, 0.932, 0.327	0.01279	5
		Intermediate:	-0.667, -0.343, 0.661	0.05881	
		Maximum:	0.728, -0.115, 0.676	0.6957	12
C3	38:39 - 38:45	**Minimum:**	0.409, 0.888, -0.209	0.0117	3
		Intermediate:	-0.286, 0.343, 0.895	0.0307	
		Maximum:	0.866, -0.306, 0.395	1.38	45
C4	38:54 - 39:03	**Minimum:**	-0.399, 0.304, 0.865	0.0207	6
		Intermediate:	-0.407, -0.904, 0.129	0.122	
		Maximum:	0.821, -0.301, 0.485	2.7	22

Table A.2: The minimum variance analysis for the CS2, the minimum, intermediate and maximum variance directions and the eigenvalues associated with each of these vectors are given.

S/C	Time frame (hh:mm)		Direction Vector	λ	λ Rat.
C1	38:58 - 39:02	**Minimum:**	-0.508, 0.126, 0.852	0.00394	2
		Intermediate:	0.077, -0.979, 0.191	0.00604	
		Maximum:	0.858, 0.163, 0.487	0.537	89
C3	38:50 - 38:52	**Minimum:**	-0.591, 0.362, 0.721	0.00309	2
		Intermediate:	-0.340, -0.922, 0.185	0.00627	
		Maximum:	0.732, -0.136, 0.668	0.0645	10
C4	39:17 - 39:22	**Minimum:**	-0.424, 0.405, 0.810	0.00189	3
		Intermediate:	-0.111, -0.911, 0.398	0.00477	
		Maximum:	899, 0.079, 0.431	0.38	80

Table A.3: The minimum variance analysis for the CS3, the minimum, intermediate and maximum variance directions and the eigenvalues associated with each of these vectors are given.

Appendix B

Event List

Tables B.2 - B.17 show a list of the events found using the algorithm described in Chapter 6. Each of the tables includes the start and end times of each of the events, the average solar wind speed over the event (SW) /$km\ s^{-1}$, the average magnetic field strength (BF) /nT, the average density (D) /particles cm^{-3}, the average Alfvén speed (AS) /$km\ s^{-1}$, the recorded duration (Dur) /s, the temperature increase (T) / MK, the magnetic field rotation (BR) / $^{\circ}$ and the Exhaust speed (ES) /$km\ s^{-1}$. If any of the variables are outside the typical solar wind conditions or typical magnetic reconnection characteristics, then they will be flagged with a relevant letter code in the final column as follows:

(a) Solar wind speeds below 250 $km\ s^{-1}$

(b) Exhaust speeds above 200 $km\ s^{-1}$

(c) Temperature changes greater than 2 MK

(d) Time lags greater than 50 s at the point of maximum correlation (for the magnetic field data in the maximum variance direction) between the Cluster spacecraft.

(e) Maximum correlations (between spacecraft using the magnetic field in the maximum variance direction) of less than 0.5

(f) Current densities over 500 $nA\ m^{-2}$

(g) Number of sheets > 5

If the characteristics of the magnetic field and solar wind conditions are what we would consider typical then a '0' is entered in the final column.

SW	Solar Wind Speed ($km\ s^{-1}$)	Dur	Duration (s)
BF	Magnetic field strength (nT)	T	Temperature increase over the exhaust (MK)
D	Solar wind density (particles per cm^{-3})	BR	Magnetic field rotation (°)
AS	Alfvén speed ($km\ s^{-1}$)	ES	Exhaust Speed ($km\ s^{-1}$)
Out	Flagged outlying characteristics		

Table B.1: Key for the following Tables B.2 - B.17.

Start Time	End Time	SW	BF	D	AS	Dur	T	BR	ES	Out
2001-02-10/06:26:40	2001-02-10/06:33:08	426	3	4	38	388	0	159	20	e
2001-02-12/10:05:08	2001-02-12/10:09:40	410	5	5	52	272	0	127	22	0
2001-02-12/13:04:39	2001-02-12/13:11:20	413	5	5	50	401	0	175	37	0
2001-02-14/19:17:31	2001-02-14/19:23:19	537	5	2	80	348	0	175	34	0
2001-04-05/22:27:01	2001-04-05/22:33:37	551	4	4	46	396	0	179	27	0
2001-04-13/09:54:59	2001-04-13/09:58:39	828	9	7	80	220	0	97	72	0

Table B.2: The event list including event characteristics for 2001. See key in Table B.1 for variable details.

Start Time	End Time	SW	BF	D	AS	Dur	T	BR	ES	Out
2002-01-12/05:46:53	2002-01-12/05:49:13	571	6	4	59	140	0	98	31	0
2002-01-12/07:33:58	2002-01-12/07:38:42	565	6	5	57	284	0	136	69	f
2002-01-21/05:45:36	2002-01-21/05:48:48	447	11	7	90	192	0	132	48	f g
2002-01-21/06:59:00	2002-01-21/07:3:57	452	9	6	82	297	0	116	55	0
2002-01-25/22:47:24	2002-01-25/22:50:57	256	26	2	405	213	0	129	98	0
2002-01-25/23:45:33	2002-01-25/23:47:58	313	25	1	455	145	0	131	58	0
2002-01-26/03:32:17	2002-01-26/03:33:34	260	26	1	485	77	0	108	212	b
2002-02-09/04:41:46	2002-02-09/04:45:07	488	4	3	51	201	0	125	45	f
2002-02-11/14:24:32	2002-02-11/14:26:08	543	8	4	89	96	0	99	69	0
2002-02-11/17:27:03	2002-02-11/17:28:03	516	6	3	79	60	0	96	32	0
2002-02-11/18:48:22	2002-02-11/18:51:43	570	7	3	85	201	0	162	89	0
2002-02-12/01:43:04	2002-02-12/01:46:53	558	6	3	75	229	0	128	63	0
2002-02-12/01:49:14	2002-02-12/01:53:07	557	6	3	76	233	0	127	73	0
2002-02-12/02:41:02	2002-02-12/02:48:36	578	6	3	71	454	0	174	37	0
2002-02-12/03:39:52	2002-02-12/03:43:33	531	6	3	68	221	0	128	56	0
2002-02-12/03:46:30	2002-02-12/03:50:19	540	6	4	70	229	0	144	55	0
2002-02-19/07:53:46	2002-02-19/07:59:23	371	7	5	65	337	0	148	27	0
2002-02-19/12:51:54	2002-02-19/12:57:39	409	6	4	69	345	0	128	53	0
2002-02-21/22:31:26	2002-02-21/22:32:30	425	10	6	85	64	0	111	26	0
2002-02-23/22:40:48	2002-02-23/22:46:33	346	6	5	56	345	0	163	112	0

Table B.3: The event list including event characteristics for 2002. See key in Table B.1 for variable details.

Start Time	End Time	SW	BF	D	AS	Dur	T	BR	ES	Out
2003-01-06/07:42:43	2003-01-06/07:49:08	403	5	5	50	385	0	118	39	0
2003-01-10/23:55:47	2003-01-10/23:58:51	319	21	3	259	184	0	112	196	0
2003-01-18/00:55:02	2003-01-18/00:58:19	375	12	14	71	197	0	124	66	0
2003-01-18/11:56:32	2003-01-18/11:59:33	401	10	19	52	181	0	156	74	0
2003-01-23/00:13:51	2003-01-23/00:17:52	659	7	5	70	241	0	147	62	0
2003:01:27/17:49:29	2003-01-27/17:55:14	470	3	22	14	345	0	115	22	0
2003-02-03/18:11:13	2003-02-03/18:16:02	499	8	9	59	289	0	133	81	0
2003-02-03/21:03:10	2003-02-03/21:09:31	496	8	10	59	381	0	127	55	f
2003-02-15/11:31:00	2003-02-15/11:33:21	628	7	4	75	141	0	155	51	0
2003-02-25/12:41:01	2003-02-25/12:45:13	419	5	10	38	252	0	103	24	0
2003-03-11/03:12:07	2003-03-11/03:13:11	420	6	9	44	64	0	126	31	0
2003-03-15/19:42:24	2003:03:15/19:45:12	637	7	4	77	168	0	122	88	0
2003-03-27/20:27:05	2003-03-27/20:32:06	499	7	7	60	301	0	125	41	0
2003-03-30/08:09:55	2003-03-30/08:10:55	493	12	9	87	60	0	111	107	0
2003-04-01/19:02:07	2003-04-01/19:07:56	523	5	4	59	349	0	128	78	e
2003-04-11/02:31:12	2003-04-11/02:33:33	719	5	2	76	141	1	101	100	0
2003-04-16/06:56:11	2003-04-16/06:57:24	695	7	4	77	73	0	102	63	0

Table B.4: The event list including event characteristics for 2003. See key in Table B.1 for variable details.

Start Time	End Time	SW	BF	D	AS	Dur	T	BR	ES	Out
2004-01-03/03:59:03	2004-01-03/04:04:22	537	13	10	88	319	0	154	38	0
2004-01-03/04:15:16	2004-01-03/04:17:05	540	12	10	89	109	0	133	26	0
2004-01-03/04:29:39	2004-01-03/04:30:56	584	11	10	76	77	0	158	32	0
2004-01-05/11:06:18	2004-01-05/11:07:22	604	6	4	64	64	0	130	86	0
2004-01-10/06:46:6	2004-01-10/06:49:31	558	11	15	61	205	0	150	63	0
2004-01-10/06:56:43	2004-01-10/07:00:46	555	11	14	66	243	0	127	37	0
2004-01-12/14:54:44	2004-01-12/14:58:10	503	4	4	43	206	0	119	44	0
2004-01-16/23:05:32	2004-01-16/23:07:17	635	6	3	78	105	0	110	51	0
2004-01-19/14:48:58	2004-01-19/14:53:29	593	5	3	61	271	0	174	34	0
2004-01-19/15:02:22	2004-01-19/15:07:04	606	5	3	58	282	0	132	51	0
2004-01-19/20:25:55	2004-01-19/20:30:05	578	4	3	49	250	0	143	25	0
2004-01-21/16:05:12	2004-01-21/16:09:10	492	5	6	45	238	0	164	41	0
2004-01-21/18:43:16	2004-01-21/18:49:52	479	5	5	47	396	0	166	42	0
2004-01-21/23:39:01	2004-01-21/23:42:52	450	6	7	51	231	0	152	53	0
2004-01-21/23:51:53	2004-01-21/23:53:01	475	5	6	49	68	0	127	61	0
2004-01-26/20:52:49	2004-01-26/20:58:00	432	10	10	67	311	0	140	43	0
2004-01-29/02:19:9	2004-01-29/02:25:44	548	5	3	64	395	0	125	37	0
2004-01-31/11:20:37	2004-01-31/11:27:17	631	8	4	85	400	0	170	67	0
2004-02-05/04:15:22	2004-02-05/04:21:41	555	5	2	86	379	0	168	68	0
2004-02-05/13:04:29	2004-02-05/13:11:05	516	5	3	66	396	0	166	27	0
2004-02-09/17:14:23	2004-02-09/17:19:02	265	6	0	154	279	6	159	388	bc
2004-02-12/07:23:11	2004-02-12/07:27:25	658	12	9	88	254	0	140	58	0
2004-02-12/08:39:58	2004-02-12/08:43:57	658	12	6	112	239	0	139	83	0
2004-02-14/12:56:31	2004-02-14/13:01:05	642	4	2	67	274	0	137	88	0
2004-02-14/13:27:24	2004-02-14/13:29:46	646	4	2	72	142	0	153	92	f
2004-02-14/20:00:24	2004-02-14/20:04:55	607	5	2	70	271	0	158	40	0

Table B.5: The event list including event characteristics for 2004. See key in Table B.1 for variable details.

Start Time	End Time	SW	BF	D	AS	Dur	T	BR	ES	Out
2004-02-22/02:14:54	2004-02-22/02:21:34	382	5	10	39	400	0	161	28	0
2004-02-24/08:33:55	2004-02-24/08:38:01	402	5	6	42	246	0	149	42	0
2004-02-29/05:34:41	2004-02-29/05:37:43	678	7	2	105	182	0	140	64	0
2004-02-29/10:55:02	2004-02-29/10:59:12	687	6	2	96	250	1	130	65	0
2004-03-02/07:56:11	2004-03-02/08:01:22	670	5	2	75	311	1	135	76	0
2004-03-02/10:02:40	2004-03-02/10:04:21	694	5	2	81	101	0	133	71	0
2004-03-05/02:43:47	2004-03-05/02:48:50	457	4	5	46	303	0	120	34	0
2004-03-09/16:14:47	2004-03-09/16:19:14	492	11	16	60	267	0	109	23	0
2004-03-09/18:41:25	2004-03-09/18:46:19	507	11	14	64	294	0	150	51	0
2004-03-09/20:55:06	2004-03-09/21:00:41	523	12	16	65	335	0	139	67	0
2004-03-09/23:10:25	2004-03-09/23:11:50	610	13	7	101	85	0	96	48	0
2004-03-11/14:50:03	2004-03-11/14:53:41	716	6	2	85	218	1	132	77	0
2004-03-11/15:10:11	2004-03-11/15:13:49	685	6	2	94	218	0	128	109	0
2004-03-11/22:00:01	2004-03-11/22:03:15	631	7	2	93	194	0	129	66	0
2004-03-21/16:29:12	2004-03-21/16:31:29	411	6	8	51	137	0	111	37	0
2004-03-21/21:01:19	2004-03-21/21:05:50	415	5	6	47	271	0	129	30	0
2004-03-26/14:25:48	2004-03-26/14:27:33	478	9	5	84	105	0	99	44	0
2004-03-30/12:02:07	2004-03-30/12:06:54	561	4	2	69	287	0	141	74	0
2004-03-30/18:42:15	2004-03-30/18:49:15	573	4	2	67	420	0	171	94	0
2004-04-06/15:05:09	2004-04-06/15:06:42	291	19	0	433	93	0	144	259	b
2004-04-06/15:28:23	2004-04-06/15:29:35	321	17	0	396	72	2	112	172	c
2004-04-06/16:32:16	2004-04-06/16:34:22	513	9	1	183	126	0	111	175	0
2004-04-07/04:42:48	2004-04-07/04:47:23	524	4	2	58	275	0	154	56	0
2004-04-09/04:25:58	2004-04-09/04:29:00	533	7	8	59	182	0	137	53	0
2004-04-13/20:00:04	2004-04-13/20:02:25	281	13	0	344	141	1	156	274	b f g
2004-04-13/20:21:33	2004-04-13/20:24:18	254	11	0	269	165	0	164	197	g
2004-04-26/00:51:24	2004-04-26/00:53:09	473	4	2	66	105	1	113	247	b

Table B.6: The event list including event characteristics for 2004 continued. See key in Table B.1 for variable details.

Start Time	End Time	SW	BF	D	AS	Dur	T	BR	ES	Out
2005-01-02/16:01:40	2005-01-02/16:06:50	548	20	1	400	310	0	139	242	b
2005-01-02/18:05:23	2005-01-02/18:09:36	704	8	2	125	253	0	150	119	0
2005-01-07/12:36:28	2005-01-07/12:42:50	563	8	6	76	382	0	173	63	0
2005-01-09/18:33:29	2005-01-09/18:35:34	336	17	2	252	125	0	121	90	f g
2005-01-09/20:52:46	2005-01-09/20:57:19	451	7	5	64	273	0	120	48	0
2005-01-12/00:17:30	2005-01-12/00:19:09	415	13	21	64	99	0	87	39	e
2005-01-12/03:08:04	2005-01-12/03:12:04	432	15	35	56	240	0	120	48	0
2005-01-12/06:51:16	2005-01-12/06:52:22	602	14	10	98	66	0	125	34	0
2005-01-12/06:54:43	2005-01-12/06:56:02	605	14	10	100	79	0	99	26	0
2005-01-12/07:29:08	2005-01-12/07:30:35	574	14	10	97	87	0	122	47	0
2005-01-12/11:12:16	2005-01-12/11:17:35	611	9	6	81	319	0	135	56	0
2005-01-12/11:32:26	2005-01-12/11:37:20	615	8	5	83	294	0	166	612	b
2005-01-14/18:05:28	2005-01-14/18:11:13	546	5	4	52	345	0	104	46	0
2005-01-17/06:03:28	2005-01-17/06:09:33	498	5	6	48	365	0	165	63	0
2005-01-18/22:46:44	2005-01-18/22:54:58	371	30	2	422	494	-2	167	461	b
2005-01-21/13:03:08	2005-01-21/13:07:58	478	4	4	49	290	0	155	131	0
2005-01-21/17:07:51	2005-01-21/17:14:00	685	18	10	122	369	0	169	159	0
2005-01-21/17:43:54	2005-01-21/17:49:51	876	14	14	81	357	0	170	42	0
2005-01-21/18:36:04	2005-01-21/18:41:44	913	31	12	193	340	0	176	96	0
2005-01-21/18:42:54	2005-01-21/18:48:34	929	35	33	134	340	0	178	91	0

Table B.7: The event list including event characteristics for 2005. See key in Table B.1 for variable details.

Start Time	End Time	SW	BF	D	AS	Dur	T	BR	ES	Out
2005-01-24/00:40:17	2005-01-24/00:43:15	571	6	2	95	178	0	152	398	b f
2005-01-31/04:46:20	2005-01-31/04:52:00	561	7	5	63	340	0	171	67	0
2005-02-07/18:55:40	2005-02-07/18:56:59	693	9	4	96	79	0	111	51	0
2005-02-09/07:03:14	2005-02:09/07:06:04	705	7	3	88	170	0	139	71	0
2005-02-09/16:31:45	2005-02-09/16:38:39	711	5	2	68	414	0	168	96	0
2005-02-09/19:21:39	2005-02-09/19:28:29	708	5	2	68	410	0	174	52	0
2005-02-10/01:23:51	2005-02-10/01:31:02	702	5	2	68	431	0	172	53	f
2005-02-14/21:25:04	2005-02-14/21:29:09	389	6	5	54	245	0	118	30	0
2005-02-26/08:33:20	2005-02-26/08:36:55	538	4	6	43	215	0	149	28	0
2005-02-26/11:14:04	2005-02-26/11:21:32	524	6	5	56	448	0	151	358	b
2005-02-28/05:34:18	2005-02-28/05:41:00	586	6	4	68	402	0	113	44	f
2005-02-28/09:52:20	2005-02-28/09:56:37	583	6	3	72	257	0	115	56	0
2005-02-28/21:52:50	2005-02-28/21:58:59	610	5	2	68	369	0	132	87	0
2005-03-01/01:00:23	2005-03-01/01:06:07	614	5	3	65	344	0	146	43	0
2005-03-07/21:26:10	2005-03-07/21:28:14	705	5	2	80	124	0	115	60	0
2005-03-22/05:55:58	2005-03-22/06:02:28	372	4	3	53	390	0	178	29	0
2005-03-24/13:52:44	2005-03-24/13:56:24	346	11	27	48	220	0	111	41	0
2005-04-14/13:13:35	2005-04-14/13:18:46	530	4	2	59	311	0	149	30	0
2005-04-15/02:46:12	2005-04-15/02:50:59	520	4	3	48	287	0	155	38	0
2005-04-21/16:09:11	2005-04-21/16:14:01	260	22	1	485	290	0	113	100	0

Table B.8: The event list including event characteristics for 2005 continued. See key in Table B.1 for variable details.

Start Time	End Time	SW	BF	D	AS	Dur	T	BR	ES	Out
2006-01-16/11:52:21	2006-01-16/11:59:11	441	7	12	46	410	0	142	22	0
2006-01-16/13:56:30	2006-01-16/14:00:26	442	6	13	41	236	0	165	43	0
2006-01-26/14:05:41	2006-01-26/14:10:02	568	10	5	95	261	0	126	54	0
2006-01-26/15:13:02	2006-01-26/15:16:29	568	9	7	80	207	0	111	55	0
2006-02-16/12:53:42	2006-02-16/12:59:26	530	5	6	49	344	0	141	44	0
2006-02-16/13:08:40	2006-02-16/13:10:23	539	6	5	55	103	0	124	49	0
2006-02-16/13:35:46	2006-02-16/13:37:37	534	5	6	52	111	0	119	31	0
2006-02-21/12:57:06	2006-02-21/13:02:25	655	5	3	59	319	0	155	47	0
2006-02-21/13:37:34	2006-02-21/13:42:57	654	5	3	62	323	1	148	69	0
2006-02-26/10:08:48	2006-02-26/10:15:37	351	6	9	47	409	0	128	32	0
2006-04-09/14:39:16	2006-04-09/14:40:47	632	13	9	97	91	0	156	60	0
2006-04-09/15:22:10	2006-04-09/15:24:19	621	10	8	78	129	0	127	36	0
2006-04-09/19:59:08	2006-04-09/20:00:14	610	11	9	82	66	0	96	41	0
2006-04-09/20:06:02	2006-04-09/20:09:12	605	10	8	78	190	0	139	24	g
2006-04-14/22:13:48	2006-04-14/22:19:06	515	6	5	61	318	0	141	37	0
2006-04-19/16:22:22	2006-04-19/16:23:33	261	8	4	92	71	0	126	161	0
2006-04-19/16:24:55	2006-04-19/16:26:47	255	15	1	257	112	1	101	114	0

Table B.9: The event list including event characteristics for 2006. See key in Table B.1 for variable details.

Start Time	End Time	SW	BF	D	AS	Dur	T	BR	ES	Out
2007-01-06/04:18:52	2007-01-06/04:21:34	315	11	0	285	162	0	134	456	b
2007-01-06/04:24:20	2007-01-06/04:28:08	363	11	0	300	228	0	156	130	e
2007-01-10/19:56:48	2007-01-10/20:00:32	416	5	6	51	224	0	113	32	e
2007-01-11/06:40:30	2007-01-11/06:46:15	434	7	9	51	345	0	154	25	d e
2007-01-15/14:25:36	2007-01-15/14:32:27	540	8	7	65	411	0	175	34	f
2007-01-17/21:09:01	2007-01-17/21:14:41	646	5	2	66	340	0	148	52	f
2007-01-18/06:33:13	2007-01-18/06:39:55	619	4	1	72	402	1	164	74	0
2007-01-20/03:03:09	2007-01-20/03:06:53	627	4	1	70	224	0	147	82	0
2007-01-29/16:58:12	2007-01-29/17:04:09	591	14	9	99	357	0	153	40	0
2007-01-29/18:34:09	2007-01-29/18:36:05	597	13	7	105	116	0	109	63	0
2007-01-29/19:37:03	2007-01-29/19:38:59	577	13	6	116	116	0	125	61	e
2007-01-29/19:43:53	2007-01-29/19:47:54	610	8	6	73	241	0	167	42	0
2007-01-29/23:46:18	2007-01-29/23:53:58	679	4	2	58	460	0	120	45	0
2007-01-30/05:53:49	2007-01-30/05:59:17	658	5	3	71	328	0	153	51	0
2007-01-30/06:00:44	2007-01-30/06:04:49	653	5	2	74	245	0	146	74	0
2007-01-31/22:01:12	2007-01-31/22:24:02	621	3	1	54	170	0	116	58	0
2007-02-01/03:41:23	2007-02-01/03:48:26	608	3	1	52	423	0	175	86	0
2007-02-01/11:28:51	2007-02-01/11:35:29	565	3	1	48	398	0	138	62	0
2007-02-05/23:55:15	2007-02-06/00:01:20	337	5	8	43	365	0	149	23	0
2007-02-06/01:04:43	2007-02-06/01:11:30	356	6	8	47	407	0	139	22	0
2007-02-06/14:02:35	2007-02-06/14:06:40	370	6	8	49	245	0	109	35	0
2007-02-08/01:14:31	2007-02-08/01:21:30	444	5	4	60	419	0	176	37	0
2007-02-08/08:48:58	2007-02-08/08:55:11	452	4	4	48	373	0	151	59	0
2007-02-08/11:38:27	2007-02-08/11:45:18	448	3	4	40	411	0	158	27	0
2007-02-08/19:02:44	2007-02-08/19:08:08	452	4	3	51	324	0	172	39	0
2007-02-12/23:43:01	2007-02-12/23:46:41	549	12	7	93	220	0	125	31	0

Table B.10: The event list including event characteristics for 2007. See key in Table B.1 for variable details.

Start Time	End Time	SW	BF	D	AS	Dur	T	BR	ES	Out
2007-02-13/06:08:33	2007-02-13/06:13:28	508	6	5	60	295	0	150	28	0
2007-02-13/09:15:49	2007-02-13/09:22:28	476	7	6	62	399	0	150	33	0
2007-02-13/11:01:15	2007-02-13/11:8:01	464	6	6	57	406	0	169	38	0
2007-03-06/14:19:51	2007-03-06/14:24:25	507	8	4	85	274	0	136	47	g
2007-03-06/15:54:59	2007-03-06/15:58:35	523	7	6	68	216	0	139	37	0
2007-03-06/16:01:50	2007-03-06/16:05:42	528	9	5	86	232	0	151	47	0
2007-03-11/06:34:08	2007-03-11/06:40:09	297	4	4	46	361	0	151	38	0
2007-03-13/18:54:46	2007-03-13/18:56:43	653	4	2	64	117	0	134	66	0
2007-03-13/22:25:32	2007-03-13/22:30:47	668	4	2	64	315	0	177	98	0
2007-03-14/01:29:48	2007-03-14/01:35:20	644	5	2	75	332	0	142	75	0
2007-03-15/22:04:19	2007-03-15/22:09:09	576	3	2	44	290	1	170	92	0
2007-03-18/17:40:17	2007-03-18/17:45:57	439	3	2	41	340	0	147	85	0
2007-03-23/17:40:30	2007-03-23/17:47:21	322	5	17	30	411	0	179	87	0
2007-04-01/09:19:13	2007-04-01/09:24:16	501	7	9	56	303	0	144	35	0
2007-04-01/15:09:57	2007-04-01/15:15:09	549	5	4	51	312	0	156	42	0
2007-04-23/02:21:32	2007-04-23/02:28:10	440	9	17	51	398	0	139	40	0
2007-04-23/09:00:00	2007-04-23/09:06:10	499	4	3	47	370	0	148	25	0
2007-04-27/17:36:18	2007-04-27/17:39:21	515	7	8	58	183	0	172	28	0
2007-05-02/15:38:17	2007-05-02/15:39:19	235	7	0	167	62	0	126	70	a
2007-05-02/16:35:45	2007-05-02/16:36:47	322	3	2	49	62	0	95	275	b
2007-05-02/17:45:24	2007-05-02/17:46:55	252	8	0	212	91	0	171	156	0
2007-05-02/17:54:36	2007-05-02/17:06:52	268	10	0	225	136	0	166	114	0
2007-05-02/18:03:35	2007-05-02/18:06:46	260	9	1	203	191	0	165	195	0
2007-05-02/18:22:28	2007-05-02/18:23:30	266	11	1	235	62	0	120	67	0
2007-05-07/14:13:42	2007-05-07/14:16:28	397	17	13	103	166	0	124	46	0

Table B.11: The event list including event characteristics for 2007 continued. See key in Table B.1 for variable details.

Start Time	End Time	SW	BF	D	AS	Dur	T	BR	ES	Out
2008-01-02/23:57:31	2008-01-02/23:59:19	216	12	1	243	108	0	140	112	a
2008-01-03/03:29:38	2008-01-03/03:31:01	219	8	9	58	83	0	162	131	a g
2008-01-07/09:00:53	2008-01-07/09:07:55	446	16	0	410	422	0	60	343	b
2008-01-07/11:21:59	2008-01-07/11:23:18	654	4	1	88	79	0	156	108	g
2008-01-07/12:53:52	2008-01-07/12:57:58	634	4	1	98	246	0	138	185	0
2008-01-09/23:50:11	2008-01-09/23:53:19	300	11	0	267	188	1	126	249	b f
2008-01-10/00:20:46	2008-01-10/00:25:42	306	11	0	279	296	0	139	277	b e g
2008-01-10/01:03:48	2008-01-10/01:11:51	283	11	0	324	483	0	149	259	b
2008-01-10/03:47:54	2008-01-10/03:50:07	271	13	0	311	133	0	167	276	b f
2008-01-12/14:48:15	2008-01-12/14:55:03	431	6	5	60	408	0	155	35	0
2008-01-14/13:04:38	2008-01-14/13:11:27	646	5	3	69	409	0	119	83	e
2008-01-14/14:21:10	2008-01-14/14:24:30	675	4	3	52	200	0	137	39	e
2008-01-14/14:27:42	2008-01-14/14:31:23	667	3	3	40	221	1	164	47	d
2008-01-14/19:41:44	2008-01-14/19:48:28	662	4	2	67	404	0	133	58	e g
2008-01-14/20:22:15	2008-01-14/20:29:04	672	4	2	70	409	0	169	68	g
2008-01-15/00:11:45	2008-01-15/00:15:52	676	4	1	71	247	1	147	62	f g
2008-01-15/02:12:54	2008-01-15/02:19:47	627	4	1	68	413	-1	149	628	b f g
2008-01-17/03:33:08	2008-01-17/03:39:10	596	4	2	63	362	0	167	70	0
2008-01-19/08:20:02	2008-01-19/08:23:39	612	4	2	67	217	0	129	55	0
2008-01-30/21:51:08	2008-01-30/21:53:05	213	10	1	164	117	0	128	177	a
2008-02-02/07:59:53	2008-02-02/08:07:11	605	4	2	58	438	0	175	38	0
2008-02-10/10:27:15	2008-02-10/10:32:11	541	11	9	82	296	0	128	38	0
2008-02-11/19:26:11	2008-02-11/19:32:18	664	4	1	69	367	0	171	84	0
2008-02-11/23:38:50	2008-02-11/23:43:54	679	3	1	56	304	0	158	77	0
2008-02-12/05:44:02	2008-02-12/05:51:28	452	4	1	77	446	1	172	736	b e

Table B.12: The event list including event characteristics for 2008. See key in Table B.1 for variable details.

Start Time	End Time	SW	BF	D	AS	Dur	T	BR	ES	Out
2008-02-21/23:28:44	2008-02-21/23:35:54	492	3	3	40	430	0	171	37	0
2008-02-24/14:09:06	2008-02-24/14:14:31	471	4	4	45	325	0	123	36	0
2008-02-29/01:56:51	2008-02-29/02:00:16	568	7	4	79	205	0	135	40	f
2008-03-09/05:19:28	2008-03-09/05:27:11	517	14	10	97	463	0	177	46	e
2008-03-09/11:35:44	2008-03-09/11:42:16	581	8	6	77	392	0	173	35	0
2008-03-09/18:23:38	2008-03-09/18:29:24	633	3	2	51	346	0	127	53	0
2008-03-09/22:09:33	2008-03-09/22:12:08	638	4	2	67	155	1	108	72	g
2008-03-14/15:30:19	2008-03-14/15:33:56	601	3	2	55	217	0	159	44	f
2008-03-23/14:59:04	2008-03-23/15:03:39	501	3	4	41	275	0	164	32	0
2008-03-23/15:26:07	2008-03-23/15:31:33	475	5	5	55	326	0	127	365	b
2008-03-27/23:58:44	2008-03-28/00:02:04	626	5	1	91	200	0	107	88	0
2008-03-28/12:27:57	2008-03-28/12:31:43	597	4	1	80	226	0	142	124	0
2008-03-28/14:09:42	2008-03-28/14:11:35	623	4	1	85	113	1	103	100	0
2008-04-04/15:04:50	2008-04-04/15:12:17	480	10	13	61	447	0	150	28	0
2008-04-04/18:48:39	2008-04-04/18:53:14	460	12	14	69	275	0	122	34	0
2008-04-08/21:22:34	2008-04-08/21:27:30	688	3	1	59	296	2	147	108	c
2008-04-09/07:02:00	2008-04-09/07:08:20	671	2	1	47	380	0	172	127	0
2008-04-14/13:47:05	2008-04-14/13:49:31	310	10	0	249	146	0	114	206	b
2008-04-16/11:46:55	2008-04-16/11:52:17	457	10	12	66	322	0	172	39	0
2008-04-16/19:15:58	2008-04-16/19:20:42	547	4	3	52	284	0	154	50	0
2008-04-19/03:51:35	2008-04-19/03:55:08	505	3	3	37	213	0	114	41	0
2008-04-23/13:08:49	2008-04-23/13:13:11	569	7	3	87	262	0	145	35	0
2008-04-23/14:35:12	2008-04-23/14:39:10	576	6	2	94	238	0	176	71	0
2008-04-28/08:34:58	2008-04-28/08:41:47	466	4	4	45	409	0	158	28	0
2008-05-05/13:36:06	2008-05-05/13:43:29	583	4	2	72	443	0	172	553	b

Table B.13: The event list including event characteristics for 2008 continued. See key in Table B.1 for variable details.

Start Time	End Time	SW	BF	D	AS	Dur	T	BR	ES	Out
2009-02-14/13:06:42	2009-02-14/13:10:40	493	5	7	39	238	0	152	21	g
2009-02-15/08:19:26	2009-02-15/08:23:04	523	5	3	60	218	0	114	38	0
2009-02-22/12:57:27	2009-02-22/13:02:37	397	4	4	44	310	0	96	30	0
2009-02-24/09:02:02	2009-02-24/09:08:57	431	3	3	39	415	0	163	56	0
2009-02-27/09:43:44	2009-02-27/09:49:27	507	7	7	64	343	0	112	28	0
2009-02-27/10:25:59	2009-02-27/10:29:57	536	7	6	66	238	0	146	27	0
2009-03-03/02:23:37	2009-03-03/02:31:38	213	4	2	67	481	0	173	155	a
2009-03-08/08:24:22	2009-03-08/08:31:16	407	8	10	56	414	0	169	43	f g
2009-03-08/15:17:16	2009-03-08/15:23:16	433	4	5	39	360	0	129	36	e
2009-03-13/04:45:59	2009-03-13/04:48:33	526	9	6	80	154	0	128	53	0
2009-03-24/20:33:49	2009-03-24/20:40:39	454	4	4	41	410	0	172	39	0
2009-03-24/20:46:31	2009-03-24/20:53:25	459	4	3	54	414	0	126	49	0
2009-03-25/01:01:40	2009-03-25/01:05:06	482	4	3	45	206	0	145	51	0
2009-04-17/21:32:20	2009-04-17/21:38:49	415	6	6	57	389	0	153	49	0
2009-04-18/02:00:18	2009-04-18/02:03:01	448	5	9	38	163	0	130	27	g
2009-04-18/05:43:04	2009-04-18/05:48:43	443	6	4	66	339	0	133	30	0
2009-04-29/23:29:31	2009-04-29/23:35:14	348	3	5	34	343	0	132	33	0
2009-05-06/18:57:58	2009-05-06/19:04:31	399	4	6	36	393	0	138	30	0
2009-05-07/01:29:01	2009-05-07/01:33:08	437	5	6	46	247	0	123	58	0
2009-05-11/20:25:49	2009-05-11/20:28:40	275	10	2	143	171	0	142	140	0
2009-05-11/20:55:48	2009-05-11/20:58:32	276	9	1	167	164	0	138	121	d

Table B.14: The event list including event characteristics for 2009. See key in Table B.1 for variable details.

Start Time	End Time	SW	BF	D	AS	Dur	T	BR	ES	Out
2010-01-05/00:14:35	2010-01-05/00:21:31	217	11	7	92	416	0	143	61	a d e
2010-01-16/02:34:32	2010-01-16/02:45:40	329	9	1	164	668	0	159	191	0
2010-01-16/03:23:14	2010-01-16/03:25:41	257	9	0	300	147	0	99	262	b
2010-01-20/18:11:10	2010-01-20/18:14:31	410	6	12	43	201	0	176	34	0
2010-01-20/18:26:16	2010-01-20/18:31:10	424	10	12	67	294	0	165	26	0
2010-01-20/20:21:15	2010-01-20/20:26:13	494	9	10	62	298	0	134	27	0
2010-01-21/03:21:44	2001-01-21/03:28:02	312	9	0	234	378	1	83	182	g
2010-01-24/23:49:49	2010-01-24/23:56:40	366	3	4	31	411	0	138	26	e f g
2010-01-25/17:38:36	2010-01-25/17:48:12	353	4	5	43	576	0	170	58	0
2010-02-03/10:32:30	2010-02-03/10:33:33	532	3	2	56	63	0	87	40	0
2010-02-12/04:33:03	2010-02-12/04:34:14	355	6	5	61	71	0	93	33	f g
2010-02-25/20:01:11	2010-02-25/20:08:49	363	4	4	47	458	0	135	43	0
2010-03-07/02:07:52	2010-03-07/02:14:48	378	7	13	46	416	0	156	24	0
2010-03-11/12:59:35	2010-03-11/13:04:42	457	4	4	49	307	0	126	43	0
2010-03-14/01:14:59	2010-03-14/01:20:18	368	5	2	78	319	0	156	83	g
2010-03-16/12:23:01	2010-03-16/12:28:04	381	5	5	50	303	0	150	36	0
2010-03-18/19:44:01	2010-03-18/19:50:45	409	3	6	28	404	0	150	33	0
2010-03-27/02:50:06	2010-03-27/02:56:49	383	7	5	69	403	0	105	33	0
2010-04-05/11:26:24	2010-04-05/11:28:26	716	16	5	158	122	0	136	36	f
2010-04-05/12:30:07	2010-04-05/12:36:33	726	21	7	162	386	0	123	52	0

Table B.15: The event list including event characteristics for 2010. See key in Table B.1 for variable details.

2010-04-07/01:27:30	2010-04-07/01:41:10	306	17	0	459	820	16	173	1940	c d
2010-04-07/07:14:17	2010-04-07/07:19:19	597	4	2	64	302	1	119	93	e f
2010-04-07/11:59:39	2010-04-07/12:05:57	585	4	1	64	378	0	126	94	0
2010-04-14/11:07:10	2010-04-14/11:14:06	398	5	6	44	416	0	175	40	0
2010-04-16/18:50:51	2010-04-16/18:57:42	442	3	5	37	411	0	144	35	0
2010-04-29/18:22:45	2010-04-29/18:27:47	361	2	5	28	302	0	160	56	0
2010-05-02/11:22:55	2010-05-02/11:28:19	393	17	35	63	324	0	129	39	0
2010-05-02/15:08:02	2010-05-02/15:12:10	549	18	12	113	248	0	109	26	0
2010-05-02/15:51:02	2010-05-02/15:53:08	557	12	11	83	126	0	114	28	f
2010-05-07/01:53:57	2010-05-07/02:00:53	515	4	4	48	416	0	169	59	0
2010-05-08/22:33:43	2010-05-08/22:37:21	282	6	1	145	218	0	119	268	b
2010-05-08/22:46:11	2010-05-08/22:48:54	289	9	0	218	163	1	153	163	e
2010-05-09/11:40:00	2010-05-09/11:42:28	313	7	1	134	148	0	158	163	0
2010-05-09/11:48:20	2010-05-09/11:49:57	263	8	1	168	97	1	142	226	b d e
2010-05-09/11:54:39	2010-05-09/11:56:40	270	7	1	158	121	0	160	159	e
2010-05-09/11:58:09	2010-05-09/11:59:58	264	7	0	170	109	0	165	298	b
2010-05-15/16:45:57	2010-05-15/16:50:18	217	7	1	152	261	0	158	136	a e
2010-05-15/18:06:21	2010-05-15/18:10:24	239	9	1	166	243	0	152	237	a b e
2010-05-15/20:44:36	2010-05-15/20:46:17	272	7	1	142	101	0	114	171	e g
2010-05-15/20:47:28	2010-05-15/20:49:51	248	8	1	140	143	0	140	300	a b e g
2010-05-15/20:53:26	2010-05-15/20:56:09	231	8	1	175	163	0	135	160	a d e g

Table B.16: The event list including event characteristics for 2010 continued. See key in Table B.1 for variable details.

Start Time	End Time	SW	BF	D	AS	Dur	T	BR	ES	Out
2011-01-04/05:50:27	2011-01-04/05:54:31	432	5	4	53	244	0	131	29	g
2011-01-06/05:45:21	2011-01-06/05:46:24	226	11	20	52	63	0	96	61	a
2011-01-08/18:48:29	2011-01-08/18:52:58	613	3	1	72	269	-1	171	48	0
2011-01-11/03:22:56	2011-01-11/03:24:20	370	8	6	76	84	1	162	184	f
2011-01-15/01:18:43	2011-01-15/01:22:43	294	16	2	242	240	0	156	236	b f g
2011-01-15/01:26:47	2011-01-15/01:28:24	415	11	3	146	97	0	122	124	0
2011-01-15/07:10:39	2011-01-15/07:16:36	294	14	0	417	357	0	147	315	b g
2011-01-17/08:06:55	2011-01-17/08:13:39	376	15	0	421	404	0	94	351	b e
2011-01-19/12:28:13	2011-01-19/12:31:56	536	3	3	42	223	0	162	43	e
2011-02-11/02:38:46	2011-02-11/02:42:38	344	5	3	57	232	0	103	45	0
2011-02-11/02:46:08	2011-02-11/02:53:17	274	10	3	132	429	0	131	141	0
2011-02-11/11:32:10	2011-02-11/11:37:29	338	5	7	45	319	0	123	33	0
2011-02-16/06:34:42	2011-02-16/06:36:23	450	4	4	52	101	0	109	45	f
2011-02-18/03:35:00	2011-02-18/03:41:56	494	9	22	44	416	0	133	22	g
2011-02-18/10:33:38	2011-02-18/10:37:26	491	6	7	51	228	0	162	41	fg
2011-02-18/11:14:28	2011-02-18/11:15:35	512	20	2	259	67	0	143	46	g
2011-02-18/11:40:25	2011-02-18/11:47:18	509	5	4	55	413	0	150	56	0
2011-02-18/13:16:40	2011-02-18/13:22:55	535	9	1	154	375	0	179	122	0
2011-02-20/17:14:53	2011-02-20/17:18:57	422	5	2	74	244	0	122	85	0
2011-02-25/13:12:49	2011-02-25/13:19:46	348	5	8	45	417	0	163	41	0
2011-02-26/19:59:30	2011-02-26/20:06:05	331	5	6	48	395	0	170	24	0
2011-02-26/20:26:47	2011-02-26/20:33:44	330	4	5	43	417	0	138	38	0
2011-03-03/09:07:33	2011-03-03/09:12:49	566	3	4	36	316	0	167	139	0
2011-03-06/03:49:12	2011-03-06/03:56:09	521	5	4	60	417	0	163	49	0
2011-03-06/05:17;44	2011-03-06/05:20:37	510	4	4	49	173	0	173	58	0

Table B.17: The event list including event characteristics for 2011. See key in Table B.1 for variable details.

Bibliography

Alfvén, H. (1942), Existence of Electromagnetic-Hydrodynamic Waves, *Nature*, *150*, doi:10.1038/150405d0

Argo, H. V., Asbridge, J. R., Bame, S. J., Hundhausen, A. J., Strong, J. B., (1967), Observations of Solar Wind Plasma Changes across the Bow Shock, *Journal of Geophysical Research*, *72*, 1989, doi:10.1029/JZ072i007p01989

Asbridge, J. R., Bame, S. J., Strong, I. B., (1968) Outward flow of protons from the Earth's bow shock, *Journal of Geophysical Research*, *73*, 57775782, doi: 10.1029/JA073i017p05777

Axford, W. I., (2002), Connection and Reconnection, *Advances in Space Research*, *29*, doi:10.1016/S0273-1177(02)00019-4

Babcock, H. W., (1961), The topology of the Sun's Magnetic field and the 22 year cycle, *American Astronomical Society*, doi:10.1086/147060

Balogh, A., Dunlop, M. W., Cowley, S. W. H., Southwood, D. J, Thomlinson, J. G., Glassmeier, K. H., Musmann, G., Luhr, H., Buchert, S., Acuna, M. H., Fairfield, D. H., Slavin, J. A., Riedler, W., Schwingenschuh, K., Kivelson, M. G., (1997), The Cluster Magnetic Field Investigation, *Space Science Reviews*, *79*, doi:10.1023/A:1004970907748.

Balogh, A., Treumann R. A., (2013), Collisionless Shock Theory: The Shock Prob-

lem, *Physics of Collisionless Shocks, Space Plasma Shock Waves*, *ISSI Scientific Report*, 12

Baumjohann W., and Treumann R. A., (1997), Basics of Space Plasma Physics, *Imperial College Press*

Beyene, S., Owen, C. J., Walsh, A. P., Forsyth, C., Fazakerley, A. N., Kiehas, S., Dandouras, I., Lucek, E., (2011), Cluster observations of a transient signature in the magnetotail: implications for the mode of reconnection, *Annales Geophysicae*, *29*, 2131-2146, doi:10.5194/angeo-29-2131-2011

Beyene, S., (2013), Understanding the formation of magnetic field and plasma structures in the magnetotail via the reconnection process. *Doctoral thesis*, *UCL (University College London)*

Biernat, H. K., Heyn, M. F., Semenov, V. S., (1987), Unsteady Petschek reconnection, *Journal of Geophysical Research*, *92*, 3392-3396

Biskamp, D., (1985), Magnetic reconnection via current sheets, *Physical Fluids*, *29*, 1520-1531

Borrero, J. M., Ichimoto, K., (2011), Magnetic Structure of Sunspots, *Living Reviews in Solar Physics*, *4*, doi:10.12942/lrsp-2011-4

Bothmer, V. (2006), The Solar Atmosphere and Space Weather, *Solar System Update*, pp.1-53, doi:10.1007/3-540-37683-6

Boyd, T.J.M., Sanderson, J.J., (2003), The Physics of Space Plasmas, *Chapter 5: MHD shocks*

Bruno, R., Carbone, V., Veltri, P., Pietropaolo, E., Bavassano, B., (2001), Identifying intermittency events in the solar wind,*Planetary and Space Science*, *49*, 1201-1210, doi:10.1016/S0032-0633(01)00061-7

Bruno, R., D'Amicis, R., Bavassano, B., Carbone, V., Sorriso-Valvo, L., (2007), Scaling laws and coherent structures in the solar wind, *Planetary and Space Science*, *55*, 2233-2238, doi:10.1016/j.pss.2007.05.005

Bruno, R., and Carbone, V., (2013), The Solar Wind as a Turbulence Laboratory, *Living Reviews in Solar Physics*, *10*, 2,doi:10.12942/lrsp-2013-2

Bryant, D. A., Cline, T. L., Desai, U. D., McDonald, F. B., (1963), New Evidence for Long-Lived Solar Streams in Interplanetary Space, *Physical Review Letters*, *11*, 144-146, doi:10.1103/PhysRevLett.11.144

Burch, J. L. and Phan, T. D., (2016), Magnetic reconnection at the dayside magnetopause: Advances with MMS, *Geophysical Research Letters*, *43*, doi: 10.1002/2016GL069787

Carlson, C. W., Curtis, D. W., Paschmann, G., Michael, W., (1982), An instrument for rapidly measuring plasma distribution functions with high resolution, *Advances in Space Research*, *2*, 67-70, doi:10.1016/0273-1177(82)90151-X

Carrington, R. C., (1859), Description of a Singular Appearance seen in the Sun on September 1, 1859, *Monthly Notices of the Royal Astronomical Society*, *20*, 13-15, doi:10.1093/mnras/20.1.13

Chao J. K., Wu, D. J., Lin, C.-H., Yang, Y.-H., Wang, X.Y., Kessel, M., Chen S.H., Lepping R.P., (2002), Models for the Size and Shape of the Earth's

Magnetopause and Bow Shock, *COSPAR Colloquia Series*, *12*, 127-135, doi: 10.1016/S0964-2749(02)80212-8

Charbonneau, P., (2010), Dynamo Models of the Solar Cycle, *Living Reviews in Solar Physics*, *3*, doi:10.12942/lrsp-2010-3

Chen, L., Hesse, M., Wang, S., Gershman, D., Ergun, R., Pollock, C., Torbert, R., Bessho, N., Daughton, W., Dorelli, J., Giles, B., Strangeway, R., Russell, C., Khotyaintsev, Y., Burch, J., Moore, T., Lavraud, B., Phan, T., Avanov, L., (2016), Electron energization and mixing observed by MMS in the vicinity of an electron diffusion region during magnetopause reconnection, *Geophysical Research Letters*, 6036-6043, *43*, doi:10.1002/2016GL069215

Colak, T. and Qahwaji, R.,(2009), Automated Solar Activity Prediction: A hybrid computer platform using machine learning and solar imaging for automated prediction of solar flares, *Space Weather*, *7*, doi:10.1029/2008SW000401

Cowley, S. W. H. (1984) The Distant Geomagnetic Tail in Theory and Observation, in Magnetic Reconnection in Space and Laboratory Plasmas, *Magnetic Reconnection in Space and Laboratory Plasmas*, *228*, doi:10.1029/GM030p0228

Craig, I. J. D., Heerikhuisen, J., Watson, P. G., (2003), Hall Current Effects in Dynamic Magnetic Reconnection Solutions, *Physics of Plasmas*, *10*, doi:10.1063/1.1590980

Dandouras, I. Barthe, A., (2015), User Guide to the CIS measurements in the Cluster Active Archive, *Cluster Active Archive*

Davis, M. S. Phan, T. D. Gosling, J. T. Skoug, R. M., (2006), Detection of op-

positely directed reconnection jets in a solar wind current sheet, *Geophysical Research Letters*, *33*, doi:10.1029/2006GL026735

De Hoffmann, F. and Teller, E., (1950), Magneto-Hydrodynamic Shocks, *Physical Review Letters*, *80*, 692-703, doi:10.1103/PhysRev.80.692

Dungey, J. W., (1953), The motion of magnetic fields, *Monthly Notices of the Royal Astronomical Society*, *113*, 679, doi:10.1093/mnras/113.6.679

Dungey, J. W., (1961), Interplanetary Magnetic Field and the Auroral Zones, *Physical Review Letters*, *6*, 47-48, doi:10.1103/PhysRevLett.6.47

Eddy, J. A., (1976), The Maunder Minimum, *Science*, *192*, 1189-1202, doi:10.1126/science.192.4245.1189,

Ergun, R. E., Goodrich, K. A., Wilder, F. D., Holmes, J. C., Stawarz, J. E., Eriksson, S., Sturner, A. P., Malaspina, D. M., Usanova, M. E., Torbert, R. B., Lindqvist, P.-A., Khotyaintsev, Y., Burch, J. L., Strangeway, R. J., Russell, C. T., Pollock, C. J., Giles, B. L., Hesse, M., Chen, L. J., Lapenta, G., Goldman, M. V., Newman, D. L., Schwartz, S. J., Eastwood, J. P., Phan, T. D., Mozer, F. S., Drake, J., Shay, M. A., Cassak, P. A., Nakamura, R., Marklund, G., (2016) Magnetospheric Multiscale Satellites Observations of Parallel Electric Fields Associated with Magnetic Reconnection, *Physical Review Letters*, *116*, doi:10.1103/PhysRevLett.116.235102

Eriksson, S. Gosling, J. T. Schwenn, R., (2006), Petschek-type magnetic reconnection exhausts in the solar wind well inside 1 AU: Helios, *AGU Fall Meeting Abstracts*

Eriksson, S., Gosling, J. T., Phan, T. D., Blush, L. M., Simunac, K. D. C., Krauss-

Varban, D., Szabo, A., Luhmann, J. G., Russell, C. T., Galvin, A. B., Acuña, M. H., (2009), Asymmetric shear flow effects on magnetic field configuration within oppositely directed solar wind reconnection exhausts, *Journal of Geophysical Research (Space Physics)*, *114*, doi:10.1029/2008JA013990,

ESA, (2013), Cluster: Mission Timeline, url = http://sci.esa.int/science-e/www/object/index.cfm?fobjectid=23160

Fairfield, D. H., (1969), Bow shock associated waves observed in the far upstream interplanetary medium, *Journal of Geophysical Research*, *74*, 3541, doi:10.1029/JA074i014p03541,

Fear, R. C., A. N. Fazakerley, C. J. Owen, E. A. Lucek (2005), A survey of flux transfer events observed by Cluster during strongly northward IMF, *Geophysical Research Letters*, *32*, doi:10.1029/2005GL023811

Fuselier, S. A., R. Frahm, W. S. Lewis, A. Masters, J Mukherjee, S. M. Petrinec, I. J. Sillanpaa (2014), The location of magnetic reconnection at Saturn's magnetopause: A comparison with Earth, *Journal of Geophysical Research (Space Physics),119*, doi:10.1002/2013JA019684

Giovanelli, R. G., (1947), Magnetic and Electric Phenomena in the Sun's Atmosphere associated with Sunspots, *Monthly Notices of the Royal Astronomical Society,*, *107*, 338, doi:10.1093/mnras/107.4.338,

Gosling, J. T., Asbridge, J. R., Bame, J., Strong, B., (1967), Vela 2 measurements of the magnetopause and bow shock positions, *Journal of Geophysical Research*, *72*, 101-112, doi:10.1029/JZ072i001p00101

Gosling, J. T., Hildner, E., MacQueen, R. M., Munro, R. H., Poland, A. I., Ross,

C. L., (1974) Mass ejections from the sun - A view from SKYLAB, *Journal of Geophysical Research*, *79*, 4581-4587, doi:10.1029/JA079i031p04581

Gosling, J. T., Hildner, E., MacQueen, R. M., Munro, R. H., Poland, A. I., Ross, C. L., (1976), The speeds of coronal mass ejection events, *Solar Physics*, *48*, 389-397, doi:10.1007/BF00152004

Gosling, J. T., Bame, S. J., Feldman, W. C., Paschmann, G., Sckopke, N., Russell, C. T., (1984), Suprathermal ions upstream from interplanetary shocks, *Journal of Geophysical Research*, *89*, 5409-5418, doi:10.1029/JA089iA07p05409,

Gosling, J. T. Birn, J. Hesse, M., Three-dimensional magnetic reconnection and the magnetic topology of coronal mass ejection events (1995), *Geophysical Research Letters*, *22*, 869-872, doi:10.1029/95GL00270,

Gosling, J. T., Skoug, R. M., McComas, D. J., Smith, C. W., (2005), Direct evidence for magnetic reconnection in the solar wind near 1 AU, *Journal of Geophysical Research (Space Physics)*, *110*, A01107, doi:10.1029/2004JA010809.

Gosling, J. T. Skoug, R. M. McComas, D. J. Smith, C. W., (2005a), Magnetic Disconnection From the Sun: Observations of a Reconnection Exhaust in the Solar Wind at the Heliospheric Current Sheet, *AGU Spring Meeting Abstracts*, A1

Gosling, J. T., Skoug, R. M., Haggerty, D. K., McComas, D. J., (2005b), Absence of energetic particle effects associated with magnetic reconnection exhausts in the solar wind, *Geophysical Research Letters*, *32*, 14113, doi:10.1029/2005GL023357

Gosling, J. T., Eriksson, S., Skoug, R. M., McComas, D. J., Forsyth, R. J., (2006),

Petschek-Type Reconnection Exhausts in the Solar Wind Well beyond 1 AU: Ulysses, *The Astrophysical Journal*, *644*, 613-621, doi:10.1086/503544

Gosling, J.T., McComas, D.J., Skoug, R.M., Smith C.W., (2006a), Magnetic reconnection at the heliospheric current sheet and the fomation of closed magnetic field lines in the solar wind. *Geophysical Research Letters*, *33*, doi: 10.1029/2006GL027188

Gosling, J. T., Eriksson, S., Schwenn, R., (2006b), Petschek-type magnetic reconnection exhausts in the solar wind well inside 1 AU: Helios, *Journal of Geophysical Research (Space Physics)*, *111*, doi:10.1029/2006JA011863

Gosling, J. T. Eriksson, S. Blush, L. M. Phan, T. D. Luhmann, J. G. McComas, D. J. Skoug, R. M. Acuna, M. H. Russell, C. T. Simunac, K. D. (2007), Five spacecraft observations of oppositely directed exhaust jets from a magnetic reconnection X-line extending $> 4.26 \times 10^6$ km in the solar wind at 1 AU,*Geophysical Research Letters*, *34*, doi:10.1029/2007GL031492,

Gosling, J. T. (2007a), Observations of Magnetic Reconnection in the Turbulent High-Speed Solar Wind, *The Astrophysical Journal Letters*, *671*, L73-L76, doi: 10.1086/524842,

Gosling, J. T. Eriksson, S. McComas, D. J. Phan, T. D. Skoug, R. M., (2007b), Multiple magnetic reconnection sites associated with a coronal mass ejection in the solar wind, *Journal of Geophysical Research (Space Physics)*, *112*, 8106, doi:10.1029/2007JA012418,

Gosling, J. T., Eriksson, S., Phan, T. D., Larson, D. E., Skoug, R. M., McComas, D. J., (2007c), Direct Evidence for Prolonged Magnetic Reconnection at a Con-

tinuous X-Line Within the Heliospheric Current Sheet, *AGU Spring Meeting Abstracts*

Gosling, J. T., Phan, T. D., Lin, R. P., Szabo, A., (2007d), Prevalence of magnetic reconnection at small field shear angles in the solar wind, *Geophysical Research Letters*, *34*, L15110, doi:10.1029/2007GL030706.

Gosling, J. T., (2009), Magnetic reconnection in the heliosphere: new insights from observations in the solar wind, *IAU Symposium*, 367-377, doi:10.1017/S1743921309029597

Gosling, J. T., (2010), Magnetic Reconnection in the Solar Wind: An Update, *Twelfth International Solar Wind Conference*, *1216*, 188-193, doi:10.1063/1.3395833,

Gosling, J. T. (2011), Magnetic Reconnection in the Solar Wind, *Space Science Review*, doi:10.1007/s11214-011-9747-2

Greenstadt, E. W., (1976), Phenomenology of the Earth's Bow Shock System. A Summary Description of Experimental Results, *58*, 13,doi:10.1007/978-94-010-1503-5_2

Güdel, M., (2007), The Sun in Time: Activity and Environment, *Living Reviews in Solar Physics*, *4*, doi:10.12942/lrsp-2007-3

Haisch, B. M. (1989), An Overview of Solar and Stellar Flare Research, *Solar and Stellar Flares*, doi:10.1007/BF00161684

Hapgood, M. A., (1992), Space physics coordinate transformations - A user guide, *Planetary and Space Science*, *40*, 711-717, doi:10.1016/0032-0633(92)90012-D

Hansen, R. T., Garcia, C. J., Grognard, R. J.-M., Sheridan, K. V., (1971), A coronal disturbance observed simultaneously with a white-light corona-meter and the 80 MHz Culgoora radioheliograph, *Proceedings of the Astronomical Society of Australia*, *2*, 57

Hansen, J., Kharecha, P., Sato, M., Masson-Delmotte, V., Ackerman, F., Beerling, D. J., Hearty, P. J., Hoegh-Guldberg, O., Hsu, S., Parmesan, C., Rockstrom, J., Rohling, E. J., Sachs, J., Smith, P., Steffen, K., Van Susteren,L., von Schuckmann, K., Zachos, J. C., (2013), Assessing Dangerous Climate Change: Required Reduction of Carbon Emissions to Protect Young People, Future Generations and Nature, *PLOS collections* doi:10.1371/journal.pone.0081648

Hassler, D. M., Dammasch, I. E., Lemaire, P., Brekke, P., Curdt, W., Mason, H. E., Vial, J.-C., Wilhelm, K., (1999), Solar Wind Outflow and the Chromospheric Magnetic Network, *Science*, *283*, 810, doi:10.1126/science.283.5403.810,

Hathaway, D. H., (2010), The Solar Cycle, *Living Reviews in Solar Physics*, *7*, doi:10.12942/lrsp-2010-1

Heyn, M. F., Biernat, H. K., Semenov, V. S., Kubyshkin, I. V., (1985), Dayside magnetopause reconnection, *Journal of Geophysical Research*, *90*, 1781-1785, doi:10.1029/JA090iA02p01781

Howard, R. A., Sheeley, Jr., N. R., Michels, D. J., Koomen, M. J., Coronal mass ejections - 1979-1981, *Journal of Geophysical Research*, *90*, 8173-8191, doi:10.1029/JA090iA09p08173

Howe, R., (2009), Solar Interior Rotation and its Variation, *Living Reviews in Solar Physics*, *6*, doi:10.12942/lrsp-2009-1

Hundhausen, A. J., (1973), Solar wind stream interactions and interplanetary heat conduction, *Journal of Geophysical Research*, *78*, 7996, doi:10.1029/JA078i034p07996

Hundhausen, A. J. and Burlaga, L. F., (1975), A model for the origin of solar wind stream interfaces, *Journal of Geophysical Research*, *80*, 1845-1848, doi:10.1029/JA080i013p01845

Hundhausen, A. J., and Gosling, J. T., (1976), Solar wind structure at large heliocentric distances - an interpretation of Pioneer 10 observations, *Journal of Geophysical Research*, *81*,1436-1440, doi:10.1029/JA081i007p01436

Huttunen, K. E. J., Bale, S. D., Phan, T. D., Davis, M., Gosling, J. T., (2007), Wind/WAVES observations of high-frequency plasma waves in solar wind reconnection exhausts, *Journal of Geophysical Research (Space Physics)*, *112*, 1102, doi:10.1029/2006JA011836

Ji, H., Yamada, M., Hsu, S., Kulsrud, R., Carter, T., Zaharia, S., (1999), Magnetic reconnection with Sweet-Parker characteristics in two-dimensional laboratory plasmas, *Physics of Plasmas*, *6*, 1743-1750, doi:10.1063/1.873432

Johnstone, A. D., Alsop, C., Burge, S., Carter, P. J., Coates, A. J., Coker, A. J., Fazakerley, A. N., Grande, M., Gowen, R. A., Gurgiolo, C., Hancock, B. K., Narheim, B., Preece, A., Sheather, P. H., Winningham, J. D., and Woodliffe, R. D. (1997), PEACE: a Plasma Electron And Current Experiment. *Space Science Reviews*, *79*, doi:10.1023/A:1004938001388

Kantrowitz, A., Petschek H. E., (1966), MHD Characteristics and Shock Waves, *Plasma Physics in Theory and Application*, *New York*

Karimabadia, H., Roytershteynb,V., Daughtonb, W., Gosling J. T., and Scudderd J. (2010), J. Why Is Reconnection in the Solar Wind so Different than in Other Environments? *AIP conference proceedings*, *1302* doi:10.1063/1.3529971

Kawano, H., and Russell, C. T., (1996), Survey of flux transfer events observed with the ISEE 1 spacecraft: Rotational polarity and the source region, *Geophysical Research Letters*, *101*, doi:10.1029/96JA02703

Kennel C. F., Edminston J. P., Hada T. (1985), A Quarter Century of Collisionless Shock Research, *Geophysical Monograph Series*, *34*, doi:10.1029/GM034p0001

Khotyaintsev, Yu. V., Graham, D. B., Norgren, C., Eriksson, E., Li, W., Johlander, A., Vaivads, A., Andr, M., Pritchett, P. L., Retin, A., Phan, T. D., Ergun, R. E., Goodrich, K., Lindqvist, P.-A., Marklund, G. T., Le Contel, O., Plaschke, F., Magnes, W., Strangeway, R. J., Russell, C. T., Vaith, H., Argall, M. R., Kletzing, C. A., Nakamura, R., Torbert, R. B., Paterson, W. R., Gershman, D. J., Dorelli, J. C., Avanov, L. A., Lavraud, B., Saito, Y., Giles, B. L., Pollock, C. J., Turner, D. L., Blake, J. D., Fennell, J. F., Jaynes, A., Mauk, B. H., Burch, J. L., (2016), Electron jet of asymmetric reconnection, *Geophysical Research Letters*, *43*, doi:10.1002/2016GL069064.

Kiehas, S. A., Semenov, V. S., Biernat H. K. (2009), Energy budget of the reconnection process, *Journal of Geophysical Research*, *Space Physics*, doi: 10.1029/2008JA013987

Kivelson M. G., and Russel, C. T., (1995) Introduction to Space Physics, *Cambridge University Press*

Kolmogorov, A., (1941), The Local Structure of Turbulence in Incompressible Vis-

cous Fluid for Very Large Reynolds' Numbers, *Akademiia Nauk SSSR Doklady*, *30*, 301-305

Kulsrud, R. M., (2001), Magnetic reconnection: Sweet-Parker versus Petschek, *53*, 417-422, doi:10.1186/BF03353251

Lee, L. C. and Fu, Z. F., (1986), Multiple X line reconnection: 1. A criterion for the transition from a single X line to a multiple X line reconnection, *Journal of Geophysical Research*, *91*, 6807-6815

Lepping, R. P., Acũna, M. H., Burlaga, L. F., Farrell, W. M., Slavin, J. A ., Schatten, K. H., Mariani, F., Ness, N. F., Neubauer, F. M., Whang, Y. C., Byrnes, J. B., Kennon, R. S., Panetta, P. V., Scheifele J., Worley, E. M. (1995), The Wind Magnetic Field Investigation, *Space Science Reviews*, *71*, doi:10.1007/BF00751330

Li, G., (2008), Identifing Current-Sheet like Structures in the Solar Wind, *The Astrophysical Journal*, *672*, doi:10.1086/525847

Lin, R. P., Anderson, K. A., Ashford, S., Carlson, C., Curtis, D., Ergun, R., Larson, D., McFadden, J., McCarthy, M., Parks, G. K., Rème, H., Bosqued, J. M., Coutelier, J., Cotin, F., D'Uston, C., Wenzel, K.-P., Sanderson, T. R., Henrion, J., Ronnet J. C., Paschmann, G., (1995), A Three-Dimensional Plasma and Energetic Particle Investigation for the Wind Spacecraft, *Space Science Reviews*, *71*, doi:10.1007/BF00751328,

Lu, P., and Ando, M., (2012), Difference of scattering geometrical optics components and line integrals of currents in modified edge representation, *Radio Sci.*, *47*, RS3007, doi:10.1029/2011RS004899.

Machado, M. E., Moore, R. L., Hernandez, A. M., Rovira, M. G., Hagyard, M. J., Smith, Jr., J. B., (1988), The observed characteristics of flare energy release. I - Magnetic structure at the energy release site, *The Astrophysical Journal*, *326*, 425-450, doi:10.1086/166106

Marsch, E., (2006), Kinetic Physics of the Solar Corona and Solar Wind, *Living Reviews in Solar Physics*, *3*, doi:10.12942/lrsp-2006-1

Matthaeus, W. H., Dmitruk, P.,Oughton, S., Mullan, D., (2003), Turbulent dissipation in the solar wind and corona, *AIP Conference Proceedings*, *679*, 427-432

McComas, D. J., Bame, S. J., Barker, P., Feldman, W. C., Phillips, J. L., Riley, P., Griffee, J. W., (1998), Solar Wind Electron Proton Alpha Monitor (SWEPAM) for the Advanced Composition Explorer, *Space Science Reviews*, *86*, doi:10.1023/A:1005040232597

McComas, D. J., Ebert, R. W., Elliott, H. A., Goldstein, B. E., Gosling, J. T., Schwadron, N. A., Skoug, R. M., (2008), Weaker solar wind from the polar coronal holes and the whole Sun, *Geophysical Research Letters*, *35*, 18103, doi:10.1029/2008GL034896,

McGregor, S. L., Hughes, W. J., Arge, C. N., Owens, M. J., Odstrcil, D., (2011), The distribution of solar wind speeds during solar minimum: Calibration for numerical solar wind modeling constraints on the source of the slow solar wind, *Journal of Geophysical Research: Space Physics*, *116*, doi:10.1029/2010JA015881.

Milan, S. E., Gosling, J. S., Hubert, B., (2012), Relationship between interplanetary parameters and the magnetopause reconnection rate quantified from ob-

servations of the expanding polar cap, *Journal of Geophysical Research*, *117*, doi:10.1029/2011JA017082

Meyer-Vernet, N., (2007), Basics of the Solar Wind, *Cambridge*

Moldwin, M. B., Ford, S., Lepping, R., Slavin, J., Szabo, A., (2007) Small-scale magnetic flux ropes in the solar wind, *Geophysical Research Letters*, *27*, 57-60, doi:10.1029/1999GL010724

Mullan, D. J. and Smith, C. W., (2006), Solar Wind Statistics at 1 AU: Alfven Speed and Plasma Beta, *Solar Physics*, *234*, doi:10.1007/s11207-006-2077-y

Mullan, D. J. (2009), Physics of the Sun: A first Course, *CRC Press*

Ness, N. F., Scearce, C. S., Seek, J. B., (1964), Initial Results of the Imp 1 Magnetic Field Experiment, *Journal of Geophysical Research 69*, 3531-3569, doi:10.1029/JZ069i017p03531

Nykyri, K., Otto, A., Büchner, J., Nikutowski, B., Baumjohann, W., Kistler L. M., Mouikis, C., (2003), Equator-S Observations of Boundary Signatures: FTE's or Kelvin-Helmholtz Waves? *Geophysical Monograph*, *133*, doi:10.1029/133GM20.

Ogilvie, K. W., and Coplan, M. A., Solar wind composition, *Reviews of Geophysics*, *33*, 1944-9208, doi:10.1029/95RG00122

Owen, C. J. and Cowley, S. W. H., (1987a), Simple models of time-dependent reconnection in a collision-free plasma with an application to substorms in the geomagnetic tail, *Planetary and Space Science*, *35*, 451-466, doi:10.1016/0032-0633(87)90102-4

Owen, C. J., and Cowley, S. W. H. (1987b), A note on current sheet stress balance

in the geomagnetic tail for asymmetrical tail lobe plasma conditions, *Planetary and Space Science*, *35*, doi:10.1016/0032-0633(87)90103-6

Parker, E. N., (1957), Sweet's Mechanism for Merging Magnetic Fields in Conducting Fluids, *Journal of geophysical research*, *62*, 509-520, doi10.1029/JZ062i004p00509

Parker, E. N., (1958), Dynamics of the Interplanetary Gas and Magnetic Fields, *Astrophysical Journal*, *128*, 664, doi:10.1086/146579

Parker, E. N., (1961) A quasi-linear model of plasma shock structure in a longitudinal magnetic field,*Journal of Nuclear Energy. Part C, Plasma Physics, Accelerators, Thermonuclear Research*, *2*, 146

Parker, E. N., (1963), The Solar-Flare Phenomenon and the Theory of Reconnection and Annihiliation of Magnetic Fields, *Astrophysical Journal Supplement*, *8*, doi:10.1086/190087.

Parker, E. N., (1965), Dynamical Theory of the Solar Wind, *Space Science Reviews*, *4*, 666-708, doi:10.1007/BF00216273

Parker, E. N., (1968), Dynamics of the Interplanetary Gas and Magnetic Field, *American Astronomical Society*, doi:10.1086/146579

Parks, G., Lee, E., Mozer, F., Wilber, M., Lucek, E., Dandouras, Y., Reme, H., Mazelle, C., Cao, J., Meziane, K., Goldstein, M., Escoubet, P., (2006), Larmor radius size density holes discovered in the solar wind upstream of the bow shock, *Physics of Plasmas*, *13*, doi:10.1063/1.2201056

Paschmann, G. Papamastorakis, I. Sckopke, N. Haerendel, G. Sonnerup, B. U. O. Bame, S. J. Asbridge, J. R. Gosling, J. T. Russel, C. T. Elphic, R. C., (1979),

Plasma acceleration at the earth's magnetopause - Evidence for reconnection, *Nature*, *282*, 243-246, doi:10.1038/282243a0

Paschmann, G., Daly, P. W., (1998), Analysis Methods for Multi-Spacecraft Data, *ESA Publications Division*

Paschmann, G., Haaland, S., Sonnerup, B.,Knetter, T. (2013), Discontinuities and Alfvénic fluctuations in the solar wind. *Ann. Geophys.*, *31*

Petschek, H. E. (1964), Magnetic Field Annihilation, *NASA Special Publication*, *50*, http://ukads.nottingham.ac.uk/abs/1964NASSP..50..425P, *Provided by the SAO/NASA Astrophysics Data System*

Phan, T. D., Gosling, J. T., Davis, M. S., Skoug, R. M., Øieroset, M., Lin, R. P., Lepping,R. P., McComas, D. J., Smith, C. W., Reme H., Balogh, A., (2006), A magnetic reconnection X-line Extending more than $390R_E$ in the Solar Wind, *Nature*, *439*, doi:10.1038/nature04393.

Phan, T. D., Paschmann, G., Twitty, C., Mozer, F. S., Gosling, J. T., Eastwood, J. P., Øieroset, M., Rème, H., Lucek, E. A., (2007), Evidence for magnetic reconnection initiated in the magnetosheath, *Geophysical Research Letters*, *34*, 14104, doi:10.1029/2007GL030343

Phan, T. D., Gosling J. T., Davis, M. S., (2009), Prevalence of extended reconnection X-lines in the solar wind at 1 AU, *Geophysical Research Lettters*, *36*, L09108, doi:10.1029/2009GL037713.

Phan, T. D., Gosling, J. T., Paschmann, G., Pasma, C., Drake, J. F., Øieroset, M., Larson, D., Lin, R. P., Davis, M. S., (2010), The Dependence of Magnetic Reconnection on Plasma β and Magnetic Shear: Evidence from Solar Wind

Observations, *The Astrophysical Journal Letters*, *719*, doi:10.1088/2041-8205/719/2/L199.

Phan T. D., Paschmann G., Gosling J. T., Oieroset M., Fujimoto M., Drake J. F., Angelopoulos V., (2013), The dependence of magnetic reconnection on plasma$\beta$and magnetic shear: Evidence from magnetopause observations, *Geophysical Research Letters*, *40*, doi:10.1029/2012GL054528

Popodopoulos K. (2009), Waves and Instabilities in Space Plasmas, *Springer*, doi:10.1007/978-3-642-00210-6

Priest E. R. (1985), The Magnetohydrodynamics of Current Sheets, *Rep. Prog. Phys*, doi:10.1088/0034-4885/48/7/002

Priest, E. R. and Forbes, T. G., (1986) New models for fast steady state magnetic reconnection, *Journal of Geophysical Research: Space Physics*, *91*, 2156-2202, doi:10.1029/JA091iA05p05579

Priest, E. R. and Forbes, T. G., (1992), Does fast magnetic reconnection exist?, *Journal of Geophysical Research*, *97*, 16757-16772

Primdahl, F, (1979), The fluxgate magnetometer, *Journal of Physics E: Scientific Instruments*, *12*, 241

Reme, H., Bosqued, J. M., Sauvaud, J. A., Cros, A., Dandouras, J., Aoustin, C., Bouyssou, J., Camus, T., Cuvilo, J., Martz, C., Medale, J. L., Perrier, H., Romefort, D., Rouzaud, J., D'Uston, C., Mobius, E., Crocker, K., Grano, M., Kistler, L. M., Popecki, M., Hovestadt, D., Klecker, B., Paschmann, G., Scholer, M., Carlson, C. W., Curtis, D. W., Lin, R. P., McFadden, J. P., Formisano, V., Amata, E., Bavassano-Cattaneo, M. B., Baldetti, P., Belluci, G., Bruno, R.,

Chionchio, G., di Lellis, A., Shelley, E. G., Ghielmetti, A. G., Lennartsson, W., Korth, A., Rosenbauer, H., Lundin, R., Olsen, S., Parks, G. K., McCarthy, M., and Balsiger, H.,(1997), The Cluster Ion Spectrometry (cis) Experiment, *Space Science Reviews*, *79*, doi:10.1023/A:1004929816409.

Retino, A., Sundkvist, D., Vaivads, A., Mozer, F., Andre, M., Owen, C. J., (2007), In situ evidence of magnetic reconnection in turbulent plasma, *Nature Physics*, *3*, 236-238

Rijnbeek, R. P., and Cowley, S. W. H., (1984), Magnetospheric flux erosion events are flux transfer events, *Nature*, *309*, doi:10.1038/309135a0

Russell, C. T., Smith, E. J., Tsurutani, B. T., Gosling, J. T., Bame, S. J., (1983), Multiple spacecraft observations of interplanetary shocks: Characteristics of the upstream ULF turbulence, *NASA Conference Publication*, *228*

Sato, T., (1979), Strong plasma acceleration by slow shocks resulting from magnetic reconnection, *Journal of Geophysical Research*, *84*, 7177-7190, doi: 10.1029/JA084iA12p07177

Scheper, R. A., and Hassam, A. B., (1998) Formation of Current Sheets in Two-dimensional Geometry, *The Astrophysical Journal*, *507*, 968, url=http://stacks.iop.org/0004-637X/507/i=2/a=968

Schindler, K., and Hornig, G., (2001), Encyclopedia of Astromomy and Astrophysics, *Magnetic Reconnection*, *Nature Publishing Group*

Schwadron, N. A., McComas, D. J., (2003), Solar Wind Scaling Law, *The Astrophysical Journal*, *599*, 1395-1403, doi:10.1086/379541,

Schwartz, S, J. (1998), Shock and Discontinuity Normals, Mach Numbers, and Related Parameters, *Analysis Methods for Multi-Spacecraft Data*, *10*

Semenov, V. S., Heyn, M. F., Kubyshkin, I. V., (1983), Reconnection of magnetic field lines in a nonstationary case, *Soviet Astronomy*, *27*, 660-665

Sibeck, D. G., Kudela, K., Mukai, T., Nemecek, Z., Safrankova, J., (2004), Radial dependence of foreshock cavities: a case study, *Annales Geophysicae*, *22*, 4143-4151

Slavin, J. A, Lepping, R. P., Gjerloev, J., Fairfield, D. H., Hesse, M., Owen, C. J., Moldwin, M. B., Nagai, T., Ieda, A., Mukai, T., (2003), Geotail observations of magnetic flux ropes in the plasma sheet, *Journal of Geophysical Research*, *108*, 1015

Smith, E. J. and Wolfe, J. H., (1976), Observations of interaction regions and corotating shocks between one and five AU - Pioneers 10 and 11, *Geophysical Research Letters*, *3*, 137-140, doi:10.1029/GL003i003p00137

Smith, C. W., L'Heureux, J., Ness, N. F., Acuña, M. H., Burlaga, L. F.,Scheifele, J., (1998), The ACE Magnetic Fields Experiment, *Space Science Reviews*, *86*, doi:10.1023/A:1005092216668

Speiser, T. W., (1973), Magnetospheric current sheets, *Radio Science*, *8*, 1944-799X, doi:10.1029/RS008i011p00973

Solanki, S. K.,(1996), Solar and stellar magnetic flux tubes (review), *Stellar surface structure: proceedings of the 176th Symposium of the International Astronomical Union*

Solanki, S. K., Wenzler, T., Schmitt, D., (2008), Moments of the latitudinal dependence of the sunspot cycle: a new diagnostic of dynamo models, *Astronomy and Astrophysics*, doi:10.1051/0004-6361:20054282

Sonnerup, B. U. O., Cahill, Jr., L. J., (1967), Magnetopause Structure and Attitude from Explorer 12 Observations, *Journal of Geophysical Research*, *72*, doi:10.1029/JZ072i001p00171

Sonnerup, B. U, O., Paschmann, G., Papamastorakis, I., Sckopke, N., Haerendel, G., Bame, S.J., Asbridge, J.R., Gosling, J.T., Russel, C.T. (1981), Evidence for Magnetic Field Reconnection at the Earth's Magnetopause, *Journal of Geophysical Research*, *86*, doi:10.1029/JA086iA12p10049

Sonnerup, B.U., Baum, P.J., Birn, J., Cowley, S.W.H., Forbes, T.G., Hassam, A.B., Kahler, S.W., Matthaeus, W.H., Park, W., Paschmann, G., Priest, E.R., (1984), Reconnection of magnetic fields. *NASA Reference Publication*, *1120*, Chapter 1.

Sonnerup, B. U. O., (1988), On the theory of steady state reconnection, *Computer Physics Communications*, *49*, 143 - 159, doi:10.1016/0010-4655(88)90222-6

Sonnerup, B. U. O., Papamatorakis, I., Paschmann, G., Lühr, H., (1990), The Magnetopause for Large Magnetic Shear: Analysis of Convection Electric Fields From AMPTE/IRM, *Journal of Geophysical Research*, **95**, doi:10.1029/JA095iA07p10541

Sonnerup, B. U. O., and Scheibe, M., (1998), Minimum and Maximum Variance Analysis, *Analysis Methods for Multi-Spacecraft data*, 185-220

Sweet, P. A., (1958), The Neutral Point Theory of Solar Flares, *Electromagnetic Phenomena in Cosmical Physics*, *IAU Symposium*, *6*, 123

Swisdak, M., Opher, M., Drake, J. F., Alouani Bibi, F., (2010), The Vector Direction of the Interstellar Magnetic Field Outside the Heliosphere, *The Astrophysical Journal*, *710*, doi:10.1088/0004-637X/710/2/1769.

Teh, W.-L., Sonnerup, B. U. Ö., Hu Q., Farrugia, C. J., (2009), Reconstruction of a large-scale reconnection exhaust structure in the solar wind, *Annales Geophysicae*, *27*, doi:10.5194/angeo-27-807-2009

Torbert, R. B., Russell, C. T., Magnes, W., Ergun, R. E., Lindqvist, P.-A., LeContel, O., Vaith, H., Macri, J., Myers, S., Rau, D., Needell, J., King, B., Granoff, M., Chutter, M., Dors, I., Olsson, G., Khotyaintsev, Y. V., Eriksson, A., Kletzing, C. A., Bounds, S., Anderson, B., Baumjohann, W., Steller, M., Bromund, K., Le, Guan., Nakamura, R., Strangeway, R. J., Leinweber, H. K., Tucker, S., Westfall, J., Fischer, D., Plaschke, F., Porter, J., Lappalainen, K., (2016), The FIELDS Instrument Suite on MMS: Scientific Objectives, Measurements, and Data Products, *Space Science Reviews*, *199*, 105-135, doi:10.1007/s11214-014-0109-8

Tu, C.-Y., Marsch, E., (1995), MHD structures, waves and turbulence in the solar wind: Observations and theories, *Space Science Reviews*, *73*, 1-210, doi:10.1007/BF00748891

Vasyliunas, V. M., (1975), Theoretical models of magnetic field line merging. I, *Reviews of Geophysics and Space Physics*, *13*, 303-336, doi:10.1029/RG013i001p00303

Wilken, B., Axford, W. I., Daglis, I., Daly, P., Guttler, W., Ip, W. H., Korth, A., Kremser, G., Livi, S., Vasyliunas, V. M., Woch, J., Baker, D., Belian, R. D., Blake, J. B., Fennell, J. F., Lyons, L. R., Borg, H., Fritz, T. A., Gliem, F., Rathje, R., Grande, M., Hall, D., Kecsuemety, K., McKenna-Lawlor, S., Mursula, K., Tanskanen, P., Pu, Z., Sandahl, I., Sarris, E. T., Scholer, M., Schulz, M., Sorass, F., Ullaland, S., (1997), RAPID - The Imaging Energetic Particle Spectrometer on Cluster, *Space Science Reviews*, *79*, 399-473, doi:10.1023/A:1004994202296

Yamada, M., Yoo, J., Jara-Almonte, J., Ji, H., Kulsrud, R. M., Myers, C. E., (2014), Conversion of magnetic energy in the magnetic reconnection layer of a laboratory plasma, *Nature*, doi:10.1038/ncomms5774